Constructive generative design methods for qualified additive manufacturing

Zhiping Wang

Par

Zhiping WANG

Constructive generative design methods for qualified additive manufacturing

Acknowledgements

First and foremost, I own my deepest gratitude to my supervisor, Prof. Alain BERNARD, for his advice, guidance and full support during the last three years. I would like to thank him for providing me the freedom and flexibility on my research topic. Furthermore, his academic attitude and responsibility inspire me a lot to pursue a scientific career.

Many thanks to my co-supervisor, Dr. Yicha ZHANG, for his encouragement and patience. He always affords me lots of suggestions. Discussions with him give me a broad mind and guide me to the right directions. I deeply appreciate his time and share. Without his continuous encouragement and support, I would not be able to finish my Ph.D. topic.

I would like to express my warmest thanks to the members of the jury, Prof. James GAO, Prof. Daniel BRISSAUD, Prof. Nabil ANWER, Prof. Grégoire ALLAIRE, Prof. Charlie C. L. WANG, and Prof. Stefania BRUSCHI for their valuable comments. Great thanks to my reporters, Prof. James GAO and Prof. Daniel BRISSAUD, for their time on reviewing my manuscript and helping me to improve the quality of my research work.

Then, I would like to thank Shujie TAN, a PhD candidate from NUAA, for case study experiments. I also have benefited a lot from discussions with him about my research. The meaning suggestions from you have facilitated my research.

I am also very grateful to the colleagues in LS2N and Centrale Nantes. I also need to thank my dear friends in France. Our friendships will be treasures for my entire life. Besides, I would like to thank the financial support of China Scholarship Council (CSC) for my research work.

Finally, I would like to express my great appreciation to my family for their unconditional support.

Zhiping

Nantes

Abstract

Additive manufacturing (AM) technologies give more and more design freedom to designers and engineers to design and define highly complex geometries and material compositions. Due to a layer-by-layer processing, the constraints, methods, tools and processes of design in AM are different from that in traditional manufacturing processes. Traditional design methods and tools cannot meet the needs of design in AM. Therefore, a new research field, design for AM (DfAM), has emerged to serve this need. However, existing DfAM methods are either guidelines or pure computation-based, which have limited consideration of coupled constraints along the AM digital processing chain and are difficult to ensure manufacturability of design in AM. To obtain qualified design in AM, this research focuses on three typical existing problems in DfAM domain: Firstly, how to ensure manufacturability in (topology optimization) TO process? Secondly, how to design support structures with lightweight, easy-to-remove for post-processing and friendly heat-diffusion properties to ensure shape accuracy and improve surface roughness of printed parts? Finally, how to avoid accuracy loss in printing preparation of complex lattice structures and ensure their manufacturability in design?

To solve the three identified problems, this research developed a set of new constructive generative design methods: 1. CSG-based generative design method to ensure manufacturability in lightweight topology optimization; 2. Pattern-based constructive generative design method to optimize support structure design and 3. Toolpath-based inversed constructive design to directly obtain processing models of corresponding complex lattice or porous structures with qualified printing toolpaths. The three proposed methods can well embed AM process constraints, realize parametric control and save computation cost in design process to obtain a set of candidate design solutions with ensured manufacturability. A set of comparison studies with existing DfAM methods and a couple of experiment case studies in medical applications demonstrated the methods' advantages. These constructive methods may have large application potential to be adopted as design and decision making tools for other industrial applications when qualified DfAM is required.

Keywords: Design for AM; manufacturability; generative design; constructive design; knowledge-based system

Résumé

Les technologies de fabrication additive (FA) donnent de plus en plus de liberté de conception aux concepteurs et aux ingénieurs pour concevoir et définir des géométries et des compositions de matériaux très complexes. En raison d'un traitement couche par couche, les contraintes, méthodes, outils et processus de conception en FA sont différents de ceux des processus de fabrication traditionnels. Les méthodes et outils de conception traditionnels ne peuvent pas répondre aux besoins de la conception en FA. Par conséquent, un nouveau domaine de recherche, la conception pour la FA (Design for AM - DfAM), a émergé pour répondre à ce besoin. Cependant, les méthodes de DfAM existantes sont soit des lignes directrices, soit des outils de calculs, qui ont une prise en compte limitée des contraintes couplées le long de la chaîne de traitement numérique de la FA et peinent à garantir la fabricabilité de la conception en FA. Pour contribuer à l'obtention d'une conception qualifiée en FA, ce travail de thèse se concentre sur trois problèmes existants typiques dans le domaine du DfAM : premièrement, comment assurer la fabricabilité dans le processus d'optimisation topologique ? Deuxièmement, comment concevoir des structures de supports allégées, faciles à retirer pour le post-traitement et de diffusion de chaleur conviviales pour assurer la précision de la forme et améliorer la rugosité de surface des pièces imprimées ? Enfin, comment éviter les pertes de précision lors de la préparation de l'impression de structures en treillis complexes et assurer leur fabricabilité lors de la conception ?

Pour résoudre les trois problèmes identifiés, ce travail de thèse propose un ensemble de nouvelles méthodes de conception générative constructive : 1. Méthode de conception générative basée sur un modèle CSG pour assurer la fabricabilité dans l'optimisation de la topologie de la structure allégée ; 2. Méthode de conception générative constructive basée sur des modèles pour optimiser la conception de la structure de supports et 3. Conception constructive inversée basée sur les « parcours d'outils » pour obtenir directement des modèles de traitement de structures poreuses ou de réseaux complexes correspondants avec des « parcours d'outils » d'impression qualifiés. Les trois méthodes proposées intègrent les contraintes de processus de FA, réalisent un contrôle paramétrique et économisent des coûts de calcul dans le processus de conception pour obtenir un ensemble de solutions de conception candidates avec une fabrication garantie. Un ensemble d'études comparatives avec les méthodes DfAM existantes et quelques études de cas expérimentaux dans des applications médicales ont démontré les avantages des méthodes proposées. Ces méthodes constructives peuvent avoir un grand potentiel d'application pour être adoptées comme outils de conception et de prise de décision pour d'autres applications industrielles lorsqu'un DfAM qualifié est requis.

Mots-clés : Conception pour la FA ; manufacturabilité ; conception générative ; conception constructive ; système basé sur la connaissance

Contents

List of Figures

List of Tables

Nomenclature

Abbreviation

3D	Three-Dimensional
AM	Additive Manufacturing
ASTM	American Society for Testing and Materials
BESO	Bi-directional Evolutionary Structural Optimization
CAD	Computer-Aided-Design
CAPP	Computer-Aided Process Planning
CIRP	Collège International pour la Recherche en Productique
CSG	Constructive Solid Geometry
DED	Directed Energy Deposition
DfAM	Design for Additive Manufacturing
FEA	Finite Element Analysis
FFF	Fused Filament Fabrication
GA	Genetic Algorithm
GD	Generative Design
LAM	Laser Additive Manufacturing
L-PBF	Laser-Powder Bed Fusion
MC	Marching Cubes
MMC	Moving Morphable Components
MMV	Moving Morphable Void
MS	Marching Square
NSGA-II	Non-dominated Sorting Genetic Algorithm-II
PSL	Principal Stress Line
PSO	Particle Swarm Optimization
RP	Rapid Prototyping
SIMP	Solid Isotropic Microstructure with Penalization
SLM	Selective Laser Melting
STL	STereoLithograph
TO	Topology Optimization
TPMS	Triply Periodic Minimal Surface
WAAM	Wire-Arc Additive Manufacturing

Chapter 1. Introduction

This chapter will give a general introduction on Additive manufacturing (AM) technologies and the main advantages of Design for AM are also summarized. In the next, research motivation and objectives will be highlighted. To facilitate the readers, a graphical structure of the whole PhD report is given in the end of this section.

1.1. Research background

1.1.1. Additive manufacturing techniques

Additive manufacturing (AM) is defined as a process of joining materials to directly fabricate physical models via three-dimensional model data, usually layer upon layer, as opposed to subtractive manufacturing methodologies [1]. In the past, AM is used to be called Rapid Prototyping and 3D printing. Rapid Prototyping (RP) is a term which includes a range of technologies for achieving a fast production of prototype models, with little need for human intervention [2-4]. This allows designers to check the assembly and function of the design as well as discussing downstream manufacturing issues with an easy-to-interpret, unambiguous prototype [2]. Hence, manufacturing errors can be minimized and development costs and lead times significantly reduced. However, with the development of this technology, the users of RP technology have realized that this technology cannot effectively describe more current applications. The label "Prototypes" is no longer suitable for this technology since functional parts can be fabricated directly in several specific AM machines. As a result, the international standards organization, American Society for Testing and Materials (ASTM), adopted a new terminology, Additive Manufacturing, to define the technology. In the manufacturing field, according to the way the product's shape was generated, all the manufacturing processes could be classified in three sets:

(1). Forming processes:

Those forming processes produce a part from the right amount of bulk material and deform it to the required shape, these kinds of processes include forging, stamping, drawing, extruding, etc. in solid state, as well as casting, injection molding, etc. in liquid or semi-liquid state [4]. There is no material added or removed in all forming processes (in a macro-scale).

(2). Material removal processes (Subtractive Manufacturing):

Subtractive manufacturing processes are used widely in manufacturing. These processes form a part by removing excess materials from a blank by using a set of sequential machining operations. The traditional way includes turning, milling, grinding, etc. Material removal processes can include material removal by electrical/chemical processes, etc.

(3). Material addition processes (Additive Manufacturing)

Additive manufacturing processes produce three-dimensional (3D) physical objects by adding materials piece-by-piece, line-by-line, surface-by-surface, or layer-by-layer [5]. According to ISO/ASTM [1], there are currently seven AM process categories: binder jetting, directed energy deposition, material jetting, powder bed fusion, sheet lamination and vat photopolymerzation. In addition, cold spraying has been added in this standard [6].

Though AM can be used to significantly shorten product development time and costs, it involves a large number of steps from a CAD model to a physical part. Figure 1.1 shows the main steps in most AM processes [7]. A CAD model is usually built by CAD solid modeling software. Since almost all AM machines can accept the STL file format, the CAD model usually will be converted into a STL file for the calculation of the slices even though some other new formats, e.g. AMF, 3AM, are emerging. Then, the STL file will be transferred to the AM machine. A set of AM machine parameters are set up based on the manufacturing constraints, material constraints, etc. Once all AM preparations are finished, the part will be built automatically. After completing the build, the part must be removed from the build base. Next, post-processing is carried out to remove the support and also involves heat treatment for metallic AM processes. Finally, part is ready for use. The prepared part may be assembled with other components to form a final product.
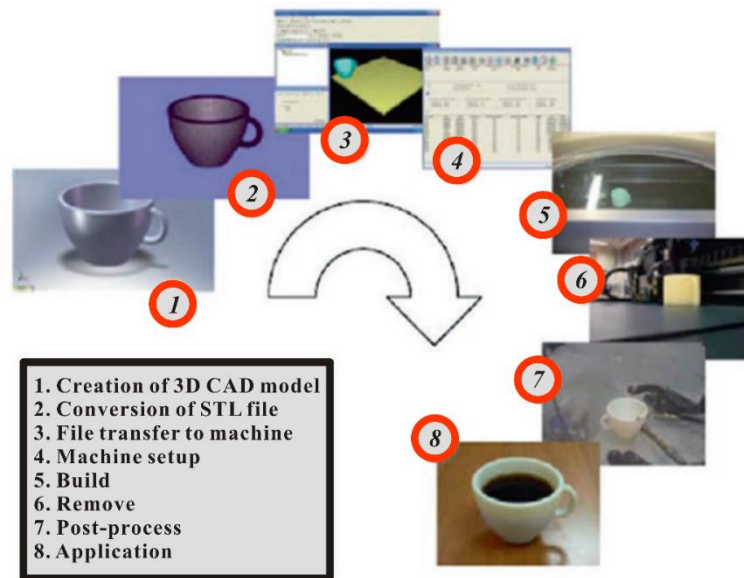
Figure 1.1. The generic process of a CAD model to a part. [7].

Due to the layer-by-layer building strategy, the unique feature allows production of complex or customized parts directly from the design without the need for expensive tooling or forms such as punches, dies or casting molds and reduces the need for many conventional processing steps [8]. Intricate parts can be produced in one-step without the limitations of traditional manufacturing processing. In addition, the count of the part can be reduced by part consolidation. Furthermore, parts can be fabricated on demand, therefore lead time is decreased, especially for critical or obsolete replacement components. Based on these reasons, AM is now widely accepted as a new digital manufacturing paradigm for the design and production of high performance components for aerospace, medical, energy and automotive applications [8]. Applications of conventional manufacturing processes in industry are mainly driven by costs and opportunities [9]. The use of AM can provide a nearly unlimited freedom of design in the manufacturing process chain. Figure 1.2 displays the influence of geometrical complexity on the final production costs. Compared to the conventional manufacturing technologies, such as milling, the cost of AM processes only slightly increases with complexity in geometry. This specific relation is especially suitable for small series production and for parts with higher geometric complexity. Therefore, it is necessary to take DfAM thinking into account in order to get more benefits from the design freedom of AM and make manufacturing processes economically competitive in the future. This also means that a fairly fundamental redesign of parts has to be performed. [9]
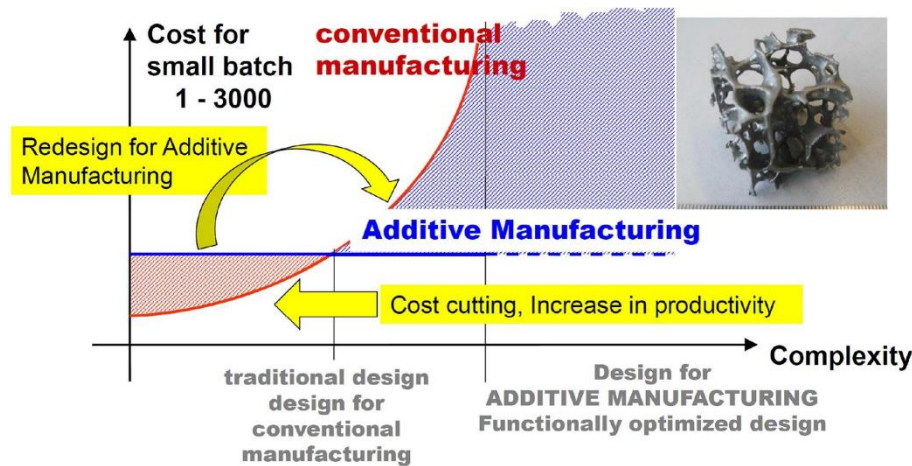
Figure 1.2. Freedom of design by AM. [9].

1.1.2. Design for Additive Manufacturing

Compared to conventional manufacturing processes, AM processes give more freedom to designers and engineers to enable them to produce highly complex geometries and material compositions [10, 11]. Since parts are fabricated layer by layer in AM processes, design knowledge, tools, rules, processes, and methodologies have set them apart from traditional manufacturing processes [5]. Therefore, design for additive manufacturing (DfAM), a new research field investigating design methods and tools in AM processes, has emerged to consider the manufacturing constraints within the design process [12-14].

Given the unique capabilities of AM, the main objectives of DfAM can be described as: "Maximize product performance through the synthesis of shapes, sizes, hierarchical structures, and material compositions, subject to the capabilities of AM technologies [10]." These unique capabilities include:

- **Shape complexity:** For conventional manufacturing processes, such as machining, tool accessibility is a key bottleneck that impacts the part complexity. However, the layer building way makes AM enable to build almost any complex shape [15].
- **Hierarchical complexity:** Due to the unique building strategy, AM enables to achieve the design of hierarchical complexity across multiple length scales. This includes part-scale macrostructures, mesostructures and nano-/microstructures [10, 15].
- **Functional complexity:** Functional devices can be fabricated directly in one build or by pausing the process to embed components and kinematic joints assembly [10, 15].
- **Material complexity:** AM technologies are able to change material composition gradually due to the layer-by-layer building strategy. A significant issue hindering the adoption of AM's ma-

terial complexity is the lack of design and CAD tools that enable representation and reasoning with multi-materials [15].

Due to the tremendous design potential waiting for designers to explore, "Design for AM" has received intensive attention as a means of broadening the freedoms and benefits of AM technologies [5, 14-16]. It can integrate multiscale structures, ranging from material-scale design with microstructural complexity to part-scale design with macrostructural complexity. Hence, AM processes can produce highly complex and lightweight structures with complex surfaces both internally and externally [14].

In general, a successful design for AM should be based on the interaction between engineering design, material science and manufacturing. As stated in [5], "The coupling between the design, representation, analysis, optimization, and manufacture still needs to be solved." Design methodologies based the material-structure-performance integrated AM (MSPIAM, shown in Figure 1.3) may deal with the extensive challenges of DfAM. The unique capability of AM enables us to consider more coupling elements into the DfAM framework.
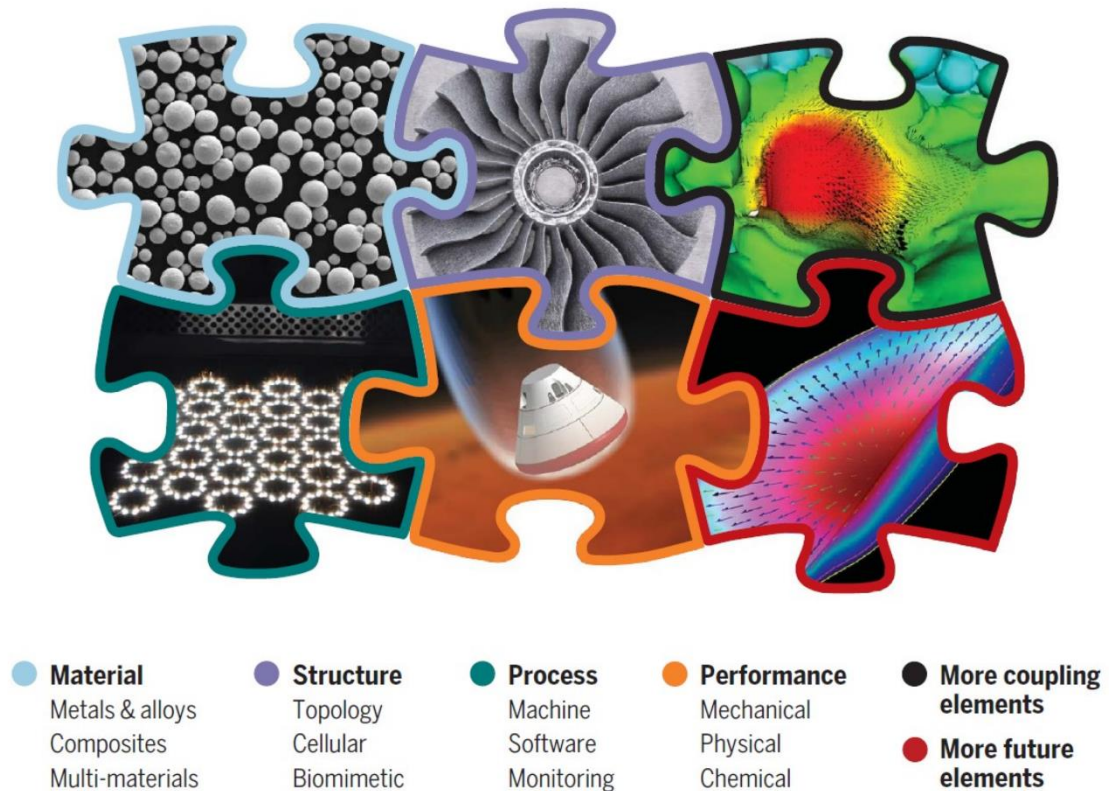
Figure 1.3. Material-structure-performance integrated additive manufacturing (MSPI-AM) framework. [16].

With the development of AM, lightweight design always has been a hot topic in structural engineering. Traditionally, lightweight design can be defined as "the science and the art of making things—parts, products, structures—as light as possible, within constraints"[17]. However, lightweight design is not the only objective or application target of AM processes. Part consolidation and functional improvement with AM have also obtained many attentions from industry and academy.

For AM processes, there is no clear relationship between the complexity of the part and the associated production cost. As a result, traditional design tools are hard to meet the requirement of lightweight design. Hence, good design tools need to be explored to support the huge design potential. There are generally four main groups of methods for lightweight design in AM [14]. It includes topology optimization, generative design, lattice structure configuration and bio-inspired design. These methods will be introduced in the next chapter in detail. The research scope of this work will be limited in lightweight design, especially topology optimization, generative design and lattice structure design, and do not pay much attention on part consolidation and functional design issues.

1.2. Research motivation & objectives

Although varieties of design methods are developed to explore the design potential of AM processes, there are many constraints that need to be considered, as that for all other technologies. The general motivation of this thesis is to explore the development of new design methodologies along the full processing chain for qualified design in AM. Based on current situations about DfAM, several research problems are summarized below.

a. Manufacturability and decision-making problem for TO:

To explore more design space, some new design methods have emerged to fully grasp the benefits of AM [14]. Topology optimization is one of the most popular methods in lightweight design methods. Although topology optimization has great potential to exploit the design freedom provided by AM, AM processes cannot always print the obtained structures with successes. This is primarily because AM still has some manufacturing constraints which need to be considered in the topology defining process. Therefore, manufacturing-oriented topology optimization for AM has seen a significant interest since industrial applications can only accept qualified design solutions. In addition, structural optimization problems in industry are usually constrained by multiple conflicting objective functions and boundary conditions in FEA. Nevertheless, most existing TO methods can only provide a single topological result

for a given optimization problem. Many of the existing optimization methods convert a multi-objective optimization problem into a single-objective optimization and obtain one particular solution at convergence. Therefore, these methods naturally eliminate other non-dominant solutions in the solution space. Due to the conflicting nature among the predefined objectives, there is a need of a Pareto-optimal set representing trade-offs for further decision making according to diverse preferences for specific requirements and compromise in engineering applications.

b. Qualified-oriented AM preparation for support structure generation

In the pre-processing, there are a couple of complicated decision-making problems. For example, for L-PBF process, support structure is needed to support the part to be printed. Support structure can also act as heat diffusion mediums and thermal distortion resisting structures [18, 19]. In addition, for many application domains, e.g. dental parts, the removing of support structures is usually manual because these components are fragile, and it is hard and costly to design special fixtures for these components in the machining of the post-processing stage. Dense support structures may have good sustaining qualities to overhang area and are able to resist the thermal stress better. However, this may increase the consumption of raw materials and cause difficulty for heat transfer, support cutting, tool accessibility constraints and extra cost for the support contact area repair in the post-processing stage. While sparse support structures could reduce the amount of raw materials, there is a risk of severe deformation caused by thermal and residual stress or even surface collapse with printing failure due to insufficient withstanding strength and heat diffusion performance. Therefore, it becomes a critical issue to design support structures with lightweight, easy-to-remove for post-processing and friendly heat-diffusion properties to ensure shape accuracy and surface roughness of printed parts.

c. Accuracy loss and computational efficiency for lattice structures

Since AM has unique capabilities, it enables to fabricate many complex lightweight or functional structures. Lattice structure filling shows lots of benefits by replacing solid volumes for optimal design solutions. Currently, the preparation process in traditional AM processing chain can be summarized as CAD model building, STL file conversion, and toolpath infill before printing. STL model conversion and slicing can lead to loss of shape accuracy and surface quality, while unqualified toolpaths may cause printing failures, e.g. pores or re-melting in the L-PBF process. These three stages will not only cause the loss of geometrical accuracy and also consume much computational time and memory, especially

while slicing and toolpath filling. Moreover, as the accuracy requirements increase and the size of parts increases, it is much easier to cause manufacturability uncertainty in AM preparation stages.

To summarize briefly, the scope of this research is to exploit generic DfAM methods for AM's manufacturability. This work will take AM manufacturing constraints into the design methodologies, so it will be more focused on AM stages and not include main post-processing constraints as well as many factors in product life cycle stages. The main objectives of this work is to develop novel design thinking (constructive design) that fits on natural AM processes, to use knowledge-based methods for qualified AM design, and to achieve design automation and decision-making assistance for designers and engineers.

1.3. Structure of the thesis

After the brief introduction to AM technologies and DfAM, a literature review will be conducted in Chapter 2 to gain a comprehensive understanding to the design methodologies for AM. The design methodologies for AM are summarized into three aspects: macroscale design, mesoscale design and microscale design. In the macroscale design, the thesis will focus on three issues: topology optimization, generative design and support structure design. In the mesoscale design, lattice structure configuration will be discussed. For the microscale design, different types of toolpath scanning strategies will be listed. Based on the literature review in the three aspects, main research problems will be summarized and highlighted. The main contributions of this thesis will be reported from Chapter 3 to Chapter 5.

- **Chapter 3:** This chapter will give a novel constructive solid geometry based generative design method for AM to facilitate AM constraint embedding and improve the performance of topological optimization for AM. The proposed method can generate a topology geometry with smooth boundaries and parametric control in an additive manner. MOEA is used to obtain a set of optimal non-dominated design solutions for the designers' further decision-making.
- **Chapter 4:** A support point determination method will be introduced to optimize the support point distribution on the support relevant overhang areas. Support points on three kinds of overhang areas, overhang point, overhang edge and overhang face, will be discussed respectively. Meanwhile, a bio-inspired tree-shaped support structure design method will be proposed to generate lightweight, easy-to-remove and heat-diffusion-friendly biomimetic support structure. In addition, two kinds of lattice configuration methods are developed to further reduce the sup-

port volume. The whole set of methods form a generic pattern-based design method for light-weight and qualified AM support structure design.

- **Chapter 5:** Toolpath-based inversed constructive design methods will be proposed to design lattice structures in 2D and 3D in this chapter. A combined scanning strategies will be conducted to generate thickness-varying Voronoi lattice structures in 2D. The proposed method uses toolpath to construct a topology shape directly without any model conversion. Meanwhile, a knowledge-based toolpath configuration design method will be developed to generate high-precision graded TPMS lattice structures. It integrates implicit modeling, variable distance field, direct slicing and fine toolpath configuration to construct different types of qualified toolpaths without any intermediate steps.

In the last chapter, the conclusion will be drawn and research perspectives will be also discussed in the end of the thesis. The outline of the thesis is provided as shown in Figure 1.4 to guide the reader.
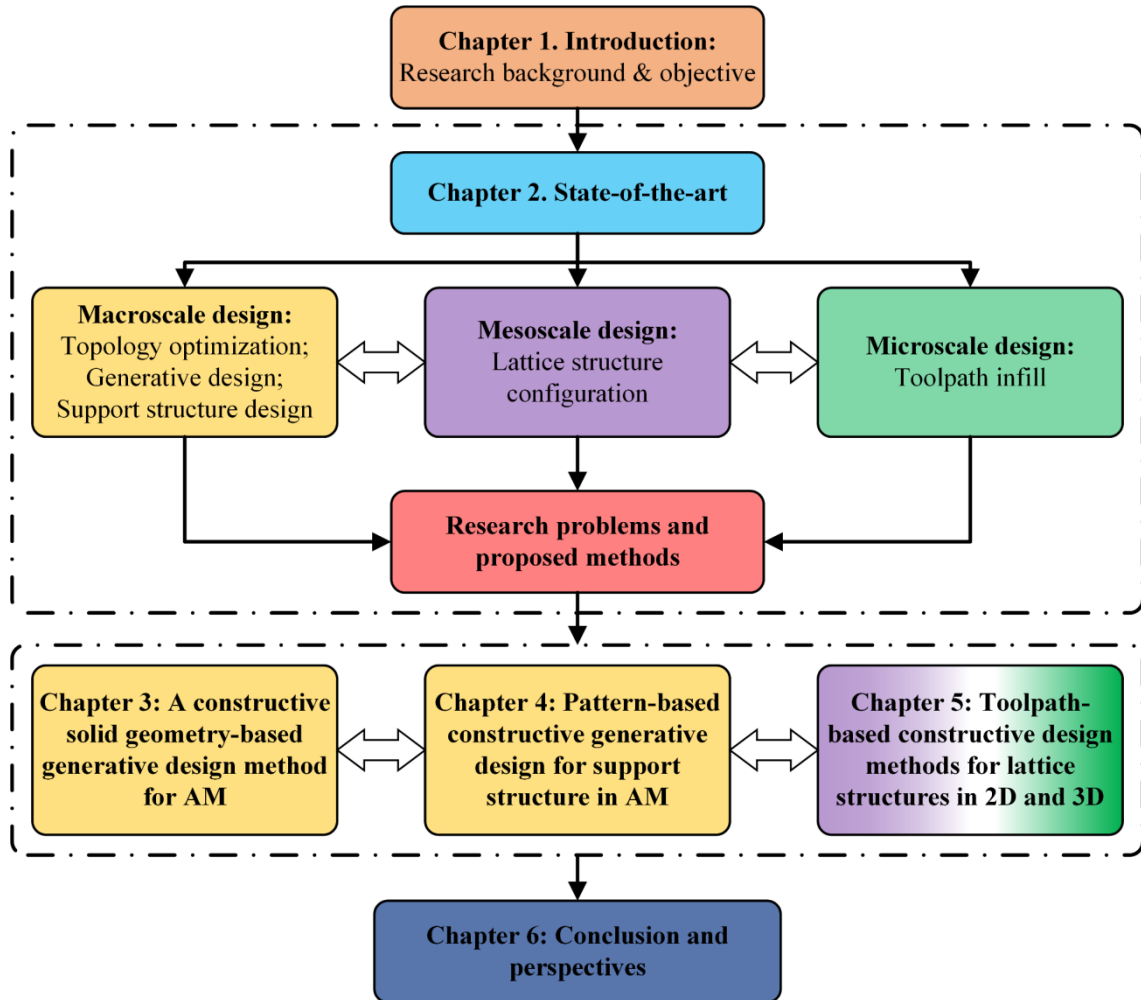
Figure 1.4. Thesis outline and structure.

Chapter 2. State-of-the-art & research questions

In this chapter, a comprehensive review is conducted to investigate the main computational design synthesis methodologies for AM, such as Topology Optimization, Generative Design, Support Structure Design, and Lattice Structure Configuration, to exhibit the current gaps in DfAM. Based on these identified gaps, the concrete research questions for this PhD study are set.

2.1. Design for Additive Manufacturing

Due to the non-linear relationship between the complexity and manufacturing cost, AM technologies have the potential to fabricate significantly complex and lightweight structures [5]. Hence, AM processes give more freedom to designers and engineers to enable them to design highly complex geometries and material compositions [10]. Although AM has gained popularity, it is still a challenge for designers to fully understand the unique capabilities of AM as well as the process-related constraints. Design for Additive Manufacturing is a design practice to encourage designers to explore new design concepts and develop new designs through exploring the unique capabilities of AM [15]. Qualitative design rules or guidelines and quantitative design evaluation frameworks were proposed for DfAM [10, 20-26]. These methods can help designers and engineers to obtain a design solution that meets limited AM constraints for manufacturability requirements, but has less optimization. However, to further benefit from AM, design methods involving structural optimization for AM should not only consider manufacturability, but also need to improve the functional performance of AM parts via quantitative justification, e.g., simulation and calculation, as well as lightweight improvement. As such, designers can exploit more design potential and have more freedom. Figure 2.1 shows a potential problem formulation for DfAM framework [10].
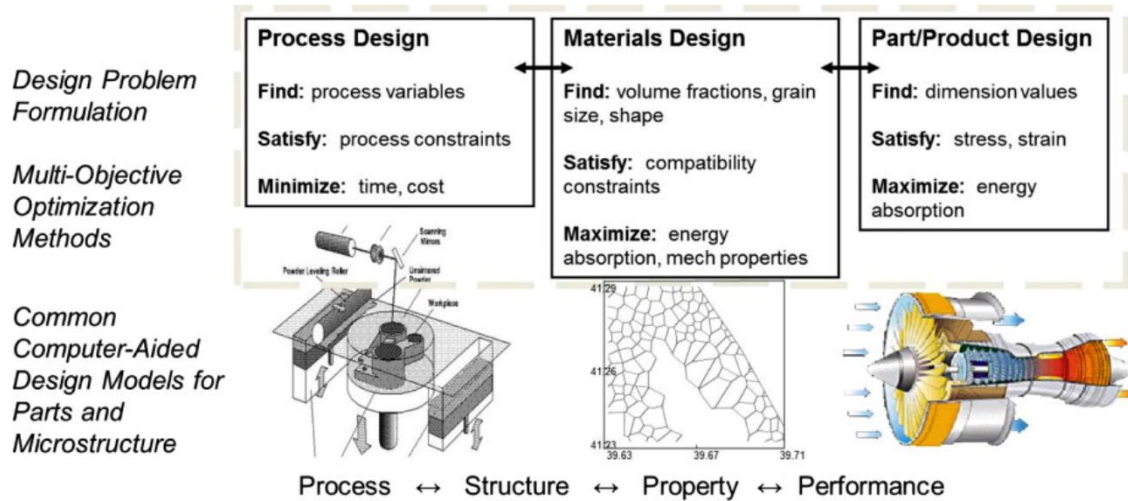
Figure 2.1. A process-structure-property-performance design problem formulation for DfAM. [10].

Design for Additive Manufacturing is about design for the whole AM product life cycle [14]. The framework of methods for DfAM shows a strong interaction between the life cycle stages and AM product design. To make the use of the design freedom of AM technologies, the existing methods for DfAM can be divided into to three aspects: rule-based, computation-based and hybrid methods. For rule-based methods, a set of design rules or cases are used to represent the design knowledge of AM to guide the design process. Different types of features are measured to analyze the manufacturability. For computation-based methods, a great amount of mathematical computation/simulation methods are used to automatically determine and define geometric elements for design solutions. Main lightweight design methods, such as topology optimization, generation design and lattice structure infill, are considered to belong to computation-based methods. Hybrid methods are defined as combining the two kinds of methods to generate design solutions.

Rule-based DfAM method

Although AM provides big potential and benefits for product design, it becomes a critical issue to understand design rules for AM [25]. To support a suitable design for AM, a design rule catalog was summarized in [25]. The main design rules are developed based on standard elements (e.g. cylinders, joints and overhangs). There are three types of groups defined in their work, basic elements, element transitions and aggregated structures. To measure the manufacturability of the standard elements, different attributes were assigned so as to examine the suitable ranges for different settings of attribute values. For laser AM process in TiAl6V4, a comprehensive design guideline was derived based on the results of experiments in [23]. Typical basic geometries were identified and built by LAM. The experimental investigations summarized the influence of part position and orientation on the dimension accu-

racy and surface quality. The design guidelines can exploit the geometrical freedom of AM process and broaden the industrial applications.

Due to the unique capabilities of AM technologies, design rules for AM can potentially improve design to process transitions thought the synthesis of shapes, sizes, hierarchical structures, and material compositions [21]. It can provide an insight into manufacturability during design and process planning. The main AM design features categorized are reported in Table 2.1 [21]. A *Guide-to-Principle-to-Rule (GPR)* approach was proposed based on the *Design Rules* from *Design Principles* in turn derived from *Design Guidelines and corresponding Design Fundamentals*. In this approach, Design Rules are developed by Design Principles, which also provide the means for existing design rules to be modified, extended or reconfigured so as to support individual needs or to promote wider applications. The GPR approach has potential to identify best-practices, correlations between process parameters, process signatures, and product qualities to extract *Design Principles* to help derive *Design Rules* for all platforms of AM [21].

Table 2.1. Design features reported in [21].

Geometric features	Freedom surfaces	Pass-fail features	Mechanical features	Related measurements
Cubes	Free flowing geometry	Thin walls	Fillet	Surface roughness
Hollow cubes	Intricate	Thin slots	Chamfer	Accuracy
Flat beam	Uniform	Slim cylinders	Gaps	Linear accuracy
Cylindrical holes	Non-uniform	Small holes	Blend	Flatness
Solid cylinders			Bracket	Straightness
Hollow cylinders			Cavities	Parallelism
Eclipse			Bores	Repeatability
Spheres				Roundness
Cones				Cylindricity
Slots				Concentricity
Holes				Symmetry
Inclined				Taper
Surface				Repeatability of radius
Overhangs				
Plates				

Computation-based DfAM method

Current solid modeling-based CAD systems have several disadvantages that limit the use of AM technologies. The main challenges of traditional CAD modeling can be stated as [15]: 1. Geometric complexity: hard to create new shapes and complex structures; 2. Property representation: hard to represent desired distributions of physical and mechanical properties for their physical basis; 3. Material representation: difficult to represent material compositions and distributions. These challenges in CAD modeling will be a huge bottleneck to widespread adoption of AM [15].

To take advantage of the unique capabilities of AM machines, more design freedom needs to be explored. Hence, knowledge-based methods can not satisfy the designers' requirements. Variable computation-based methods are developed to achieve the requirements of lightweight designs. One main difference between rule-based and computation-based methods is that the former tends to guide design based on experiments and knowledge, while the latter is more inclined to explore the design space followed by a great amount of computation iterations considering AM constraints. Take support structure design as an example, rule-based methods usually use simple standard geometries to support overhang areas and computation-based methods can search for more lightweight support design solutions driven by computational approaches, such as using parametric tree-shaped generative design method [27].

The unique capabilities of AM have inspired designers and engineers to design lightweight structures without regard to geometric complexity. Lightweight design has been a hot topic in structural engineering as AM techniques become more mature. Current lightweight design methods for DfAM are identified as topology optimization, generative design, lattice structure filling and bio-inspired design in [14].

Both DfAM methods can help explore the benefits of AM. The third method can be realized as a hybrid DfAM method, usually combines the rule-based and computation-based methods to design solutions. The hybrid method has more potential to apply DfAM rules and guidelines to achieve a lightweight design with ensured manufacturability.

In this thesis, main computation-based DfAM methods for lightweight design are reviewed. The following subsections will review the representative works from literature in five main categories: topology optimization, generative design, support structure design, lattice structure configuration and toolpath configuration.

2.1.1. Topology Optimization for Additive Manufacturing

Topology optimization (TO) is totally different from shape optimization and size optimization as it can obtain more complex shapes as shown in Figure 2.2 [28]. It is used to answer to the fundamental engineering question: how to find an optimal material distribution within a given design space for a given set of constraints [29]. Generally, TO is driven by an objective function to maximize the mechanical properties at a minimum material use. Finite element analysis (FEA) is performed typically to update the design solution during each iteration. Since TO can obtain a wide range of shapes, AM can provide an advantageous route for part fabrication. The shapes produced by TO are often too complex for traditional manufacturing [15].
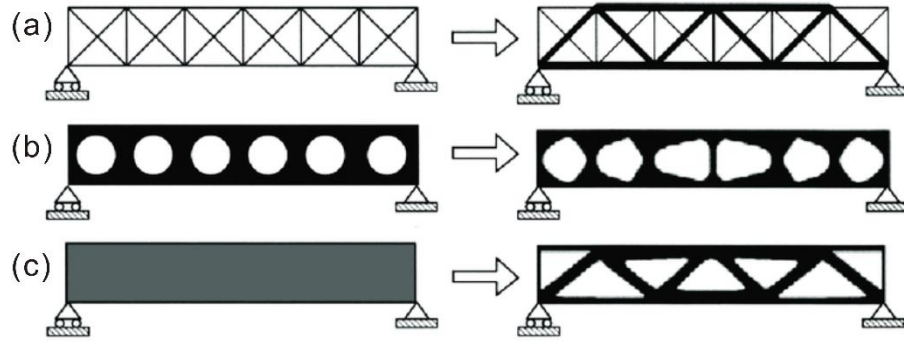
Figure 2.2. Three categories of structural optimization [28]. (a). Size optimization; (b). Shape optimization and (c). Topology optimization.

2.1.1.1. Incorporating manufacturing constraints into topology optimization

AM processes can bring more design freedom to realize extremely complex geometries, but still have manufacturing limitations or constraints. These should be considered in the topology optimization process to guarantee manufacturability when designing for AM. One of the most important constraints is the support structure for many powder bed based processes, e.g. Selective Laser Melting (SLM). In general, a support structure needs to be designed to sustain the overhang areas during the printing process. Support structure wastes print time and material. In addition, the removing of these structures in the post-processing stage is still challenging and costly. Therefore, design self-support or support-free structures is desirable.

Due on the popularity of density-based TO method, most studies investigated self-support structure for TO are based on density filter-based methods. There are two main methods to obtain self-supporting structure in density-based TO methods. A direct method for obtaining a self-supporting structure is to add additional materials to regions that do not meet self-supporting criteria. Leary [30] proposed a density-based support-free structure generation method by changing the optimal geometry to meet the angle constraints. The method is a post-processing approach which alters the mass and performance of the original optimal part as shown in Figure 2.3(a). Other research has concentrated on integrating overhang constraints with density-based TO methods. The main idea is to transform AM constraints into a filter that incorporates the characteristics of a generic AM process. A filter-like projection function was introduced by Gaynor and Guest [31, 32]. The projection-based topology optimization scheme can guarantee the maximum printable angle as shown in Figure 2.3(b). One of the limitations in the method is that the topology variables are multiple non-linear functions. Hence, it may cause convergence issues for complex design problems.
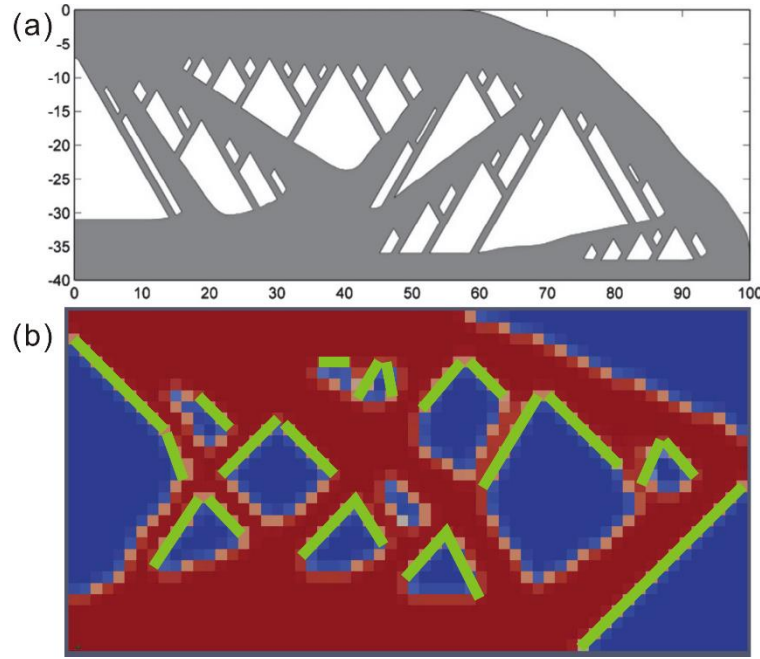
Figure 2.3. Two categories of self-supporting TOM methods. [30, 31].

To decrease the computational cost of both the filter and its sensitivity analysis, Langelaar [33] proposed a nonlinear spatial filter that imitates the powder-bed-based AM process. The proposed AM fabrication model was defined on a regular mesh. The method has also been implemented in 3D topology optimization problems [34]. It can generate self-supporting designs that respected the specified critical overhang angle for a specific building orientation.

Wang et al. [35] proposed a density gradient-based boundary slop constraint (density filter) method to control the overhang angle. The boundary slope of a part can directly affect the amount of the support structure and also has a direct relation with the resulting surface roughness. A heat conduction problem was used to demonstrate the effectiveness and efficiency of the proposed formulation in controlling boundary slopes. The AM filter proposed by Langelaar [33] was used by several authors. Barroqueiro et al. [36] addressed the minimum feature size and overhang angle constraints in a simplified fabrication model using an AM filter. Fu et al. [37, 38] integrated a smooth boundary representation with an AM filter to solve overhang constraints with SIMP. A slightly extended version of the AM filter was used by Thore et al. [39]. Zhao et al. [40] proposed an explicit local constraint for a density-based TO problem. By efficiently detecting the overhang regions using discrete convolution, the number of unsupported elements is required to be zero. Due to the linear sensitivity that only depends on the design density, the method has a higher convergence rate.

While some other studies have attempted to design self-supporting structures based on geometric feature-driven topology optimization, such as the Level set method [41, 42], the Moving Morphable Components (MMC) method [43, 44] and the Moving Morphable Void (MMV) methods [45]. Allaire et al. [46] addressed the self-supporting design using a level set method. They proposed an implicit constraint function based on a simplified model for the manufacturing. However, the method cannot fully eliminate the overhang. Wang et al. [47] proposed a single domain integral form to detect the overhang constraints for a level set method. By comparison with density-based methods, the level set approach can obtain smoother geometrical information of the structural boundary but would encounter more difficulties regarding convergence. MMC and MMV methods establish a direct connection between structural topology optimization and CAD modeling [43]. These methods are different from the traditional TO methods by eliminating materials from the design domain. The optimal topology structure is obtained by using a gradient-based optimization method. Based on the explicit characteristics of MMC and MMV, Guo et al. [48] established and optimized a set of explicit geometry parameters to obtain the self-supporting structure. Figure 2.4 show the level set method and MMC method.
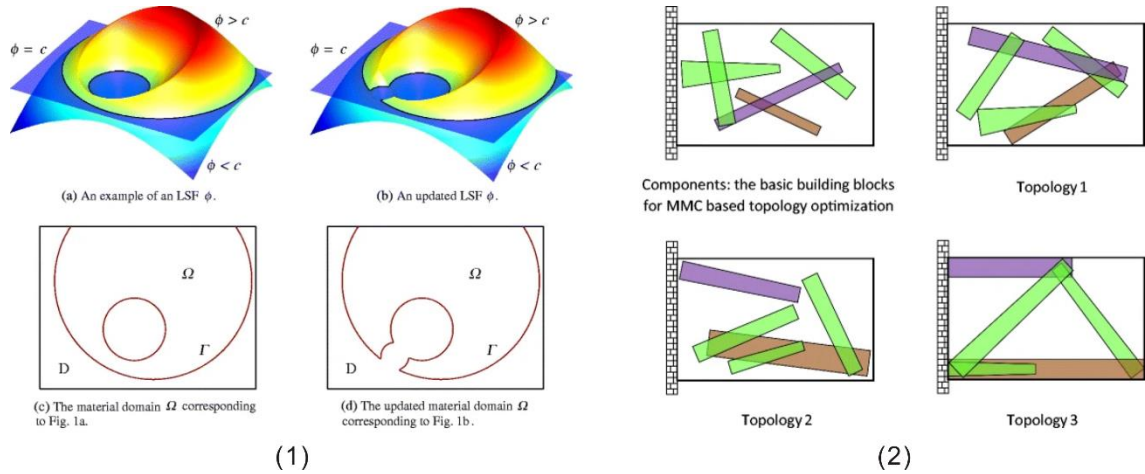
Figure 2.4. (1). Level set method [42]; (2). MMC method [44].

For these investigations discussed above, main self-supporting TO methods were listed to integrate AM constraints into TO methods. The self-supporting structures obtained are self-supported in the design domains. Although the use of support structures is avoided in printing, it is hard to ensure an optimal design solution. In [49], the authors proposed a TO framework that leads to designs with reduced support structures. A simple vertical structure was assumed to provide support. The support sensitivity was integrated into performance sensitivity to lead to a TO result that maximizes part performance, subject to support structure constraints. To obtain a better compromise between necessary support structure and part performance, an improved TO method was proposed in [50]. The proposed method is also capable

to integrate AM overhang restriction and post-machining considerations into component-support TO method. AM constraints have a direct effect for TO results. There are a couple of complicated decision-making problems in the AM pre-processing, e.g. build orientation determination [51], support structure generation, slicing and printing path planning, etc. These tasks are defined as CAPP (computer-aided process planning) stages, which have a direct impact on the feasibility, suitability and stability of AM [52]. A combined optimization method was proposed to integrate the optimization of self-support geometry, support layout and the build orientation determination into the density-based TO method in [53]. The improved method allows designers to obtain a tradeoff between manufacturing cost and part performance. Figure 2.5 shows the three TO methods.
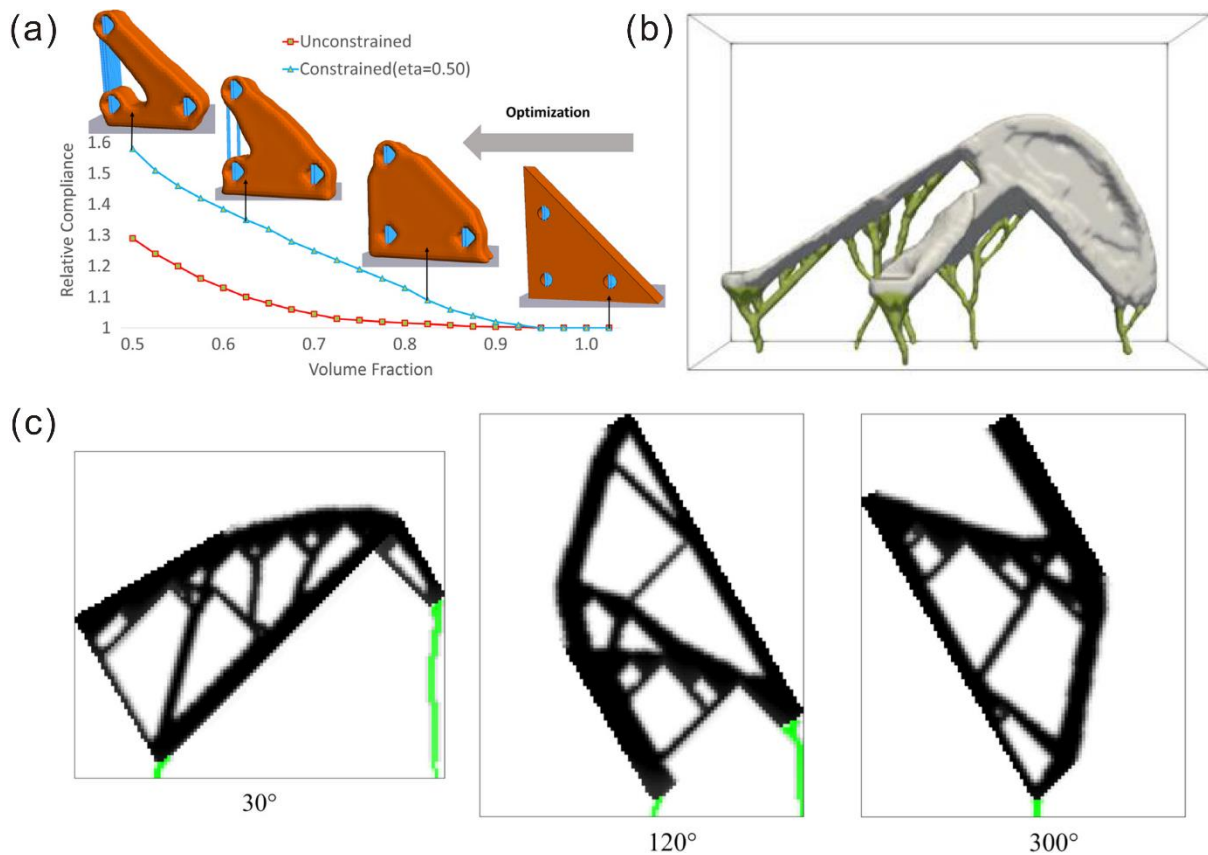
Figure 2.5. (a). Unconstrained and constrained Pareto curves for a bracket optimization [49]; (b). Topology optimized component (white) and support layouts (green) for a case [50]; (c). Fixed-orientation AM-restricted TO results for 3 different orientations [53].

Based on the above observations, almost all existing AM-oriented TO methods use gradient-based optimization by using mathematical programming or shape sensitivities to update and drive the geometry topology to optimality. Although the gradient-based methods are efficient with respect with function evaluations [54], a gradient is not easy to obtain due to the complexity of engineering problems. Compared to gradient based TO methods with local searching, evolutionary-based TO methods are based on

evolutionary algorithms which have more potential to identify global optima for multi-objective problems [55, 56]. Evolutionary algorithms can run more efficiently by using parallel computing [8]. In addition, the rapid development of computing hardware, like Graphics Processing Unit (GPU), also opens up new possibilities to accelerate these solvers. The following subsection reviews this category in detail.

2.1.1.2. Evolutionary computation for multi-objective topology optimization

In engineering optimization problems, there are large numbers of conflicting objectives, such as obtaining maximum compliance and minimum mass for the final design. Traditional optimization methods usually convert a multi-objective problem into a single-objective problem by converging one particular single solution on the Pareto frontier. Compared to mono-objective optimization problems, the presence of multi-objective optimization problems paves a way to obtain a set of so-called non-dominated alternative solutions, widely known as Pareto-optimal solutions, instead of a single optimal solution for better decision making. Such Pareto-optimal solutions give more options for designers to select the one that best fits their needs and requirements [57]. One powerful method to obtain a Pareto-optimal set is to utilize metaheuristics-based techniques, such as multi-objective evolutionary algorithms, multi-objective particle swarm optimization. Metaheuristics, e.g. randomized black box algorithms can solve problems with non-linear and non-differentiable objectives. Evolutionary algorithms are one type of the popular metaheuristic algorithms. They are biologically inspired algorithms based on the concepts of genotype and phenotype. The phenotype (or individual) is a population of candidate solutions of an optimization problem. The genotype is defined as a set of variables that can be mutated and altered. In evolutionary algorithms, phenotype (solutions) are encoded into the genotype (variables) where operators are used. Eiben and Smith [58] give a definition of representation, "mapping from the phenotypes onto a set of genotypes". In geometric topology optimization, the representations for evolutionary computation proposed in [55, 56] are categorized into three types: grid, geometric and indirect representation, as shown in Figure 2.6.
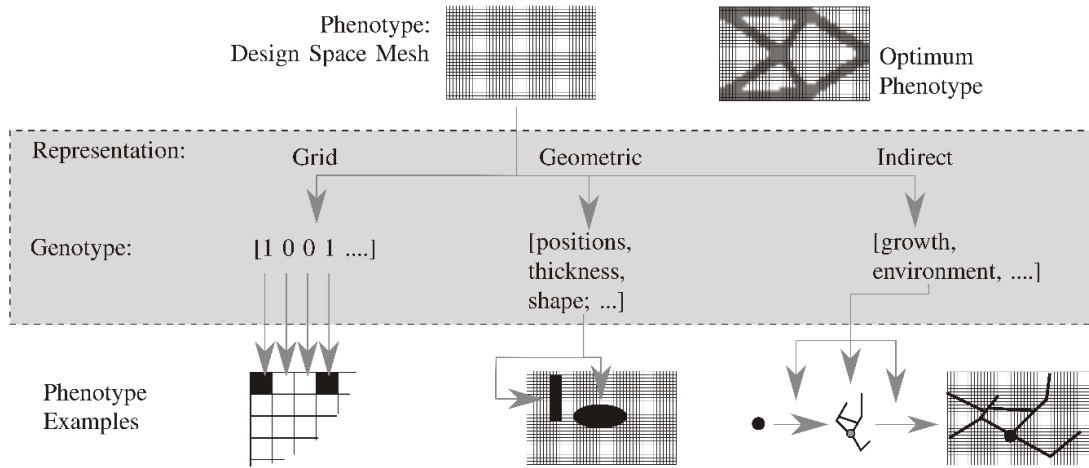
Figure 2.6. Three types of representations for evolutionary-based topology optimization. [55, 56].

In grid representation, the genotype encodes properties of fixed locations in a grid that decomposes the design space. The representation is applied in density-based topology optimization. In indirect representation, the genotype encodes variable properties of a generative model which implicitly defines material locations or geometry. The Lindenmayer system (L-system) [59, 60], neuro-evolution [61] and compositional pattern producing networks (CPPNs) [62] are applied in order to obtain topology structures. In geometric representation, the genotype encodes properties of a set of fixed or movable shape primitives that define the geometry of the structure within the design space. Properties of the shape primitives are position, shape or thickness, et al. The potential of structural complexity depends on the number of primitives. Voronoi-cells [63], Delaunay-triangulation [64, 65] and the Level set methods belong to the geometric representation.

Although evolutionary-based algorithms are widely used for multi-objective topology optimization [66-68], they are not sufficient or efficient enough to deal with many thousands of design variables when applied to large-scale optimization problems [57]. Traditional evolutionary-based topology optimization methods, e.g. the density-based method, operate the design space divided into many small elements and uses the gradient information (local stresses and strain energy densities) to improve the search updates. However, large quantities of small elements cause a great deal of design variables that limit its effectiveness and convergence. In order to improve the efficiency and convergence for topology optimization algorithms, a critical issue for evolutionary-based topology optimization method is to reduce the design variables [54, 55]. Therefore, it is essential to choose the suitable topology representation. In grid representations, the structure is represented by fine grid elements (up to several million). Within the vast search space, it is impossible to obtain the convergence to the global optimal within reasonable computational efforts. Compared to grid representations, geometric representations [55] can reduce the

dimensionality of the design space significantly. Although many evolutionary algorithms have been applied in topology optimization problems, the manufacturing constraints for AM processes have rarely been mentioned.

2.1.2. Generative Design for Additive Manufacturing

Generative design methods, a set of design exploration methods, are widely known in architectural [69] and industrial design. There are many explanations for generative design methods, including shape grammars [70], L-system, cellular automata [71], etc. In structural design, evolutionary algorithms are usually applied to generate design solutions that are close to predefined objectives and criteria [14]. A generative CAD based design exploration method was proposed in [72]. The proposed method can help designers to develop design possibilities from early conceptual to detailed stages of design. By using geometric filters, designs with unacceptable performance can be eliminated that can release the selection load on the designers. In addition, the selected designs can be further improved or modified manually by designers. Figure 2.7 shows a genetic model of MP3 player and a selection of the generated & fine-tuned MP3 player designs. To explore AM design solution space, a data visualization dashboard was developed to understand the tradeoff among any performance indicators [73]. The proposed visualization tool was composed of a web-based three stage interactive dashboard that allows the designer to compare numerous design solutions. A case study was developed to analyze a number of evaluation criteria including AM elements such as part manufacturability and cost. By understanding DfAM knowledge and using the interactive visualization tool, designers can make decision better to select more suitable design solutions.

Figure 2.7. A genetic model of MP3 player and a selection of the generated & fine-tuned MP3 player designs. [72].

Instead of focusing on one optimal solution such as traditional TO, generative design can populate a large number of design solutions from the design space for designer's reference and further decision making. Hence, the application of a generative design method for topology optimization may avoid the existing limitations, such as mono-optimal solutions, difficulties in obtaining gradients, etc., of conventional TO methods as discussed above. Recently, a set of commercial software provides new functions of the generative design method for AM processes in their structure design module, such as Autodesk and Altair. However, these tools, based on traditional multi-objective topological optimization, only alters the way of removing materials from the design space to populate alternative solutions, most of which are invalid. Key manufacturing constraints of AM processes have been ignored in the material removing procedure. The result is that these commercial tools usually generate very complex geometries without validation for manufacturing. Hence, designers have to use their own knowledge to evaluate and select the optimal solution from the large number of populated non-valid alternatives, which is quite difficult for operation in design practice. In the academic community, similarly, quite few researchers have considered the manufacturing constraints in generative design algorithms. In [74, 75], a new design methodology using generative multi-agent algorithms for AM process was developed to mimic termite colony behavior. The proposed generative design tool can simultaneously design, optimize and evaluate the manufacturability of an AM concept part. It provided a new method to preserve manufacturability and required functionality. Figure 2.8 shows the proposed method. However, the method only takes support structures as the only AM constraint.

22
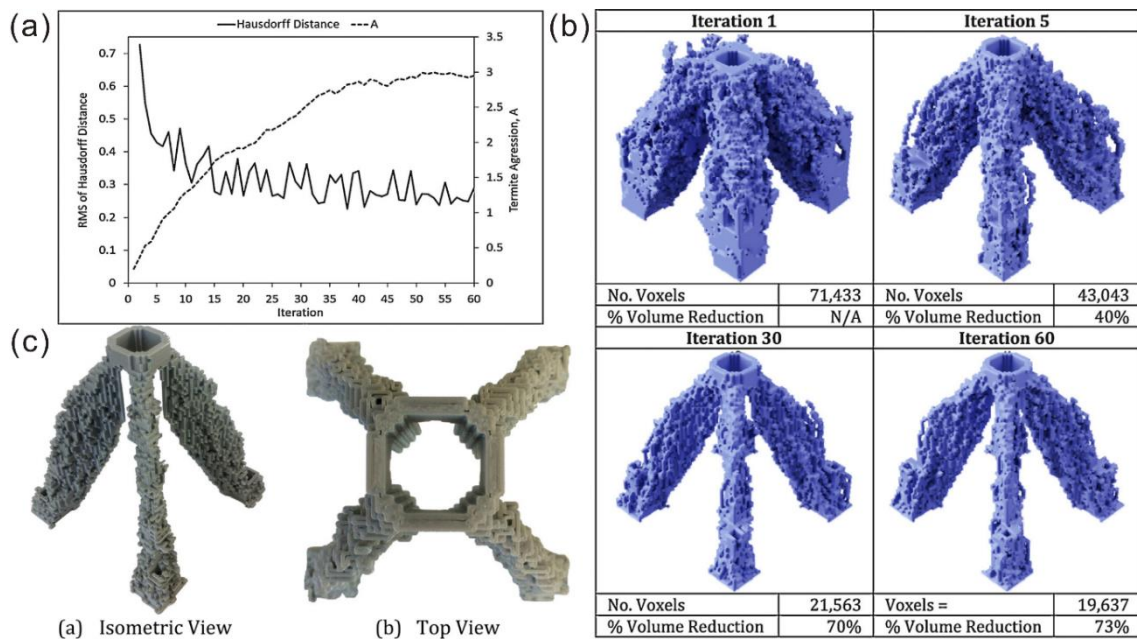
Figure 2.8. A plot of the Hausdorff distance between consecutive design iterations; (b). A value for each iteration; (c). Rendering of part geometries. [74].

Recently, a new concept combining generative design with deep learning was provided to explore more design space [76]. The proposed GANs (generative adversarial networks) gave the possibility to embed existing AM process knowledge into generative design methods as shown in Figure 2.9. However, the method only concentrates on design exploration and generating numerous design solutions without optimization. In addition, it is difficult to evaluate candidate solutions and obtain a large amount of training data. A work was proposed to use reinforcement learning to explore vast number of design solutions based on density-based TO methods, SIMP and BESO in [77]. Different search algorithms were used to evaluate on compliance minimization problems from 2D to 3D. Case studies showed almost all methods are able to generate various acceptable design solutions only by controlling one or two parameters. Figure 2.10 shows the generated options and stacked views of the cantilever beam by different search algorithms. However, low efficiency is still the bottleneck of the development of reinforcement learning. Hence, how to find a balance between searching ability and computation complexity is still a question that needs to be solved.
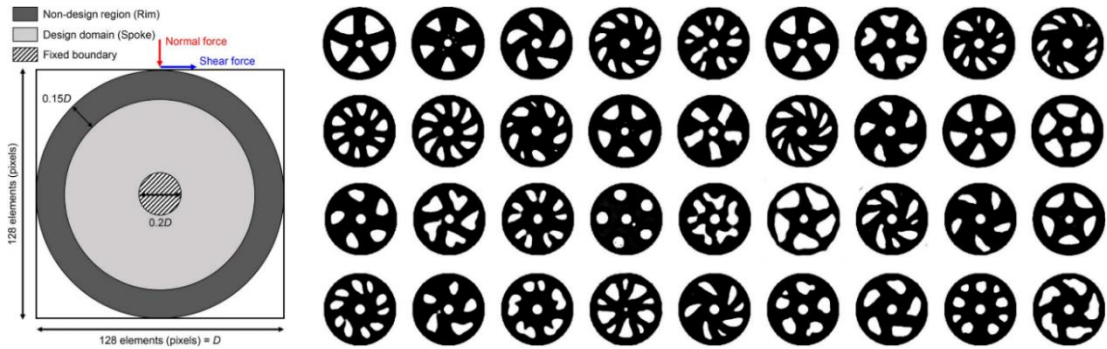
Figure 2.9. Design domain and boundary conditions of a 2D wheel design; Generated wheel designs by the proposed GAN method. [76].
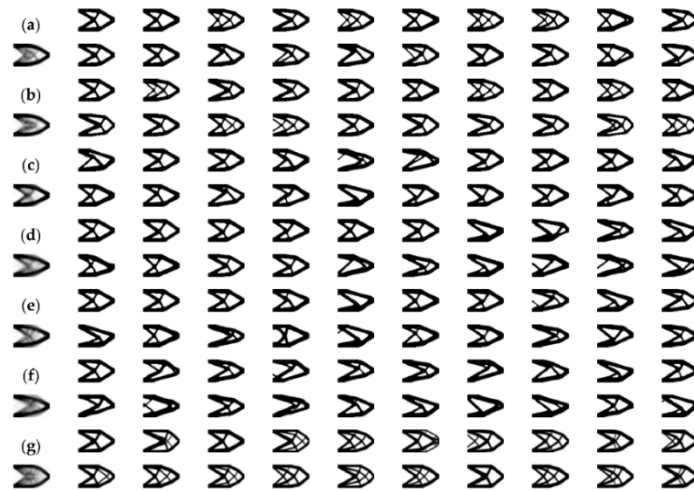
Figure 2.10. Generated options and stacked views of the cantilever beam by different search algorithms. [77].

According to the application of generative design in the architectural design field, generative design is described as a design exploration approach to support designers in automating the design process [69]. In contrast with high design freedom and aesthetic needs in the architectural field, engineering problems in the manufacturing field are usually driven by the performance and manufacturability. Therefore, in this thesis, the generative design for AM is defined as a new design process that integrates the specific manufacturing information into the geometry definition procedure and can populate a large quantity of qualified alternative design solutions to meet the application requirements and AM constraints.

2.1.3. Support Structure Design for Additive Manufacturing

Due to the layer-by-layer building strategy in AM processes, a CAD or STL model is transferred into a processing model that can be recognized by an AM machine. In the pre-processing, there are a couple of complicated decision-making problems, e.g. build orientation determination [51], support structure generation [78], slicing and printing path planning [79], etc. These tasks are defined as CAPP (computer-aided process planning) stages, which have a direct impact on the feasibility, suitability and stability of AM [52]. Among these tasks, support structure generation is a critical issue for the powder bed based metallic AM processes, e.g. SLM (selective laser melting). The support structures not only sustain the overhang areas of a component during the printing, but also act as heat diffusion mediums and thermal distortion resisting structures [18, 19]. In medical applications, e.g. dental, the removing of support structures is usually manual because these components are fragile, and it is hard and costly to design special fixtures for these components in the machining of the post-processing stage. Dense support structures may have good sustaining qualities to overhang area and are able to resist the thermal stress better. However, this may increase the consumption of raw materials and cause difficulty for heat transfer, support cutting, tool accessibility constraints and extra cost for the support contact area repair in the post-processing stage. While sparse support structures could reduce the amount of raw materials, there is a risk of severe deformation caused by thermal and residual stress or even surface collapse with printing failure due to insufficient withstanding strength and heat diffusion performance. Therefore, it becomes a critical issue to design support structures with lightweight, easy-to-remove for post-processing and friendly heat-diffusion properties to ensure shape accuracy and surface roughness of printed parts.

Support structure design is one of the unavoidable preparation tasks in the printing preparation for many AM processes, especially for the powder bed based metallic AM processes. There are four main functions of support structures: to sustain overhang areas for printability; to maintain manufacturability of

the printed parts during printing; to allow easy-removing from the build base and to assist heat diffusion or resist residual stresses in a gradual thermal field [80, 81]. Current research on support structures focus on finding lighter support structure types and support algorithm optimization. The strategies of support structure design & optimization usually have two categories: direct and indirect. In direct methods, overhang areas in a given build orientation are directly projected onto the build plane, and then support structures are generated via different volume generation methods according to the projected overhang areas. Indirect methods mean the redesign of a component, e.g. topology adaptation to minimize support, switching of build orientation and adapting the geometric shape of identified overhangs to achieve self-support. Both direct and indirect methods aim to minimize the volume of support while ensuring easy removing of the supports and printing quality of the component. Since the goal of this thesis is to propose a new method for the support structure design of extremely complex components in AM, such as freeform medical components on which indirect support design methods have limited effects, the research scope of this thesis focuses on the direct support design and optimization.

To generate support structures for a component with a fixed or switched build orientation, there are two main steps: 1. Obtain support points for identified overhang points, edges and faces; 2. Generate a support topology to connect the support points to the build base. To identify different types of overhang areas, the geometric facet information and the component slices are usually used as inputs. Then, AM manufacturing constraints, e.g. maximum lateral bridge length printing and maximum available inclination angle, are used to find qualified overhang areas. Generally speaking, support points are selected to support different types of overhang areas. Direct projection methods are widely used in many commercial AM preparation tools since it can be easily manipulated. In the projection method, support points are projected onto the build base or sustaining surface, then linear support structures with predefined cross-section profiles are generated along the projection trajectories. In recent years, more lightweight support structure generation methods have been proposed, such as cellular filling structures and tree-shaped structures. For the cellular filling methods, predefined lattice support structures were proposed in [78, 82, 83]. Lattice cells are provided to replace solid walls in projection methods to form lattice supports in order to reduce the volume of support materials. However, there is still excessive material used for the supports. In addition, in [84], a bridge support structure design method was proposed to simplify the support structure generation procedure. Manufacturability, e.g. lateral maximum bridge length was considered in the support structure design.

Though there are many support structure generation methods in the literature [85], tree-shaped support structures have been widely studied in the last few years. This is mainly because tree-shaped structures have more potential to construct lightweight support structures. In [86], Autodesk® MeshmixerTM demonstrated that tree-like supporting structures can greatly reduce time and materials by generating space-efficient branching structures in fused-filament 3D printing. A top-down generation procedure was used to obtain support structures starting from a series of support points. In general, the tree-shaped support structure optimization problem can be described as the Euclidean Steiner Minimal Tree (ESMT) problem which belongs to the NP-hard problem [87]. According to different generation strategies of tree-shaped support structures, top-down and trimmed lattice-based generation methods are developed in current research. In direct top-down methods, a tree-shaped structure starts from support points on overhang areas. A tree-shaped structure grows downward based on search algorithms until it connects to the ground or other parts of the component, such as Meshmixer. To explore the potential of tree-shaped support structures, a geometry-based support structure generation method was proposed to minimize the support materials in [87]. A greedy algorithm was used to construct the tree-shaped structure which starts with support points and converges into a single strut. However, since some AM manufacturing constraints, such as the critical angle and sampling distance, were not considered, they cannot ensure the stability of support structures. To obtain a robust fabrication process, a set of formulas based on physical constraints for fused filament fabrication (FFF) machines was introduced in [88]. An adaptive particle swarm optimization (PSO) algorithm was developed to minimize the volume of support structures. Similarly, by constructing a grid to support projection space for populating tree nodes, advanced searching algorithms were applied to obtain the shortest accumulative path length to form lightweight tree support structures [89]. However, it is difficult to efficiently converge to the global solution when addressing a huge tree-shaped support structure issue. A new Local Barycenter based Tree Support algorithm with constant time complexity was developed to deal with the low calculation efficiency problem [90]. Supporting points were divided into sub-regions using a divide and conquer iterative strategy. New nodes were calculated based on the local barycenter of children nodes.

The trimmed lattice-based method differs from the top-down methods as it generates a tree-shaped structure by trimming a predefined lattice structure filling. In [91], a uniform manufacturable lattice structure was generated to support overhang areas. To minimize the volume of the support, a maximum number of lattice struts were removed. The pruned support structure was optimized by a genetic algorithm (GA). Design of experiments was used to obtain the most suitable control parameters of the genetic algorithm. However, deformation and heat diffusion problems have been left aside. Similar to

trimmed lattice-based methods, predefined 'Y' and 'IY' shaped lattice unit cells were explored to find friendly heat-diffusion support structures [92]. However, only a simple overhang plane example was applied to test the feasibility. Figure 2.11 lists main lattice and tree-shaped support structures below.
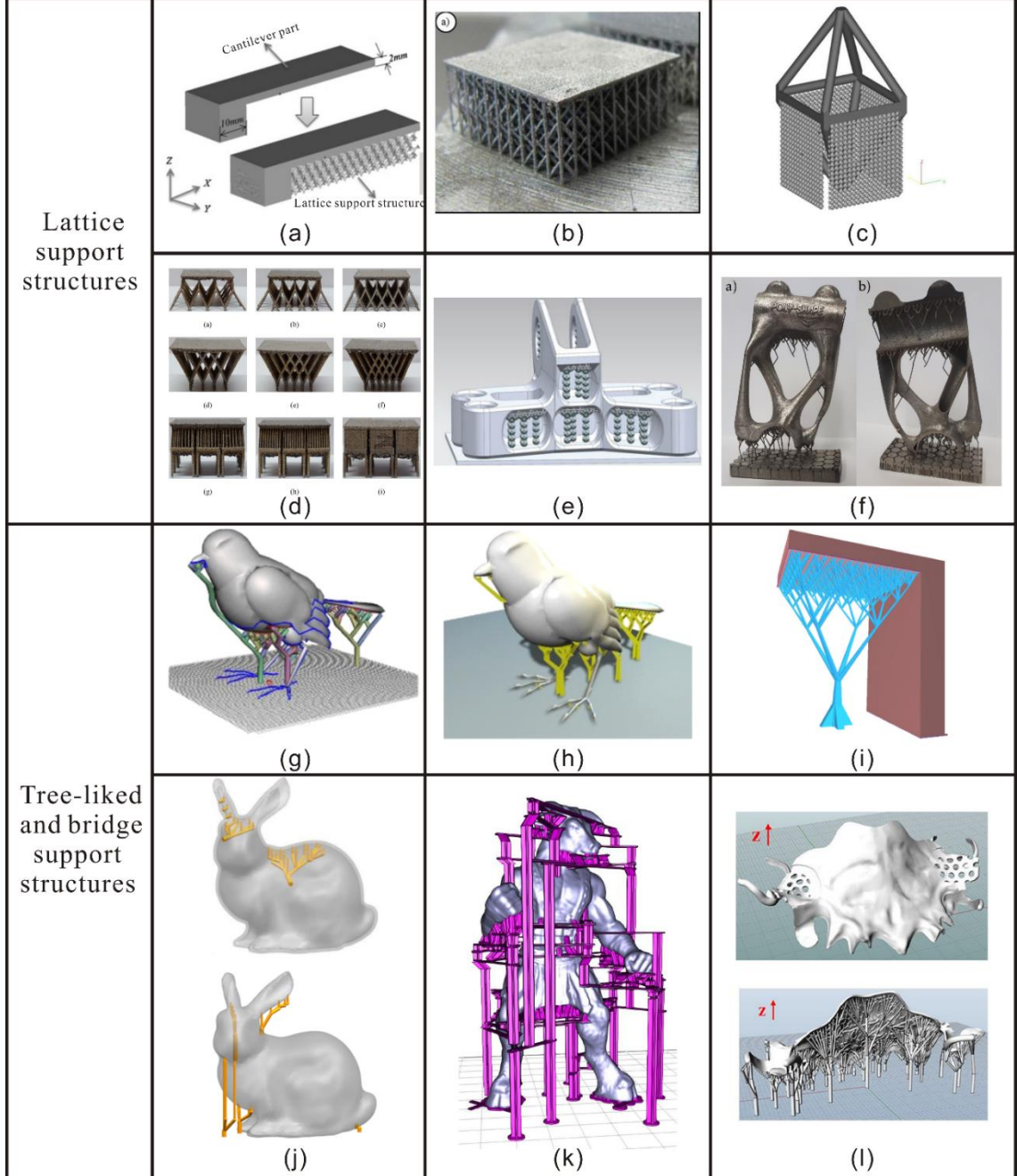
Figure 2.11. Main representative methods of lattice and tree-shaped support structure generation: (a). TPMS-based lattice support structure-1 [78]; (b). Strut-based lattice support structure-1 [93]; (c). TPMS-based lattice support structure-2 [82]; (d). Strut-based lattice support structure-2 [92]; (e). Lattice support with hollow unit cells in the interface [94]; (f). Pruned strut-based lattice support structure [91]; (g). Meshmixer: tree-shaped support structure [95]; (h). Clever support: tree-shaped support [87]; (i). Tree-shaped support structure-1 [90]; (j). Internal and external tree-shaped support structure [88, 89]; (k). Bridge support structure [96]; (l). Bio-inspired tree support structure [27].

2.1.4. Lattice Structure Configuration for Additive Manufacturing

Nature evolved architected cellular materials for many situations where low density as well as high stiffness and strength are needed [97]. Two examples in Figure 2.12 show beaks and bones of birds that composed of thin, solid skins attached to a highly porous, cellular core. These kinds of cellular structures are so complex, with intricately shaped ligaments and gradients in density [97]. Although human can design various sophisticated structures, it is difficult to fabricated by conventional manufacturing processes. The emergence of AM technologies enables fabrication of cellular material with more complex shapes. With the development of many novel architected cellular materials, computational design synthesis methods for AM need to be improved to enable qualified design of cellular structures for different AM processes.

Figure 2.12. Architected cellular structures in the core of bird beaks and bones provide optimum strength and stiffness at low density. [97].

In AM processes, lattice structures, a type of cellular materials, are defined in literature as objects that are periodic in nature, continuously repeating unit cells that interconnect in three dimensions [98]. Traditional topology optimization and generative design methods usually use solid material to obtain lightweight design solutions at a macroscale. Lattice structure design is usually carried out at a mesoscale. Typically, a mesoscopic structure refers to a structure consisted of a great number of the units between 0.1 and 10 mm [99]. The geometry complexity of lattice structures brings more freedom to guide the design for AM [100-102]. A lattice structure can be considered as a material with its own mechanical performances. Due to the geometry complexity of AM, lattice structure got more attention

recently, especially when AM becomes more mature [11]. Current studies have reported that SLM process shows significant advantages for fabrication of fine metallic lattice structures. In [103], a great number of lattice cell topologies are categorized as strut-based and triply periodic minimal surface (TPMS).

2.1.4.1. Strut-based lattice structure

The most common strut-based lattice cells are body-centered cubic (BCC), face-centered cubic (FCC), octet-truss, dodecahedron units, etc. [103]. Maxwell criterion can be described as a sufficient condition to characterize the mechanical response of a strut-based structure. The Maxwell rule in 3D is given by [104]:

$$M = s - 3n + 6$$

(2-

Where s and n are the number of struts and nodes, respectively. If $M < 0$, the strut-based cell will exhibit a bending-dominated behavior. Whereas if $M \geq 0$, it can make the struts stretch-dominated [105]. Bending-dominated structures have a relatively low strength and high compliance and stretch-dominated structures play a strong and stiff performances [106].

Typically, there are two main categories of lattice topologies: stochastic and periodic [11, 107]. For stochastic lattice structures (Figure 2.13(a)), the shape and size of a lattice unit cell are distributed through a random probability strategy in the design space. These randomized structures can be generated by using the Voronoi diagram algorithm used in bone tissue engineering [108]. Periodic lattice structures are usually further divided into two types: uniform and conformal [109]. The uniform lattice structures, called periodic lattice structures, are described as those kinds of lattice structures which repeat the unit cells in 3D space. Due to the periodic properties, all unit cells have the same size and topology. For the conformal lattice structure, known as pseudo-periodic lattice structure, the shape and size are designed to conform to the original geometry of a hull part. Figure 2.13(b) and (c) show the two types of lattice structure configurations in 2D.

(a) (b) (c)
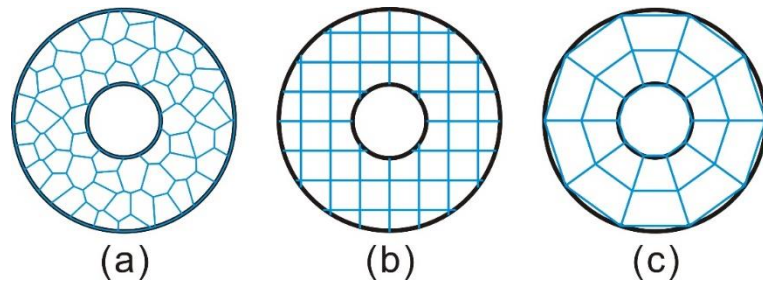
Figure 2.13. Three types of lattice structures: (a). Stochastic lattice; (b). Uniform lattice; (c). Conformal lattice.

Lightweight design of strut-based lattice structures

In order to optimize the material distribution, such as the lattice, shape, size and topology, topology optimization is usually used to address the structural design problem. A heuristic optimization method, called the augmented size matching and scaling (SMS) method, was proposed to optimize the thickness distribution of conformal strut-based lattice structure [110]. Based on local stress status, unit cells from a predefined library were selected and sized to support those stress statue. Figure 2.14 shows the final topology of the lattice structure design as well as the intermediate steps. A BESO based optimization method proposed by Huang and Xie [111] was used to optimized thickness distribution of lattice struts for an engine bracket part in [112]. In the proposed method, a kernel based lattice frame generation algorithm was applied to generate lattice wireframes within a given functional volume. Compared to the original design, the optimized lattice design can reduce weight by nearly 75% as shown in Figure 2.15. Similarly, to help engineers and designer to achieve a lightweight design via lattice structure configuration, Lebaal et al. [11] proposed a combined method that adopts knowledge-based engineering and mathematical optimization tools to provide decision support for lattice structure design as shown in Figure 2.16. More specifically, to optimize the parameters and topologies distribution of lattice unit cells, the authors used design of experiment and surrogate model to configure lattice structures in specified 3D hulls to gain both mass and computation efficiency for structural design.
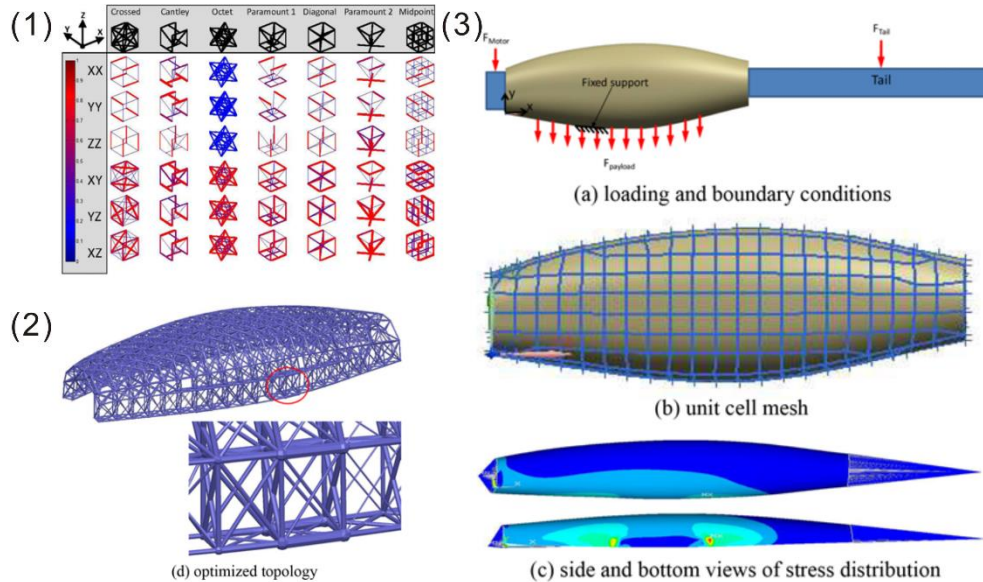
Figure 2.14. Solution process of a fuselage example: (a). A predefined library; (b). The final lattice topology; (c). The results of the intermediate steps. [110].
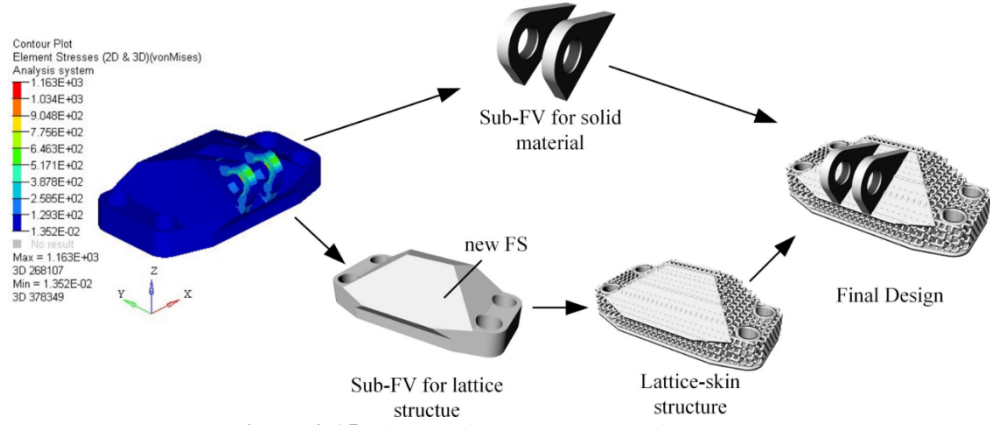
Figure 2.15. Final lattice design generation. [112].
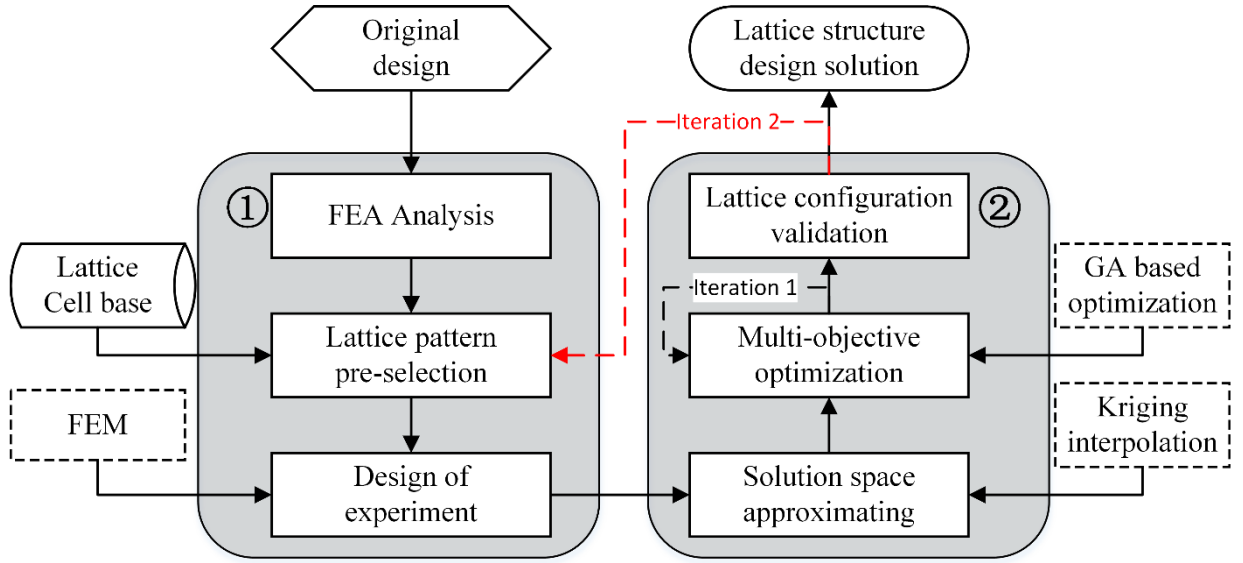
Figure 2.16. The lattice structure configuration optimization method proposed in [11].

Currently, various topology optimization methods are focusing on optimizing lattice structure configuration for AM. An effective design framework was proposed to design graded lattice structures for AM as shown in Figure 2.17 [113]. Level set method was used to represent the configuration of lattice units. Then, a configuration interpolation technology was developed to ensure the connectivity of two neighboring Graded Mesostructures (GMs). A reduced-order model was used to evaluate the properties of the interpolated GMs. Compared to the uniform lattice configuration design, the optimized GM can provide a higher stiffness. Likewise, a conformal lattice structure optimization method was introduced to solve size distribution problem in [114]. To explore more kinds of lattice unit cells for lattice configuration problems, a multi-topology lattice design method was proposed based on unit-cell library in [115]. Various different types of lattice unit cells predefined were calculated and stored into a unit-cell library. Then, a selective filling function of unit cells and geometric parameter computation algorithm were

carried out to obtain the final lightweight lattice structure configuration with uniformly varying densities. Figure 2.18(c) lists an optimum lightweight lattice structure for the cantilever beam problem.
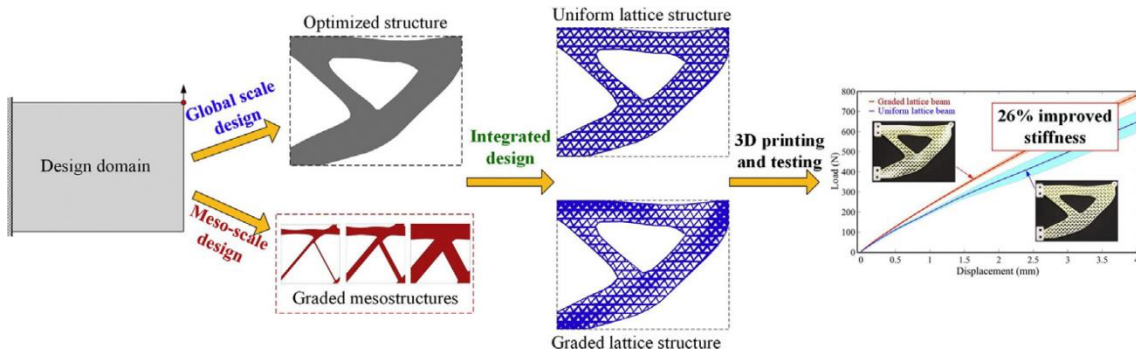
Figure 2.17. Graded lattice structures with optimized mesostructures for AM. [113].

(a)

(b)

(c)
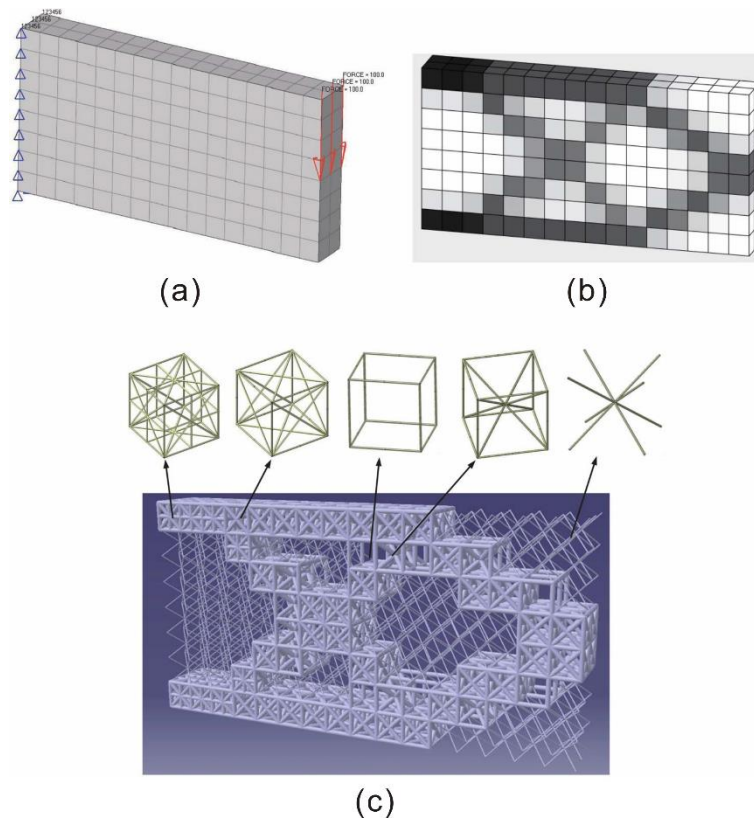
Figure 2.18. 3D cantilever beam design: (a). Boundary conditions; (b). Relative density distribution; (c). The optimized lattice structure. [115].

Another design method of multi-topology lattice structure, called solid lattice hybrid structures, was also presented in [116]. Compared to the pure lattice structure in [115], lattice unit cells were infilled with the pure solid structure as shown in Figure 2.19. The hybrid structure is able to achieve a lightweight graded lattice structure, but also solve the manufacturability problem due to the lattice structure supporting the overhangs. As Figure 2.19 shows, the hybrid structure has the best mechanical performance.
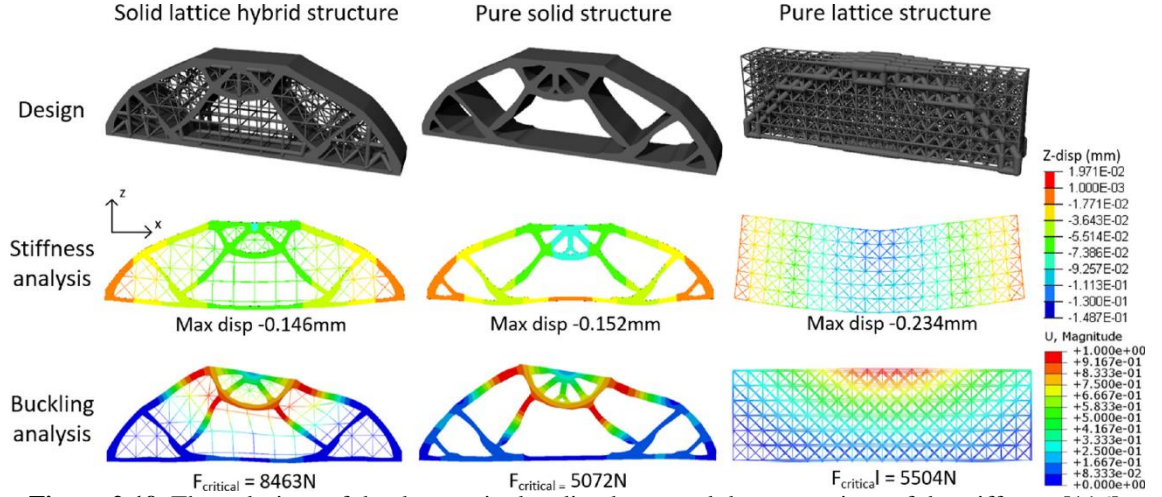
Figure 2.19. Three designs of the three-point bending beam and the comparison of the stiffness. [116].

A multi-scale topology optimization method was proposed to achieve a design with coated exterior and spatially-varying orthotropic exterior in [117]. The proposed systematic design procedure was summarized in Figure 2.20. Through a homogenization step, an effective elasticity tensor of the orthotropic infill microstructure is used as a design variable function of the multiscale TO method. Figure 2.21 shows MBB design results with different design variables. Inspired by Voronoi tessellation algorithm, a homogenization-based design method was proposed to create 2.5D wall-based functional graded Voronoi cellular structures [118]. A two-dimensional density field was used to control the wall thickness of the designed structures. Two design examples were provided to verify the applicability of the proposed method in Figure 2.22. The proposed method can exhibit two features which are the "near-isotropic" property and the robustness to local defects.
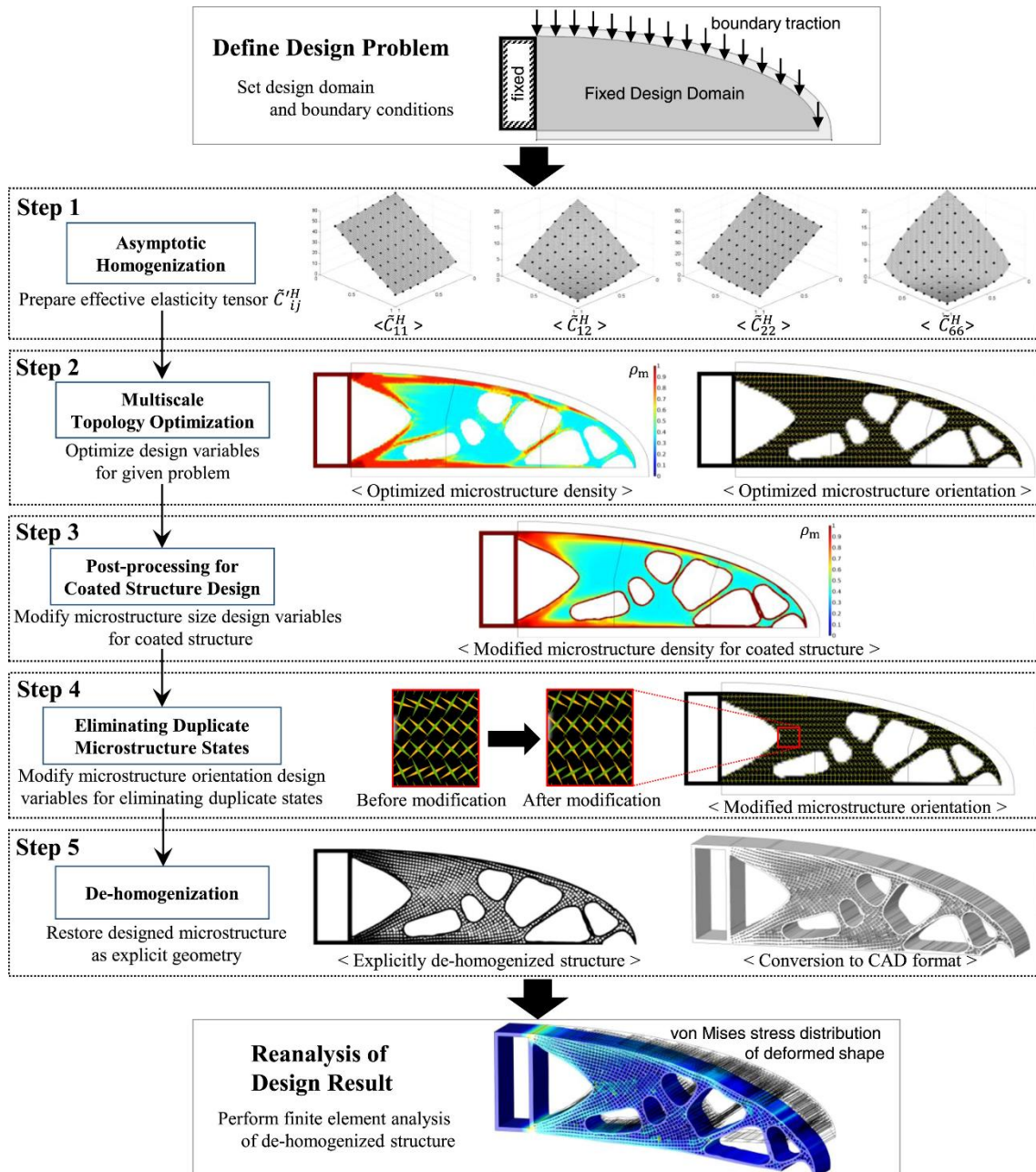
Figure 2.20. Design procedure consisting of five sequential steps proposed for spatially-varying orthotropic structure design and main results obtained at each step are provided in a cantilever design example. [117].
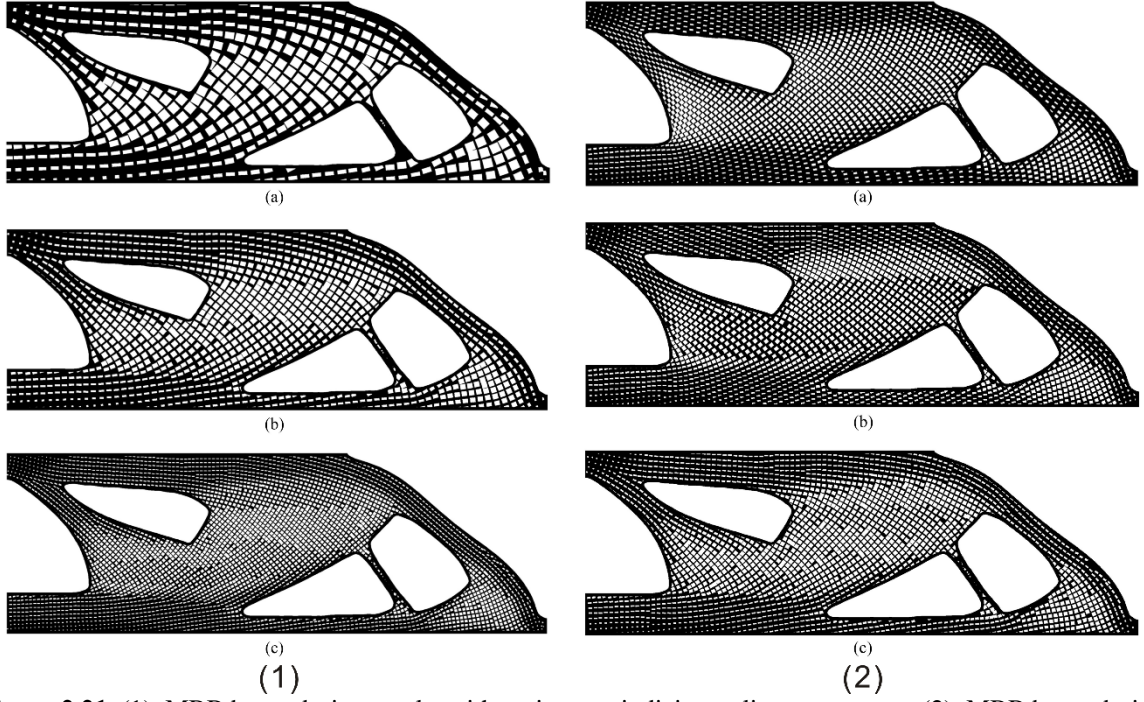
Figure 2.21. (1). MBB beam design results with various periodicity scaling parameters; (2). MBB beam design results with various number of partitioned areas. [117].
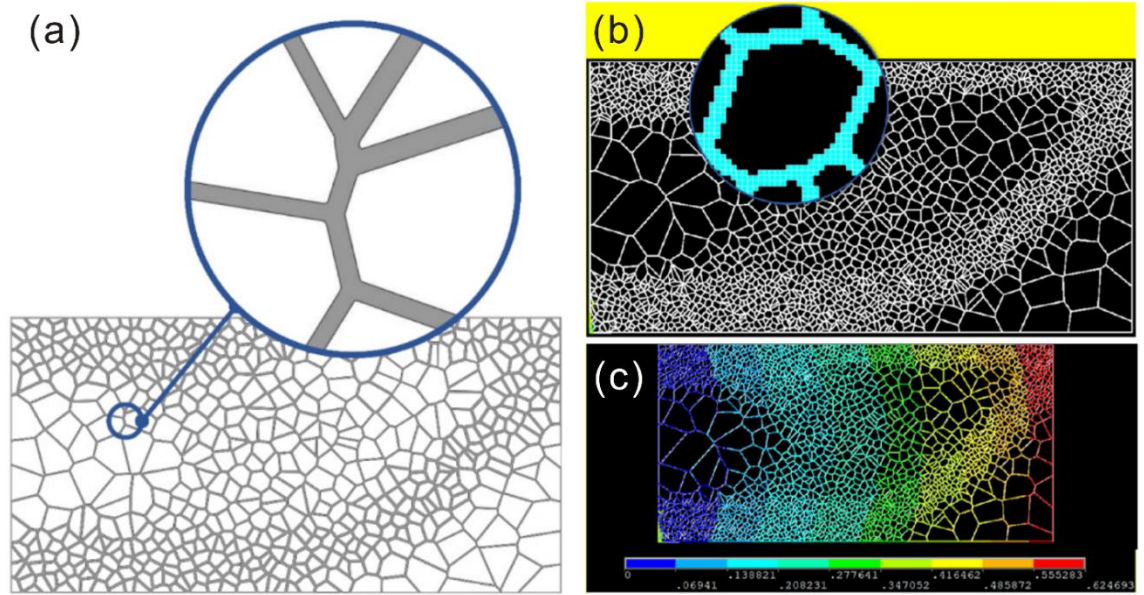
Figure 2.22. (a). Voronoi cellular structure; (b). An example of Voxel-FE model with Voronoi structure; (c). Voxel-FEA result. [118].

A 3D parametric design method for the design of Voronoi-based lattice porous structures, as shown in Figure 2.23, was presented in [119]. A functional relationship of Voronoi tessellation between the porosity, the number of seed points, and the beam radius was established to obtain a fine graded lattice porous structure. Hence, the lattice porous structures designed by the proposed method were globally controllable and locally uniform. A new practical design method was proposed to design a functional

hydraulic manifold component in [120], as shown in Figure 2.24. The proposed method enabled to combine functional design and lattice structure filling for a self-support design with ensured function and manufacturability. Hence, functional requirement and AM knowledge can be integrated within the final design solution for the easy-to-use DfAM method.

$$P = \left[1 - \frac{nr^2 \left(\frac{3\pi a}{\sqrt[3]{n}} - 8\sqrt{2}r \right)}{a^3} \right] \times 100 + C_n$$

Functional relationship between porosity and the number of seed points and beam radius

Regular lattice unit cell

Voronoi-based lattice porous structure globally controllable and locally uniform
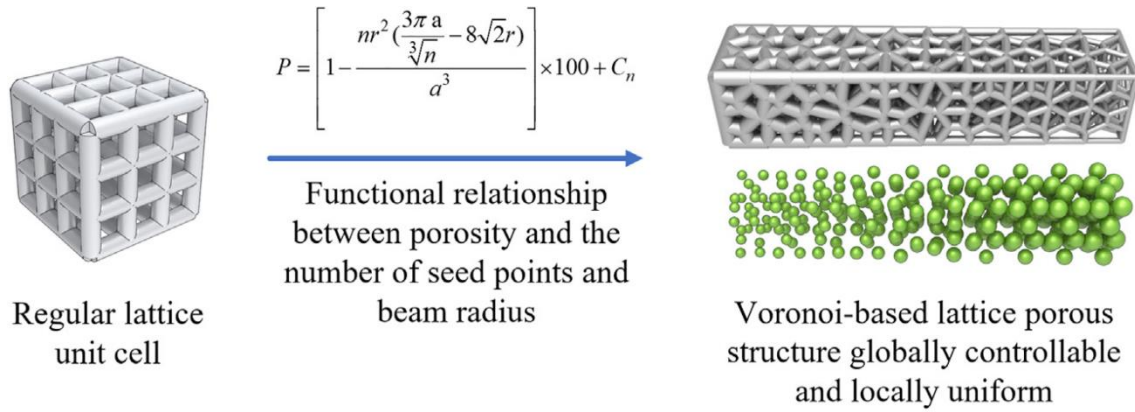
Figure 2.23. The parametric design method of Voronoi-based lattice porous structures. [119].

(a)   (b)
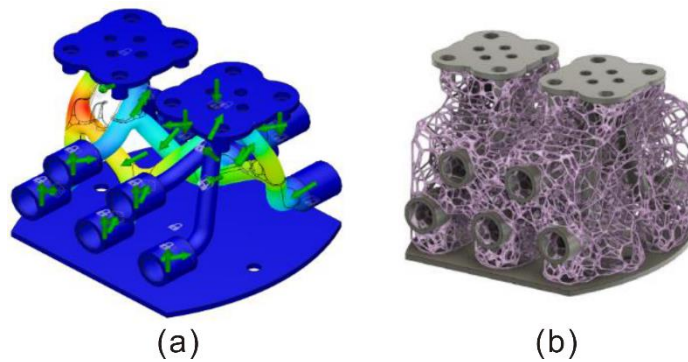
Figure 2.24. A practical redesign method for functional AM: (a). Simulation result; (b). Final design. [120].

Multi-function applications of strut-based lattice structures

The strut-based lattice structures are used not only for lightweight design, but also for multi-functional design. In [121, 122], Voronoi lattice structures were applied to design cooling channels for the thermoplastic injection process in mold design. The Voronoi Diagram algorithm was used to generate conformal cooling circuits that can improve the efficiency and the quality of production in plastic injection molding. Figure 2.25 shows the comparison on the temperature distribution in the Voronoi-based cooling channels and spiral cooling channels. Another cooling channel designed by lattice configuration was proposed by Tang et al. [123]. Two porous cooling structures, conformal and uniform, were used to compare the cooling performance. The results showed that conformal cooling structure can achieve better cooling performance and significantly reduce the pressure drop under the same cooling condition. A parametric design for graded truss lattice structures was also applied to design a heat sink as shown in

Figure 2.26 [124]. The experiments showed a lattice-based heat sink has a better thermal dissipation performance, compared to traditional fin-based geometries.
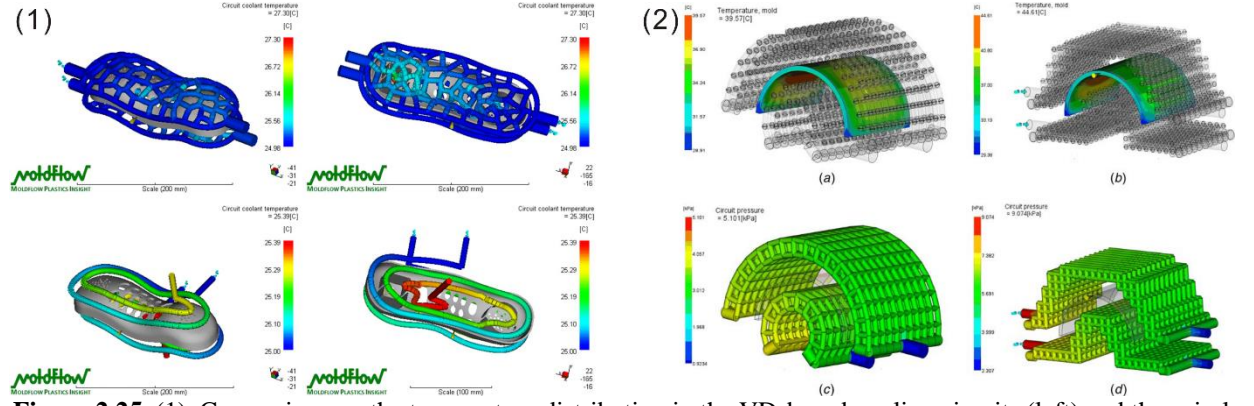
Figure 2.25. (1). Comparison on the temperature distribution in the VD-based cooling circuits (left) and the spiral cooling channels (right) [122]. (2). Comparison between conformal and uniform porous structures on the injection mold of half-cylindrical part. [123].
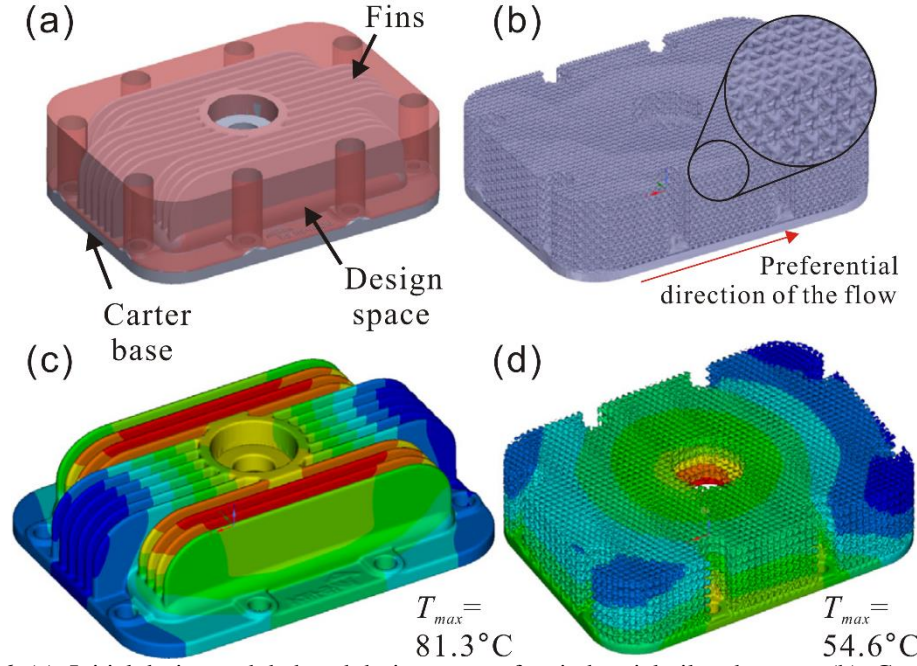
Figure 2.26. (a). Initial design and deduced design space of an industrial oil tank carter; (b). Graded oriented lattice-based heat sink; (c). Simulation of the initial design; (d). Simulation of the final design. [124].

Based on the geometry complexity of AM processes, the thermal performance of graded strut-based lattice structure was analyzed by Yun et al. [125]. In the work, the thermo-fluid-structural properties of different graded types of lattice channels were investigated using a coupled model. Compared to a uniform and other graded lattice channels, the W-type channel exhibited the highest thermos-fluid performance. The conclusion can be used to serve for the design of heat sink or exchangers.

2.1.4.2. TPMS-based lattice structures

Recently, a great amount of investigations has been concentrated on nature-inspired TPMS structures. This kinds of surface-based structures are represented by mathematical formulations according to level-set functions [126]. Three common TPMS structures, Schwarz Primitive, Diamond and Gyroid, are widely used. Their mathematical expressions can be described by the following equations.

$$\phi_P(x,y,z) = \cos(\omega x) + \cos(\omega y) + \cos(\omega z) = C$$
$$\phi_D(x,y,z) = \cos(\omega x) * \cos(\omega y) * \cos(\omega z) - \sin(\omega x) * \sin(\omega y) * \sin(\omega z) = C \qquad (2\text{-}2)$$
$$\phi_G(x,y,z) = \sin(\omega x) * \cos(\omega y) + \sin(\omega y)\cos(\omega z) + \sin(\omega z) * \sin(\omega x) = C$$

Where x, y, z are the spatial coordinates, $\omega = 2\pi/l$ and l is applied to define the length of lattice cell, and C can control the expansion of the surface in three dimensions.

Currently, most TO-based lattice design methods use strut-based lattice unit cells to generate a graded lattice structures. One main reason is that various thickness is easy to be achieved by controlling the radius of strut. However, the mutation of the structural topology and the strut diameter causes large stress concentrations and weak strengths in the connected nodes of various cells [127]. Due to the implicit modeling of TPMS, it is suitable to achieve a gradient optimization by governing the parameters. Li et al. [128] proposed a generative design algorithm to optimize functional graded TPMS structures. The scaling law of the elastic tensor was calculated to achieve the optimum density distribution of graded TPMS structures. To obtain a lightweight design, a graded structure design based on TPMS structures was also proposed by Li et al. in [127]. The proposed method uses homogenization method to obtain the effective elastic properties of the TPMS structures. Based on the density mapping of TO method and experiment results of various TPMS structures, a selective filling function is used to obtain a suitable cell topology distribution. Figure 2.27 shows the optimization procedure of the TPMS-based lattice structures.
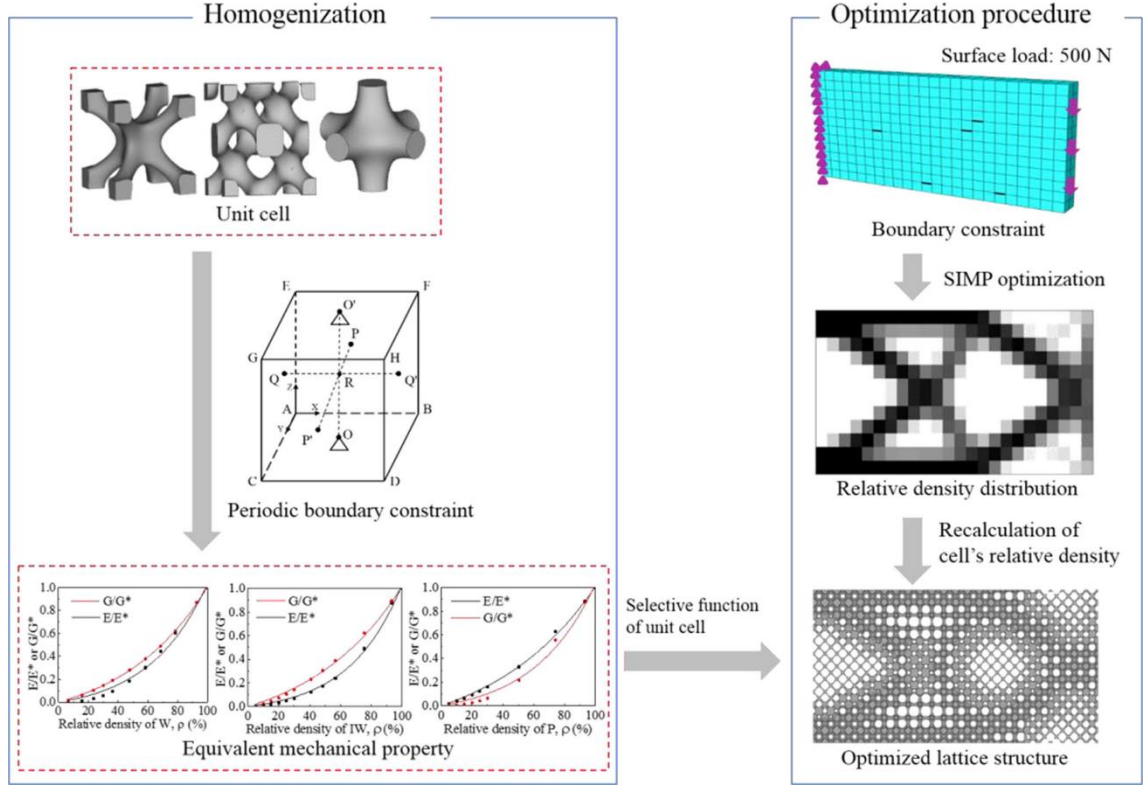
Figure 2.27. Optimization procedures for TPMS-based multi-morphology lattice structures. [127].

TPMS-based lattice structures present high surface-area-to-volume ratios, which makes them good candidates for thermal dissipation [107, 129]. In [107], the thermal conduction for three surface-based lattice unit cells was studied to find the relationship between thermal conductivity and the lattice parameters, types and sizes. Schwarz Primitive unit cell showed the best conductivity. The mechanical properties of TPMS structures were widely studied on the effect of type, size and porosity of TPMS unit cells [130, 131]. These research data can be also used to guide the DfAM.

Due to the natural capability of TPMS, many researches started to use TPMS structures for designing the tissue engineering porous scaffolds [132, 133]. In [134] , a 3D porous scaffold design method of tissue engineering was presented based on the distance field and TPMS unit cells, as shown in Figure 2.28. The proposed method can construct a patient-specific 3D porous scaffold model accurately. In addition, distance field algorithm can enable to avoid difficult and time-consuming trimming and re-meshing processes. However, graded TPMS structures are not discussed in the work.
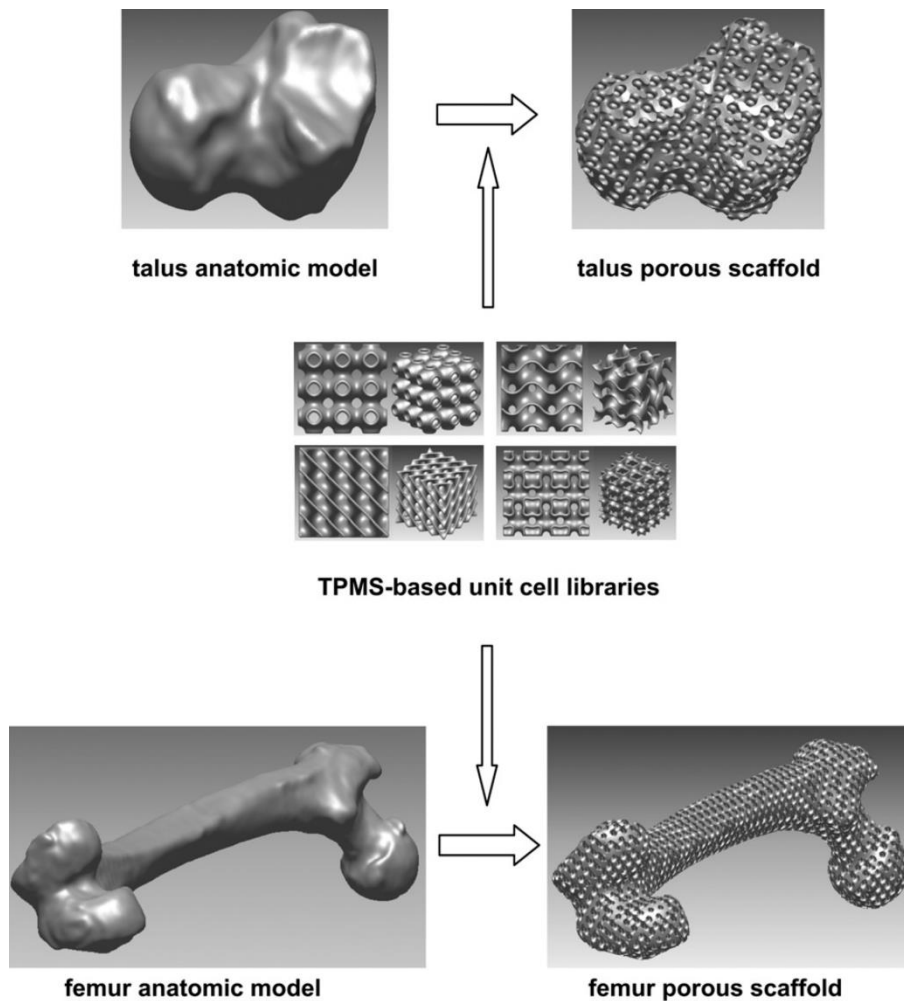
Figure 2.28. Porous scaffolds structures with intricate internal architecture and high quality external surface. [134].

2.1.5. Toolpath configuration for Additive Manufacturing

Nowadays, STL files are the most common standard interface between a CAD model and the AM system. Figure 2.29 shows a process flow for the AM process [135]. In general, there are three methods for processing STL files. The first method is based on a geometric CAD model. A CAD system can map a 3D-CAD model accurately. The second method is through imaging by using computer tomography (CT) or magnetic resonance imaging (MRI) to create a CAD model or STL model. The last one is the reverse engineering (RE) process to fabricate the prototype. A smaller triangular mesh tends to increase the size of a STL file. At the same time, it will require a longer time to create the STL file. Hence, in order to obtain a prototype with high accuracy, the mesh size should be close to the size of the layer thickness of the AM machine, especially of L-PBF process.
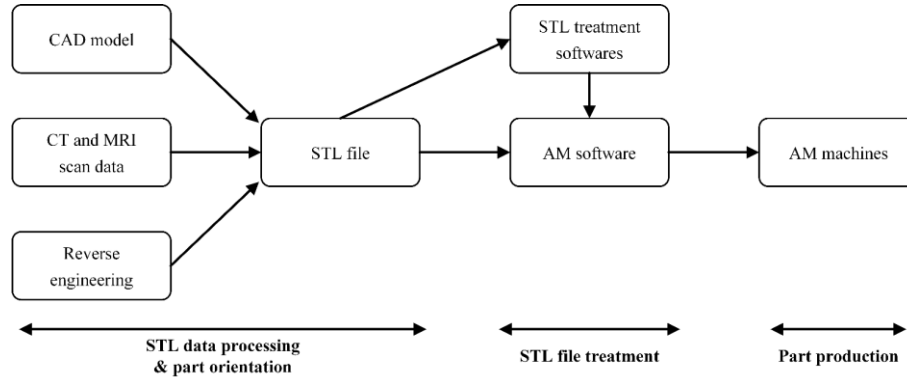
Figure 2.29. Process flow for the AM process. [135].

In all AM processes, 3D CAD model needs to be broken down to 2D slice. To obtain the slice file, there are usually two slicing procedures, uniform and adaptive slicing. Figure 2.30 shows the two slicing procedures. Uniform slicing has been widely used in all kinds of AM processes. This process enables to obtain a set of horizontal planes with the same thickness. For the adaptive slicing, it uses variable layer thickness based on the geometry change along the build orientation. Hence, it can reduce the build time and improve the surface quality.
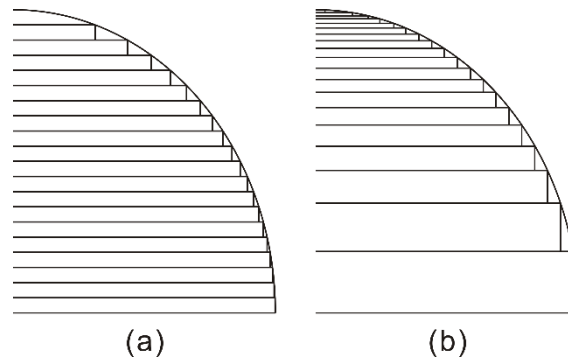
Figure 2.30. Two slicing procedures: (a). uniform slicing; (b). adaptive slicing.

Figure 2.31 lists the common scanning strategies [136]. For L-PBF process, there are generally two types of scans: contour and infill. Contour scan (Figure 2.31(f)) is usually used to scan the boundaries and infill scan is used to scan across all areas. The unidirectional (Figure 2.31(a)) and bidirectional scanning strategies are the most common scanning strategies, where the difference lies on the variation of the scanning vector. The bidirectional scan is also called zigzag scan. It can be used in the island scanning strategy (Figure 2.31(c)). Figure 2.31(d) and (e) change the scanning sequence in one layer to change the temperature distribution during printing. Double pass scan in Figure 2.31(h) is generally used to obtain fine microstructure. Figure 2.31(i-m) rotate the scan vectors among layers. A discontinuous scanning strategy is introduced in Figure 2.31(n). A new toolpath strategy, Hilbert curve [137], was studies in [79, 138]. Figure 2.32 shows the Hilbert curve.
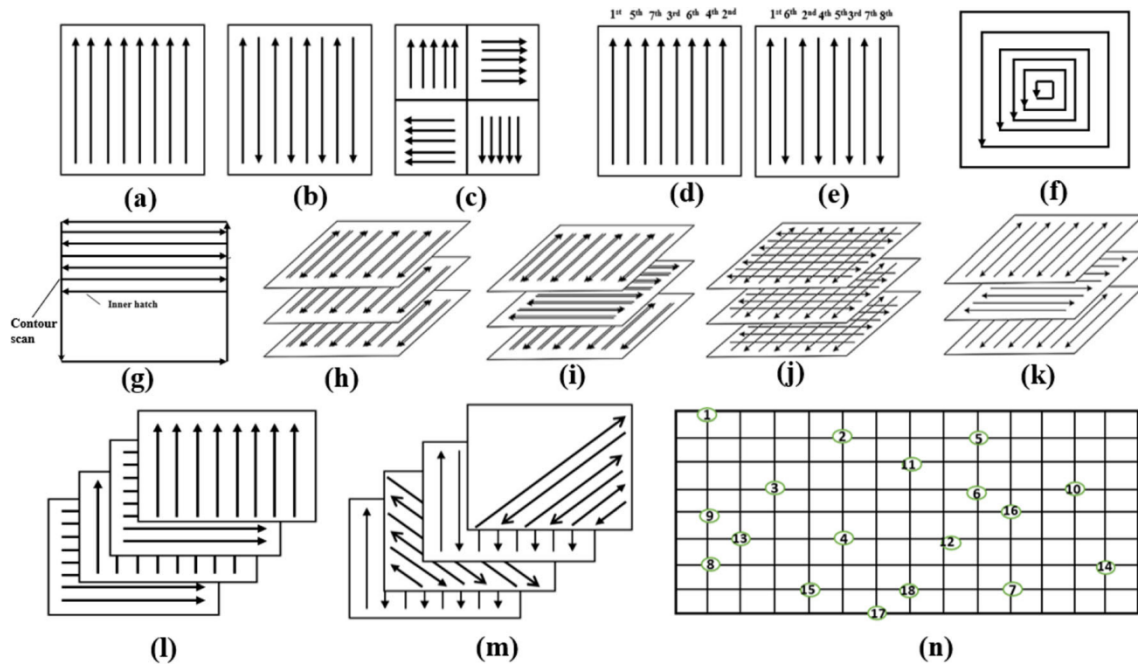
Figure 2.31. Schematic of different types of scanning strategies for SLM: (a). Unidirectional scan; (b). Bidirectional/zigzag scan; (c). Island scan; (d). Variation of scanning sequences based on unidirectional scan; (e). Variation of scanning sequences based on bidirectional scan; (f). Contour scan; (g). Contour scan and zigzag; (h). Bidirectional, double pass of laser beam; (i). Bidirectional, double pass of laser beam, 90° rotation scan vector between layers; (j). Cross scan; (k). Bidirectional, single pass of laser beam, 90° rotation of scan vector between layers; (l). 90° rotation of uni-directional scan between successive layers; (m). 45° rotation of scan vector; (n). Point melting scan. [136].
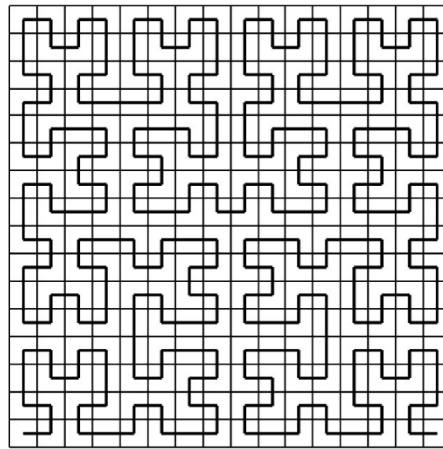
Figure 2.32. Hilbert's pattern. [137].

SLM process can be used to fabricate high-performance parts with complex structures. However, process parameters in SLM can influence properties of AM parts significantly, such as hatch spacing, scanning speed, and laser power etc. Many researchers investigated the effect of process parameter settings on density, surface quality, microstructure, residual stress, and mechanical properties of SLM parts [139, 140]. The process parameters in SLM are shown in Figure 2.33 [140].
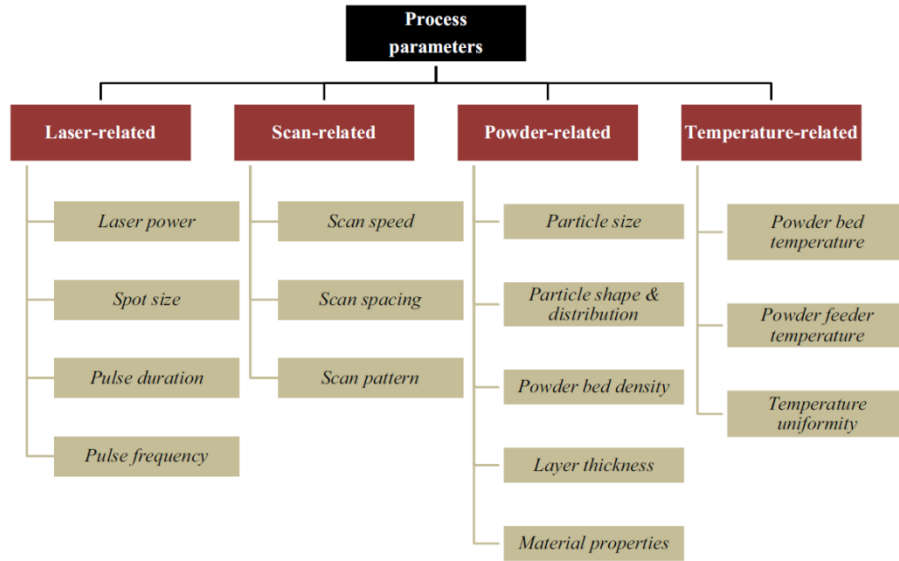
Figure 2.33. Controlling parameter in SLM process. [140, 141].

Parameters related to toolpath geometry are mainly hatch spacing, scan pattern, scan angle and layer thickness. Hatch spacing can result in the overlap rate between adjacent tracks for various hatch spacing as illustrated in Figure 2.34. According to melt pool characteristics, scan pattern and scan strategy can have a profound impact on residual stress accumulation within a part [141]. In addition, the melt pool depth must be more than the layer thickness for a high-density part. Hence, hatch spacing should be selected for a sufficient degree of melt pool overlap between adjacent toolpaths of fused material to ensure a robust mechanical property [141]. Process parameters have a deep influence on the dimensional accuracy, surface finish, build rate, and mechanical properties. Hence, how to balance these parameter becomes a critical issue to provide the best trade-off.
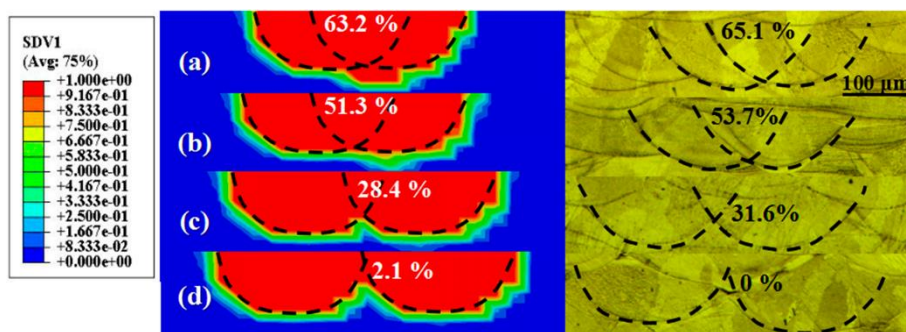
Figure 2.34. Simulated (left) and experimental (right) overlap rate between adjacent tracks for various hatch spacing. [139].

As said above, the preparation process in traditional AM processing chain can be summarized as CAD model building, STL file conversion, and toolpath infill before printing. In literature, many studies were

proposed to improve the efficiency and precision issues of part-scale lattice structure designs by reducing the steps of traditional toolpath generation or improving the precision.

Steuben et al. [142] proposed an implicit slicing method based on the level set function or physics-based fields defined over the input geometry. Hence, the functional performance fields, such as strain and stress distribution, had a crucial effect for final toolpath generation. To avoid to slice the solid TPMS model, Feng et al. [143] proposed to use the Marching Square (MS) algorithm to slice open-surface TPMS structures directly. Then, based on the uniform thickness information, a bidirectional-offset-union strategy was developed to generate valid toolpath infill. Figure 2.35 shows an infill area of I-WP surfaces. However, it is still costly to deal with part-scale lattice design issues using the solid-free method. In addition, the proposed method can only construct TPMS structure with uniform thickness.
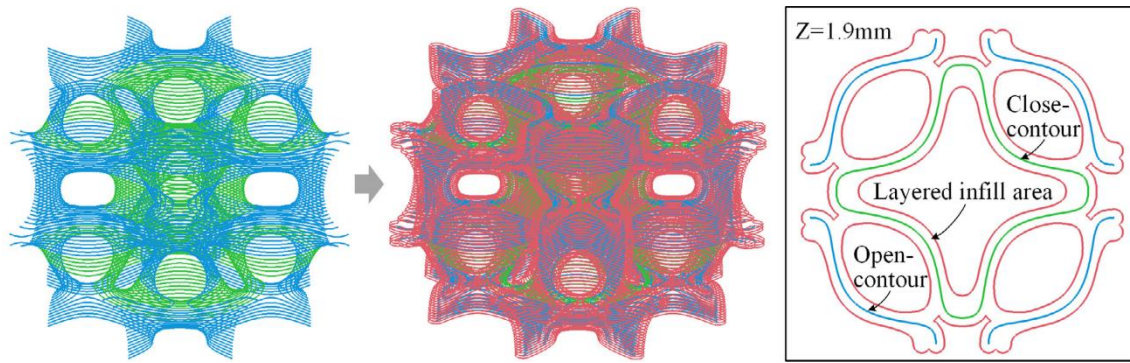
Figure 2.35. Infill areas of I-WP TPMS surface. [143].

To obtain high-precision TPMS structures, another STL-free design method was proposed by Ding et al. [144]. Implicit solid modeling and direct slicing method are used to construct toolpath configuration. Hence, it can ensure a high-precision toolpath infill for the powder bed fusion process when fabricating multi-level TPMS structures. Figure 2.36 shows a generation of multiscale TPMS in 3 levels. However, it is difficult to handle complex graded TPMS structures for the STL-free method. In addition, the cost of slicing and toolpath generation was omitted in the implicit method. The toolpath configuration is still conducted for the whole part model.
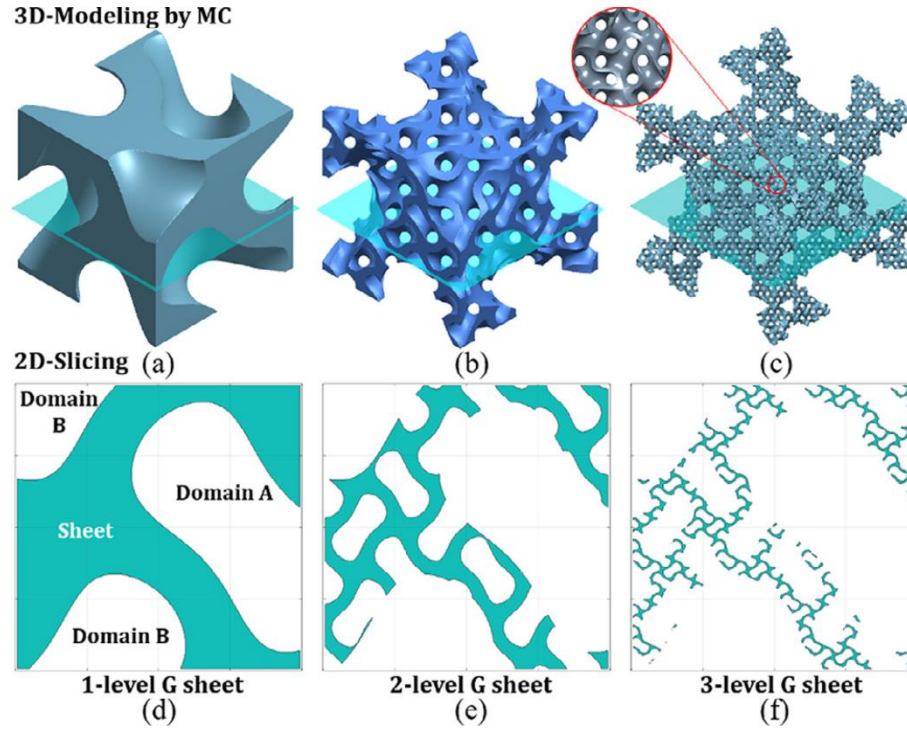
Figure 2.36. The generation of multiscale TPMS in 3 levels. [144].

Ponche et al. [145] proposed a novel methodology of design for AM to optimize the part geometry from toolpath directly. Hence, it provided a new horizon to bridge the gap between CAD model and the corresponding manufactured part. Inspired by the pioneering work [145], a new toolpath-based layer construction method is proposed to design micro-scale porous structures in [146]. The proposed method used an implicit modeling method to construct printable parametric toolpath/processing model directly.

Some researchers are focusing on integrating the deposition path into topology optimization methods. The proposed methods are mainly suitable for extrusion-based AM processes, such as fused filament fabrication (FFF) [147] and wire-arc additive manufacturing (WAAM) [148, 149], and concrete engineering [150]. A concurrent deposition path planning and structural topology optimization method was firstly proposed under a unified level set framework by Li et al. [151]. For achieving a contour planning, the deposition paths were optimized by extracting the iso-value level set contours. In addition, zigzag path problem was also studied in the paper. Another deposition path planning method [152] was also introduced to solve the 2D TO problem. Figure 2.37 shows the two toolpath planning for two TO problems. A 3D TO method was introduced by Liu et al. in [153] . Moreover, self-support manufacturing constraint was considered into the proposed multi-level set modeling method.
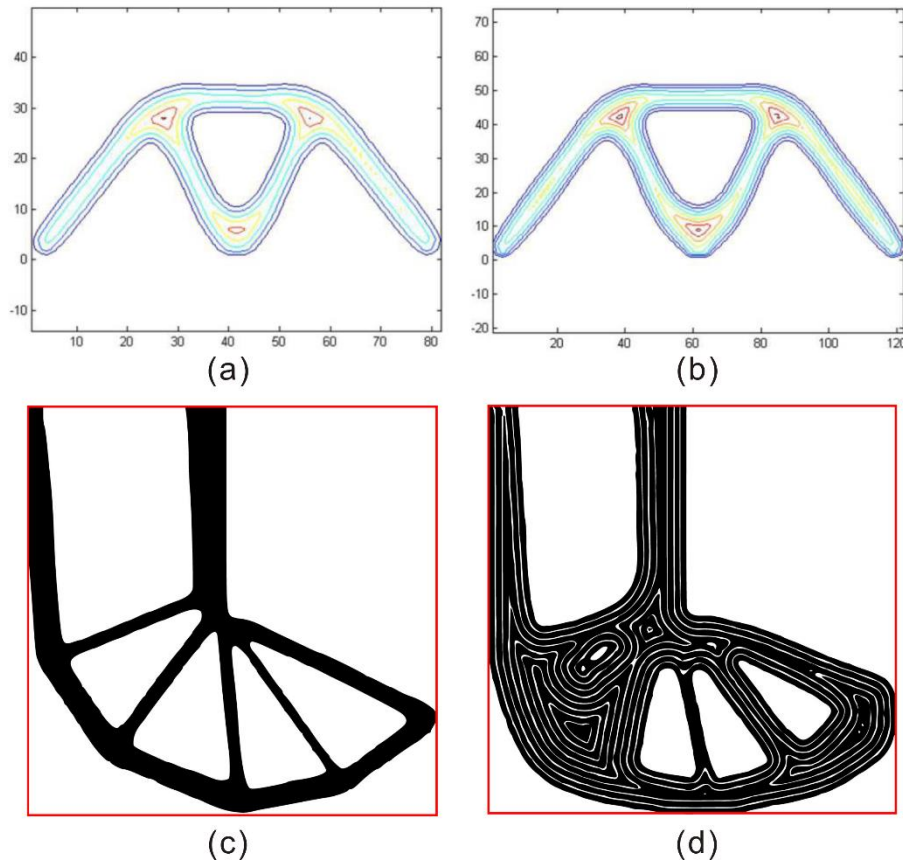
Figure 2.37. Numerical results given different mesh sizes: The Michell structure [151]: (a). The optimization result given mesh size 80*40; (d). The optimization result given mesh size 120*60; The L-shaped beam [152]: (c). Optimized shape; (d). Optimized shape using offset model.

More recently, a topology-optimized design method suitable for WAAM process was proposed in [148]. The nozzle size constraint was integrated into density-based topology optimization method in order to generate optimized designs suitable to the process resolution. Figure 2.38(1) shows the deposition paths with different nozzle sizes. Due to the remarkable elastic anisotropy property of AM parts, a combined design method was proposed to simultaneously optimize the structural design layout and the local deposition path direction for WAAM in [149]. The proposed method can improve the structural stiffness compared to conventional deposition path. Figure 2.38(2) shows an illustration of a possible deposition path in line with the optimal post-processed deposition directions.
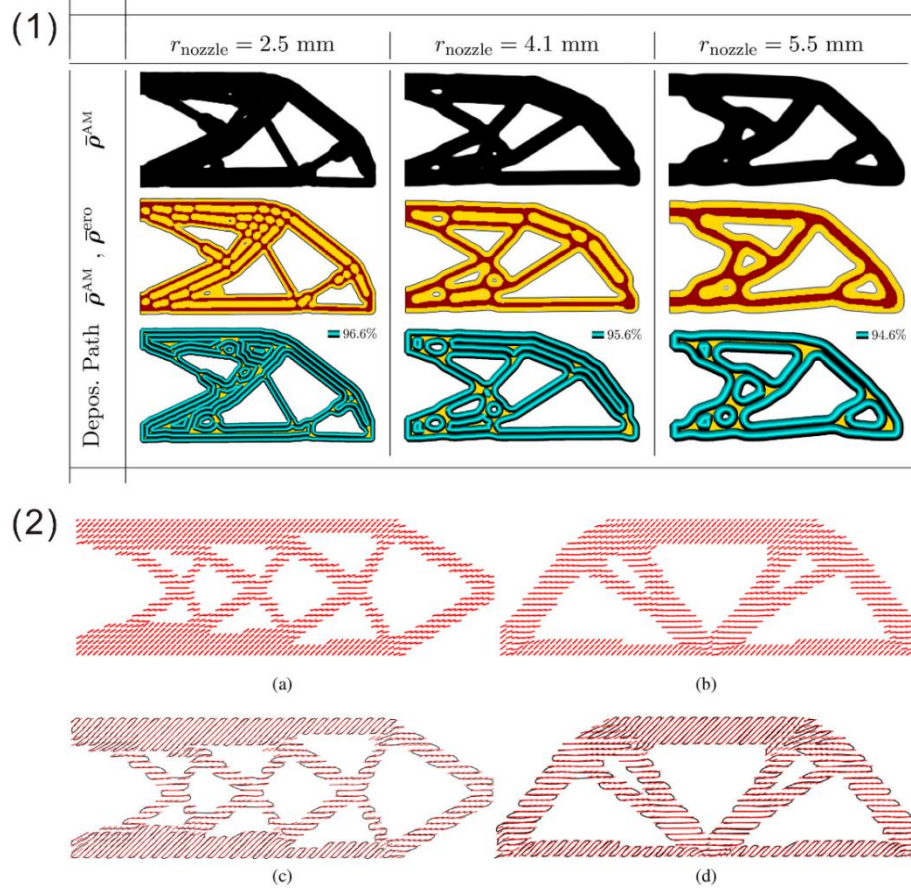
Figure 2.38. (1). AM-constrained designs for different nozzle sizes [148]; (2). Post processed optimized deposition directions for (a) cantilever and (b) bridge problems; an Illustration of a possible deposition path (black) along the post processes optimized deposition directions (red) for (c) cantilever and (d) bridge designs, respectively [149].

Instead of only TO consideration, a function-aware toolpath planning method was proposed to generate lattice configuration using principal stress line (PSL) [154]. The PSL was the first used as a guidance to generate toolpaths that can improve the structural rigidity of AM parts. In addition, the PSL-based method is able to consider AM constraints. Figure 2.39 shows the overall pipeline of the PSL-based framework. To enhance load-bearing capacity of filament fabricated parts, in [155], a region-based path planning strategy using image representation was proposed for optimizing printing paths to align with the principle stress field of parts. The proposed stress-oriented printing path strategy used image processing algorithm to partition the principal directional field and generate printing paths aligned with principle directions. Figure 2.40 gives three results of the stress-oriented path optimization method for different loading conditions.

(a) CAD domain   (b) 3D Stress field   (c) 2D Plane slices

(d) Single plane PSL   (e) Toolpath   (f) 3D printed component
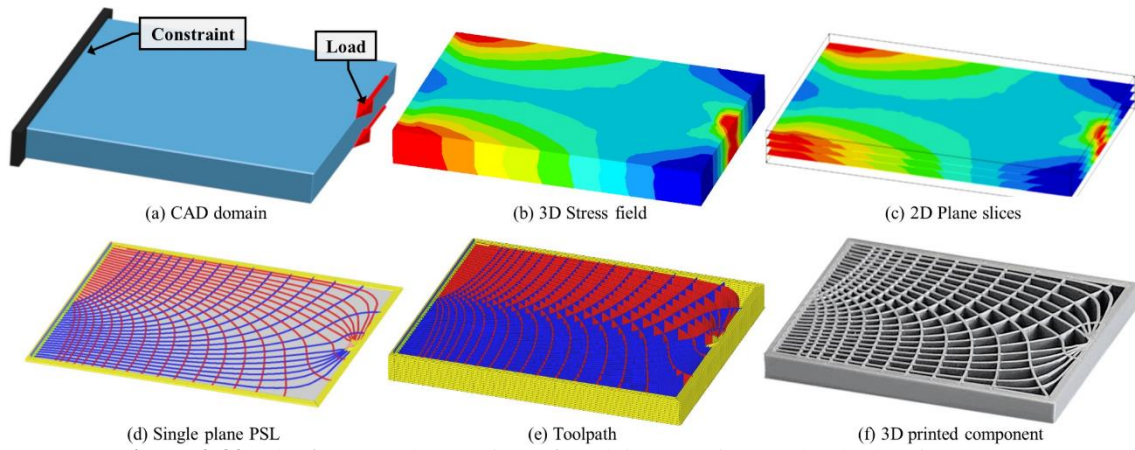
Figure 2.39. The framework overview of applying PSL into toolpath planning. [154].
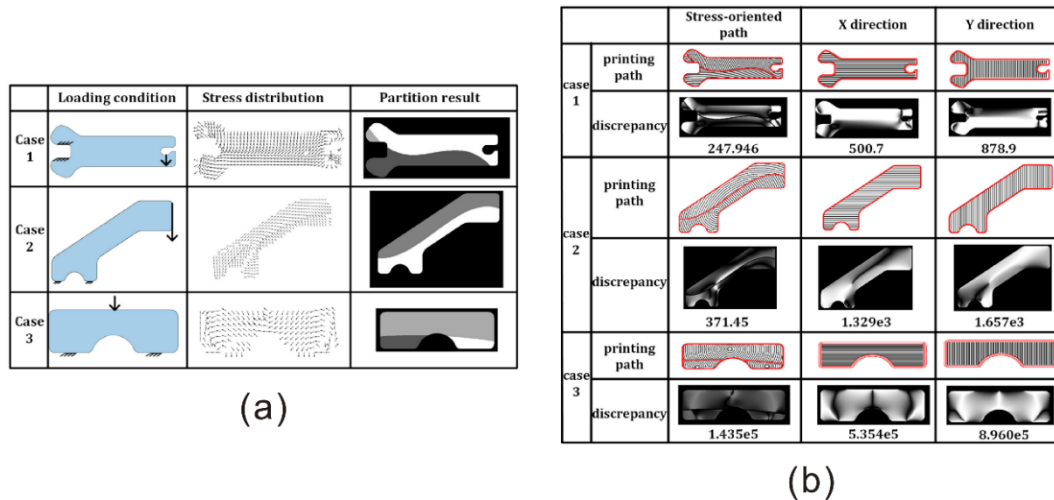
Figure 2.40. (a). Load-bearing parts under different loading conditions; (b). Printing path generated via different strategies and their alignment score. [155].

2.2. Problems of current DfAM methods

Although there are plenty of investigations in the design for AM domain, many design methods still rely on the subtractive thinking to design a model by removing material, such as topology optimization. In this process, it is hard to integrate AM manufacturing constraints into the optimization procedures since mathematical models to describe AM processing constraints explicitly are difficult to obtain. In addition, the model conversion will not only cause the loss of geometrical accuracy, and also consume much computational time and memory, especially for part-scale porous structure design. Moreover, it becomes worse when using intricate TPMS structure to infill within the part-scale lattice structures. The following sections summarize the existing main problems related to DfAM in different scales.

2.2.1. Problems in Macroscale: Topology optimization & Support structure design

2.2.1.1. Topology optimization for AM:

To obtain an optimal topology structure, traditional macroscale design methodologies for AM, topology optimization, usually remove excess material for a raw material or design domain. The design thinking is still impeded by traditional subtractive manufacturing. Currently, topology optimization methods have several limitations that impede industrial application. Firstly, although topology optimization has great potential to exploit the design freedom provided by AM, AM processes cannot always print the obtained structures with successes. This is primarily because AM still has some manufacturing constraints which need to be considered in the topology defining process. Therefore, manufacturing-oriented topology optimization for AM has seen a significant interest since industrial applications can only accept qualified design solutions. In addition, structural optimization problems in industry are usually constrained by multiple conflicting objective functions and boundary conditions in FEA (finite element analysis). Nevertheless, most existing methods can only provide a single topological result for a given optimization problem. Many of the existing optimization methods convert a multi-objective optimization problem into a single-objective optimization, called mono-objective optimization, and obtain one particular solution at convergence. Therefore, these methods naturally eliminate other non-dominant solutions, called the Pareto set, in the solution space. Due to the conflicting nature among the predefined objectives, there is a need of a Pareto-optimal set representing trade-offs for further decision making according to diverse preferences for specific requirements and compromise in engineering applications.

Furthermore, from the perspective of optimization techniques, topology optimization methods are usually classified into two main categories: gradient-based TO and non-gradient-based TO methods [54]. Gradient-based methods rely on the gradient information, called sensitivity, to search for the optimal solutions. They are widely used in the density (SIMP) approach, the level-set approach, topological derivatives, etc. The main reason is that the gradient-based methods can efficiently solve fine-resolution problems with up to millions of design variables by using a few hundred function evaluations [54]. Non-gradient-based TO methods, also called black-box TO [55, 56], usually use evolutionary algorithms and other soft computing techniques to generate near-optimal topologies of mechanical structures. Evolutionary-based TO methods are more flexible for problems without gradient information.

Moreover, evolutionary computation applies global search techniques and hence can tend to converge towards a global optimal rather than a local optimal [55]. One of the main challenges that limits the wide use of an evolutionary algorithm in TO is that the elements using fine grid representation causes a great deal of design variables, which limits its effectiveness and convergence [55, 56].

Instead of focusing on one optimal solution such as traditional TO, generative design can populate a large number of design solutions from the design space for designer's reference and further decision making. Hence, the application of a generative design method for topology optimization may avoid the existing limitations, such as mono-optimal solutions, difficulties in obtaining gradients, etc., of conventional TO methods as discussed above. Recently, a set of commercial software provides new functions of the generative design method for AM processes in their structure design module, such as Autodesk and Altair. However, these tools, based on traditional multi-objective topological optimization, only alters the way of removing materials from the design space to populate alternative solutions, most of which are invalid. Key manufacturing constraints of AM processes have been ignored in the material removing procedure. The result is that these commercial tools usually generate very complex geometries without validation for manufacturing. Hence, designers have to use their own knowledge to evaluate and select the optimal solution from the large number of populated non-valid alternatives, which is quite difficult for operation in design practice.

2.2.1.2. Support structure design for AM:

Although the research works have made so many efforts in the support structure optimization, they have ignored the importance of support point determination, where the optimal number and locations of support points should be identified. The selection of support points on the overhang areas has a direct influence on the volume of support structures, the ease of material removal and the heat-diffusion property. Many existing solutions for support structure design are limited to simple metallic components but can hardly meet the requirements from real industrial applications, where a large number of complex freeform and porous structures exist, such as the complex components from medical applications. For these kinds of components, it is hard to detect the reasonable overhang regions and determine the corresponding support points. One main reason is that most papers in literature have used simple STL files with regular shape overhang regions, which are easy for support design and generation, as cases for method demonstration but have omitted the real complexity of industrial cases. In addition, the key steps and related complexity to determine the support points have not yet been fully discussed. Fur-

thermore, there is no research to investigate the generation sequence of support points to assign in different locations of a component with a predefined build orientation.

The support structures not only sustain the overhang areas of a component during the printing, but also act as heat diffusion mediums and thermal distortion resisting structures [18, 19]. In medical applications, e.g. dental, the removing of support structures is usually manual because these components are fragile, and it is hard and costly to design special fixtures for these components in the machining of the post-processing stage. Dense support structures may have good sustaining qualities to overhang area and are able to resist the thermal stress better. However, this may increase the consumption of raw materials and cause difficulty for heat transfer, support cutting, tool accessibility constraints and extra cost for the support contact area repair in the post-processing stage. While sparse support structures could reduce the amount of raw materials, there is a risk of severe deformation caused by thermal and residual stress or even surface collapse with printing failure due to insufficient withstanding strength and heat diffusion performance. Therefore, it becomes a critical issue to design support structures with lightweight, easy-to-remove for post-processing and friendly heat-diffusion properties to ensure shape accuracy and surface roughness of printed parts. Currently, the existing methods for support structure design in AM have limitations to meet the requirements above.

2.2.2. Problems in Mesoscale and Microscale: lattice structure configuration & toolpath population

AM technologies have the potential to produce highly complex geometries and material compositions with a layer-by-layer printing strategy enabling to achieve a non-linear relationship between the geometry complexity and manufacturing cost [5, 11, 14]. Since the layer construction way is totally different from conventional manufacturing processes, designers and engineers enable to use intricate structures, e.g. triply periodic minimal surface (TPMS), to have more freedom in product design, such as tissue engineering [126] and heat sink [107]. As AM technology becomes more mature, it is possible to fabricate metal parts with high-precision complex geometry and extremely fine features, especially using laser powder bed fusion (L-PBF) process. However, high manufacturing precision also leads to more preparation time in AM processing chain. In addition, Boolean operation would cause a large computing time and data storing space while generating high-precision porous structures. In particular, with the increase of the CAD model size, these issues make fabrication of part-scale porous structures become more and more difficult.

Currently, the methods to print part-scale lattice or porous structures usually follow the traditional design and printing preparation method. At first, a CAD model or design domain filling with complex lattice unit cells is designed by conventional CAD tools. Then, the CAD model obtained is converted into a STL file that can be recognized by many AM machines' preparation software tools. In general, it will cause the loss of geometrical accuracy in the model manipulation and conversion. Then, the mesh file is processed by a preprocessing software to obtain a slicing model. It is also easy to lead to accuracy loss in the cross-sections from STL model to slicing model, especially for fine porous TPMS structures. In the end, different types of toolpath patterns are infilled within the layers of a slicing model. The infilling process usually cause additional accuracy loss when facing shape concave contours since toolpaths at those locations may have overlaps or voids. Hence, the generated toolpaths should be validated before printing in real manufacturing context. Currently, the preparation process in traditional AM processing chain can be summarized as model design, STL file conversion, and toolpath infill before printing. These three stages will not only cause the loss of geometrical accuracy, and also needs to consume lots of computational time and memory for part-scale porous structure design. Moreover, it becomes worse when using intricate TPMS structure to infill within the part-scale lattice structures.

2.3. Concrete research questions and proposals

To solve the problems above, this PhD work proposes two new DfAM methods in the macroscale and one in the microscale. The main target is to apply knowledge-based tools with computational algorithms to obtain qualified design solutions automatically for AM.

2.3.1. Proposed DfAM methods in macroscale

Proposal for traditional TO problem

A new generative design method with manufacturing validation is proposed. This proposed method uses a CSG (constructive solid geometry)-based technique to generate and represent topology geometries with smooth boundaries and parametric control. A set of non-dominated design solutions on the Pareto front are obtained and presented for the designer's further decision making.

Proposal for unqualified support design problem

A novel bio-inspired knowledge-based generative design method, integrating parametric L system rules and lattice structure configuration, is proposed to generate lightweight, easy-to-remove and heat-

diffusion-friendly biomimetic support structures. The proposed method enables to reduce the number of support points on support relevant overhang areas with a given build orientation, generate qualified tree-shaped support structures with less support volume and friendly heat diffusion.

2.3.2. Proposed DfAM methods in microscale

Proposals for lattice and toolpath configuration problems

A direct toolpath constructive method with scanning parameter consideration of AM process is proposed to design thickness-varying Voronoi-based multi-topology lattice structures in 2D. Different kinds of scanning strategy are developed to infill within Voronoi lattice cells. In addition, a novel knowledge-based toolpath constructive design method is proposed to generate high-precision graded lattice unit cells with manufacturability. It enables to integrate implicit modeling, graded distance field, direct slicing and fine toolpath configuration for constructing qualified toolpaths without any preprocessing steps. The two new toolpath-driven DfAM digital frameworks can greatly reduce geometric modeling time and printing preparation time and improve printing accuracy in AM chain process.

2.4. Summary

This chapter conducts a comprehensive review of current design synthesis methodologies in AM. The main DfAM methodologies are discussed from three scales, Macroscale, Mesoscale and Microscale. Due to the unique capabilities of AM processes, it is critical to ensure the manufacturability for qualified design solutions based on the specific settings of AM process. Therefore, the main concentration of the research is to develop new design methodologies in order to embed AM constraints into design methods easily. Since there are lots of processing tasks in AM process chain, another focus of this PhD work is to take into consideration that design should be coupled with the process chain of AM, such as model conversion and post processing. Figure 2.41 describes the expected solution proposals. In the following chapters, the three proposed DfAM methods will be introduced with details and demonstration cases.

Design for Additive Manufacturing
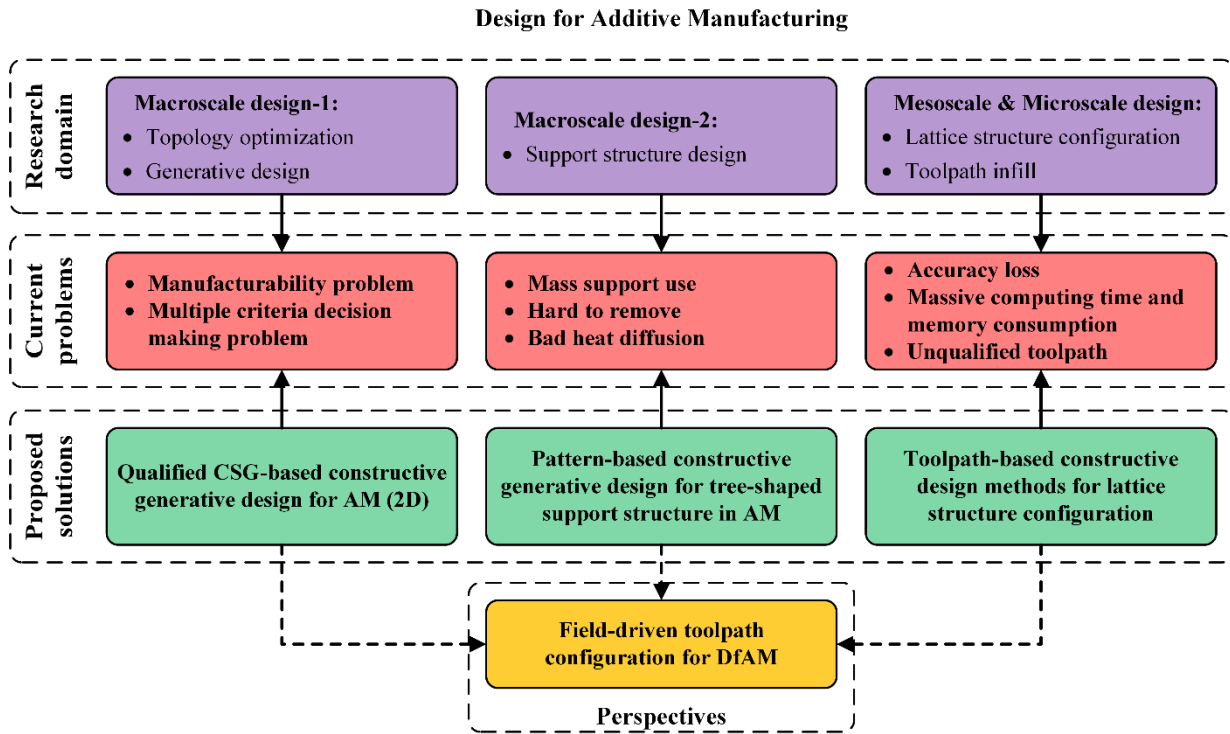
Figure 2.41. Research problems and expected solutions in this thesis.

Chapter 3. Qualified CSG-based generative design for AM

This chapter proposes a new constructive generative design method with a manufacturing validation so that the designer's decision-making is more efficient. This method first uses a CSG (constructive solid geometry)-based technique to generate and represent topology geometries with smooth boundaries and parametric control. Then, a genetic algorithm is used to operate the CSG geometries in order to search for optimal solutions. Finally, a set of finite optimal non-dominated design solutions on the Pareto front are located and presented for the designer's further decision making. The proposed method can generate a large quantity of qualified pre-optimal alternative solutions with smooth geometric boundaries but the computation cost is less.

3.1. Geometry representation with reduced variables

To reduce the number of design variables and release the potential of evolutionary algorithms, the CSG representation is applied to obtain optimum geometry. The detailed steps to generate a CSG geometry topology are described in Figure 3.1. One principle difference from other topology optimization methods is that the build orientation is determined before topology optimization. The basic idea in the proposed method is to utilize a set of moving and fixed nodes to obtain Delaunay triangulation skeletons. Then, by allocating a radius to each node, a set of overlapped primitives connected with different nodes can be obtained. Manufacturability analysis and continuum topology validations are then utilized to guarantee the design validity. For a primitive meeting manufacturability analysis, Boolean operators are applied to obtain the final continuum structure. The workflow can be summarized in the following steps:

- Define the fixed nodes
- Determine the pre-optimal build orientation
- Define the variable/moving nodes
- Generate primitive units
- Manufacturability analysis
- Continuum topology validation
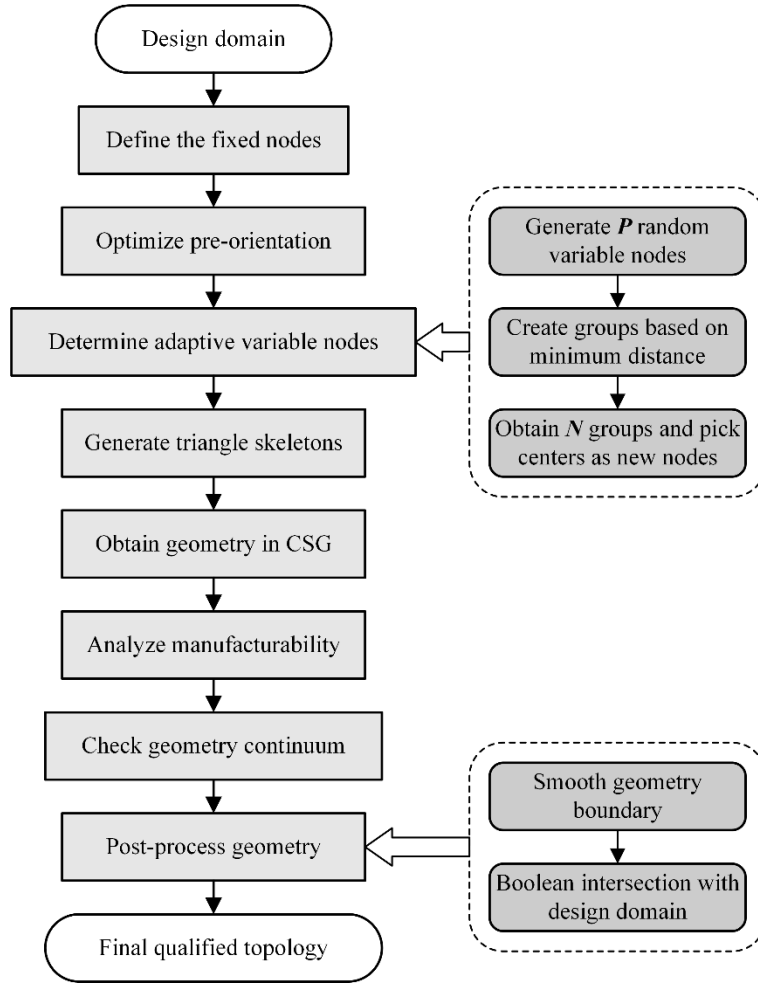
Figure 3.1. Flowchart of the generation of qualified AM design solutions with CSG-based geometric representation of the AM-oriented generative design method

3.1.1. Define the fixed nodes

The proposed geometric representation scheme defines the structural topology by position of a set of nodes in the design space. For a design domain as shown in Figure 3.2(a), we firstly need to define a set of fixed nodes representing spatial locations where materials must exist. Generally, loading contact points and support boundary limits are regions where fixed nodes are placed. Hence, they are usually on the boundaries of a design domain. Within the design domain, a set of moving nodes, which can be located anywhere, are defined as design variables. A point force F is applied to the boundary and Z is the build orientation. Section 3.1.3 below will show how to define these points in the design domain. As shown in Figure 3.2(b), green nodes represent the variable nodes and red nodes represent the fixed nodes. Connecting the fixed nodes and the variable nodes by the edges, a topology skeleton can be generated via the use of the Delaunay triangulation algorithm (Figure 3.2(b)).
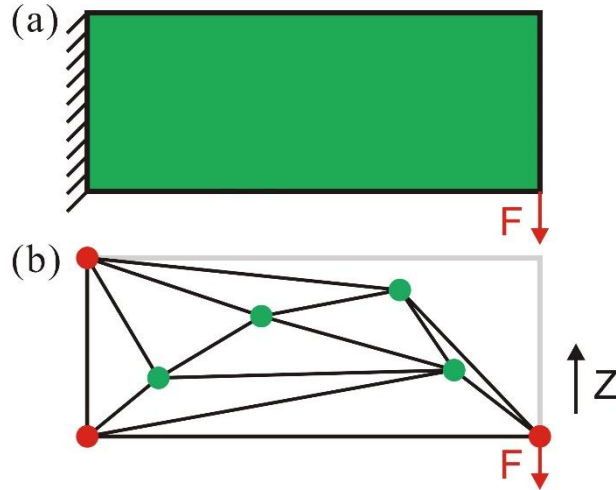
Figure 3.2. Node definition for design domain: (a) original design domain; (b) node definition (red nodes represent fixed nodes; green nodes are variable nodes)

3.1.2. Determine the pre-optimal build orientation

Build orientation concerns the direction along which the AM machine deposit materials. It has significant impact on the printing results, such as the final cost, accuracy, and surface roughness of the part as well as the mechanical properties. Hence, it is important to determine an optimal build orientation before any printing [51, 156, 157]. There has been a lot of research on build orientation determination for a well-defined CAD model, but much less work on the build orientation in the design stage and TO. In [158], an approach to simultaneously optimize build orientation and part topology was utilized to minimize the amount of supported surface area and support material. However, this work, also including previous research, omitted an important fact that AM processes have specific printable overhang length or bridge length without the need of any support. This length is determined by the material properties and the geometric parameters, e.g. layer thickness and successive inclination angles. Hence, in some conditions of the overhang area, the materials can be supported by themselves. This phenomenon is also called self-supporting. Figure 3.3 shows bottom layers of materials supporting upper layers of materials in inclination. In this chapter, this method looks at self-supporting and applies it to the pre-build orientation optimization for design domain. A design domain with a pre-build orientation means the following detail design will respect the orientation constraints. Hence, the build orientation will be integrated in the following TO process from the beginning. Generally, there are two main steps to determine the pre-build orientation for a design domain.
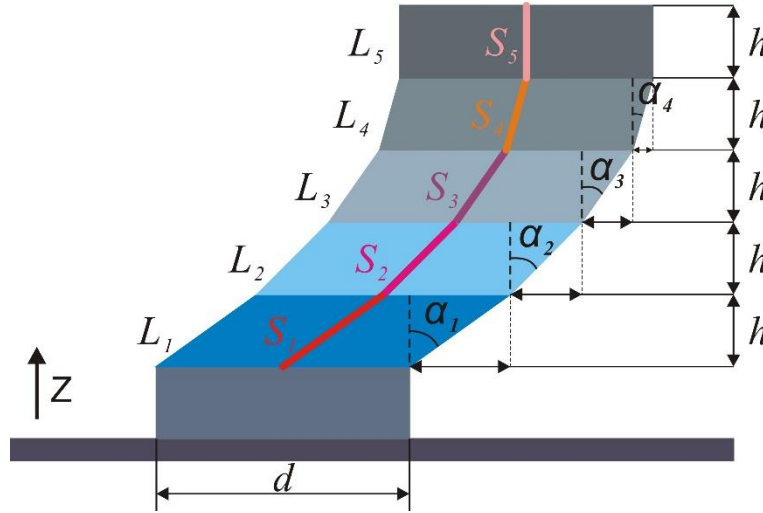
Figure 3.3. Overhang downward-facing inclination with different angles and skeleton positions. (h represent the height of each overhang region in build orientation; L_i, S_i and α_i represent *ith* overhang region, overhang skeleton and overhang angle, respectively.)

Firstly, as the overhang inclination angle directly determines if the overhang region is self-supporting, it is crucial to obtain as many inclination angles as possible to meet self-supporting requirements in the design domain so as to harness the benefits of this phenomenon in AM. Figure 3.3 provides a relationship between the overhang inclination angle and the overhang region. In the overhang regions L_i, S_i and α_i represent the corresponding skeleton and inclination angle, respectively. The skeleton angle has a direct impact on the overhang downward-facing inclination angle. Therefore, a transformation relationship between self-supporting primitive and self-supporting skeleton is proposed to help to determine the optimal build orientation. In order to acquire more self-supporting skeletons in the design domain, an objective function for a regular rectangular design domain is formulated as:

$$f_1(\theta) = min(P_x/P_z) \tag{3-1}$$

Where θ is the rotation angle, P_X and P_Z in Figure 3.4 are the projected lengths of the design domain on the X and Z direction, respectively. Mathematically, the objective can be represented by minimizing the proportional value of the projected length of the design domain on the X and Z direction to enable to obtain more self-supporting primitives along the Delaunay triangulation skeleton. Figure 3.4(c) and (d) are two examples of the optimal build orientations by using the objective expressed via Equation (3-1).
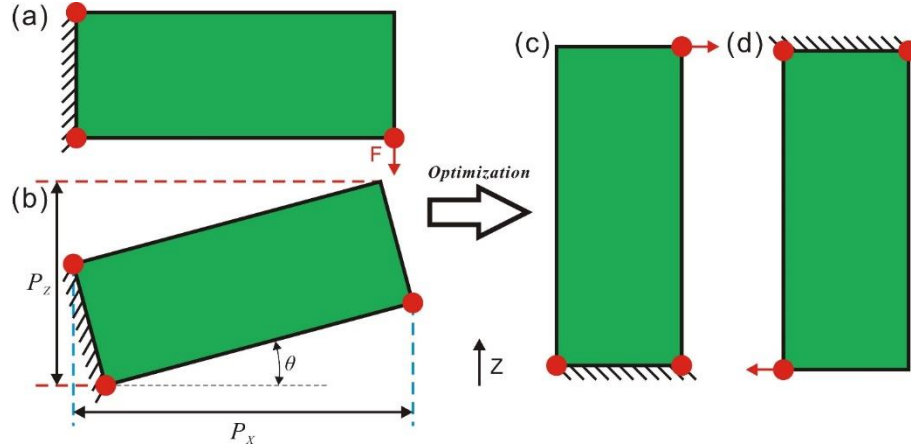
Figure 3.4. The pre-optimal build orientation for the design domain

Secondly, in many AM processes, there is a spacing Δ filled by support structures between part bottom and baseplate, as illustrated in Figure 3.5. This space is necessary to facilitate the post processing, e.g. removing a part from the base without damage. Hence, this space is also called the mandatory support cost region (base support region between the base and the part [53]). Therefore, the second objective is to minimize the support cost regions. Since this region and its related support volume depend on the pre-build orientation of the design domain and the detailed bottom shape of the part, it would be hard to estimate the exact support volume before the determination of the final topology geometry of the part. However, the projection length of the bottom boundary in the design domain has a positive proportional relationship with the support volume in this support cost region. In this situation, the minimization of the support structure (S_Δ) is converted to minimize the number of fixed nodes that need support. The objective for the rectangular design domain in Figure 3.4(a) is given by:

$$f_2(\theta) = min\sum S_\Delta \Rightarrow f_2(\theta) = min\sum N_i (i = 0,1,2,...,m) \qquad (3\text{-})$$

Where N_i indicates whether *ith* fixed node is the lowest point, where 0 and 1 imply the absence and presence of fixed nodes. Figure 3.5(b) is the final optimal build orientation for the illustrative design domain. In this illustrative example, the design domain is a rectangular simple shape and it is easy to identify the optimal pre-build orientation. However, it is necessary to consider the stability of part in printing for large-scale TO problems. From this perspective, the build orientation in Figure 3.4(c) is more stable. For real design cases, in particular redesign cases for AM, the design domain with complex boundaries may require the support of other defined objectives for searching. It should be noted that the goal of the pre-optimal build orientation is summarized as to obtain as many self-supported skeletons as possible in the design domain and to minimize the support cost on the premise of ensuring printing stability.
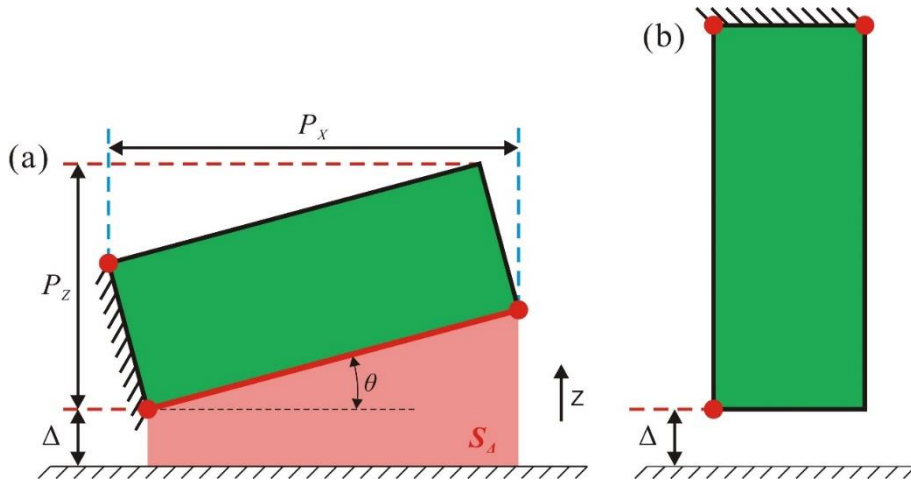
Figure 3.5. Determination of build orientation for the design domain via minimizing the support cost region

3.1.3. Define the variable/moving nodes

In the CSG topology generation, geometry skeletons are determined by the number and position of nodes. Fixed nodes are defined by the boundary conditions. Hence, the influence of the number of variable nodes on the triangle skeletons is crucial. Generally, the more points that are within the design domain, the more complex the Delaunay triangulation mesh is. As a result, more CSG volume would be generated based on the Delaunay triangulation mesh. In contrast, if there are fewer moving points defined in the design domain, then a sparse Delaunay triangulation mesh will be generated and less volume would be defined. Both of the two cases are hard to approach the global optimal solution. Hence, it is critical to define a set of suitable numbers of moving points within the design domain for optimization. To solve this problem, an adaptive method is proposed to determine the optimal number of variable nodes based on the minimum distance in Figure 3.6.
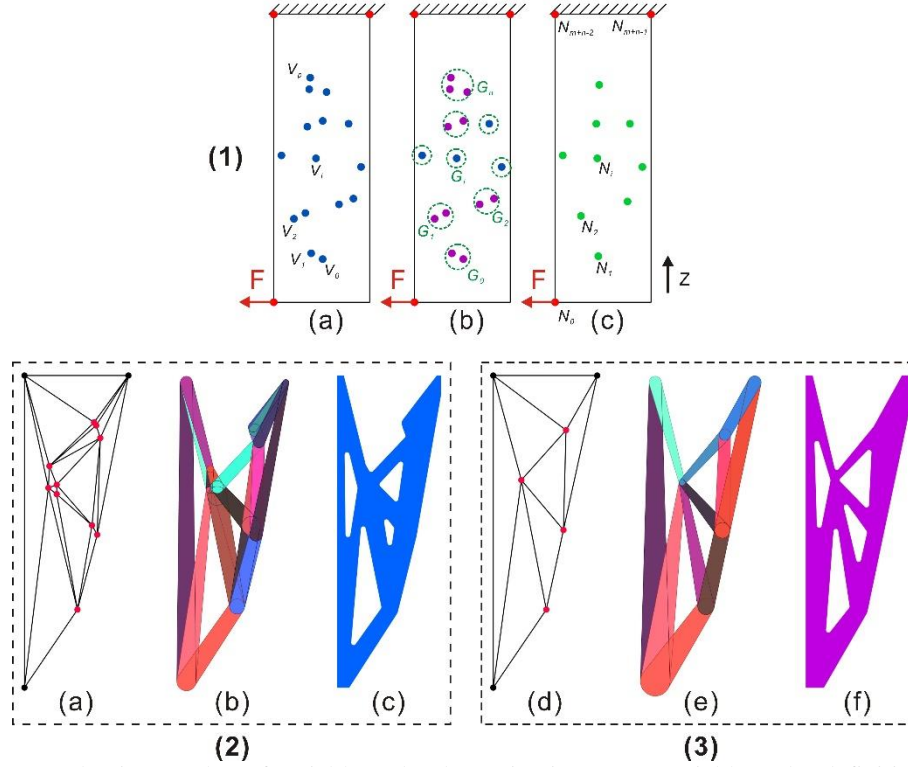
Figure 3.6. (1): Adaptive number of variable nodes determination: (a). p variable nodes definition; (b). Create group clustering from nearby variable nodes; (c). All nodes definition (n variable nodes in green and m fixed nodes in red). (2) and (3): Comparison before and after group clustering analysis. (a, d). Delaunay skeletons; (b, e). manufacturable primitive units; (c, f). final topology shapes.

Firstly, a maximum number of variable nodes (shown in Figure 3.6(1-a)) are randomly set for generating a sufficiently complex triangular mesh. Then, a clustering analysis is carried out based on the minimum Euclidean distance between variable nodes as shown in Figure 3.6(1-b). Finally, the center of each group is determined as a final variable node as shown in Figure 3.6(1-c). After adaptive variable node determination, the number of variable nodes is reduced from p to n ($1 \leq n \leq p$). If the distance D_{ij} of any two variable nodes is less than the minimum group distance, N_i and N_j are in the same clustering group. We use an average value of the nodes in a group as the radius of new node.

$$D_{ij} \leq D_{group}(i, j \in 0,1,2,...,p, i \neq j)$$

(3-

An example in Figure 3.6(2, 3) shows the Delaunay skeletons, manufacturable primitive units and final topology shapes before and after group clustering analysis. Before clustering analysis, the number of manufacturable primitive units is 25 and most of them are overlapping. However, there are 11 primitive units after group clustering. Group clustering can help reduce the number of the overlapping units. In addition, the number of adaptive variable nodes can be controlled by the minimum group distance. By using group clustering analysis, we only need to define a maximum number of variable nodes and ena-

ble to obtain a wide range of Delaunay triangular skeletons with different numbers of variable nodes. This clustering process will be conducted within each iteration loop in the following evolutionary optimization procedure to be introduced in Section 3.1.2.

3.1.4. Generate unit primitives

Once the design domain orientation is determined, the following step is to generate alternative topology geometries within the design domain. There is a need to give a generic representation of topologies. In this method, as said above, CSG generation and representation are adopted. Figure 3.7 presents an illustration to explain the geometry generation and its post-processing.
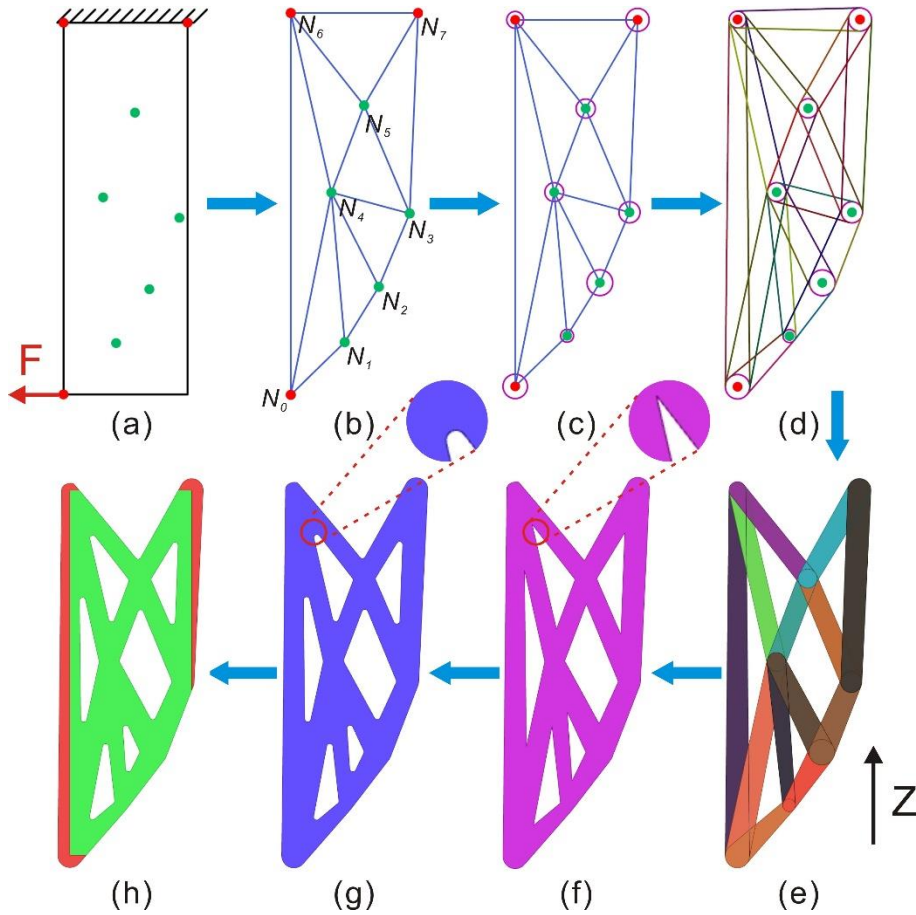
Figure 3.7. A schematic illustration of CSG-based topology optimization method: (a) fixed (red points) and variable (green points) node definition; (b) Delaunay triangulation skeleton; (c) assign radius to every node; (d) obtain primitive units; (e) manufacturable original primitive units; (f) perform Boolean union for all units; (g) smooth the shape; (h) obtain the final topology geometry (green color) by performing Boolean intersection operation in the design domain.

In Figure 3.7(a), the optimal build orientation is determined, fixed and moving nodes are defined in the design domain. All defined nodes are sorted by the position of those nodes that node N_{i-1} is always below node N_i. If the z positions of node N_{i-1} and node N_i are equal, node N_{i-1} is always located to

the left of node N_i. In other words, nodes are arranged in ascending order of position values (first z, then x). The skeleton of geometry (Figure 3.7(b)) is formed by using Delaunay triangulation algorithm. The triangulation returns the upper triangular matrix T_{ij} ($T_{ij}(i, j \in [0,1,...,p\text{-}1], i \neq j, p = m+n)$), as shown in Figure 3.8, where 0 and 1 imply the absence and presence of connection between nodes i and nodes j, respectively. Then, every node is assigned one radius variable to generate a corresponding circle, as shown in Figure 3.7(c). In Figure 3.7(d), the tangent lines are created from each skeleton edge with the corresponding circles. Then, the manufacturability of each primitive unit is analyzed by calculating the slope and length of the first tangent line for every primitive unit. The detail of manufacturability analysis will be explained in the next subsection. The manufacturable primitive units are shown in Figure 3.7(e). In Figure 3.7(f), the Boolean union is operated to obtain an initial topological structure. In order to avoid the sharp angles or corners causing stress concentration, the boundary of the initial structure is rounded down to r_0 as shown in Figure 3.7(f) and (g). The last step is to remove the material (red color in Figure 3.7(h)) outside the design domain using the Boolean intersection operation. The final topology structure (green color in Figure 3.7(h)) is obtained by a set of nodes and radius represented by p and r.

$$
\begin{array}{c}
\begin{matrix} N_0 & N_1 & N_2 & N_3 & N_4 & N_5 & N_6 & N_7 \end{matrix} \\
\begin{matrix}
N_0 \\ N_1 \\ N_2 \\ N_3 \\ N_4 \\ N_5 \\ N_6 \\ N_7
\end{matrix}
\begin{bmatrix}
0 & 1 & 0 & 0 & 1 & 0 & 1 & 0 \\
& 0 & 1 & 0 & 1 & 0 & 0 & 0 \\
& & 0 & 1 & 1 & 0 & 0 & 0 \\
& & & 0 & 1 & 1 & 0 & 1 \\
& & & & 0 & 1 & 1 & 0 \\
& & & & & 0 & 1 & 1 \\
& & & & & & 0 & 1 \\
0 & & & & & & & 0
\end{bmatrix}
\end{array}
$$

Figure 3.8. Upper triangular matrix representing the connection between nodes/skeletons for the given example

In contrast to traditional topology optimization approaches where structures are represented either by element density or nodal values of a level set function, with the CSG-based approach, a set of dynamic primitives is adopted as basic geometric blocks. These primitives are allowed to move, deform, overlap and merge freely in the design domain by changing the design variables (of the fixed and variable nodes with their assigned radius). The structure topology can be optimized by moving the nodes' positions and changing their radius. The method provides a new paradigm for topology optimization in a generative way (generate geometric volume in an additive way and control with parameterization). This method is convenient for the integration of manufacturing constraints in order to adjust the generated parametric alternative solutions with smooth geometric boundaries. Hence, as discussed above, it has great

potential to solve some of the current challenges in the topology optimization domain. The following subsection presents the integration of manufacturing constraints for manufacturability analysis.

3.1.5. Manufacturability analysis

To ensure all the generated topology structures are valid for printing, manufacturability analysis should be performed in the TO process. Due to the convenience of parametrization, the minimum printable shape feature size, maximum overhang angle and length can be well embedded. The flowchart presented in Figure 3.9 below shows the manufacturability analysis procedure in the proposed CSG-GD method. With the aim that it should be applied at a generic level, this method focuses on two principle factors, minimum printable feature size and a feasible self-supporting structure, from the perspective of manufacturability.
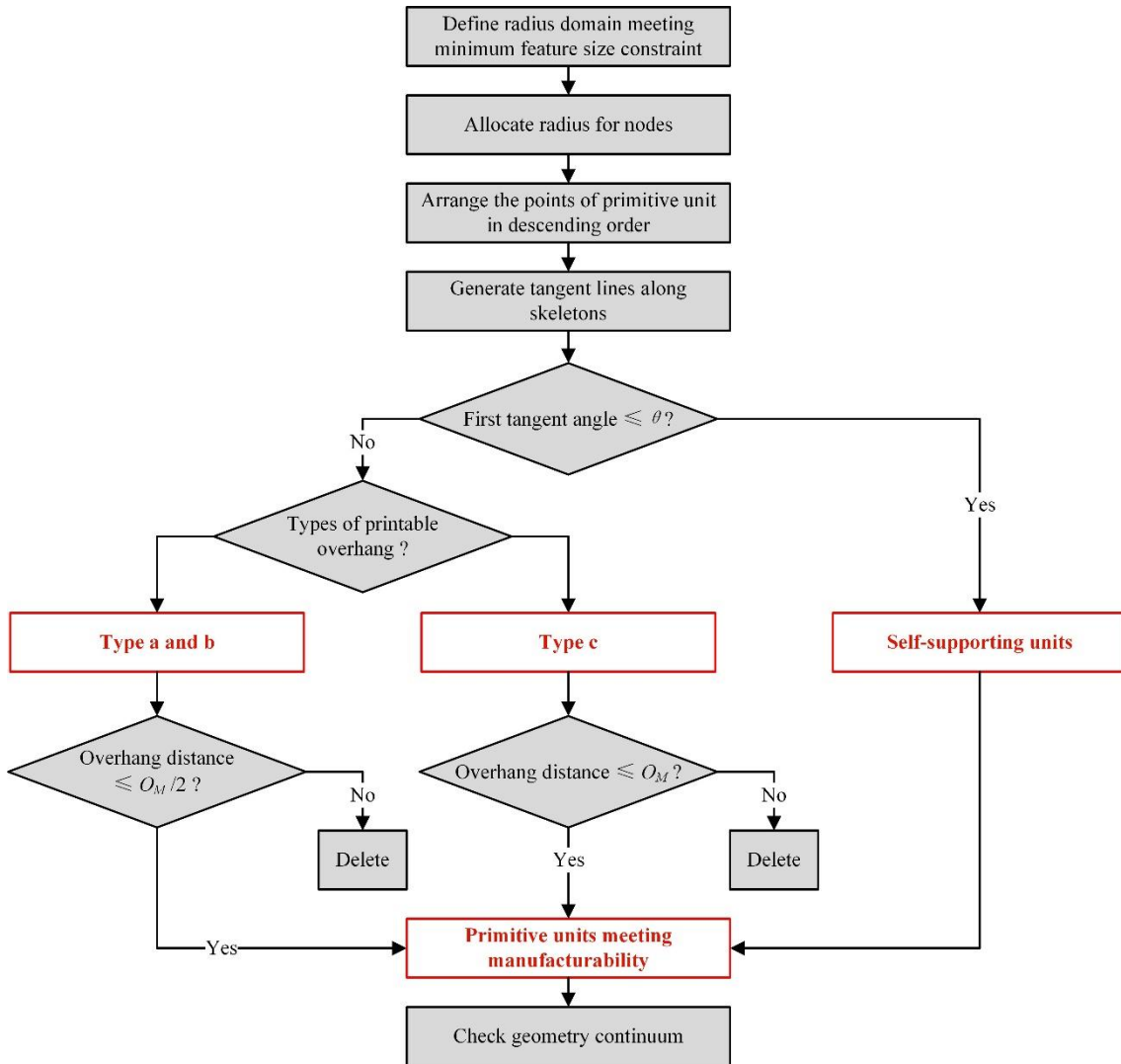
Minimum printable feature size

Minimum printable feature size concerns the minimum shape feature that can be achieved and controlled by AM processing. Different AM processes have different printable size limitations. This size can be obtained via process benchmarking. With a value of this size, the proposed method can easily integrate the minimum size constraints by defining the range of radius r to control the CSG geometries. Considering the nodes appearing on the boundary, the minimum feature size should meet the following constraint:

$$r_{min} \geq 2r_{mfs}$$

(3-4)

In Equation 3-4, r_{mfs} denotes the minimum feature size constraints, r_{min} represents the minimum radius of nodes.

Feasible self-supporting structure

As discussed in the previous section, especially for powder bed-based AM processes, a critical issue for self-supporting structures is to control the inclined angles of structural components. A maximum overhang angle is required to ensure that the design can be produced without the need of any supporting structure. In the CSG-based generative design method, the requirement of a self-supporting structure can be met by giving an angle constraint for controlling every primitive shape. Figure 3.10 illustrates an example that the primitive unit is obtained along the Delaunay triangulation skeleton.
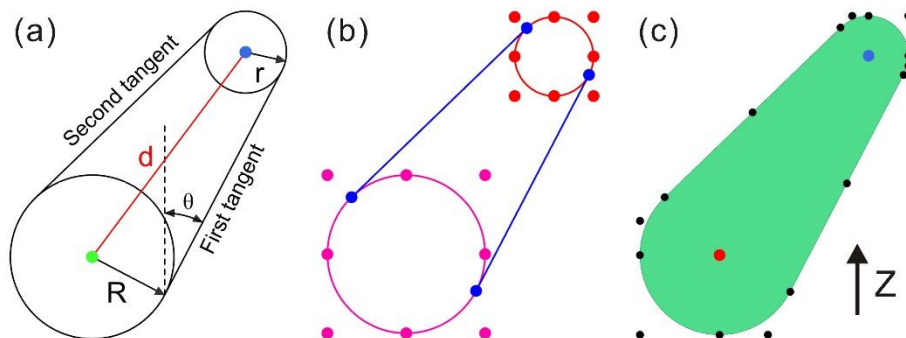
Figure 3.10. Primitive unit shape along Delaunay triangulation skeleton: (a) two external tangents along Delaunay triangulation skeleton. (b) parametric geometric control points for subparts of a primitive unit before Boolean union. (c) parametric geometric control point for primitive unit after Boolean union operation

Figure 3.10(a) represents two external tangent lines created by two circles defined by points, moving notes or design variables, on both sides of the skeleton. From a geometric perspective, two tangent lines

and circles are determined by control points (blue points as shown in Figure 3.10(b)). Figure 3.10(c) shows a primitive unit with updated geometric controlling points generated by conducting a Boolean union operation. Regarding the manufacturability of the final topology shape, the feasible self-supporting property of every primitive unit can be expressed by a set of parameters related to the tangent lines as shown in Figure 3.11 on the XOZ plane. Z represents the build orientation in printing.
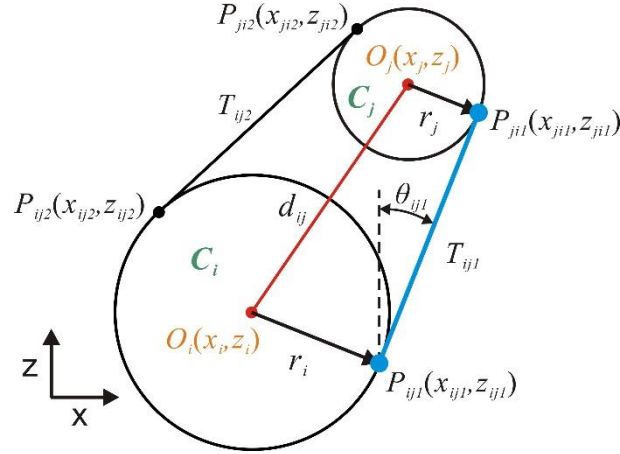
Figure 3.11. Detailed definition for points and tangent lines of a primitive unit

The distance between two nodes (O_i and O_j) on the skeleton is

$$d_{ij} = \sqrt{(x_i - x_j)^2 + (z_i - z_j)^2} \qquad (4\text{-}5)$$

Where (x_i, z_i) and (x_j, z_j) are the centers of circles, C_i and C_j, with radius r_i and r_j respectively. The first tangent line T_{ij1} and second tangent line T_{ij2} always satisfies the following inequality function:

$$z_{ij1} \le z_{ij2} \qquad (4\text{-}6)$$

Where (x_{ij1}, z_{ij1}) and (x_{ji1}, z_{ji1}) are the intersection points between first tangent line T_{ij1} and two circles, C_i and C_j, respectively. (x_{ij2}, z_{ij2}) and (x_{ji2}, z_{ji2}) are the intersection points between second tangent line T_{ij2} and two circles, C_i and C_j, respectively. The mathematical equation of tangent lines is defined as:

$$T_{ijk} : \frac{z - z_{jik}}{z_{ijk} - z_{jik}} = \frac{x - x_{jik}}{x_{ijk} - x_{jik}} (k = 1, 2) \qquad (4\text{-}7)$$

$P_{ijk}(x_{ijk}, z_{ijk})$ is the intersection point of C_i and the *kth* tangent line defined by C_i and C_j ($k = 1, 2$). Hence, the overhang angle θ_{ij} denotes the angle between build orientation Z and first tangent line T_{ij1}. It can be shown as the following:
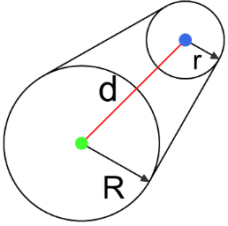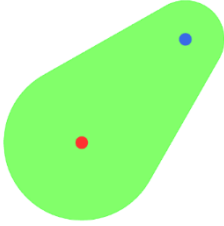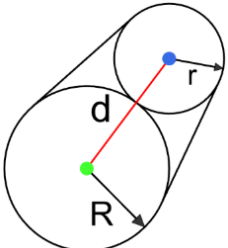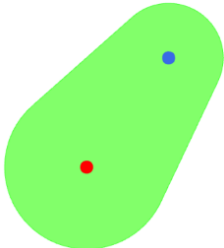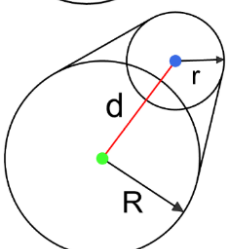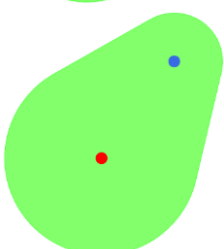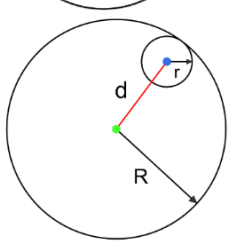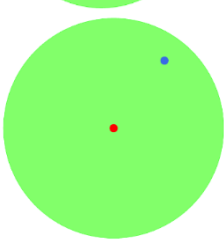
$$\theta_{ij} = \arctan \frac{\left| x_{ij1} - x_{ij2} \right|}{\left| z_{ij1} - z_{ij2} \right|}$$

(4-

As can be seen from Eq. (4-8), the advantage of the present formulation is that the self-supporting re-quirement can be achieved by introducing several explicit geometry constraints. The first tangent line is always denoted as the tangent that is on the inclination side of the primitive unit. Hence, this illustration is similar for the symmetric case as compared to the current case in Figure 3.11.

The existence of the first tangent line is closely related to the values of the distance d_{ij} and the radius corresponding to the center of circle. Table 6 below lists all geometric relationships between the two circles on both sides of the skeleton. These relationships can be used as rules to evaluate the manufac-turability of primitive unit via the calculation of inclination angles using Eq. (4-8).

Table 3.1. Five kinds of primitive units defined by two circles on both sides of the Delaunay triangulation skeleton

No.	Relationship between circles	Geometric domain	Primitive unit	First tangent line exists?
1	$d > \left| R + r \right|$			Yes
2	$d = \left| R + r \right|$			Yes
3	$\left| R - r \right| < d < \left| R + r \right|$			Yes
4	$d = \left| R - r \right|$			No

| 5 | $0 \leq d < \|R - r\|$ | | No |
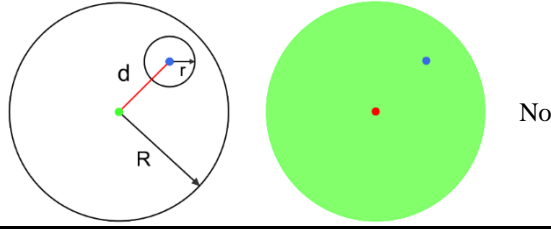
As discussed above, most existing self-support TO methods only control the overhang inclination angle to less than a predefined maximum overhang angle value. However, the maximum overhang angle is not the only factor that defines the self-support structure. The printable overhang distance also plays a key factor in guaranteeing self-supporting manufacturability. Therefore, this factor should be included in the TO process. For example, in the SLM processes, the support point respecting the maximum bridge printing length of process capability can provide a stable support for local overhang regions and avoid any surface collapse in printing. This factor was considered for the support structure design in [27], where support points were carefully selected to support the overhang regions. An illustrative example to explain this factor is described in Figure 3.12, where the printable bridge length with different values of the SLM process was investigated in [159, 160]. It is clear that small overhangs can be printed when the bridge size is less than a certain overhang distance. Hence, it is essential to consider the maximum overhang angle and the printable overhang distance simultaneously in developing a self-supporting structure.
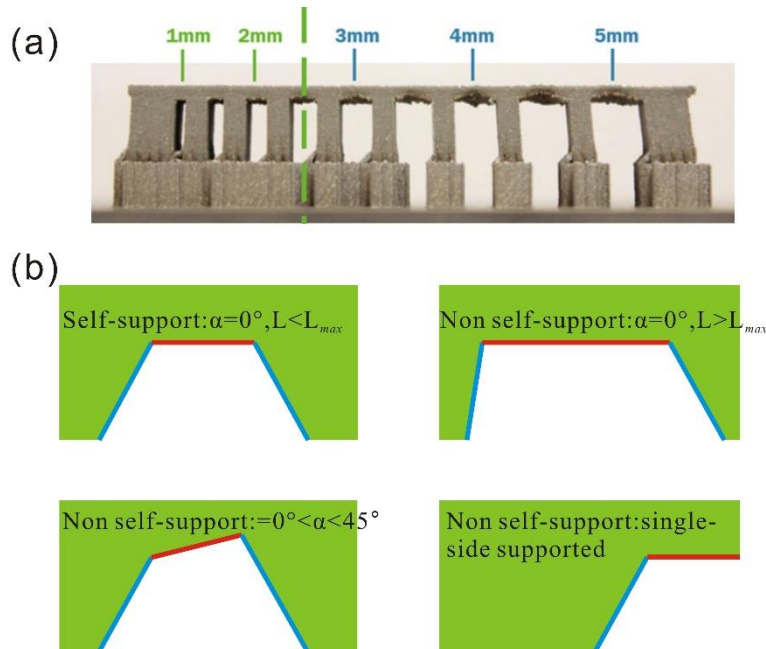
Figure 3.12. (a). Effect of unsupported bridge for metal 3D printing [159] and (b). Self-support bridge guaranteeing manufacturability [160]

Based on the previous work, the proposed method in this chapter defines three types of printable self-support/overhang structure conditions to guarantee the manufacturability as shown in Figure 3.13.

Situation 1: The overhang angle θ is large than the maximum overhang angle θ_M and the horizontal overhang L_H is less than half of the maximum overhang distance $O_M/2$.

(a). Both lower sides of the overhang are self-supported.

(b). The one lower side of the overhang is self-supported.

Situation 2: The overhang angle $\theta \approx 90°$ and the horizontal overhang L_H is less than the maximum overhang distance O_M.

(c). Both sides of the overhang are self-supported.

In essence, type (c) is subordinate to type (b). The connected non-self-supporting overhang should be represented as a whole overhang and then manufacturability needs to be analyzed.

(a) $\theta > \theta_M : L_H < O_M/2$ (b) $\theta > \theta_M : L_{H1} < O_M/2$ & $L_{H2} < O_M/2$ (c) $\theta \approx 90° : L_H < O_M$
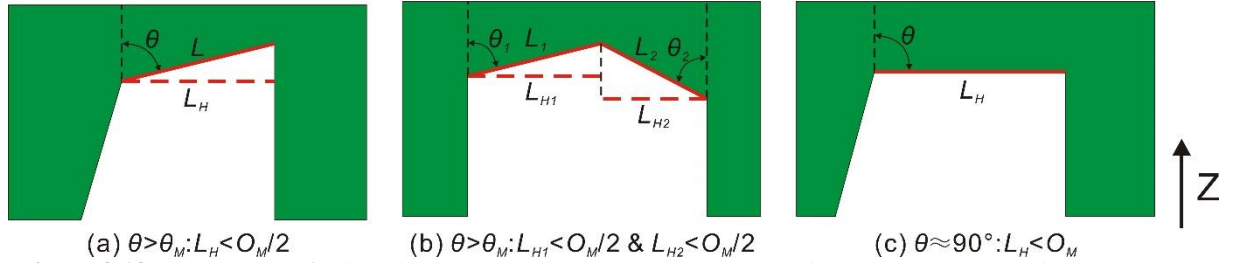
Figure 3.13. Three types of printable overhang where the overhang angle is larger than the maximum overhang angle

With the parametric characteristic of the proposed CSG-GD method, it is easy to control these factors simultaneously as discussed above. In Figure 3.14. N_i, N_j and N_k are defined fixed or variable nodes. $T_{ij}(P_{ij}P_{ji})$, $T_{kj}(P_{kj}P_{jk})$ corresponds to the first tangent lines of non-self-supporting primitive units, respectively. Blue and green primitive units dictate self-supporting structures; grey and orange primitive units represent non-self-supporting structures.
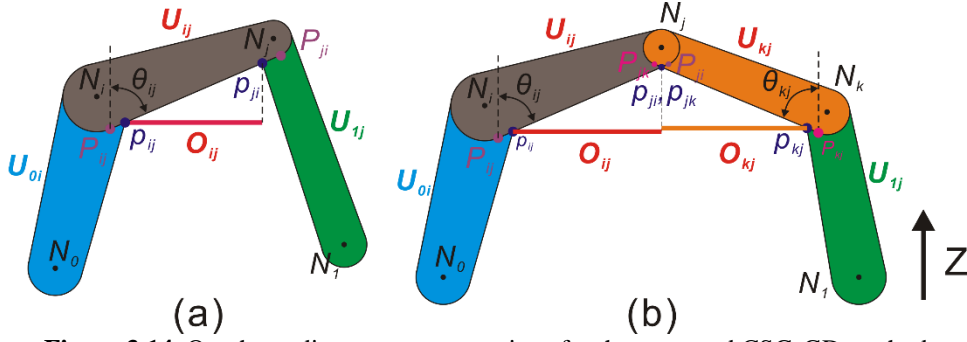
Figure 3.14. Overhang distance representations for the proposed CSG-GD method

In Figure 3.14(a), a non-self-supporting primitive unit U_{ij} is connected to two self-supporting units, U_{0i} and $U_{1,j}$. This type belongs to the situation 1-(a). In Figure 3.14(b), the lower sides of two interconnected non-self-supporting structures are connected to two self-supporting structures, respectively. The maximum overhang distance constraint should satisfy the following mathematical expressions at the same time:

$$\begin{cases} t_{ij}\sin\theta_{ij} \leq \dfrac{O_{max}}{2} \quad (\theta_{ij} > \theta_{max}) \\ \sum t_{ij}\sin\theta_{ij} \leq O_{max} \end{cases} \tag{3-9}$$

In Equation 3-9, $t_{ij}(p_{ij}p_{ji})$ represents the overhang distance of a non-self-supporting primitive unit U_{ij}. θ_{ij} denotes the overhang angle. O_{max} and θ_{max} are the maximum overhang distance and maximum overhang angle, respectively.

3.1.6. Continuum topology validation

As discussed above, the initial topology skeleton is defined by the Delaunay triangulation algorithm. A manufacturability analysis is performed to obtain the manufacturable primitive units. However, since the manufacturability analysis is conducted to check each primitive unit before the Boolean operation in the post-processing step, which may cause discontinuity of invalid topologies, hence there is a need to check the volume continuum after the Boolean operation and other post-processing operations for the geometries. To check the connectivity of the topology structure, it is necessary to ensure all the fixed nodes are in the design domain and the topology structure is a continuous volume. Figure 3.15 gives a flowchart of continuum topology validation and repaired geometry generation.
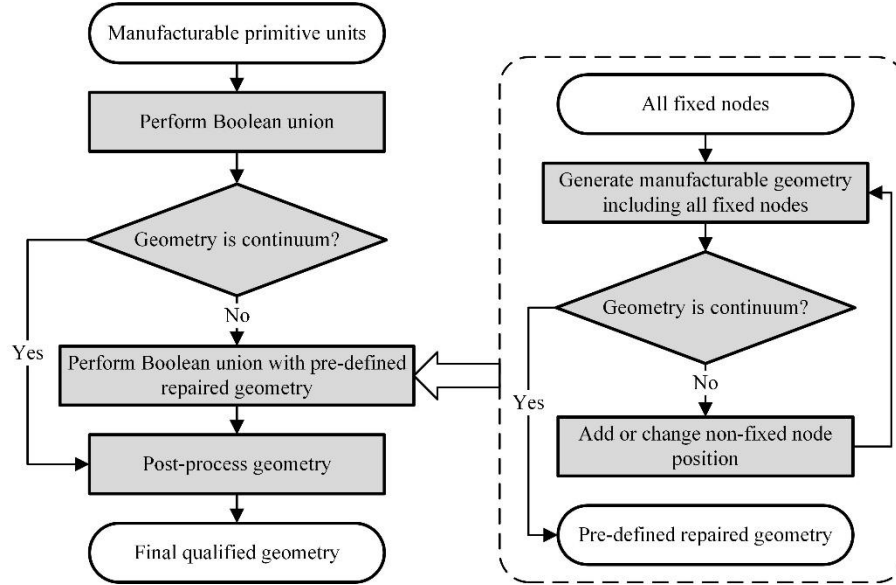
Figure 3.15. Flowchart of continuum geometry validation and repaired geometry generation

In the geometry continuum check, there are usually two circumstances for an inconsistent topology: 1) not all the fixed nodes are connected to the continuum structure. 2) there are two or more disconnected topology structures. Under these circumstances, the inconsistent topology structure must be detected and repaired. One solution is to delete these inconsistent topologies, but this may reduce much of the original solution space. Hence, a continuum geometry repair approach is employed to detect and repair the geometry. In [64], a graph based geometry repair algorithm is used to repair the geometry by adding minimum possible segments to the Delaunay triangulation mesh to form a volume connection set. The details on the related graph based repair can be found in [161] on water distribution networks.

An example of continuum topology validation is exhibited in Figure 3.16. Figure 3.16(a) represents the original primitive units via the Delaunay triangulation algorithm. The topology structures in Figure 3.16(b1) and (b2) are manufacturable and unmanufacturable primitive units after manufacturability analysis, respectively. The topology structure shown in Figure 3.16(c1) is checked as an invalid continuum structure. Hence, a continuum geometry repair operator is required to repair the invalid structure by adding some primitive units to connect all printable units. Initially, it is mandatory to find a connection strategy to connect all the fixed nodes and ensure the manufacturability of these primitives. Such a connection strategy among fixed nodes should guarantee that repair segments obtain all fixed nodes. The inconsistent geometries (Figure 3.16(c1)) are connected to repaired segments (Figure 3.16(c2)). The repaired geometries via the Boolean union and post-processing are shown in Figure 3.16(d) and (e), respectively. After the continuum geometry repair operation, a final qualified AM-oriented continuum topology is formed.

71
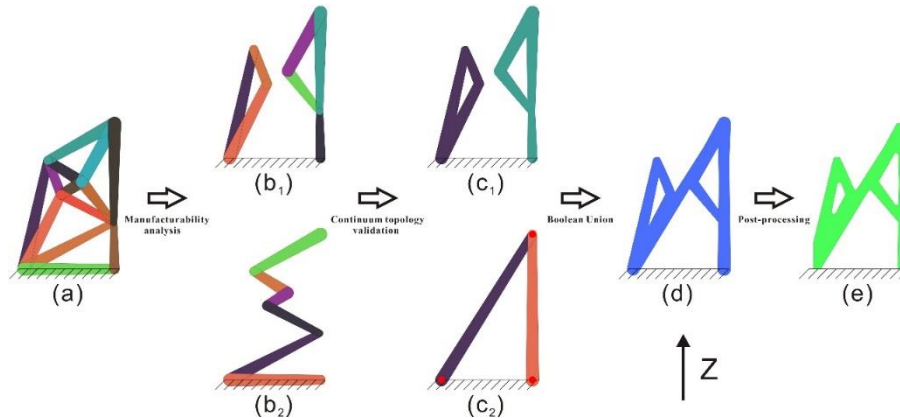
Figure 3.16. Continuum topology validation: (a) original primitive units obtained by Delaunay triangulation skeletons; (b1) manufacturable primitive units; (b2) unmanufactNonurable primitive units; (c1) manufacturable primitive units after Boolean union; (c2) pre-defined manufacturable & repaired geometry; (d) geometry of c1 and c2 after Boolean union; (e) final qualified geometry after post-processing.

3.2. Alternative design solution generation and optimization

As introduced above, a generative design in structural design mainly uses evolutionary algorithms to populate numerous alternative solutions to respond to predefined objectives and constraints. In this chapter, in order to conduct multi-objective optimization and generate a large number of alternative topology structures, a multi-objective evolutionary algorithm, NSGA-II [162], is adopted to obtain a set of Pareto-optimal solutions. NSGA-II is a very popular algorithm and it has been demonstrated as one of the most efficient algorithm for the most efficient algorithms for multi-objective optimization on many benchmark problems. The algorithm flowchart is presented in Figure 3.17.
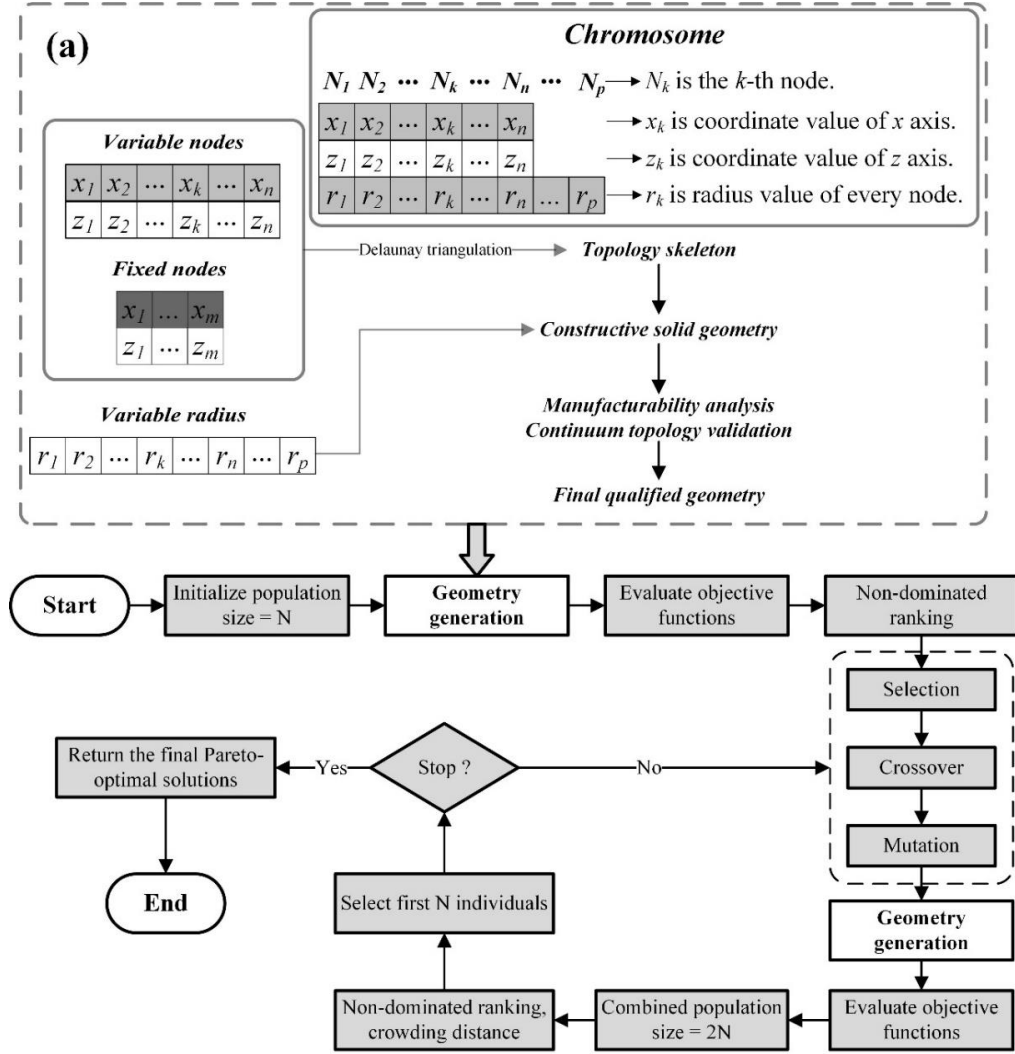
Figure 3.17. Flowchart of a Pareto-optimal solutions search.

In Figure 3.17(a), the relationship between chromosome and topology geometry is set out to explain the geometry generation. The topology skeleton is defined by the position of variable and fixed nodes on the XOZ plane using the Delaunay triangulation algorithm. Three types of variables are set for constructing topology geometry. Manufacturability analysis and continuum topology validation can enable the final geometry to be qualified. Two objective functions are defined to minimize the volume and compliance. 2D triangular mesh is used to complete the finite element analysis. The GA parameters and its coding are also shown in Figure 3.17(a).

3.3. Case study

In this section, bi-objective optimization for compliance minimization problems is selected to demonstrate the performance of the proposed method. Parameters in the standard NSGA-II algorithm are defined in Table 3.2. For all cases, the values of the crossover probability of 0.9 and the crossover distribution index are set as 0.9 and 20 respectively, and a mutation probability of 0.3 and a mutation distribution index of 20 are adopted. In order to solve the compliance minimization problem volume V and compliance C are minimized simultaneously. The optimization problem is formulated as:

$$Min:\begin{cases} f_1 = V/V_{max} \\ f_2 = u^T Ku \end{cases}$$
(3-10)

Where V is the volume of the final geometry, V_{max} is the volume of the design domain, u is the displacement vector, K is the global stiffness matrix. 2D triangular meshing technique is applied to mesh the geometry and calculate the compliance.

Table 3.2. Parameters definition of NSGA-II algorithm

Option	Description
Crossover probability	0.9
Crossover distribution index	20
Mutation probability	0.3
Mutation distribution index	20

3.3.1. Asymmetric design domain case

The design domain and boundaries for the cantilever beam problem is defined by using a previous build orientation method in Figure 3.18. The design domain is $3L \times L$ and a point force F is applied to the boundary and Z is the build orientation. Table 3.3 lists a series of parameters used in the problem.
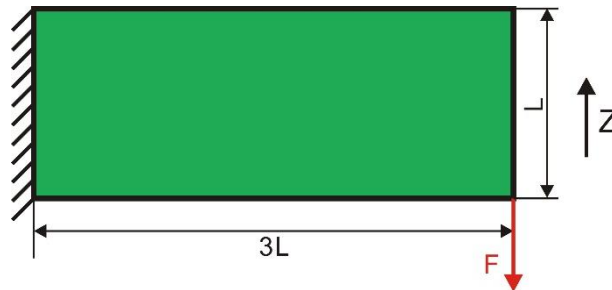
Figure 3.18. Design domain for case 1.

Table 3.3. Parameters used in the cantilever beam problem.

Option	Description
The number of fixed nodes (m)	3
The number of variable nodes (p)	15
Population size	100
Generations	500
Force (F)	100 N
Radius range (r)	0.5-3 mm
Maximum overhang distance (O_M)	2 mm
Maximum overhang angle (θ)	45°

According to the proposed geometry representation method, three fixed nodes are defined on the load and support boundary, and seven variable nodes are applied in the design domain. Subsequently, a pre-optimal build orientation is determined in order to obtain more Delaunay triangulation skeletons that meet the manufacturing constraints (as shown in Figure 3.19(a)) The number of adaptive variable nodes are n $(1 \le n \le p)$. Hence, the number of variable is $6 \le 2n+(m+n) \le 48$. The range of x and z position variable varies from 0 to 20 and 0 to 60, respectively. Fixed nodes are defined at (0, 0), (0, 60) and (20, 60). The sorting of nodes is shown in Figure 3.19(b). A commonly accepted value of the maximum overhang angle is 40°-50°. In this case, the maximum overhang angle and distance are defined as 45° and 2 mm respectively.
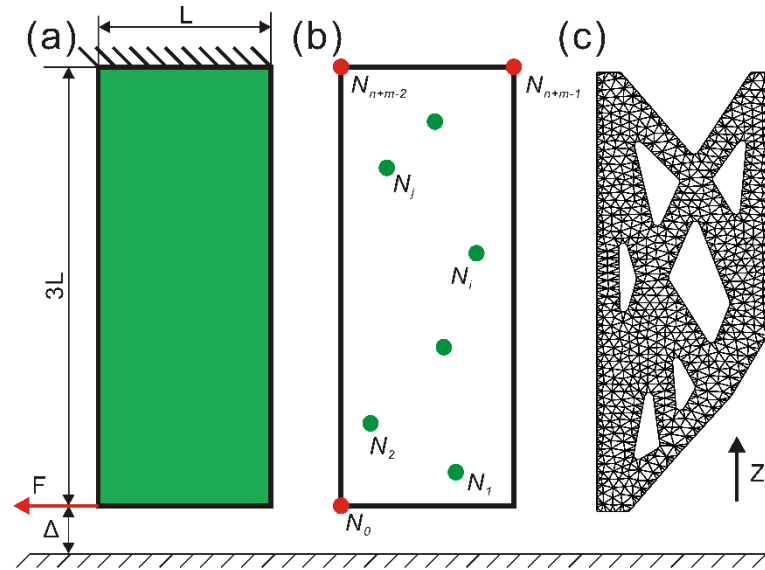
Figure 3.19. (a). the optimized build orientation; (b). adaptive node definition; (c). 2D triangular meshing.

The initial parameter of the proposed GD method is set as: population size, 100; stop criterion of the optimization, 500 generations. The Pareto-optimal solutions obtained for the optimization problem are indicated in Figure 3.20. Each point on the Pareto front represents a design structure for the corresponding volume ratio.
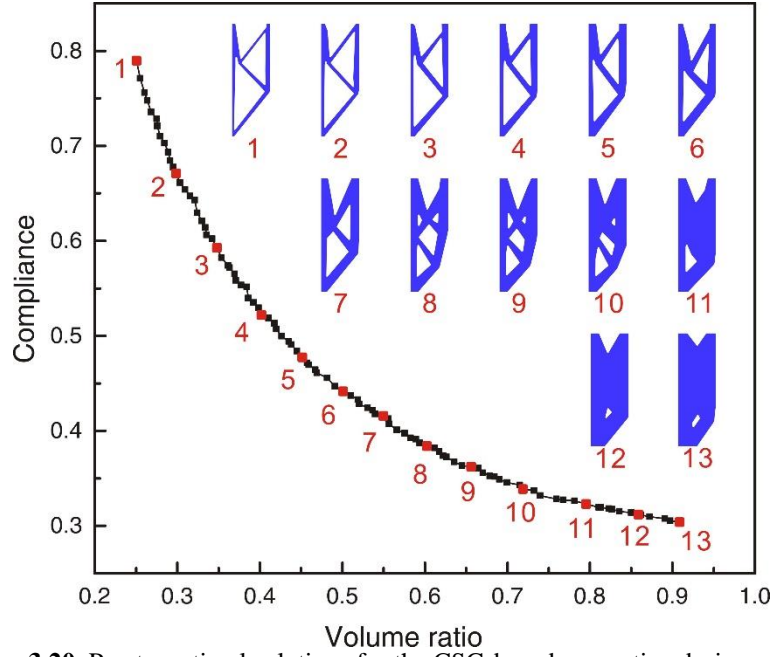
Figure 3.20. Pareto-optimal solutions for the CSG-based generative design method

It is assumed that solutions with a volume ratio less than 0.25 are infeasible. In Figure 3.20, thirteen sample optimal solutions for different volume ratios on the Pareto front are selected and corresponding structures are indicated. Sample 1 to 7 have a similar shape, but variations in the radius provide differences in the objective values. The evolution of the structure is illustrated in Figure 3.21. Six different generations are marked and the corresponding volume ratios are also shown.
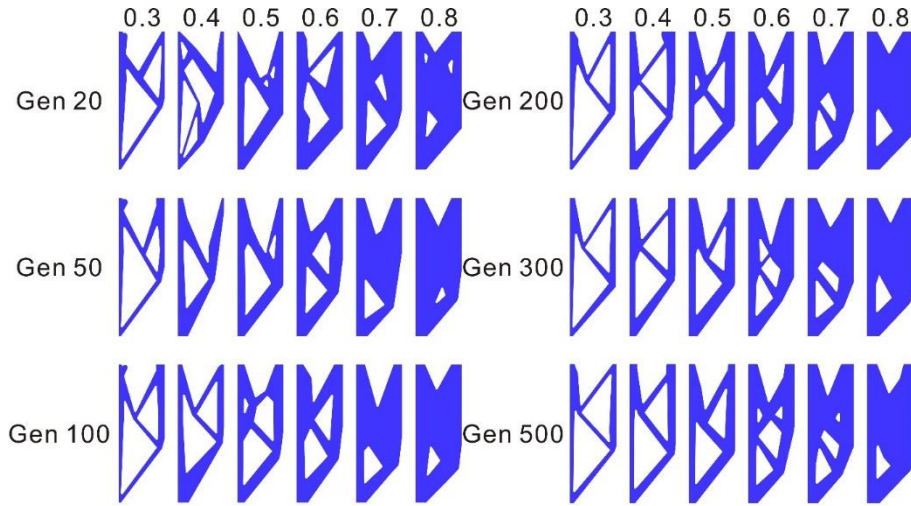
Figure 3.21. Evolutionary trend of Pareto-optimal solutions

Figure 3.22 compares the results of the proposed method with that of two other methods in literature. In [163], the topological sensitivity method was used to generate Pareto-optimal topologies. However, the author focuses on the material distribution and ignores the manufacturability. Nevertheless, the proposed method in this chapter still shows a good performance. In [164], a parameterized level set method

is applied to minimize the compliance of a single-objective two-dimensional (2D) structure problem. The level set method can maintain a smooth level set function and does not need to implement any filter during the optimization process. Though level set method provides a slightly better trade-off front than that of the proposed CGS-based GD method, it needs to make multiple runs with different volume constraints each time and does not consider manufacturing constraints a problem. The results of the level set are not qualified AM design solutions. Compared to these gradient-based topology optimization methods, the proposed method utilizes a small number of design variables and populates a set of qualified and relatively optimal candidate solutions on the Pareto front. More importantly, all the generated alternative solutions are valid solutions for the AM process, which is critical for industrial design practice in AM.
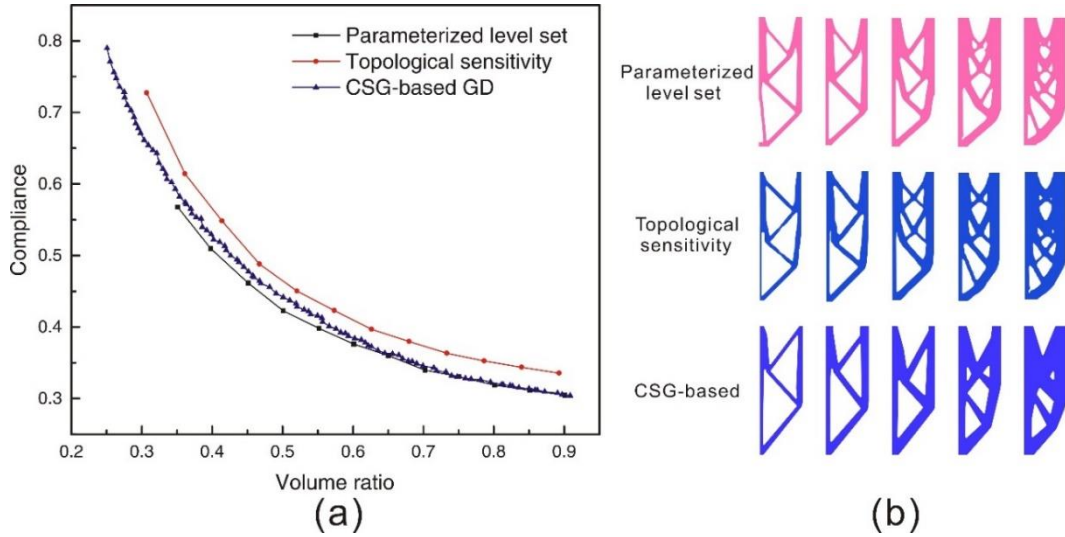
Figure 3.22. The Pareto-optimal curves and corresponding sample solutions for three methods.

Most research in literature has suggested that the maximum overhang angle for L-PBF was $45°$. However, this angle depends on the parameter setting of specific AM machines. Hence, the design optimization method should have the capability to include this flexibility. Due to the parametric control for all variables, the proposed method is convenient in that it adjusts all the parameters according to the needs of specific AM processes. In order to further verify the effectiveness of the proposed CSG-based method, different maximum manufacturing overhang angle constraints are investigated. Figure 3.23 gives a part of the Pareto-optimal solutions for two maximum overhang angles, $60°$ and $75°$, respectively.
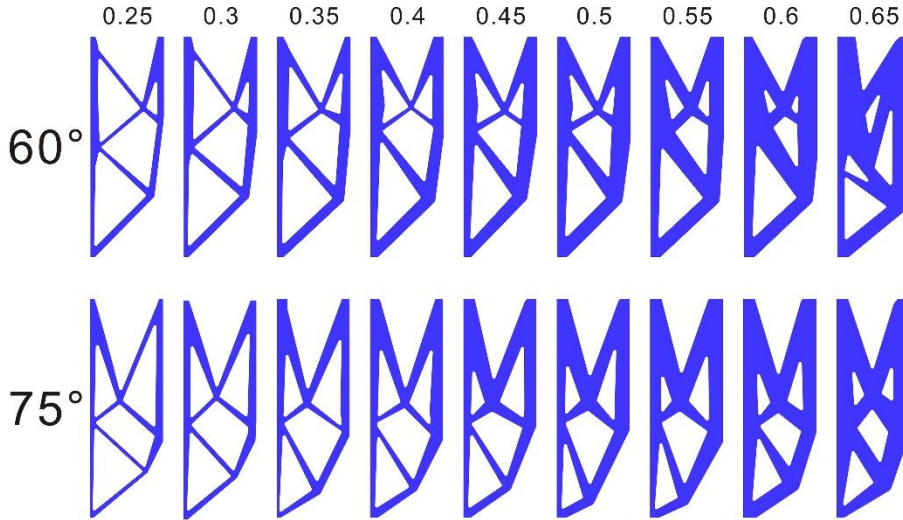
Figure 3.23. Pareto-optimal solutions for different overhang angle constraints

3.3.2. Symmetric design domain case

In topology optimization problem, design domain with symmetric boundary conditions is often encountered. To show the effectiveness of the proposed method, a symmetry beam problem is tested. To solve this problem, a simple skeleton mirroring method is designed to obtain symmetry skeletons as an adaption of the Delaunay triangulation algorithm. According to the proposed method framework above, the pre-optimal build orientation definition and the fixed and variable nodes determination results are presented in Figure 3.24.
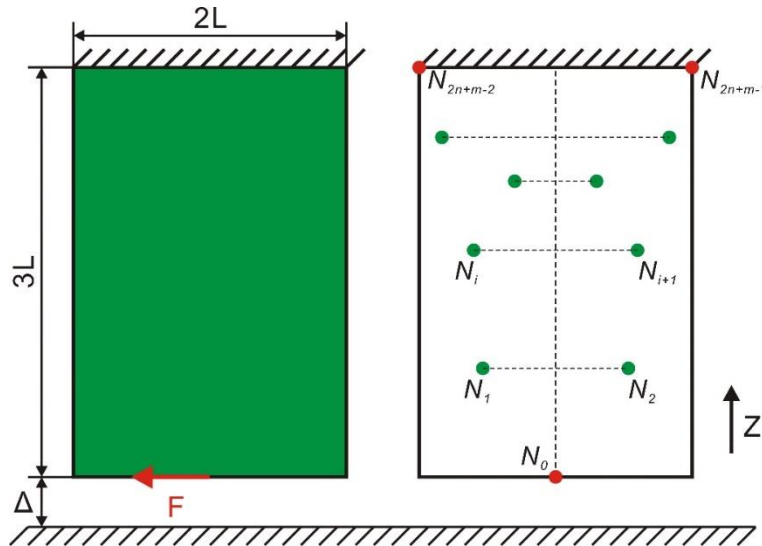
Figure 3.24. Design domain and adaptive node definition for case 2 (Z: build orientation).

In this case, three fixed nodes and fifteen variable nodes are defined and the corresponding mirror nodes are generated as shown in Figure 3.25(a). A Delaunay triangulation skeleton is represented by a set of connected nodes. In Figure 3.25(b), the skeletons that do not meet the symmetry condition are colored

in red. The symmetry problem can be solved by mirroring the skeleton on the other side. The mirror skeletons are shown in blue in Figure 3.25(c). The final skeleton is composed of the original skeleton and mirror lines. Once the symmetry skeleton is obtained, the subsequent operations are the same, as shown in Figure 3.7.
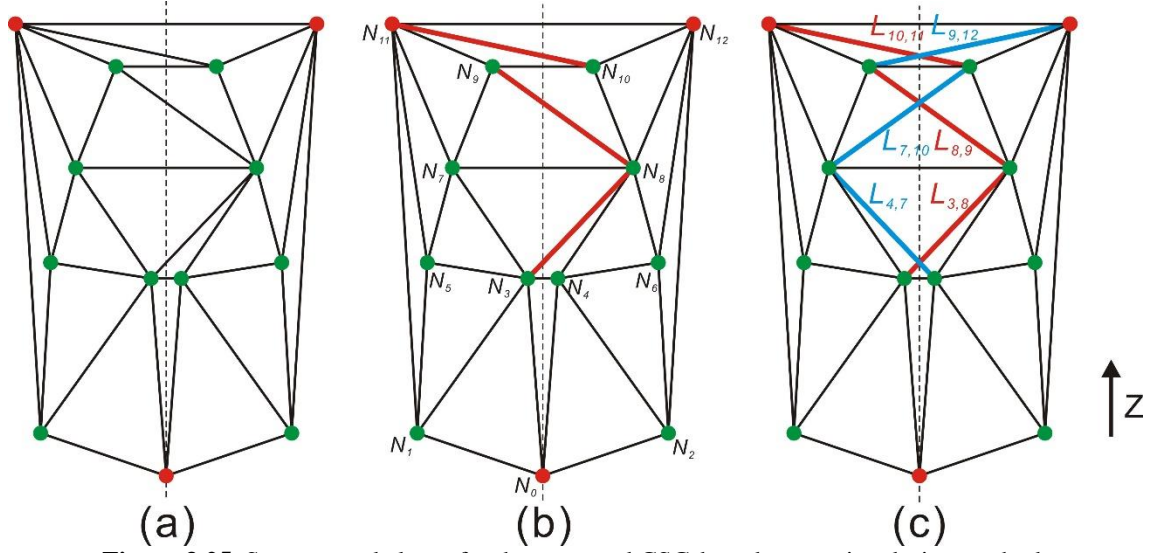
Figure 3.25. Symmetry skeleton for the proposed CSG-based generative design method.

Regarding the symmetry problem, fixed nodes are defined at the positions of (20, 0), (0, 60) and (40, 60). The number of adaptive variable nodes is n $(1 \leq n \leq p)$. Hence, the number of all variables is $6 \leq 2n + (m - 1 + n) \leq 47$. The range of x and z position variable varies from 0 to 20 and 0 to 60, respectively. The maximum overhang angle and distance are also defined as $45°$ and 2 mm. Figure 3.26 captures the Pareto-optimal solutions obtained by the proposed CSG-based generative design method. Solution 2 to 9 have a similar shape with different widths. With the increase in the width of primitives, the internal gaps gradually decrease. In solution 11, the internal holes/cavities disappear.
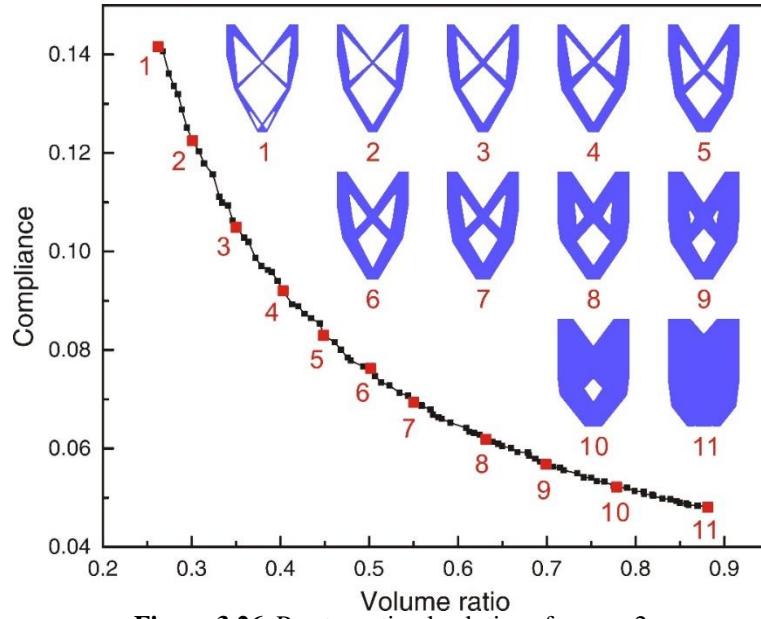
Figure 3.26. Pareto-optimal solutions for case 2

To further demonstrate the proposed method, the results obtained are compared with that of two other existing methods. The Pareto-optimal curves and the corresponding structure of three methods are shown below in Figure 3.27. As shown in Figure 3.27(a), three Pareto-optimal curves have the same trend. The CSG-GD method and topological sensitivity perform similarly when the volume ratio is less than 0.3 or more than 0.45. However, the parameterized level set method has a better Pareto front on average. When the volume ratio is higher than 0.65, three methods exhibit similar Pareto-optimal values.
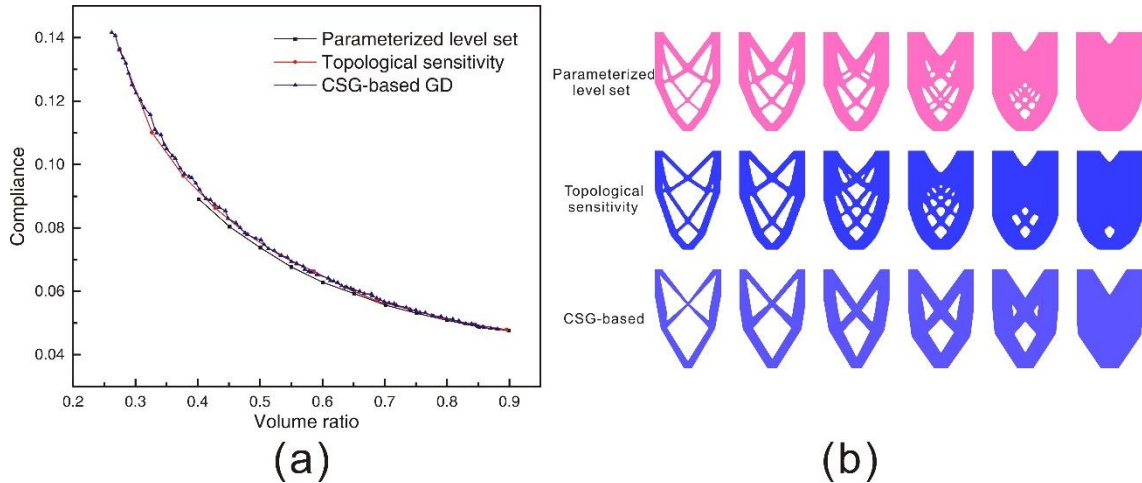
Figure 3.27. The Pareto-optimal curves for three methods in symmetry beam problem

As discussed above, though the proposed CSG-based GD method does not exhibit a better performance than that of the level set method, it better integrates AM manufacturing constraints into generative design algorithm. In addition, the proposed method has the potential to achieve a good compromise for multi-objective optimization problems via the providing of a set of qualified alternative solutions to

facilitate decision-making for the designers. Generally, compared to the sensitivity-based TO method, the proposed approach has a better trade-off in Pareto-optimal tracing and has a similar performance to that of the level set method. Due to the consideration of many manufacturing constraints in AM, the proposed method can better exert the potential of AM and generate qualified design solutions.

To validate the manufacturability of the obtained Pareto optimal solutions, several Pareto solutions of the two cases were selected and printed by an SLA (Stereolithography) machine. The printing sizes were set as $20 \times 60 \times 5$mm and $40 \times 60 \times 5$mm respectively for the asymmetric design domain case and the symmetric design domain case respectively. Figure 3.28 presents the printing results, which shows the structures are self-supported and there is no failure in the printing. Similarly, other AM process, e.g. SLM, can also be used for evaluation, but we only need to reset some of the manufacturing constraints' values, such as the maximum bridge length of the AM process, in the TO procedure.
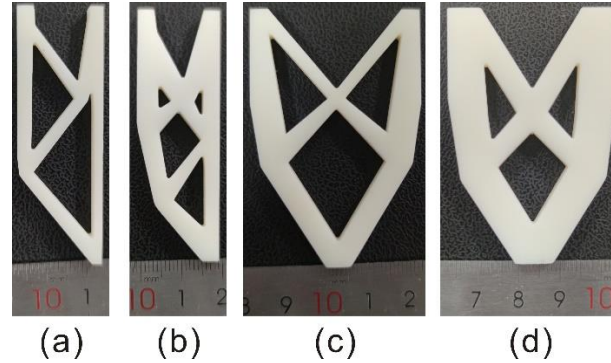
Figure 3.28. Asymmetric design domain case: (a). volume ratio = 0.4; (b). volume ratio = 0.6; Symmetric design domain case: (c). volume ratio = 0.4; (d). volume ratio = 0.6.

3.4. Summary

In this chapter, a new CSG-based generative design method is proposed to generate and search for optimal qualified AM design solutions. General AM manufacturing constraints are analyzed and modelled to support practical DfAM needs. The main contribution of this work is the introduction of a CSG geometry representation for topology optimization for AM and the realization of parametric control of explicit geometries with smooth boundaries. The application of geometric shape control points in the TO operation can greatly reduce the number of design variables and release the potential of evolutionary algorithm-based TO methods. Furthermore, a major advantage of the proposed method is to obtain strong convex Pareto sets, which are qualified design solutions for conflicting objective functions.

Hence, a Pareto-optimal set can represent the trade-off for further decision making when compromise should be made with diverse preferences in specific applications.

Chapter 4. Pattern-based constructive generative design for support structure in AM

This chapter proposes a pattern-based constructive generative design method for support structure generation. First, a support point determination method is developed for an optimal support structure design with a targeted AM application in biomedical engineering. It at first addresses how to detect and select a reasonable support region in an optimal way taking into consideration AM constraints and application requirements. Then, an optimization algorithm is applied to optimize the number and position of support points on the selected support regions. A new support point pattern is developed so that the redundancy of current support point distribution is alleviated. To reduce support structure volume, post-processing time and improve the printing quality, the proposed bio-inspired generative design method integrates parametric L system rules and lattice structure configuration, to generate lightweight, easy-to-remove and heat-diffusion-friendly biomimetic support structures.

4.1. Pattern-based support point determination method

A new support point optimization method is proposed to detect support relevant overhang areas and generate optimal support points on the overhang areas of complex components in AM. Figure 4.1 describes a general workflow for the proposed support point determination method. The input to the methodology is an STL model represented by a boundary mesh with a predefined build orientation. Then, the following key step is to identify three types of overhang areas, including points, edges and faces. Facet geometric information and specific AM manufacturing constraints are used to detect and classify the support areas. This step of the proposed method is unique and different from that reported in research literature. After this, the next critical step is the application of a combined optimization method for support point optimization for the three main types of support areas: overhang face, overhang edge and overhang isolated tip point, separately. An optimal periodic support point pattern is defined and used for face overhangs while a special support point generation scheme is applied to edge and tip point overhang types to sequentially identify the valid support points. Finally, all the generated support points are combined to a support point set for the whole STL model in a pre-defined build orientation. The details of the two main modules of the proposed method are presented in the next two sections.
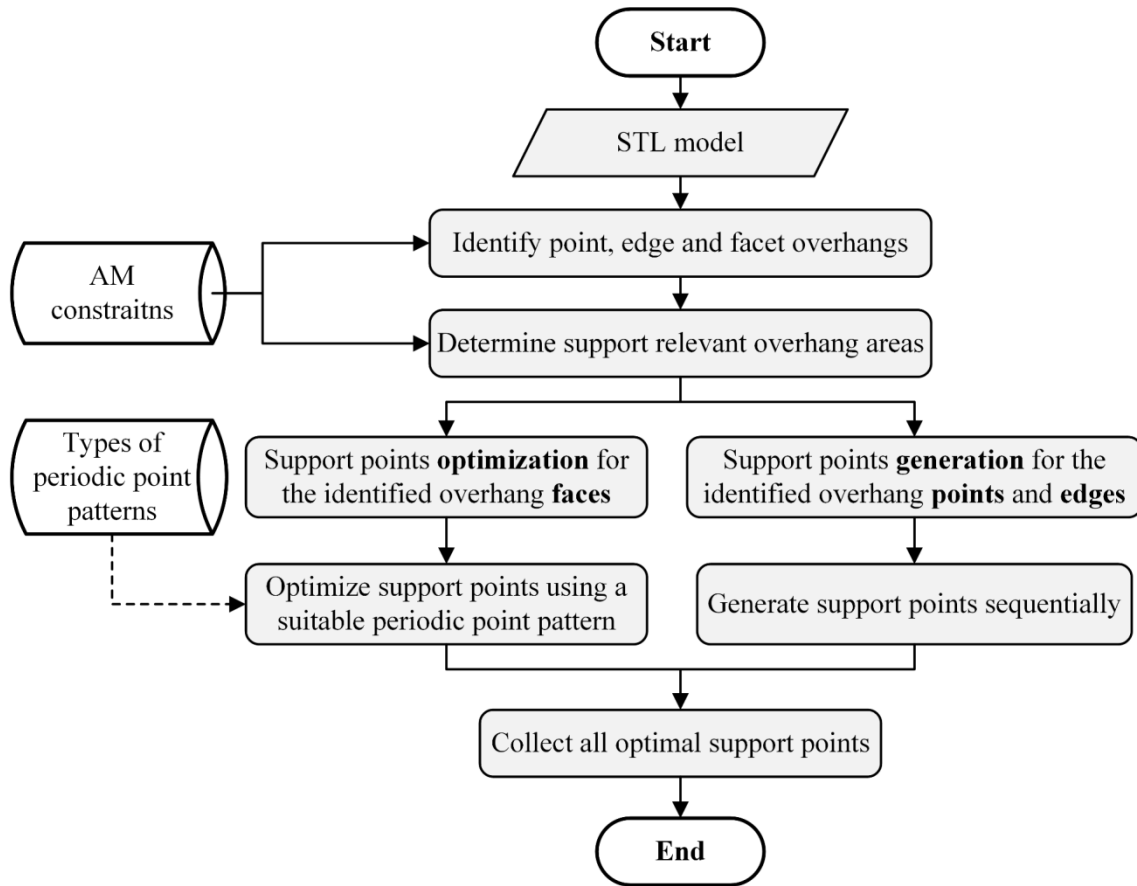
Figure 4.1. Workflow of the support point generation & optimization method.

4.1.1. Analysis of support relevant overhang areas

If there is no underlying layer to support overhang areas, a structure will deform or even collapse, especially for the powder-based fusion process. Facet geometric information and AM constraints are usually employed to help identify overhang areas. Regarding an overhang region, overhang features can usually be divided into face overhang, edge overhang and point overhang [80, 87] as shown in Figure 4.2.
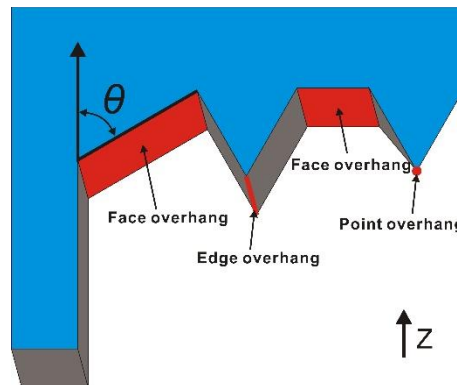
Figure 4.2. Illustration of point, edge and face overhangs.

Since the overhangs are different, the way to determine support points may be different. For isolated overhang points, they should be seen as support points directly. However, support point generation and optimization on or near overhang edges and faces should be discussed separately and treated differently. Three types of overhangs can be determined by geometric information of mesh models and corresponding AM process constraints, e.g. maximum overhang length and angle. More detailed definitions for these overhang types are explained and discussed below.

- A point overhang is a point that is located lower than all other points in neighboring meshes on condition that the angle θ between the normal vector of an adjacent mesh (at least one) and the printing direction Z is bigger than 90°. Figure 4.3(a) and (b) describe two types of overhang points and Figure 4.3(c) shows a non-overhang point where all normal vectors are not facing the base.

- An edge overhang is considered as an overhang if other edges of the two incident faces are located higher with at least one normal vector of the two incident faces facing the building base. Edge overhang is determined similarly to that for the point overhang. Figure 4.3(a) and (b) can also be seen as section views of two edge overhangs.

- A mesh face is defined as a downward overhang face if the angle, θ, between the mesh face plane and the printing direction vector Z is bigger than the printable overhang angle.
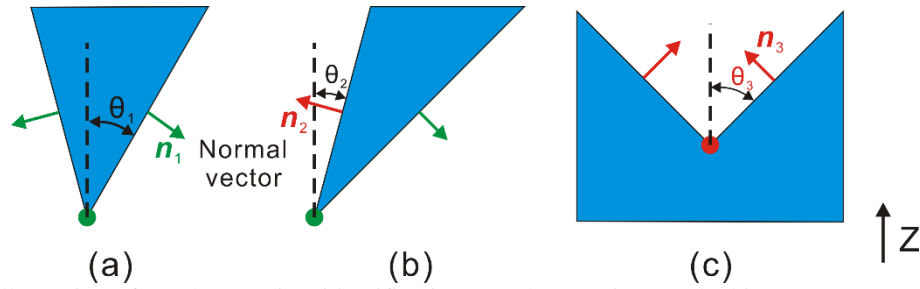
Figure 4.3. Illustration of overhang points identification (overhang points marked in green). (a). Overhang point: all incident faces are facing the base; (b). Overhang point: at least one normal vector of the adjacent meshes is facing the base; (c). Non-overhang point: all normal vectors of the incident faces are not facing the base.

4.1.1.1. Support relevant overhang areas

Geometric information can help to detect all the overhang types. However, not all of them need support or require support point assignment since the manufacturability of AM processes can further help filter the detected overhangs to reduce the support volume in the end. The filtered overhangs, which need to be supported, are regarded as support relevant overhangs in this research.

Support relevant overhang points

After detecting all overhang points, support relevant overhang points that must be supported need to be discovered. Figure 4.4 gives an illustration of filtering by finding the nearest non-supported points on an active plane that is parallel to the building base. The non-supported points should be located on mesh faces that do not contain any types of overhang areas. In other words, the non-supported points are intersection points between the active plane (parallel with the build base plane) and non-overhang areas (point D in Figure 4.4) that does not include overhang points and edges. Usually the principle of judging whether an overhang point needs support is whether distance D between the overhang point and the nearest non-supported point in the active plane is less than the maximum overhang distance. However, the maximum overhang distance is suitable for evaluating the position of support points on the overhang faces. Due to the islanding characteristic of the overhang points on the active plane, it is undesirable to use a maximum overhang distance to detect whether an overhang point needs to be supported. Here, the minimum feature size for the AM process is used to help judge whether an overhang point needs support. If distance D is more than the minimum feature size, the feature point cannot be printed under the premise of ensuring the feature. Hence, the overhang points identified are defined as support relevant overhang points here.
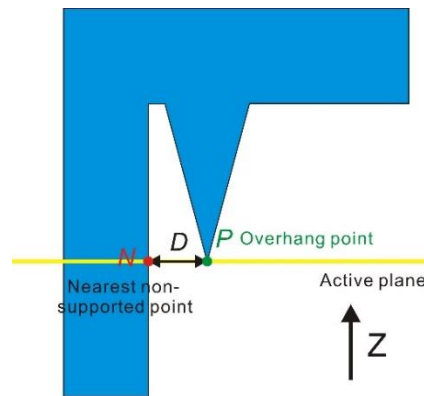
Figure 4.4. Illustration of a support relevant overhang point identification (Point N is the non-supported point closest to the overhang point (P). Distance (D) is the distance between N and P. Z is the printing direction).

Support relevant overhang edges

For cases of isolated overhang edges, the edges are broken down into overhang points by active planes (yellow lines in Figure 4.5). The lower endpoint of each overhang edge is seen as a decomposition point. When the length of an overhang edge projected onto the XOY plane is less than the maximum bridge length, the decomposition point is the lower endpoint. If the projected length is more than the critical length, the edge is divided into several segments which are shorter than the critical length. These active

planes parallel to the XOY plane pass through the decomposition points of overhang edges. Figure 4.5(a) shows the example of overhang edges decomposed into several overhang points. With reference to Figure 4.3, the discussion is whether these decomposition points of overhang edges need support. For those points that need support, the overhang edges containing these points are considered as support relevant overhang edges. With regards to the support relevant overhang edges that must be supported, they are projected as polylines onto the XOY plane. The sequence of generating projected support points for these support relevant overhang edges is determined as shown in Figure 4.5(b). Due to the bottom-up printing characteristics, local and global lowest points on the overhang edges should be supported first. Hence, the local and global lowest points of these support relevant overhang edges are found to generate projected support points preferentially. The generation sequence of projected support points should be derived from the global point along both sides of the edges until covering all overhang edges. The series of numbers indicate a generation sequence of the projected support points.
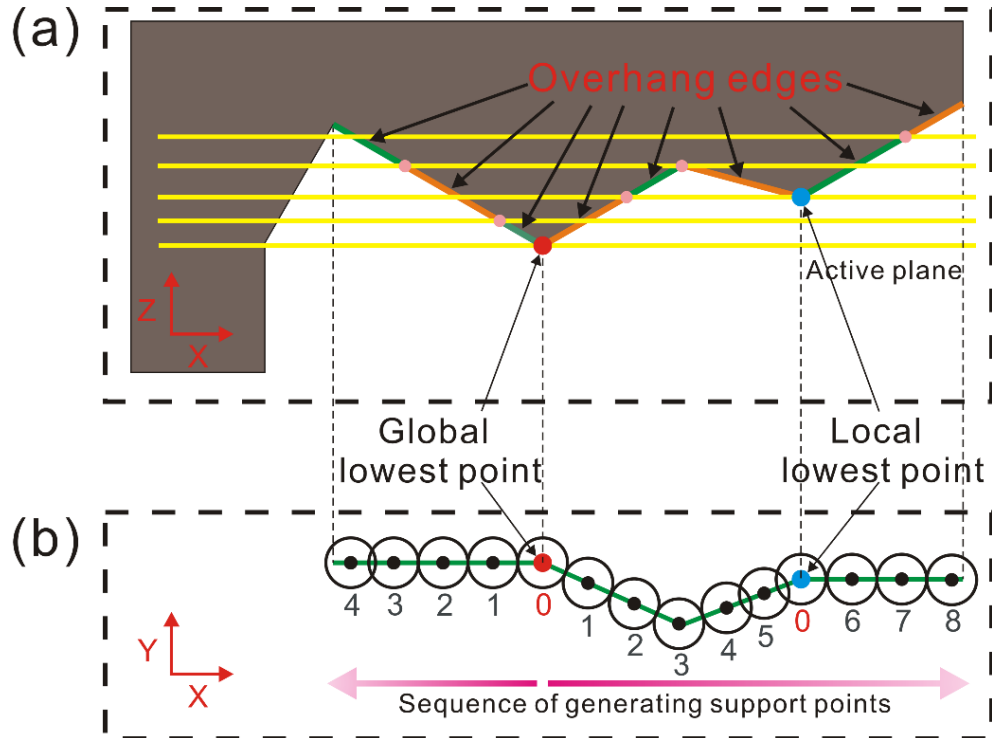
Figure 4.5. Support point generating on support relevant overhang edges: (a). These edges on XOZ plane (red and blue points are the global and local lowest points on the support relevant overhang edges, respectively); (b). Generation sequence of support points projected on the XOY plane.

Support relevant overhang faces

In terms of continuous overhang faces in Figure 4.6(a, b), the projection of the overhang faces is extracted in Figure 4.6(c). Boundary meshes and their corresponding adjacent non-overhang meshes are

identified using mesh geometric information illustrated in Figure 4.6(d, e). Since the intersecting boundary between the overhang faces and lower neighboring non-overhang areas can provide support within the maximum printing bridge length, the boundary of the lower non-overhang meshes (Figure 4.6(f)) is obtained as shown in Figure 4.6(g). Each edge of the neighboring non-overhang mesh faces has a support region in Figure 4.6(h). To clarify the support area of a non-supported edge, Figure 4.6(i) presents an enlarged support area that an edge can cover. r indicates the maximum printing bridge length. To obtain the overhang faces that need support, the support region is removed from the original overhang faces. Hence, the filtered or identified overhang area, called support relevant overhang area, is finally shown in Figure 4.6(j, k).
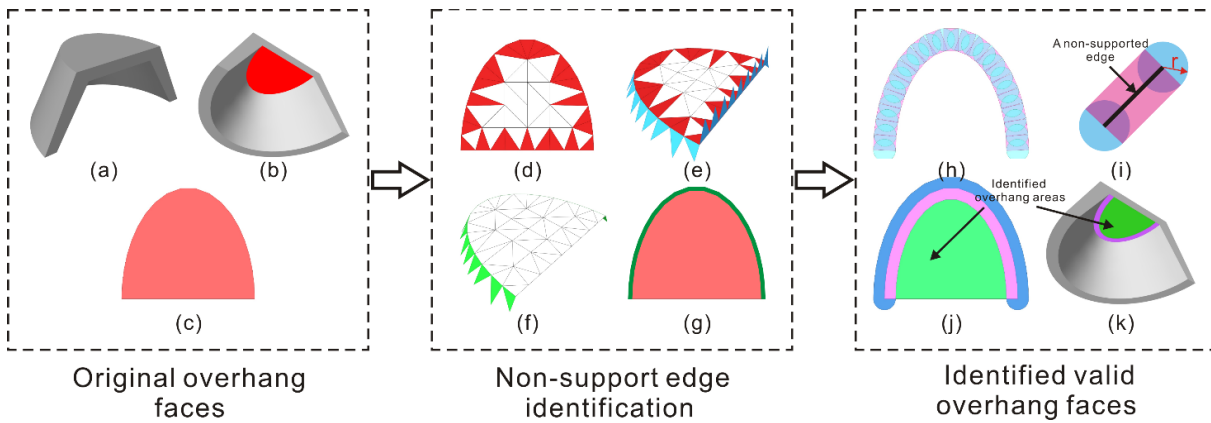
Figure 4.6. Illustration of support relevant overhang faces area. (a). A STL model; (b). Original overhang faces; (c). Projection of the overhang area onto the XOY plane; (d). Boundary meshes of the original overhang faces; (e). Neighboring non-overhang meshes (blue) at the edge of the original overhang faces; (f). Identified neighboring meshes that can support the edge of the original overhang face; (g). Intersecting curve (green) between identified neighboring mesh and the original overhang faces; (h). Support areas that intersect edges between the neighboring non-overhang mesh and the face overhang can play a support role; (i). A cover area that a non-supported edge can support; (j, k). Final support relevant overhang area in green and non-supporting overhang area in pink.

4.1.1.2. Classification for different types of support relevant overhang areas

Since the way of support point generation is different for these three types of overhang regions, a classification method is proposed to facilitate the analysis of support points. Generally, isolated overhang points can be considered as support points. With regard to overhang edges with overhang points, the overhang points should firstly be marked as support points, and then support point generation method for overhang edges is applied to generate support points. For overhang faces, overhang points and edges on the overhang faces should be analyzed and identified first as predefined support points. Then, a support point pattern should be applied to the overhang faces. By considering the geometry relationship of the three overhang types, three overhang sets are defined in Table 4.1. These overhangs on the same set should be analyzed together to help generate and optimize support point distribution. In *Set* 1, over-

hang points, O_{p1}, that are not located on the overhang edges and faces are classified as isolated over-hang points. This type of independent or isolated overhang points needs to be supported separately. In *Set* 2, overhang points that are on the overhang edges and not on the overhang faces, O_{p2}, and over-hang edges that are not on the overhang faces, O_{e1}, are combined to analyze the generation sequence of support points on the overhang areas as illustrated in Figure 4.5. In terms of overhang faces that contain overhang points and edges, support points on the overhang points and edges are generated first. These support points are then defined as predefined support points.

Table 4.1. The definition of overhang set based on classification of support relevant overhang regions

Types of overhangs	Set	Definition
Support relevant overhang points	*Set 1*	O_{p1}: points that are not on the overhang edges and faces
	Set 2	O_{p2}: points that are on the overhang edges and not on the overhang faces.
	Set 3	O_{p3}: points that are only on the overhang faces.
Support relevant overhang edges	*Set 2*	O_{e1}: edges that are not on the overhang faces (isolated overhang edges)
	Set 3	O_{e2}: edges that are on the overhang faces
Support relevant overhang faces	*Set 3*	O_f: all faces

In the next step the support areas, covered by these predefined support points, are removed to the over-hang faces. Usually, these overhang faces are porous structures. Figure 4.7 gives an illustration to show the transition from a non-porous overhang area to a porous overhang area. Once the identification and classification of the overhang areas are finished, support point generation and optimization should be conducted to generate optimal numbers and positions for the three types of support relevant overhang sets. In the next section, a periodic support point pattern and its optimal generation method are intro-duced. Then, the non-porous and porous overhang areas are defined and the corresponding support point optimization methods for the two types of overhang areas are introduced, especially for porous overhang areas.
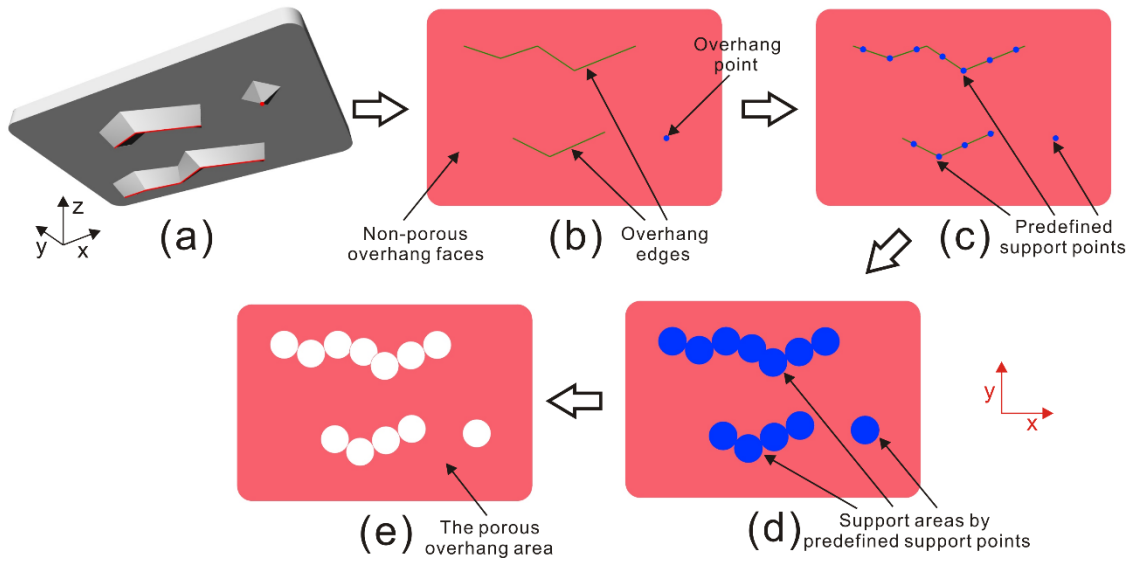
Figure 4.7. A transition from a non-porous overhang area to a porous overhang area: (a). Overhang point and edges on overhang faces; (b). Projection area of the three types of overhang areas; (c). Predefined support points on the overhang point and edges; (d). Support areas supported by the predefined support points; (e). The porous overhang area.

4.1.2. Support point optimization

In this section, a support point optimization method is proposed to optimize support point distribution on support relevant overhang areas. The proposed approach is divided into two main steps. The first is to select a type of predefined periodic point pattern. The second step is to apply the selected periodic support point pattern and an optimization algorithm to optimize support point distribution. A square periodic point pattern is applied in most existing studies. Here, more kinds of support point patterns are analyzed to search for a better support point distribution.

4.1.2.1. Determination of periodic support point pattern

Before analyzing the periodic support point pattern, the maximum bridging length of AM process is applied to determine the radius of nearby areas that a support point can support. In other words, a support point can support an overhang area projected as a circle onto the XOY plane, the radius of which is the maximum printing bridge length of AM capability. Figure 4.8 shows two examples to describe the effect of unsupported bridges and horizontal holes without a support structure. As the distance of the unsupported overhang area increases in Figure 4.7(a), it shows a poor quality on the downward facing surfaces [159]. Hence, holes below a certain size can be printed without supports. In Figure 4.8(b), holes with a diameter of less than 8 mm can be self-support. Hence, a small overhang can be printed when the size of bridges or holes is less than a critical overhang distance.
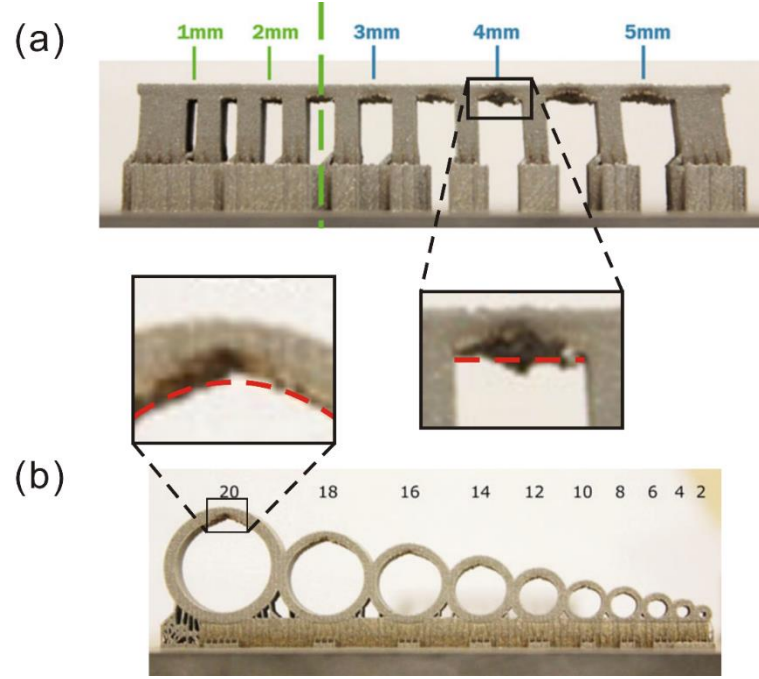
Figure 4.8. The maximum printing bridge length of AM capability: (a). Effect of unsupported bridge for the powder bed fusion process [159]; (b). Horizontal holes printed without support structure [159].

Generally speaking, more support points on the overhang areas means more support structures for a certain overhang area. In tree-like or lattice supporting structures, a periodic support point pattern with square uniform sampling, as shown in Figure 4.9(1-3), had been widely used in support structure design. In terms of geometry characteristics, periodic support point patterns in Figure 4.9(a) and (b) have the same distribution type. To enlarge the solution space for optimization, more patterns, represented by regular polygons, are discussed in the following.
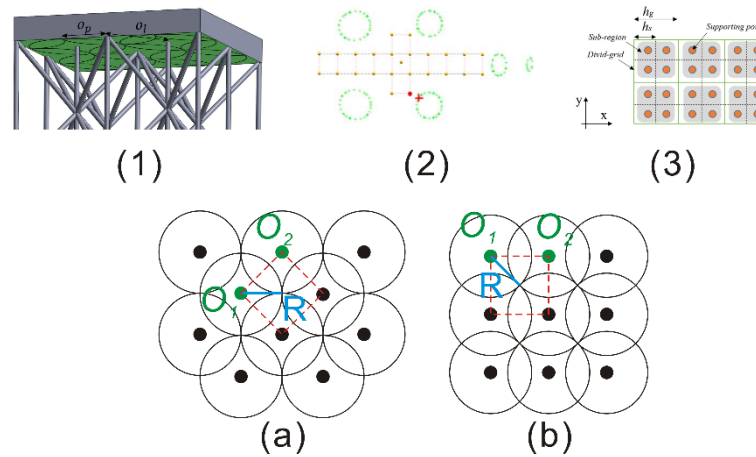
Figure 4.9. Periodic support point patterns: (a). Supporting points on the overhang areas for lattice support structure in (1) [91]; (b). The sampling support points on the overhang regions for tree-like support structure in (2) and (3). [88, 90].

With regard to a simple regular n-gon $(n \geq 3)$ in Figure 4.10(a), the sum of all the internal radians is $(n-2)\pi$. Hence, the internal angle of regular n-gon is $\alpha = (n-2)\pi/n$. The circumradius R from the center of the regular polygon to one of the vertices is related to the side length L. The equation is written as:

$$L = 2R\sin\frac{\theta}{2}(\theta = \frac{2\pi}{n})$$
(4-1)

To avoid excessive support overlapping (blue area in Figure 4.10(b)) between the support regions defined by two adjacent vertices, the size relationship between the side length L of a regular polygon and the circumradius R should be constrained as:

$$R \leq L \leq 2R$$
(4-2)
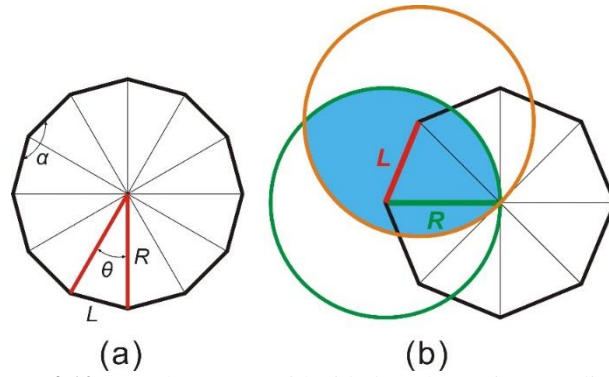
Figure 4.10. Regular n-gon with side length L, circumradius R.

From equation 4-1 and inequality 4-2, the number of sides n should be constrained as: $6/5 \leq n \leq 6$. Considering $n \geq 3$, n should be $3 \leq n \leq 6(n \in N^{+})$ or $n = 3,4,5,6$. Figure 4.11 provides the four kinds of periodic support point patterns of regular polygons.
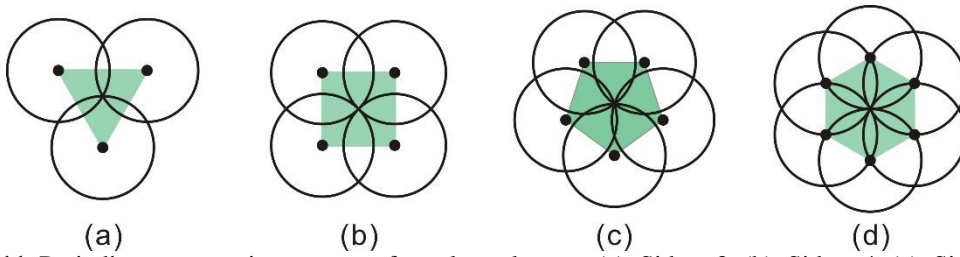
Figure 4.11. Periodic support point patterns of regular polygons: (a). Side = 3; (b). Side = 4; (c). Side = 5; (d). Side = 6.

To analyze support areas for the four patterns, Figure 4.12 gives the four types of multi-group regular polygon patterns. In order to avoid the overlapping situation (Figure 4.12(c)), the number of regular polygons for specific multi-group support point patterns, noted a in formula (4-3), is suggested to be integer. The equation can be written as:

$$a = \frac{2\pi}{\alpha} = \frac{2\pi n}{\pi(n-2)} = 2 + \frac{4}{n-2} (a \in N^+)$$

(4-

Hence, n is constrained to be 3, 4, 6. To further filter the support point patterns, the hexagon support point pattern group is analyzed firstly in Figure 4.13. The periodic points can be broken down into two equilateral triangle patterns, as shown in Figure 4.13(c_1) and (c_2). In essence, the hexagon periodic support point pattern can be seen as two overlapping equilateral triangular patterns. Either of the two equilateral triangular patterns can play a good supporting role on the regular hexagon overhang area. Hence, the periodic support point pattern of equilateral triangle has a better performance than the regular hexagon.
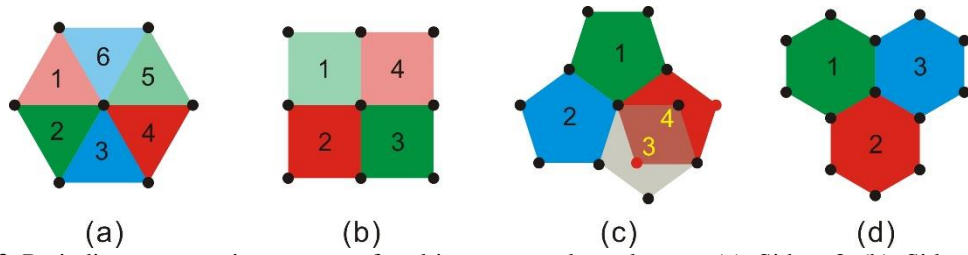
Figure 4.12. Periodic support point patterns of multi-group regular polygons: (a). Side = 3; (b). Side = 4; (c). Side = 5; (d). Side = 6.
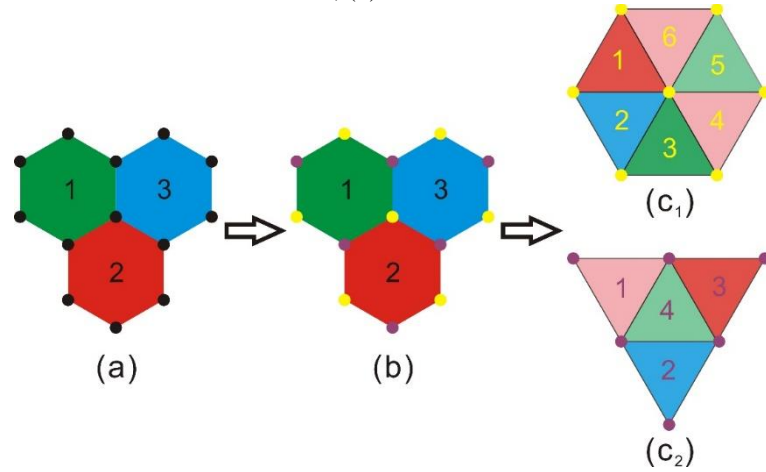
Figure 4.13. Periodic support point pattern decomposition of a multi-group regular hexagon pattern.

Figure 4.14 gives the comparison between equilateral triangular and regular quadrilateral periodic point patterns. As to an equilateral triangle periodic support point pattern in Figure 4.14(a), the area of the overlapping part of two adjacent circles (S_0^3) can be written as:

$$S_0^3 = 2\left(\frac{\pi r^2}{6} - \frac{\sqrt{3}r^2}{4}\right)$$

(4-

All overlapping areas for circle O in Figure 4.14(c) can be measured as $6S_0$ and the ratio (η^3) of the area of the non-overlapping area to circle O is:

$$\eta^3 = \frac{\pi r^2 - 6S_0^3}{\pi r^2} = \frac{3\sqrt{3}}{\pi} - 1 = 65.40\% \tag{4-5}$$

Regarding regular quadrilateral periodic support point pattern, S_0^4 and η^4 can be calculated as:

$$S_0^4 = 2(\frac{\pi r^2}{4} - \frac{r^2}{2}) \tag{4-6}$$

$$\eta^4 = \frac{\pi r^2 - 4S_0^4}{\pi r^2} = \frac{4}{\pi} - 1 = 27.32\% \tag{4-7}$$

In terms of overlapping areas, an equilateral triangle pattern has a better efficiency than a regular quadrilateral pattern on overhang regions.
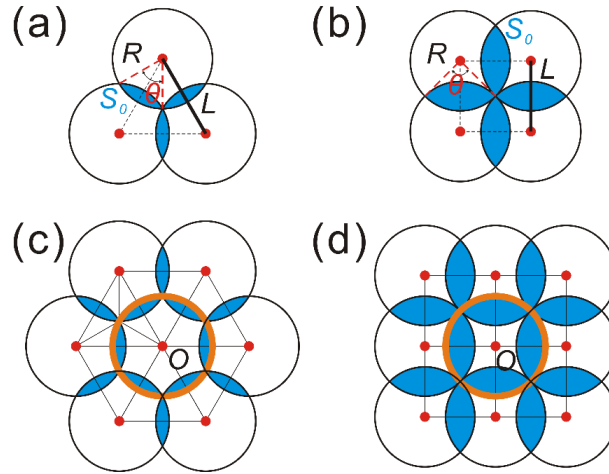
Figure 4.14. Comparison of periodic support point patterns: (a) Side length $L = \sqrt{3}R$, internal angle $\theta = \pi/3$; (b) Side length $L = \sqrt{2}R$, internal angle $\theta = \pi/2$; (c) Multi-group support point patterns of equilateral triangle; (d) Multi-group support point patterns of regular quadrilateral.

In order to further validate the efficiency of the equilateral triangle support point pattern, a square overhang region is provided to cover support points by using two types of periodic support point patterns as shown in Figure 4.15. The result shows that 941 triangle support points can support the overhang areas, but 1225 quadrilateral support points are needed to support the same region.

$$\eta = \frac{n^4 - n^3}{n^3} \times 100\% = 30.18\% \tag{4-8}$$

The triangular point pattern can reduce the support points by at least 30% when compared to the quadrilateral pattern. Therefore, the equilateral triangular periodic support point pattern has a better support

performance than the quadrilateral pattern. The former will be applied to optimize support point distribution in the next subsection.
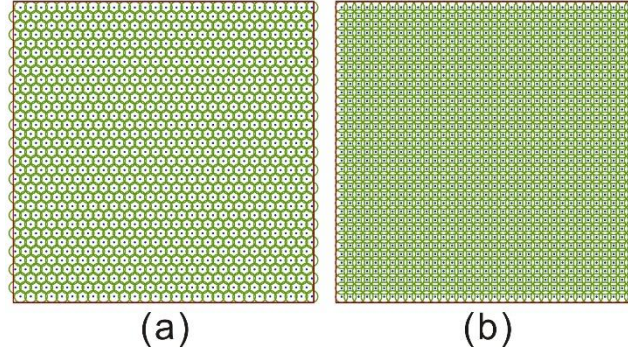
Figure 4.15. Two support point distributions for a square overhang region (100 * 100): (a). Equilateral triangular pattern (the number of support points = 941); (b). Regular quadrilateral pattern (the number of support points = 1225).

4.1.2.2. Support point optimization for support relevant overhang areas

Usually, a key goal of support structure design is to minimize the volume of support structures. Many factors can impact the objective, such as the geometric shape of support structure, the number of support points, the position of support points, etc. Among them, the number and position of support points on support relevant overhang areas have a direct influence on the support structure generation. Hence, the aim of support point optimization in the proposed approach is defined to find the most suitable support point distribution, or to minimize the sum of z coordinate value of support points on the support relevant overhang areas. The objective function is described below:

$$F(x):min\sum_{i=1}^{n} z_i (i = 1, 2,...,n)$$

(4-

Where z_i is the z value, overhang height at support point P_i $(i = 1,2,...,n)$. The constraint is that all support relevant overhang areas should be covered by support point areas. The proposed method uses overhang areas projected onto the XOY plane to optimize the support point distribution. Once overhang areas are projected onto the XOY plane, they are converted into a set of polyline boundary surfaces. Therefore, the projected overhang areas for a non-porous overhang area is a polyline boundary. However, in terms of porous overhang areas, the projected overhang areas are several closed polylines, including outer and inner closed polylines. Notice that the support points should be located in the outer closed outlines and not in the inner polylines. Hence, in this subsection, non-porous and porous overhang areas are discussed, respectively.

Support point optimization for a non-porous overhang region

Figure 4.16 describes the workflow of support point generation & optimization on a non-porous over-hang area. A re-projection optimization strategy is developed. Here, a non-porous overhang area illus-trated in Figure 4.17 is discussed in more detail. At first, the overhang area is projected onto the build base, XOY plane. The mesh projection area (Figure 4.17(a)) is converted into a closed polyline bounda-ry (Figure 4.17(b)). Then, the overhang projection is covered by a set of equilateral-triangular periodic support points in an enlarged bounding box. Figure 4.17(c) represents the periodic support point pattern using an equilateral triangle. These points inside the projected region are found to provide support for the overhang area. The support area obtained is shown in Figure 4.17(e). However, these support points cannot support all overhang projection areas. A non-supported enlarged area is shown to the left of Fig-ure 4.17(e). Figure 4.17(f) describes all unsupported overhang areas in green that the triangular point pattern cannot support. In order to support the unsupported overhang regions, supplementary points are generated to provide support for these areas. In addition, small unsupported projected regions will be ignored. Repeat this process until all unsupported areas are supported. The final support region (Figure 4.17(h)) is obtained by combining identified equilateral triangular support points and supplementary points on the projected overhang region. Finally, these points within the area are re-projected onto the 3D overhang areas to obtain an alternative solution.

```
                    ┌─────────┐
                    │  Start  │
                    └─────────┘
                         │
              ┌──────────────────────┐          ┌ ─ ─ ─ ─ ─ ─ ─ ─ ─ ─ ─ ─ ─ ─ ─
             /  Non-porous          /           │  Supplementary support points
            /   overhang area      /                     generation
           └──────────────────────┘             │
                         │                                 ┌─────────┐
          ┌──────────────────────────┐          │         │  i = 1   │
          │ Project the overhang     │                     └─────────┘
          │ area to XOY plane as Set O│         │              │
          └──────────────────────────┘                 ┌──────────────────┐
                         │                    │─────────│ S_i = C_i^c ∩ O   │
          ┌──────────────────────────┐                 └──────────────────┘
          │ Cover Set O with         │        │              │
          │ equilateral triangular   │             ┌──────────────────────┐
          │ points                   │        │    │ Delete small overhang │
          └──────────────────────────┘             │ areas                 │
                         │                    │    └──────────────────────┘
```

Generate supplementary points (P_{Si})

Collect all points $(P_0$ and $P_{Si})$

Re-project onto the 3D overhang surface

Calculate objective function

Converged ?

New support point pattern variables

Final optimal support points

End

Supplementary support points generation

$i = 1$

$S_i = C_i^c \cap O$

Delete small overhang areas

$S_i = \varnothing$?

Generate points (P_{Si}) and make circles to cover Set S_i

Perform Boolean union for all circles as Set D_i

$C_{i+1} = C_i \cup D_i$

$i = i + 1$

Collect all supplementary points (P_{Si})

Project the overhang area to *XOY* plane as *Set O*

Cover *Set O* with equilateral triangular points

Pick these points (P_0) within *Set O*, make circles, perform Boolean union as *Set C_1*

Figure 4.16. Workflow of support point generation & optimization on a non-porous overhang area.

Figure 4.17. Equilateral triangular support point pattern for a non-porous structure: (a). Overhang mesh projected onto the XY plane; (b). Polyline boundary surface; (c). Equilateral triangular support points projected onto the overhang regions in the enlarged bounding box; (d). Support points in the projected overhang areas; (e). Support area that support points inside the overhang areas can support; (f). Unsupported areas; (g). Supplementary support points on the non-support areas; (h). All support points on the overhang region and support area.

After that, a genetic algorithm is applied to search for the optimal triangular point patterns. Taking the support structure design into account, fewer support points are obtained to minimize the volume of support structures. Since the support structure volume has a direct positive correlation with the number and position of support points, the formula (4-9) is used as the objective function to optimize support point distribution. Two variables, the translation vector and rotation angle of the periodic support point pattern on the XOY plane, are set to populate the alternative solution. The 2D triangular support point pattern can be translated and rotated to achieve the minimal objective function value. It should be noted that the distance between 2 points in the support point pattern should respect the maximum printing bridge length of AM capability to ensure that there is no collapse in printing. Figure 4.18 below describes an illustration of the variable definition in support point optimization.
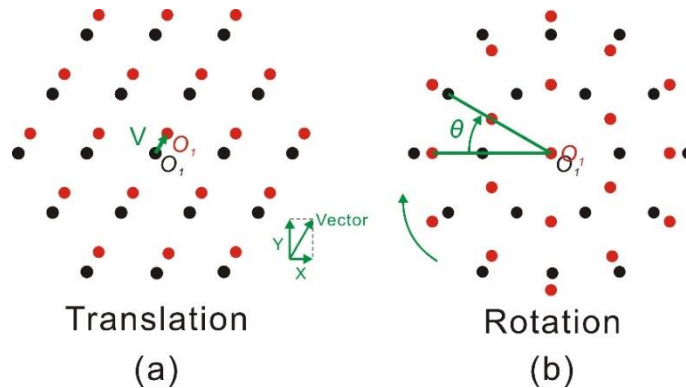
Figure 4.18. Two variables defined for the evolutionary algorithm in the support point optimization (original pattern in black): (a). Translation vector $\vec{V}$ of the periodic support point pattern; (b). Rotation angle θ of the periodic support point pattern.

Support point optimization for a porous overhang region

In terms of a porous overhang region, the overhang area can be divided into two parts, the outer overhang outline and the inner non-overhang areas. It can be noticed that support points should be located inside the outer overhang outline and outside the inner non-overhang areas. Figure 4.19 and Figure 4.20 below describe the proposed workflow of support point generation & optimization on a porous overhang region. The additional module of supplementary support point generation is the same as the one used in the non-porous overhang areas above.
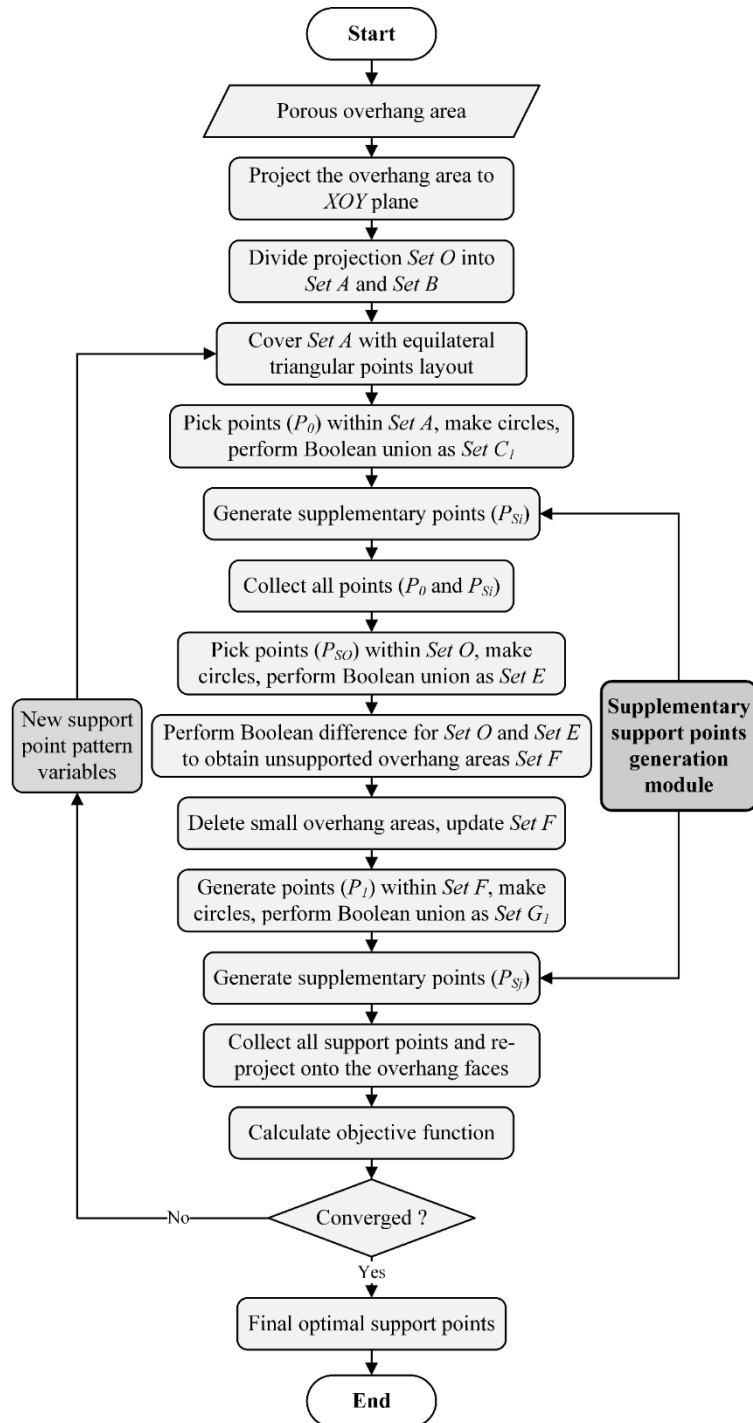
Figure 4.19. Flowchart of support point generation & optimization for a porous overhang area.
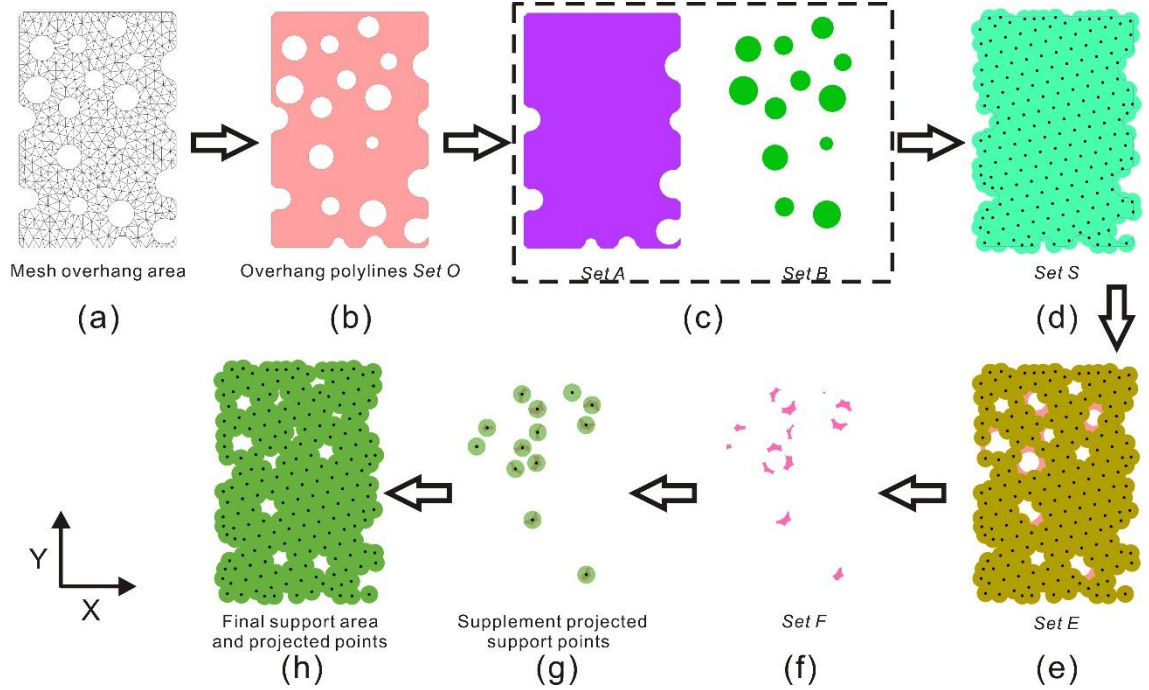
Figure 4.20. Workflow of support point generation for a porous overhang area: (a). A support relevant porous overhang area projected; (b). The overhang polylines boundary surface; (c). An outer overhang outline surface ($Set\ A$) and inner non-overhang areas ($Set\ B$); (d). Apply equilateral triangular periodic point pattern to find all support points on $Set\ A$ and the corresponding support area ($Set\ S$); (e). The support points on $Set\ A$ are checked to find identified support points on $Set\ O$ and $Set\ E$ is the corresponding support area of the identified support points; (f). Identified unsupported areas ($Set\ F$) after deleting small unsupported areas; (g). All supplementary points on $Set\ F$; (h). All support points projected and the actual support area.

First of all, a support relevant porous overhang area (Figure 4.20(a)) is projected onto the XOY plane and converted into 2D projection polylines area as shown in Figure 4.20(b). The projection area can be divided into an outer outline surface ($Set\ A$) and inner polylines surfaces ($Set\ B$). Then, the workflow of a non-porous overhang area is applied to cover $Set\ A$ with a 2D projected support point pattern. Figure 4.20(d) describes all projected support points on $Set\ A$. However, only the projection support points located on $Set\ O$ can play a supporting role. Identified projected support points on $Set\ O$ are illustrated in Figure 4.20(e) and the corresponding support area is named $Set\ E$. Red regions represent unsupported areas obtained by performing a Boolean difference operation between $Set\ O$ and $Set\ E$. After ignoring some small unsupported areas, the actual unsupported areas are presented in Figure 4.20(f). To support these unsupported areas, a set of supplementary points are generated onto these areas. Figure 4.20(g) displays the supplementary projected support points and the corresponding support areas. At last, the identified equilateral triangular support points and the supplementary points are collected into a support point set. The final support area and projected support points are shown in Figure 4.20(h). As with the non-porous overhang area, a genetic algorithm is used to obtain the optimal support point distribution.

4.1.2.3. Pre-process overhang regions with predefined support points

In medical applications, e.g. printed dental components, it is hard to design fixtures for machining in cutting removing due to the fragile characteristic of the components. Therefore, support structures of these dental component are usually removed manually. In [27], cone tips arranged at support points can achieve the removal of support structures more easily. It is essential to find an optimal support point solution under AM capability while ensuring all support relevant overhang areas supported. Based on the discussions above, support points located in the overhang points and edges need to be supported firstly in order to avoid collapse in the printing process and scraped in the laying powder process. Hence, a pre-processing with predefined support points should be carried out in the specific overhang regions to maintain printing stability. By doing a pre-processing support points selection, a non-porous overhang area with overhang points and edges can be converted into a porous overhang area. A more general workflow for a porous overhang area is shown in Figure 4.21. In the workflow, support points on the overhang points and edges can be seen as predefined support points. The support areas covered by the predefined support points are predefined support areas called *Set X* . The set is combined with *Set B* to act as updated inner non-overhang areas. After that, the support point generation and optimization module is applied to obtain a set of optimal support points. The proposed method has the potential to optimize support point distribution for SLM process and can also be adopted for support structure generation in other AM processes.
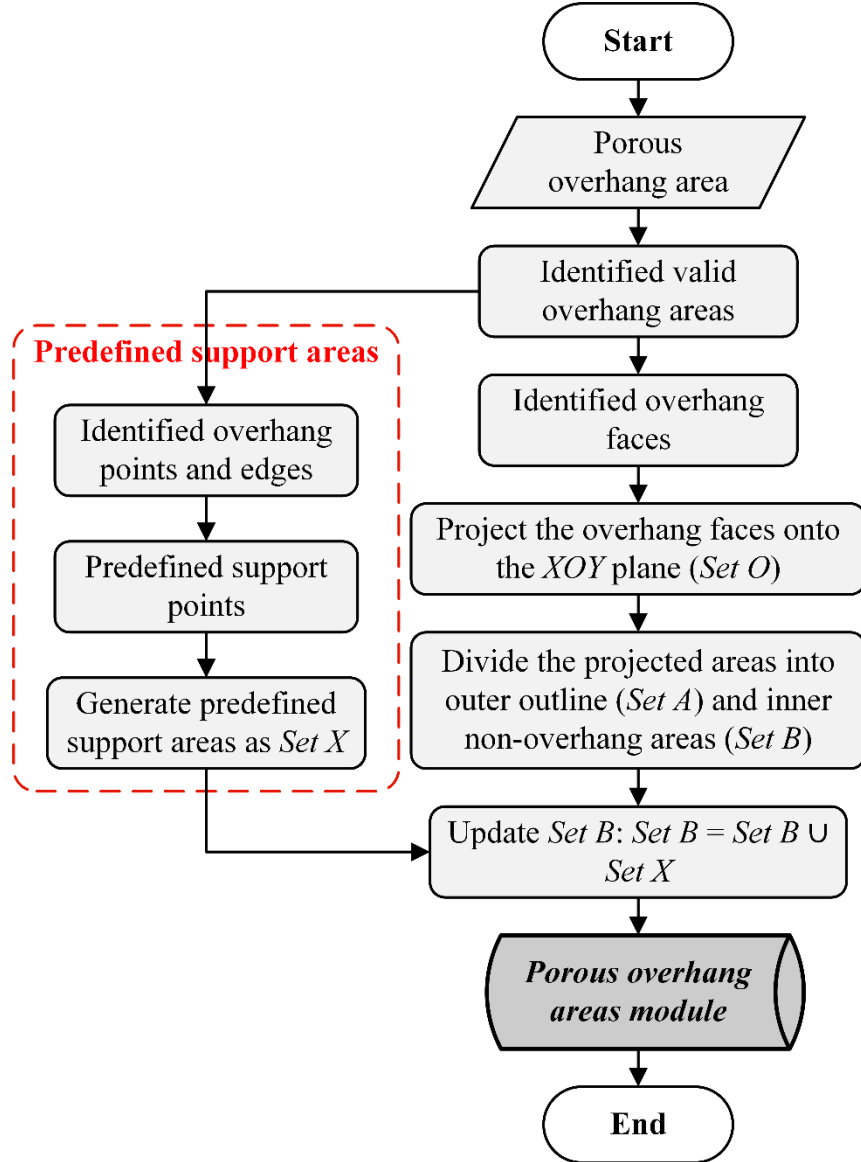
Figure 4.21. A general workflow of a porous overhang area with overhang points and edges.

4.1.3. Case study and discussion

In this section, a real dental part of a patient is selected for a case study to validate the proposed method. The proposed method is validated in an open-source graphical programming tool, Grasshopper, which runs within the Rhinoceros 3D CAD software. As seen above, the edge of the equilateral triangle should respect the maximum radius of a support point under AM capability, maximum printing bridge length and maximum overhang angle, in order to avoid any surface collapse in printing. In this example, the maximum bridge length and overhang angle are set as 1 mm and 45°, respectively, to ensure shape accuracy though the SLM machine used can have a maximum printing bridge length of up to 4 mm (for

the selected material and adopted processing parameters in this case). Hence, the side length of the equilateral triangular pattern is $\sqrt{3}$ mm.

According to the method above, the first step is to identify and determine support relevant overhang areas. Figure 4.22(a) gives the build orientation of the dental part. In terms of overhang points on the overhang edges, a sequence of support point generation is determined as shown in Figure 4.22(b). Support points on the support relevant overhang points and edges are defined as predefined support points. Figure 4.22(c) shows the results of all predefined support points. In addition, the support relevant overhang faces are also shown in Figure 4.22(d). Once all predefined support points are obtained, these support points on the overhang faces are selected to convert the original overhang areas into modified areas.
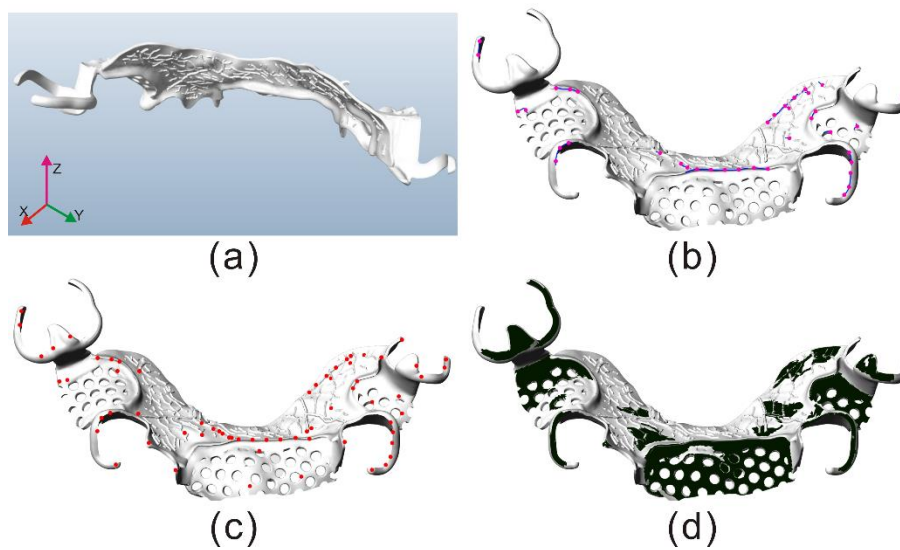
Figure 4.22. (a). Build orientation (Z direction) of the part; (b). Support points on the overhang edges; (c). All predefined support points; (d). The support relevant overhang faces.

A porous overhang area in the dental component, as shown in Figure 4.23, is introduced to list the support point generation procedure. The porous overhang area is broken down into an outline area in *Set A* and inner non-overhang areas as *Set B*. Moreover, self-supporting overhang areas (*Set C*) are identified by using the method as presented in Figure 4.6. Predefined overhang points are shown in *Set P*. Based on the workflows in Figure 4.18 and Figure 4.19, the optimal support points and corresponding support area are presented in Figure 4.23(h).
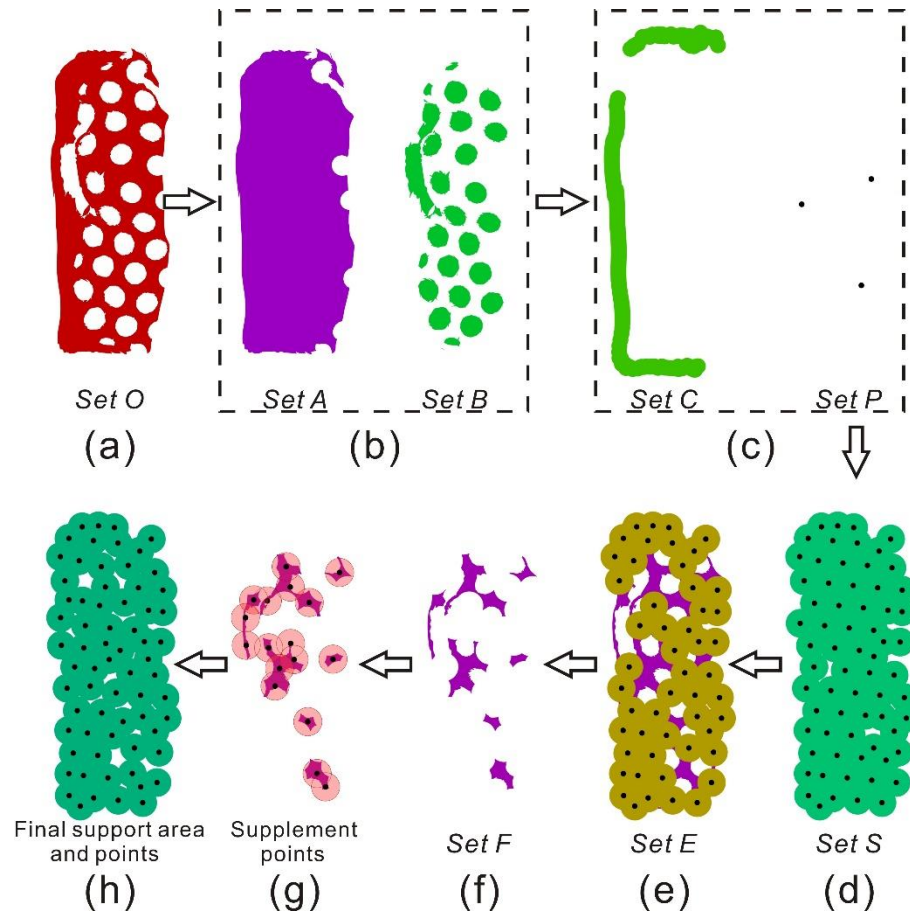
Figure 4.23. Support point generation workflow of a porous overhang structure on the dental part (middle bottom section in Figure 4.22-d): (a). The projected porous overhang area; (b). An outer overhang outline surface (*Set A*) and inner non-overhang surfaces (*Set B*) (c). Self-supporting overhang areas (*Set C*) and predefined support points (*Set P*); (d). Support points on identified outline overhang areas (*Set S*); (e). Support points on the support relevant overhang areas (*Set E*); (f). Unsupported areas after deleting small regions (*Set F*); (g). All supplementary points on *Set F* ; (h). All support points and actual support area.

Due to the huge difference in shape and distribution of the overhang faces on the part, it is hard to obtain an optimal support point distribution by populating a varying periodic point pattern on all overhang faces. Therefore, the overhang faces are divided into different groups. A genetic algorithm is applied to find the optimal solution group by group. The final optimal support points on the support relevant overhang areas is presented in Figure 4.24.
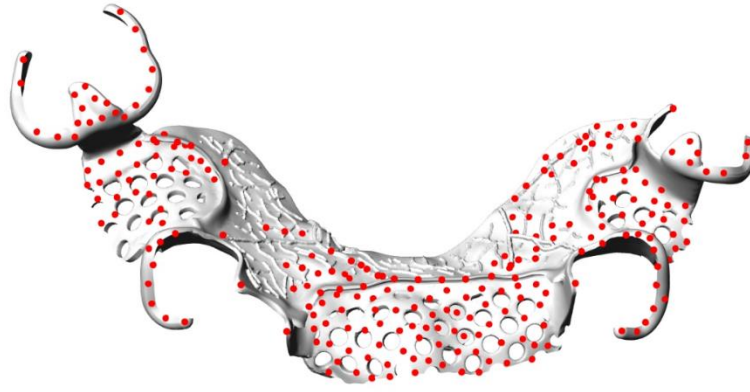
Figure 4.24. All support points on the support relevant overhang areas.

The proposed method has two main objectives: one is to decrease the number of points for reducing the total support structure volume and the number of support contact points for post-processing. The other objective is that the obtained optimized support points can be used as input for different support generation/design methods to generate lightweight but solid support structures to ensure printing quality, usually including surface roughness and shape accuracy. To show the effectiveness of this method, the dental part is processed, first, by using three different methods, two popular commercial methods and the proposed method, to compare the number of support points/contact points. Figure 4.25 shows the comparison results. It is obvious that the proposed method has the least number of support points, which means this will usually result in the least number of support volumes in total for same support relevant overhang areas.
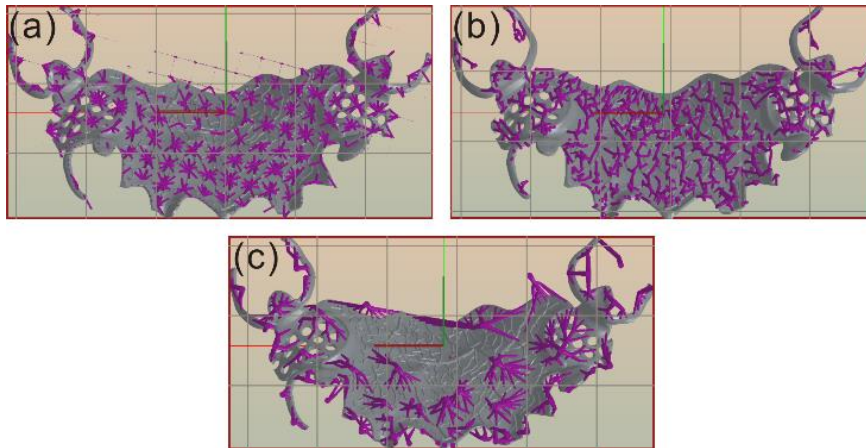
Figure 4.25. Contact area/points comparison: (a). E-stage; (b). Meshmixer; (c). The proposed method.

To demonstrate the effectiveness for the second objective, the optimized support points of the dental part are used as input in two different support generation methods: the direct cone method (used by many commercial software tools) and the bio-inspired tree-shaped structure design method (an academic tool) [27], to check whether the printing quality can be achieved. A Ti-6Al-4V powder material and a

Profeta SLM medical fabrication machine [165] with an existing recommended industrial working parameter setting are used for printing. A heat treatment is applied to relief the thermal stress. The temperature of the stress relief annealing treatment is set as 820℃ keeping for 2 hours and cooling with the furnace. Fig. 4.26 gives the results of a printing experiment, where two copies of the case part with the same set of support points but different support structures are printed successfully without any collapse. This means the two different support structures have sufficient support strength. Then, after removing the support structures and conducting other simple post-processing steps (e.g. sanding), the two printed parts are measured by a scanner to generate two 3D surface deviation maps for quality evaluation. According to the shape accuracy requirement of the dental part, the standard deviation of a surface should be estimated to be ± 0.2 mm. However, the 3D deviation maps in Figure 4.26(c, d) show that the final parts after simple post-processing can meet the dimensional accuracy requirement. This means that the proposed method can achieve the second objective as stated above. It is clear that with reduced support points, the total support volume and post processing time can be reduced no matter what kinds of support design methods are used in combination with the proposed method. In addition, with reduced support points, the total contact areas on overhang areas are also reduced, which can better protect the initial surface printing quality.
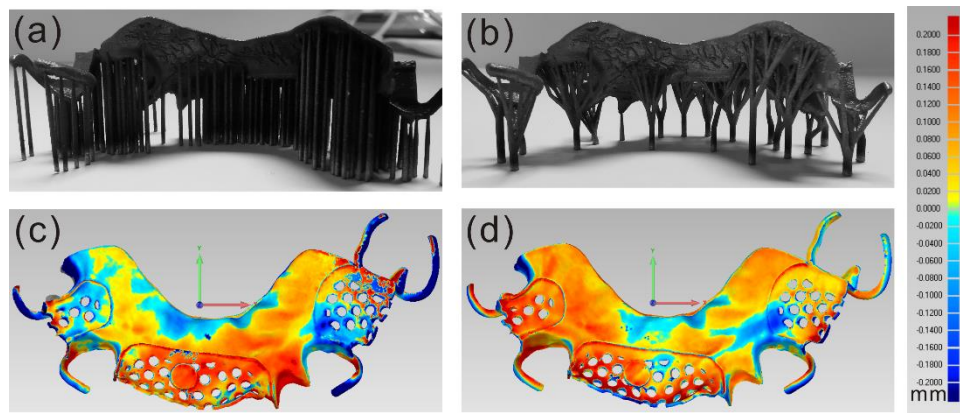
Figure 4.26. Printed examples with the supports from two support structures. (a). Direct cone support; (b). Bio-inspired tree-shaped support; (c). 3D surface deviation map after removing support structures for the cone support; (d). 3D surface deviation map after removing supports for the tree-shaped support.

The case study shows that the proposed method can improve the support design preparation for the SLM process. Although extensive testing is difficult since many AM preparation software tools are not open source and it is hard to directly control the input of assigned support points, the proposed method has the potential of being able to be applied in different AM preparation software tools as an integrated function for support design. It can also be applied to other AM processes where support design is neces-

sary. For other specific AM processes, specific manufacturing constraints should be considered and integrated into the proposed support point optimization process, which means adaptation is necessary.

4.2. Bio-inspired tree-shaped support structure generation

Build orientation determination has a direct impact on the support structure design. For complex components, the coupling relationship makes the support generation problem more complicated. To limit the scope of research, the proposed support structure design method starts with an input of a fixed component with a defined build orientation. Concerning the build orientation optimization for complex medical components, readers can find an AI-based solution in [156]. Figure 4.27 below describes the proposed method workflow.
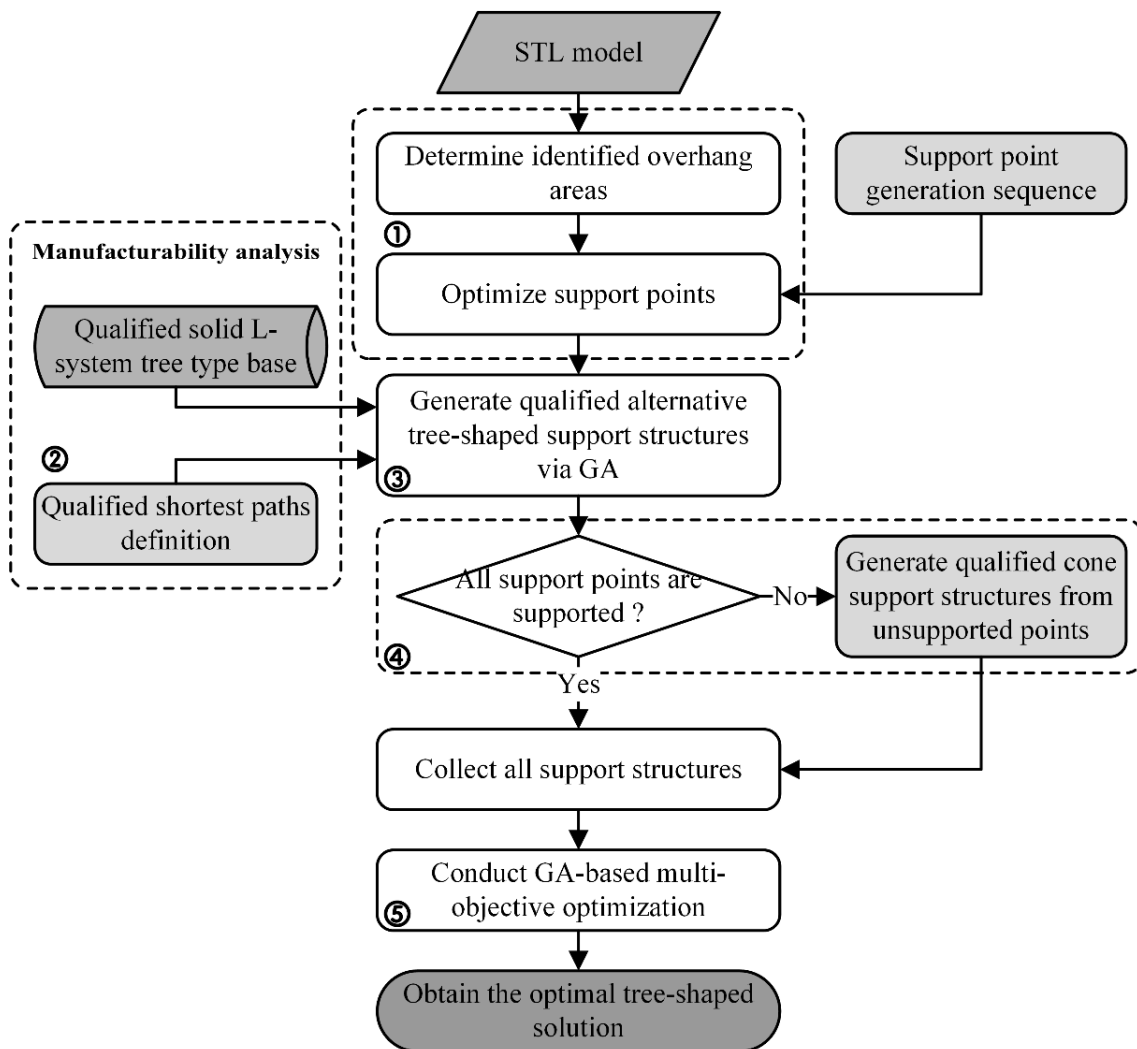
Figure 4.27. Workflow of the knowledge-based bio-inspired generative design & optimization method.

For small-size metallic parts, e.g. in dental applications, the distribution of parametric L-system tree-shaped support structures proposed has little effect on thermal distortion on a reasonable maximum printing bridge length. To explain the parametric L-system support structures further, this chapter focuses on proposing an enhanced bio-inspired generative design method for support structure generation and optimization. First, an equilateral triangular periodic support points pattern is applied to optimize support points distribution for the identified overhang areas. Based on the height of the support points and the distribution of the support points projected onto the build base, all support points projected are arranged within a set of parametric square regions. To support these support points, qualified tree-shape skeletons in the knowledge-based data base are randomly selected then rooted in the square areas with random rotation angles around the build orientation. Then, the shortest paths meeting manufacturability are selected as support connection paths. Moreover, invalid L-system tree branches are removed to obtain pruned trees. In addition, with regard to surface accuracy and fine geometric features of medical components, the number of collision/interference between support structures and the part is defined as an objective function to minimize support contacts on these surfaces. Therefore, the popular NSGA-II algorithm is used to generate a set of qualified non-dominated design solutions of support structures for better decision-making.

4.2.1. Bio-inspired tree-shaped support structures generation and manufacturability analysis

In this subsection, the bottom-up tree-shaped structure generation method is employed to provide a stable support for optimal support points on the identified overhang areas. To build a set of parametric knowledge-based tree-shaped support structures, the mathematical theory of L-systems [166], which is inspired by the growing of plants, is adopted as the growing rule for the base of a tree-shaped structure development. Figure 4.28 shows the definition of a directed-graph L-system tree in 2D.
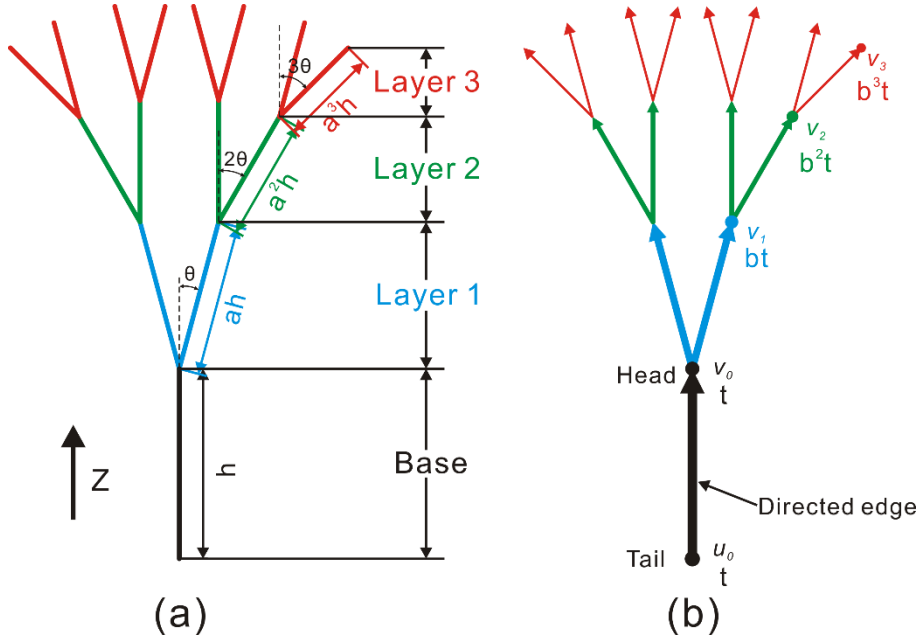
Figure 4.28. The parameter definition of a 2D directed-graph hieratical L-system tree. h: step length; a: step length scale; θ: step angle; t: diameter; b: step diameter scale.

The L-system tree consists of a base branch and sub-branches on multiple layers. According to the iteration rule of the L-system, the maximum inclination angle θ increases with the number of layers. The length of branches in each layer also scales accordingly. In Figure 4.28(a), the length of base is h. As the number of layers increase, the lengths of branches in different layers are expressed as ah, a^2h and a^3h, respectively. By controlling the length of the base branch and its length scale, the height and width of the L-system tree can be changed parametrically.

The directed-graph L-system tree (Figure 4.28(b)) is defined as $G = (V, E)$, which consists of two set V and E. Set V is called vertices or nodes and *Set E* is called edges. Each directed edge includes two endpoints, tail node and head node. Head nodes v_i in the same layer have the same weight t_i. The weights are responsible for controlling the diameter of nodes in each layer during the generation of solid support structures.

To ensure the manufacturability of the L-system tree structure, the maximum inclination angle in the last layer should be limited according to specific AM processes. Here, the maximum inclination angle is set at 45°. To generate valid self-supported L-system trees, a set of predefined qualified tree shapes are stored in a knowledge-based dataset as inputs of the tree population algorithms. Figure 4.29 shows four types of qualified L-system tree-shaped structures with different layers of branches, from a single layer to four layers. By adding extra operating parameters, translation and rotation, to 2D L-system structures,

3D tree-shaped structures can be obtained. All qualified tree structures are collected into the knowledge-based data set.
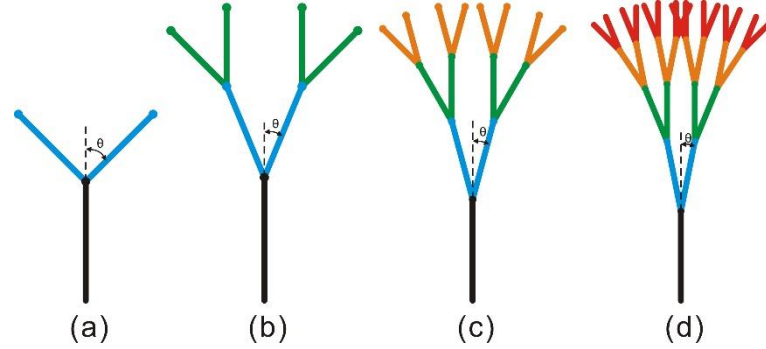
Figure 4.29. Four kinds of predefined valid L-system tree-shaped structures with different layers of branches. (a). θ = 45°; (b). θ = 22.5°; (c). θ = 15°; (d). θ = 11.25°.

In order to connect support points with L-system tree-shaped support structures, a support sector, shown in Figure 4.30, is adopted to search for the shortest qualified connection path between the support point and the tree nodes. The size of the support sector should meet the following manufacturing constraints: minimum connection length, maximum connection length and maximum inclination angle. Because cone tips (discussed in Section 4.2.4) are used to achieve support structures which can be easily re-moved from the model, the minimum connection length L_{min} should be less than the height of the tip cones. To avoid the large deformation of the tree support, a maximum connection length L_{max} is applied to limit the search space of qualified support nodes. In addition, all connection nodes within the support sector should also meet the maximum inclination angle constraint.
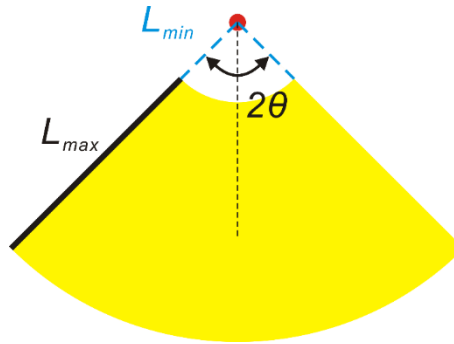
Figure 4.30. The definition of a qualified support sector.

Figure 4.31 illustrates a support structure generation method using an L-system tree-shaped structure. In the figure, Z represents the build orientation in printing. Every support point $p_i \in P$ should be linked to the tree-shaped structure. Here, support sectors are populated below the support points to filter the valid space based on printability. All head nodes within the support sector S_i can be seen as a valid nodes set. The closest node in the set is selected as a connection node. For example, a set of head nodes

$(v_0, v_1, v_2...)$ is inside the support sector S_i. In this case, the closest node (v_3) is selected as the connection node to construct the shortest path between valid tree nodes and the support point. Once all the shortest paths are generated, the direct-graph theory of L-system trees is applied to find the corresponding tail nodes of these selected head nodes. Subsequently, the tail nodes identified are seen as head nodes in the lower layers. This process is looped until the head point on the base is located. In this process, the pruned tree branches are obtained to generate final support skeletons by removing all invalid tree branches. To obtain a lightweight and stable support structure, the weights of the head nodes are used to construct solid tree-shaped structures (on the right of Figure 4.31).
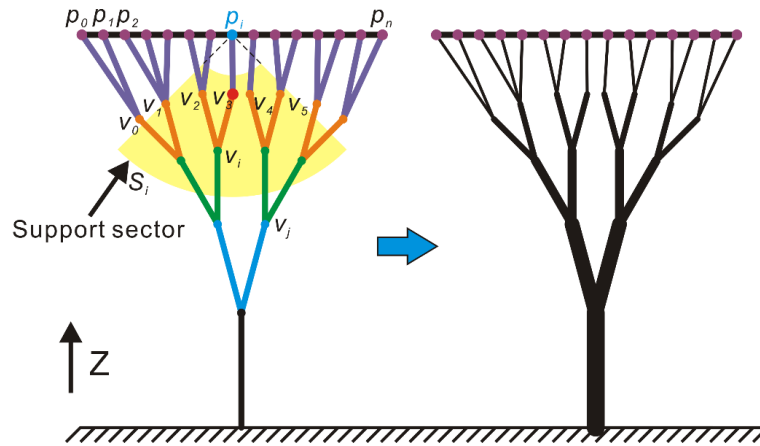
Figure 4.31. The definition of qualified shortest connection paths between support points and L-system tree nodes.

Figure 4.32 gives an example to show the generation of a solid tree-shaped structure. Two circle sections are generated on the endpoints of each branch. The diameter of endpoints is related to the weight of head nodes. Then, a solid sphere is applied to connect the solid branches in the different layers. Finally, a Boolean union operation is adopted to obtain a stable tree-shaped structure, as shown in Figure 4.32(d). All parameters that define the parametric L-system tree can be changed according to the requirements of support strength and specific AM constraints.

(a)   (b)   (c)   (d)
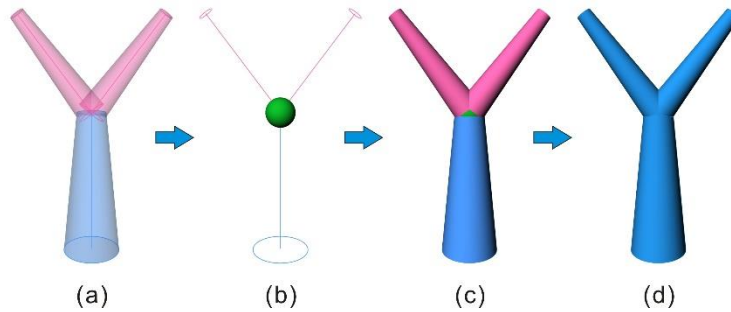
Figure 4.32. A solid tree-shaped structure generation.

4.2.2. Genetic algorithm for populating alternative solutions

Due to the bottom-up support generation strategy, it is a key research question to plant different types of L-system trees in a set of limited design spaces. Figure 4.33 shows the main steps of a set of tree-shaped support structure generation via a mandible implant part. Here, a decomposition method is used to decompose the optimized support points into several groups based on the height and position of the support points. Figure 4.33(b) shows different groups in different colors. Considering the distance of support points in the same group, these groups are further divided into several sub-groups. In Figure 4.33(c), three types of groups (G_1 , G_2 and G_3) are divided into sub-groups ($G_1 \rightarrow G_{11}, G_{12}$, $G_2 \rightarrow G_{21}, G_{22}, G_{23}, G_{24}$ and $G_3 \rightarrow G_{31}, G_{32}$). To support all support points in each sub-group, these points are projected onto the build base. Then, a set of feasible square design spaces, called L-system root bases, as shown in Figure 4.33(c), is generated to cover these projected points. The size of each L-system root base is based on the lowest height of support points in the corresponding sub-group. In the L-system root bases, different types of L-system trees in the knowledge-based data set are planted randomly and support points will be connected to the nearest head nodes of the L-system trees within the support sectors. Directed graph information of an L-system tree is applied to obtain valid tree edges by removing invalid tree branches. After that, weight information of head nodes on the pruned trees is utilized to construct solid tree-shaped support structures as illustrated in Figure 4.33(f).
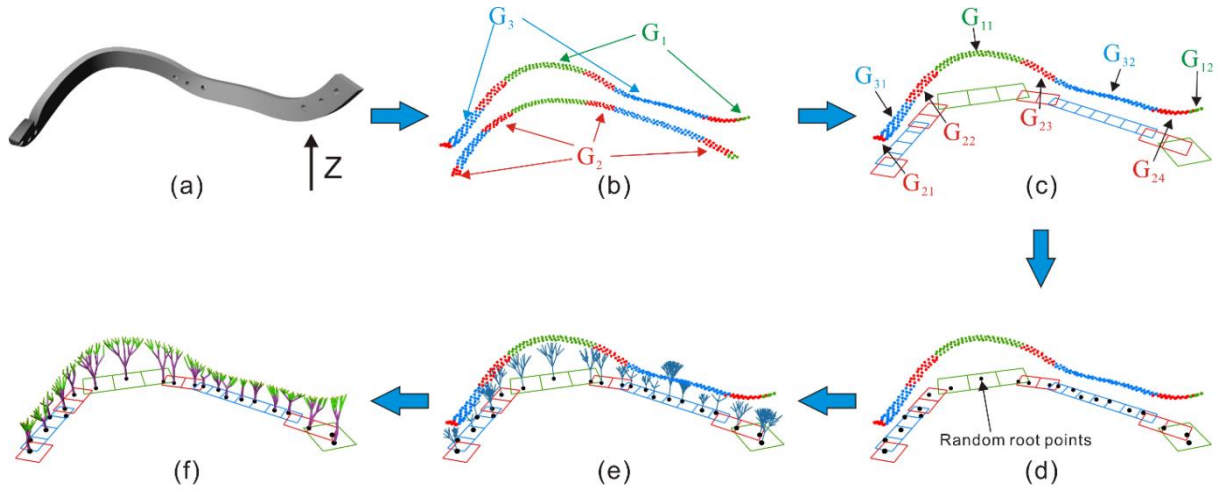
Figure 4.33. (a). The build orientation (Z direction) of the mandible implant part; (b). Optimal support points; (c). Decomposition of projection areas; (d). Random initial tree positions; (e). Random L-system tree types and sizes; (f). Final pruned trees.

4.2.3. Support validation for all support points

Though support points can be connected with head nodes of the L-system trees, there is one situation for a support point p_i where there are no head nodes within the support sector S_i. To ensure all support points are supported, a support validation process is adopted to connect these unsupported points with the build base. Figure 4.34 shows the support generation method for the unsupported points. For p_0 and p_1, none of the tree nodes is located in the support sectors (S_1 and S_2). Two vertical lines (p_0B_0 and p_1B_1) are applied to link the unsupported points (p_0 and p_1) to the build base. These vertical lines are used to construct solid conical frustum structures to support the unsupported points. To avoid large deformations of the slim conical frustum, the diameter and length of each shortest connection path should meet the manufacturability requirements. In this case, the diameter of the head nodes in the last layer is 0.15 mm and the shortest connection path is more than 0.5 mm and less than 8 mm.
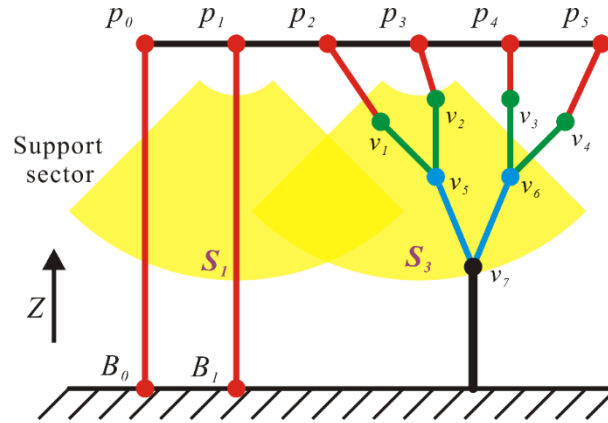
Figure 4.34. Support generation between unsupported points and the printing base.

4.2.4. GA-based multi-objective optimization

In general, the goal of support structure optimization is to minimize the volume of support structures. However, with regards to some medical components with fine geometries, how to minimize support contacts on the surface is still a critical issue to ensure shape accuracy of the components. In this work, the support contact is defined as the collision/interference between tree-shaped support structures and the part to be printed. Therefore, considering the lightweight design of support structures and surface quality requirement for medical parts, there are two objective functions: the volume of support structures and the number of collisions. These functions are applied to transfer a single-objective optimization problem to a multi-criteria decision-making problem. The objectives can be described as follows:

$$Min\ F = \left(f_1(\mathbf{L}), f_2(\mathbf{L}) \right)$$

$$\begin{cases} f_1(\mathbf{L}) = \sum_{i=1}^{n} v_{Li} + \sum_{j=1}^{m} v_{Fj} \\ f_2(\mathbf{L}) = \sum_{i=1}^{n} c_{Li} + \sum_{j=1}^{m} c_{Fj} \end{cases}$$

(4-1(

Where v_{Li} is the volume of i-th L-system tree-shaped support structure and v_{Fj} is the volume of i-th vertical support structure. c_{Li} is the number of collisions between i-th L-system tree and the part and c_{Fj} is the number of collisions between j-th vertical support structure and the part. Theoretically, the solution space of the support structure design problem is infinite since the tree-shaped support structure optimization problem can be described as the ESMT problem which belongs to an NP-hard problem [87]. By virtue of a parametric control of the proposed method, a popular multi-objective genetic algorithm, NSGA-II [167], is used to obtain a Pareto front with a set of finite non-dominated solutions for further decision making. Figure 4.35 represents the GA parameters and its coding for the proposed method. The topology shape and position of each tree can be defined by five variables: tree types, step length, length scale, initial position and initial orientation. The 'type' means the four types of predefined parametrized tree-shaped structures. The 'step length' and 'length scale' can change the size of the tree. The initial position determines the position of the root of a tree in the corresponding root base and the initial orientation is responsible for the rotation angle of a tree around the tree base. The decoding of these GA parameters for k-th L-system tree is described in Figure 4.36. One random tree s_k is rooted on the parameter point p_k which is located on a root base from a domain dividing $\{u\}$ and $\{v\}$ parameter. The length of the base branch is h_k and the length scale is a_k. A rotation variable α_k can control the rotation angle around the base branch.

Figure 4.35. Optimization problem description and GA coding.
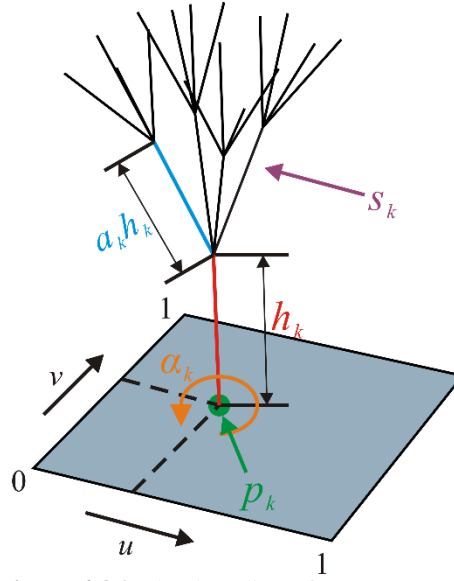
Figure 4.36. The decoding of GA parameter.

Generally, the support structures will be removed during the post-processing. To allow the support structures to be easily removed from the model, a cone tip is added to connect with the support point at the head of the shortest path, as illustrated in Figure 4.37. In addition, the added cone tips can ensure surface accuracy and avoid surface repair after printing.
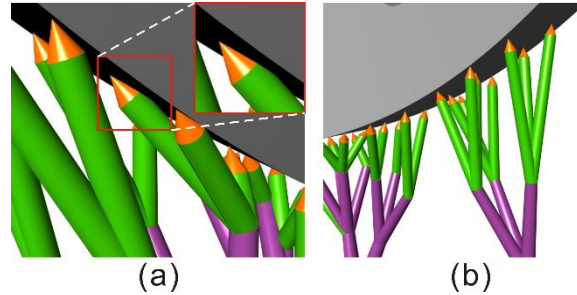
Figure 4.37. Collision cases and the definition of cone tips: (a). Collision; (b). No collision.

4.3. Lightweight support structure design via lattice structure configuration

The manufacturability and stability of support structures play an important role in metallic AM processes. A bio-inspired support structure with manufacturability, stability and friendly heat-diffusion characteristics is proposed in this section. Based on the proposed tree-shaped support structures, two lattice structure configuration approaches are also developed to further reduce the volume of support structures and alleviate the deformation caused by thermal stress. Figure 4.38 shows a general flowchart of the proposed knowledge-based bio-inspired tree support structure design method.
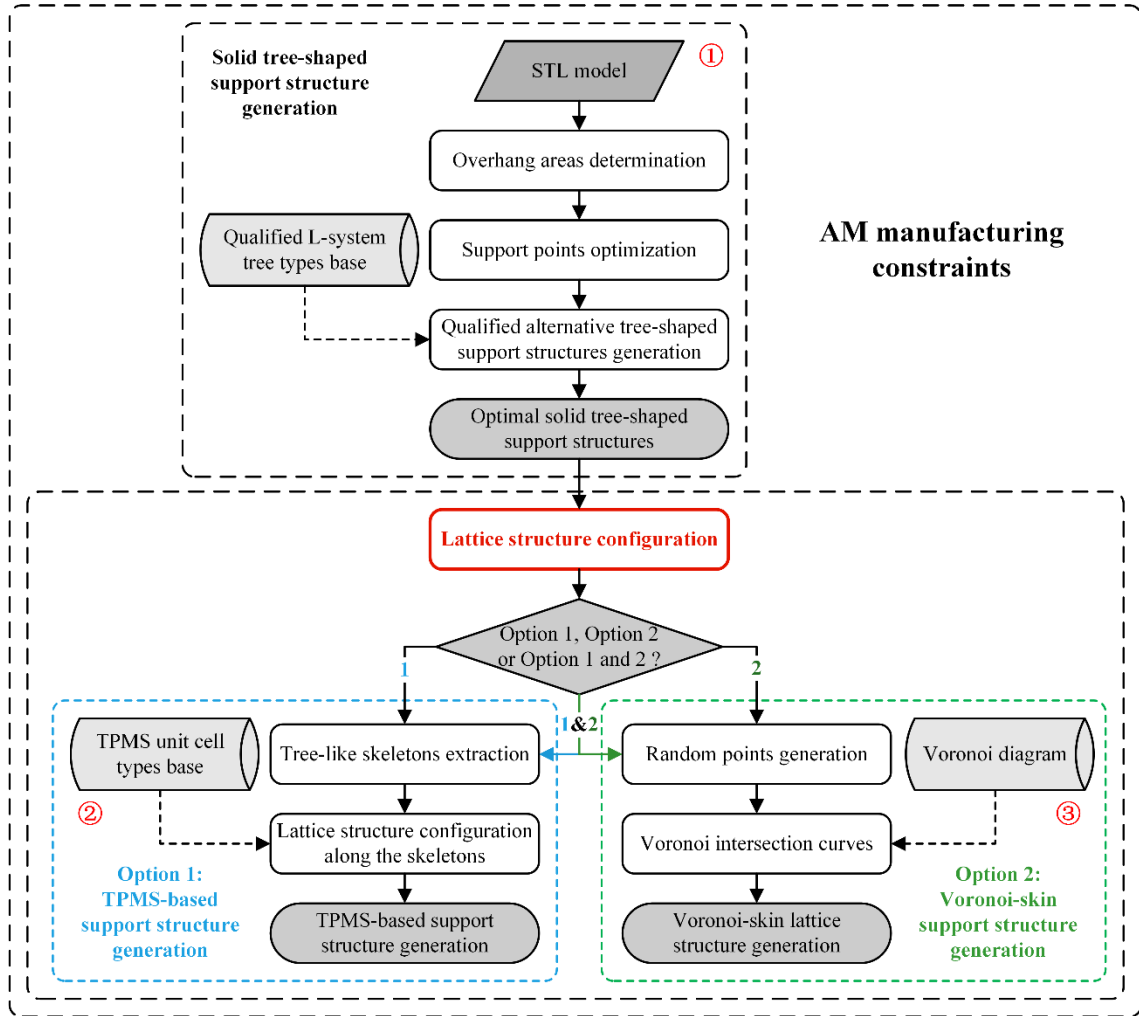
Figure 4.38. General flowchart of the proposed knowledge-based bio-inspired support structure design method

The proposed knowledge-based bio-inspired support design framework has three modules to manage support structure generation. The three modules should meet the manufacturing constraints for the specific AM process. The proposed parametrized solid tree-shaped structures differ from other top-down generation strategies of tree-shaped structures as they can be seen as a bottom-up generation method where the tree structure grows from the base to support points. First, overhang areas are determined based on AM manufacturing constraints and geometry information. Then, a novel support point optimization method is used to obtain an optimal support point distribution. Moreover, different types of pre-defined tree-shaped structures in a knowledge-based system are rooted on the building ground randomly to provide support for optimized support points. Due to friendly heat-diffusion properties of lightweight lattice structures [124], two lattice structure configuration methods, TPMS-based and Voronoi-skin, are developed to further enhance the thermal conductivity characteristic of the solid tree-shaped support structures. Regarding the TPMS-based configuration method, Schwarz P surface is utilized to populate

along pruned L-system tree skeletons. For the Voronoi-skin configuration method, random points are uniformly distributed on the surface of the solid tree-shaped support structures. Then, the volumetric Voronoi tessellation method is used to generate a new hollow structure on the skin of the solid tree-shaped support structures. Both lattice structure configuration methods are able not only to reduce the support volume, but also to enhance the heat-diffusion performance due to the high surface-area-to-volume ratios.

Regarding powder bed based metallic AM processes, support structures usually need to provide a friendly heat-diffusion performance to resist thermal distortion [78]. The thermal deformation of support structures can directly influence the shape accuracy of a part. To make the most of the unprecedented capability of the AM process, lattice structures have been used to enhance heat dissipation. Nowadays, the strut width of a micro-lattice structure can reach 90~120 micros [146]. Therefore, the advent of micro-lattice structure has made it possible to produce more lightweight support structures with a tree-shaped support structure. Compared to solid tree-shaped support structures, lattice support structures are not only able to reduce weight significantly, but also have a better heat-diffusion performance during printing. In this section, two lattice structure configuration methods based on the L-system tree-shaped support structures are proposed to further explore more lightweight and heat-friendly support structure for the metallic AM processes.

4.3.1. TPMS-based lattice structure configuration method based on L-system tree-shaped skeletons

Due to the high surface-area-to-volume ratio, nature-inspired triply-periodic minimal surface (TPMS) lattice structures have been demonstrated that they can provide an excellent heat-diffusion performance [107]. Surface-based TPMS lattice structures are represented by mathematical formulations according to level-set functions. Three kinds of TPMS structures, Schwarz Primitive, Diamond and Schoen Gyroid [168], are widely used in many research. They can be described by the following equations.

$$
\begin{aligned}
\phi_P(x,y,z) &= \cos(\omega x) + \cos(\omega y) + \cos(\omega z) = C \\
\phi_D(x,y,z) &= \sin(\omega x)\sin(\omega y)\sin(\omega z) + \sin(\omega x)\cos(\omega y)\cos(\omega z) \\
&+ \cos(\omega x)\sin(\omega y)\cos(\omega z) + \cos(\omega x)\cos(\omega y)\sin(\omega z) = C \\
\phi_G(x,y,z) &= \cos(\omega x)\sin(\omega y) + \cos(\omega y)\sin(\omega z) + \cos(\omega z)\sin(\omega x) = C
\end{aligned}
$$

(4-11)

Where x, y, z are the spatial coordinates, $\omega = 2\pi/l$. l is the size of a unit cell. C can control the expansion of the surface in three dimensions. Figure 4.39 shows the three types of TPMS lattice unit cells.

In [107], the author measured the thermal conductivity of these three TPMS lattice unit cells. Among these three cells, the consistency Schwarz P unit cell was demonstrated to have the best thermal conductivity.
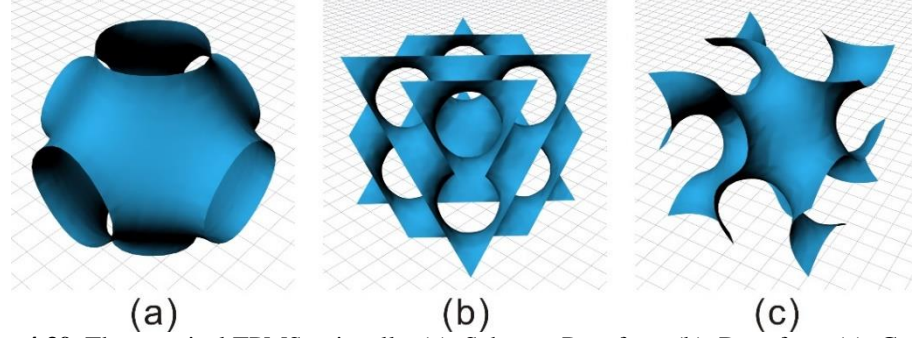
Figure 4.39. Three typical TPMS unit cells: (a). Schwarz P surface; (b). D surface; (c). G surface.

To enhance the heat-diffusion properties of solid tree-shaped support structures, a small-size Schwarz P unit cell is used to replace the solid support structure. Here, we propose a lattice configuration method along L-system tree skeletons obtained by the bio-inspired generative design method above. Figure 4.40 shows an illustration of a simple lattice structure configuration method along a skeleton. The skeleton is divided into several segments. The length of the segments depends on the size of lattice unit cells. Then, a set of voxels are populated along the skeleton. Finally, a predefined lattice unit cell, Schwarz P, is infilled within the voxels.
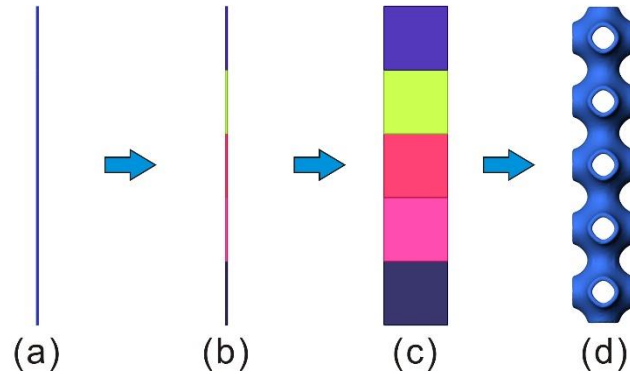
Figure 4.40. Schematic introduction of lattice structure configuration along a skeleton: (a). A skeleton; (b). Decompose the skeleton into several segments based on the size of the lattice unit cell; (c). Populate parametrical voxels along the divided skeleton; (d). Schwarz P unit cells configuration.

With regards to two continuous skeletons with different directions, a sphere connection is proposed to connect the two lattice structures. Figure 4.41(a) presents two continuous skeletons with a certain angle. The Schwarz P surface is populated along the skeletons. After that, a sphere joint is arranged at the

intersection of the two skeletons to ensure the stability and strength of the support structures. The final lattice support structure is shown in Figure 4.41(d).
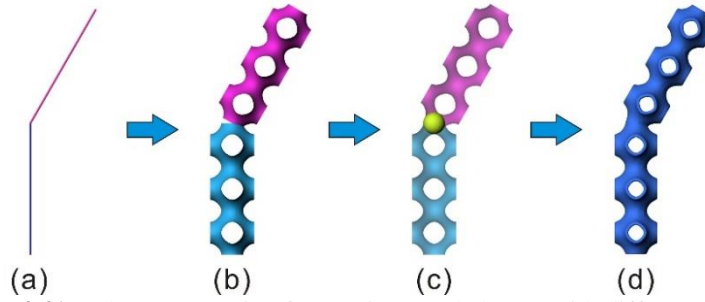
Figure 4.41. Sphere connection for continuous skeletons with different angles

To elaborate the method for more complex tree-shaped skeletons, Figure 4.42 introduces key steps of the TPMS-based lattice configuration method along pruned L-system tree skeletons. The pruned L-system trees are obtained by using the bio-inspired generative design method. First, the branches of the pruned L-system tree are seen as separate skeletons. Based on the manufacturability of AM processes, the voxel size and thickness of the lattice unit cell are calculated and evaluated. After that, TPMS-based lattice unit cells with different sizes are populated within the corresponding voxels, as presented in Figure 4.42(c). To ensure the strength and stability of TPMS support structures, a solid sphere joint is arranged at the intersection points of the skeletons. In addition, an attractor point is applied to form support structures with gradient thickness. Finally, cone tips are used to connect the support points with the TPMS support structures. Since there is no guarantee that the length of each skeleton is an integer multiple of the proposed voxel's size, the size of the actual voxel on each skeleton needs to be recalculated. Notice that the number of voxels along each skeleton is calculated using the mathematical equation below:

$$\lceil n_i \rceil = \frac{L_i}{a}$$

(4-12)

Where $\lceil n_i \rceil$ represents the number of voxels along the $i\text{-}th$ skeleton, L_i is the length of $i\text{-}th$ skeleton, a is the size of a predefined voxel. Therefore, the real size of the voxel in z direction for the $i\text{-}th$ skeleton is as follows:

$$z = \frac{L_i}{\lceil n_i \rceil}$$

(4-13)
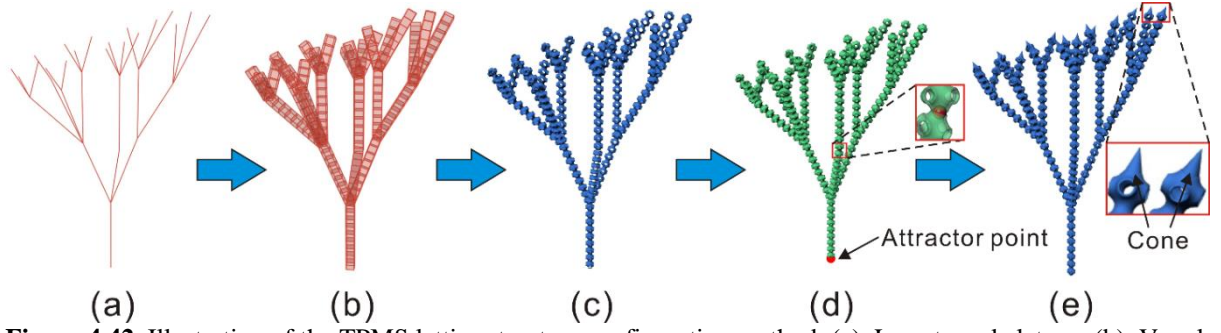
Figure 4.42. Illustration of the TPMS lattice structure configuration method: (a). L-system skeletons; (b). Voxel configuration; (c). TPMS lattice structure filling; (d). Variable thickness for the lattice structures with attractor point on the base; (e). Final TPMS support structures.

Figure 4.43 shows an alternative solution of TPMS-based lattice support structures for the mandible implant part. To remove the support structures easily, cone tips are also added to connect the support points.
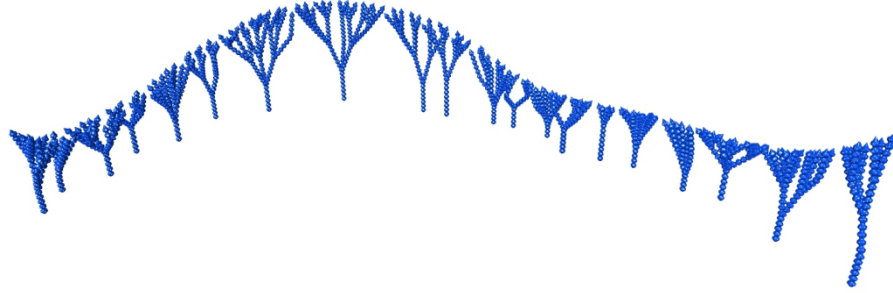
Figure 4.43. TPMS-based lattice support structures

4.3.2. Voronoi-skin lattice support structure generation

4.3.2.1. General Voronoi-skin lattice structure generation

To further reduce the weight of the support structure and improve the thermal conductivity, another solution is to construct a Voronoi-skin lattice support structure based on the solid tree-shaped support structure. Due to the variable size of porosity, Voronoi-based lattice structures were widely used for bone scaffolds. In [108], the authors proposed a generative design method to construct biomimetic lattices based on the Voronoi diagram. To find a functional relationship between porosity, the number of seed points and the strut diameter, a new parametric Voronoi-based lattice configuration method was proposed in [119]. With this design method, uniform, graded and customized lattice structures can be generated according to the given porosity function. Inspired by the Voronoi diagram method, a Voronoi-skin generation method on the surface of the given solid tree-shaped support structures is developed

to create a new hollow surface support structure. Figure 4.44 below introduces a workflow of the proposed method.
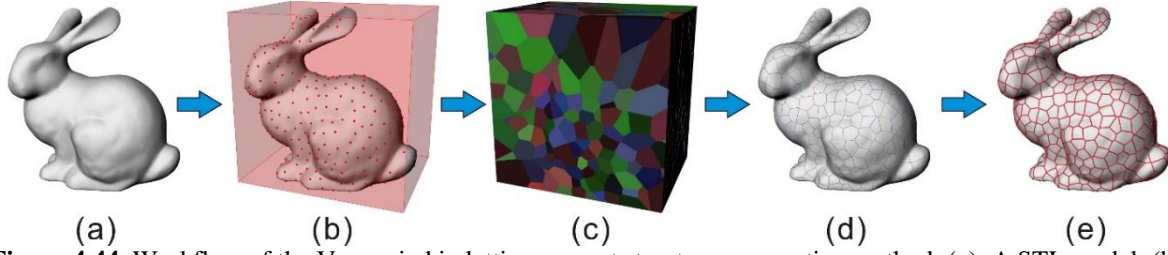
Figure 4.44. Workflow of the Voronoi-skin lattice support structures generation method: (a). A STL model; (b). Bounding box and random points generation; (c). Voronoi cells; (d). Intersection polylines between the STL mesh and the Voronoi cells; (d). Voronoi-skin lattice structures.

The framework enables us to design a Voronoi-skin structure on the surface of any geometries. Firstly, a bounding box is created to cover the entire geometry. Then, the predefined number of random seed points are arranged on the surface of the given geometry. The points, called generators, are uniformly distributed on the surface. The number of points and the diameter of a deformed strut can directly impact the porosity of lattice structure. Hence, the number of the points can be determined by a predefined density.

$$n = \frac{S}{\rho} \tag{3-14}$$

Where S means the area of the given geometry and ρ is the density of points on the skin surface. By a 3D Voronoi tessellation operation, a series of Voronoi cells is generated within the bounding box shown in Figure 4.44(c). With the aim of obtaining intersection polylines on the surface of the geometry, a Boolean intersection operation between the geometry and the surfaces of the Voronoi cells is performed. Figure 4.43(d) shows the polylines obtained on the surface of the geometry. A radius value is set to construct the Voronoi-based lattice structure, as presented in Figure 4.44(e).

In addition, two STL files and the corresponding Voronoi-skin lattice structures are shown below. The number of seed points is 800 and the radius of the deformed beams is 1mm.
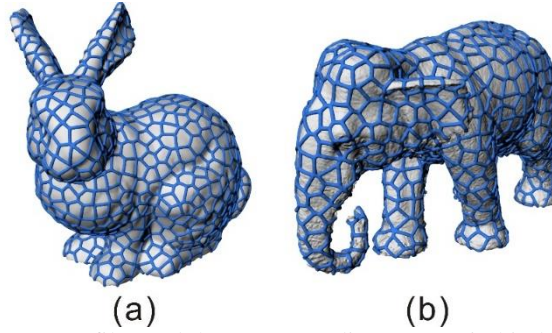
Figure 4.45. Two STL files and the corresponding Voronoi-skin lattice structures.

4.3.2.2. Qualified Voronoi-skin support structure generation

Although the Voronoi-skin lattice configuration method can create complex hollow structures on the surface, it is difficult to provide a stable support for support points due to the random point generation strategy. To ensure a good support, the random point strategy should be analyzed and improved.

A tree-shaped support example, as illustrated in Figure 4.46, is used to verify the Voronoi-skin support structures. Four tip cones are connected to the overhang areas in Figure 4.46(a). In Figure 4.46(b-d), a uniform random point generation strategy is employed to populate random points on the surface of the solid structures with tip cones. As shown in Figure 4.46(c), the support points in the red circles are unsupported due to the stochastic characteristic of random Voronoi structures. To support overhang areas effectively, support points must be contained on the Voronoi-skin structure. A modified random point generation strategy is introduced in Figure 4.46(e-g). Four support points are added as pre-existing points to a random point set. In the modified stochastic strategy, the four tip cones are stilled unsupported. Since the support points are in the center of the Voronoi polyhedral, there are no intersection curves passing through the support points after performing a Boolean intersection operation between the Voronoi cells and the tree structure. After a series of experiments, a new random strategy, as shown in Figure 4.46(h-j), is proposed to achieve a qualified support to the overhang areas. The main difference is that random points are created on the solid tree-shaped structure without tip cones and multiple division points for circles on the bottom of tip cones are added to the random point set. In Figure 4.46(h), trisection points for the circles are added as seed points. The improved random strategy can ensure all support points are located on the intersection polylines of the Voronoi-skin structures obtained.
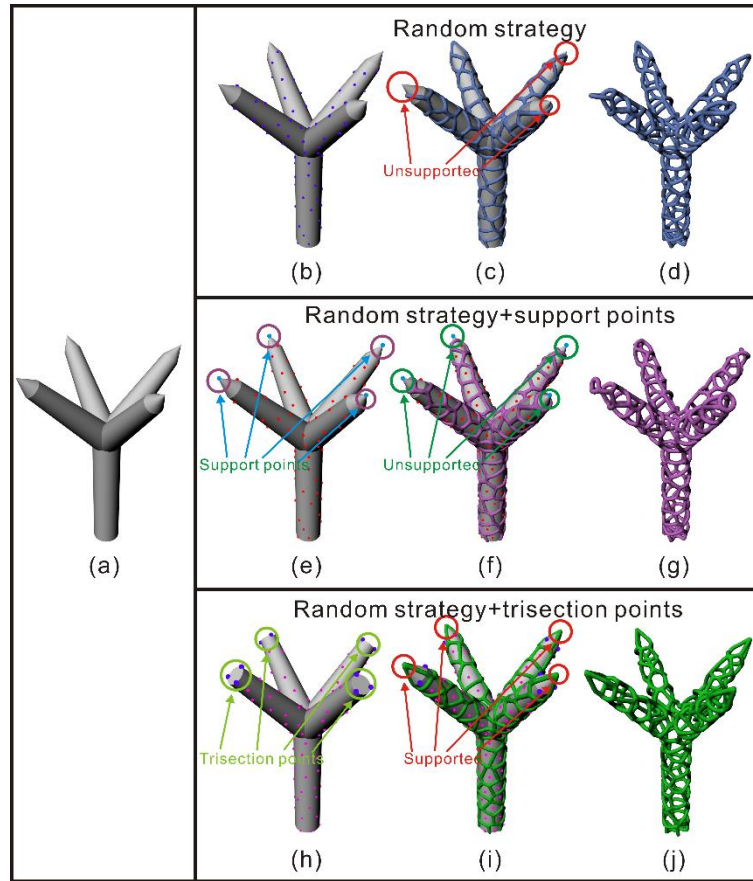
Figure 4.46. (a). Voronoi-skin structure generation for a tree-shaped support structure. **Random strategy**: (b). Random points on the surface of the solid structure with tip cones; (c). A Voronoi-skin structure and the solid structure; (d). A final Voronoi-skin support structure. **Random strategy with pre-defined support points**: (e). A random strategy with pre-defined support points on the surface of the solid structure with tip cones; (f). A Voronoi-skin structure and the solid structure; (g). A final Voronoi-skin support structure. **Random strategy with trisection points**: (h). A random strategy with trisection points on the surface of the solid structure without tip cones; (i). A Voronoi-skin structure and the solid structure; (j). A final Voronoi-skin support structure.

Figure 4.47 explains the qualified support via the random point strategy with trisection points. In the improved strategy, each trisection point is seen as a generator to the corresponding Voronoi cell as illustrated in Figure 4.47(c). The Voronoi cells containing the trisection points are evenly distributed in the cone tips. Each cone tip is divided into three sections via the intersection faces, as presented in Figure 4.47(d). To obtain the intersection polylines, a Boolean intersection operation is performed between the faces of the Voronoi cells and the given tree structure. As shown in Figure 4.47(e), the lattice skin structure can provide a qualified support for all support points. Other multi-section points are also discussed below in Figure 4.48. Voronoi-skin support structures cannot provide a stable and qualified support for single points and bisection points. As the number of section points increases, random strategies with multi-section points can provide a qualified support.
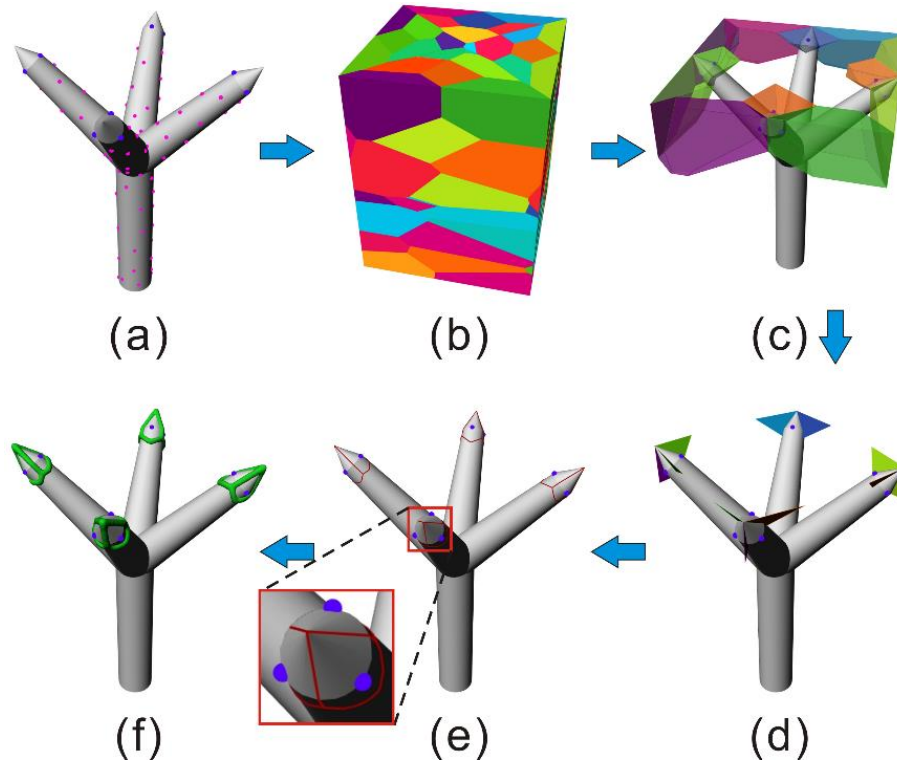
Figure 4.47. A Voronoi-skin lattice support structures with a new random points generation strategy: (a). A tree-shaped solid structure; (b). Voronoi polyhedral cells; (c). Voronoi cells containing trisection points; (d). Intersection faces between the Voronoi cells and tip cones; (e). Intersection polylines between the Voronoi cells and the tree structure; (f). Voronoi lattice structures.
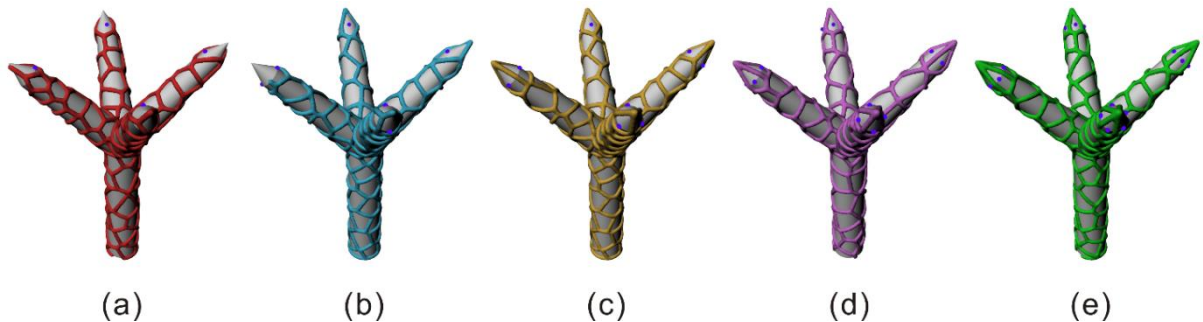
Figure 4.48. A Voronoi-skin structure generated via random points strategies with multi-section points: (a). Single point; (b). Bisection points; (c). Trisection points; (d). Quadrisection points; (e). Quinquesection points.

4.3.2.3. Voronoi-skin support structures based on the solid tree-shaped support structures

Given the stability of the triangular structure, the random strategy with trisection points is used to generate a qualified Voronoi-skin support structure. Figure 4.49 lists the main steps to explain the Voronoi-skin lattice structure generation for a complex L-system tree-shaped support structure. First, an optimal tree-shaped support structure is obtained by using the bio-inspired design method in Section 4.2. Then, the random point generation strategy with trisection points is applied to generate uniform random points

on the surface of the solid structure without cone tips. Next, a volumetric Voronoi tessellation method is used to obtain Voronoi cells on a bounding box defined by the solid structure with cone tips. In Figure 4.49(f), a Boolean intersection operation is used to obtain intersecting polylines between the Voronoi cells and the surface of the solid support structure with cone tips. The last step is to supply a thickness to all polylines to create pipes around the polylines and perform a Boolean union operation to obtain a final Voronoi-skin lattice support structure. Here, the radius is set as 0.05 mm. Due to the self-supporting characteristic of the solid tree-shaped support structure, the micro-lattice Voronoi-skin support structure is also self-supporting. Figure 4.50 shows an alternative solution of Voronoi-skin support structures of the mandible implant part.
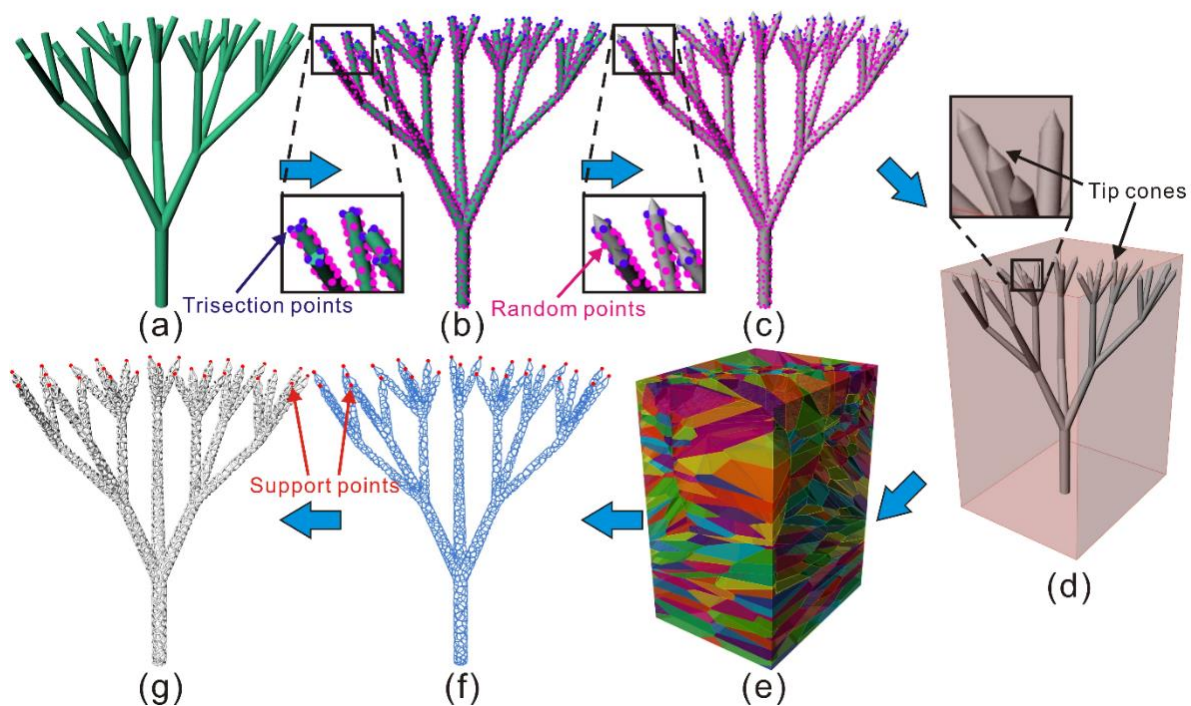
Figure 4.49. Illustration of a Voronoi-skin support structure for a complex tree-shaped support structure: (a). A solid L-system tree-shaped support structure without cone tips; (b). Random point generation strategy with trisection points on the tree structure without cone tips; (c). Seed points on the solid support structure with cone tips; (d). Define a bounding box; (e). Voronoi cells generation based on the uniform random point generators; (e). Intersection polylines between the solid support structure and the Voronoi faces; (f). The final Voronoi-skin support structure.
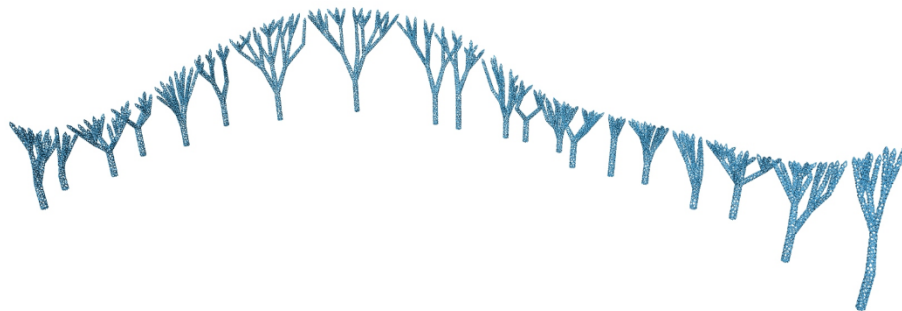
Figure 4.50. An alternative solution of Voronoi-skin lattice structures of the mandible implant part

4.3.3. Case study

In this section, a complex dental part (Figure 4.51(a, b)) of a patient is selected to demonstrate the manufacturability performance of the proposed bio-inspired generative design methods for solid and lattice support structures. The component is also tested by two other popular industrial support generation tools (Profeta and Meshmixer) for comparison. The application requirements of the component are to maximize the shape accuracy of the fine geometric features and minimize support contacts on these surfaces. Firstly, to reduce the support contacts on the overhang areas, support points are optimized by using the new periodic point pattern method. Then, solid tree-shaped support structures are generated and printed to verify the merits of this approach.

4.3.3.1. Support point optimization results

It is noticed that the maximum distance between 2 projected support points should respect the maximum radius of a support point under AM capability in order to avoid any surface collapse during printing. Here, the value is set as 1 mm although the SLM machine used can have a maximum printing bridge length of up to 4 mm. Hence, the side length of the equilateral triangular periodic point pattern is calculated to $\sqrt{3}/2$ mm. The maximum overhang angle is set as 45°. A Ti-6Al-4V powder material and a Profeta SLM medical fabrication machine with an existing working parameter setting are used for printing. A genetic algorithm is applied to search for the optimal support points distribution. The objective function is defined as the sum of z value of all support points. The final support points on the identified valid overhang areas are presented in Figure 4.51(d).
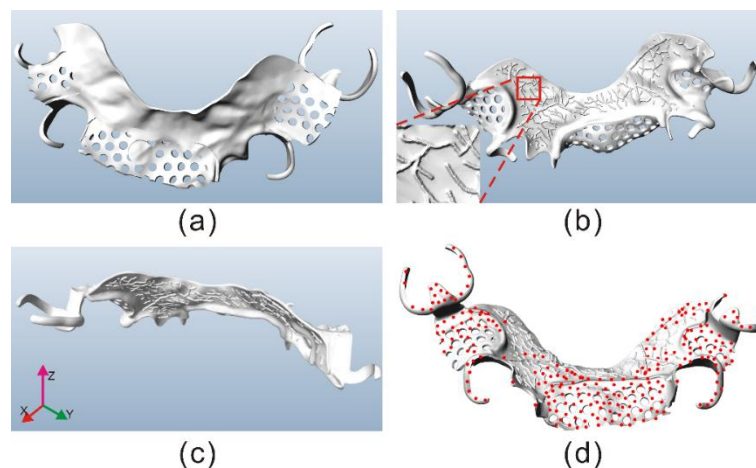
Figure 4.51. (a, b). A medical component; (c). The build orientation (Z direction) of the component; (d). An optimal support points distribution.

4.3.3.2. Solid tree-shaped support structures: results and comparisons

After determining the optimal support points, the predefined parametric L-system tree-shaped support structures are populated underneath the component. To ensure the lightweight support and shape accuracy of the fine geometric features, two objective functions are defined to minimize the volume of support structures and the number of interferences between the support structures and the component. The NSGA-II algorithm is applied to optimize the support structures. The crossover and mutation rates are set as 0.9 and 0.2, respectively. A crossover distribution index of 10 and a mutation distribution index of 20 are also set for Pareto front searching. The run will end when the maximum number of generations is obtained. Table 4.2 shows the parameter definition. A convex Pareto front with a set of non-dominated design solutions can be found below in Figure 4.52. One of the solutions in the Pareto front is selected for physical experiments and comparison. To validate the advantages, two commercial support automation generation tools from Profeta, are used to compare it with the bio-inspired support method. Figure 4.53 shows the printing results. The results show that solid tree-shaped support structures can support the complex overhang areas without any collapse. The shape accuracy can satisfy assembly requirements.

Table 4.2. Parameter definition of the NSGA-II algorithm

Option	Description
Crossover probability	0.9
Crossover distribution index	20
Mutation probability	0.3
Mutation distribution index	20
Population size	50
Generations	100
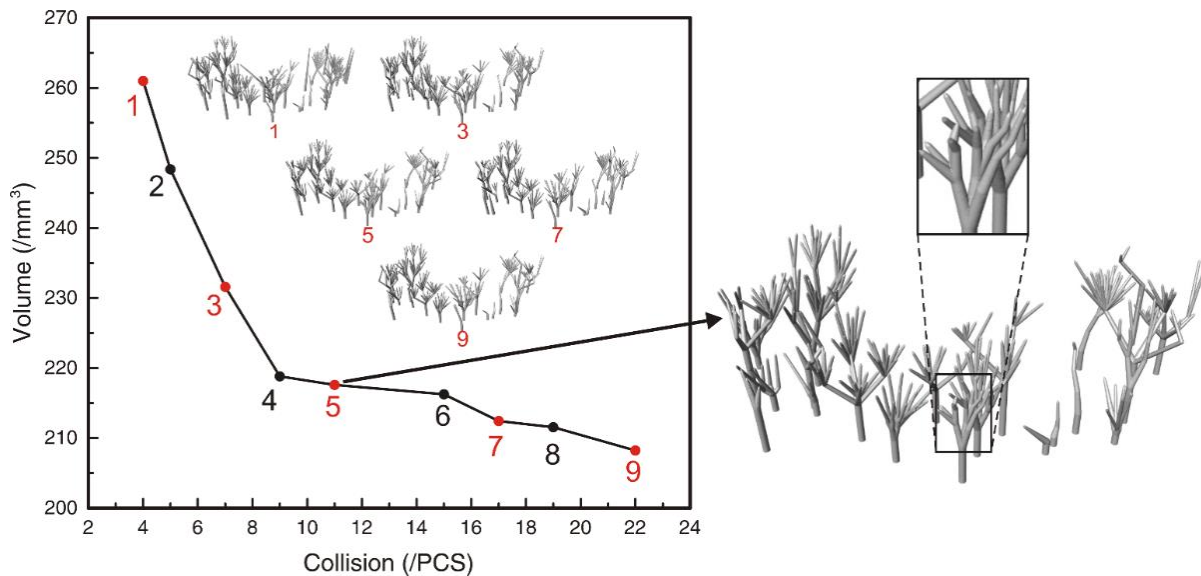
Figure 4.52. Non-dominated solutions on the Pareto front.
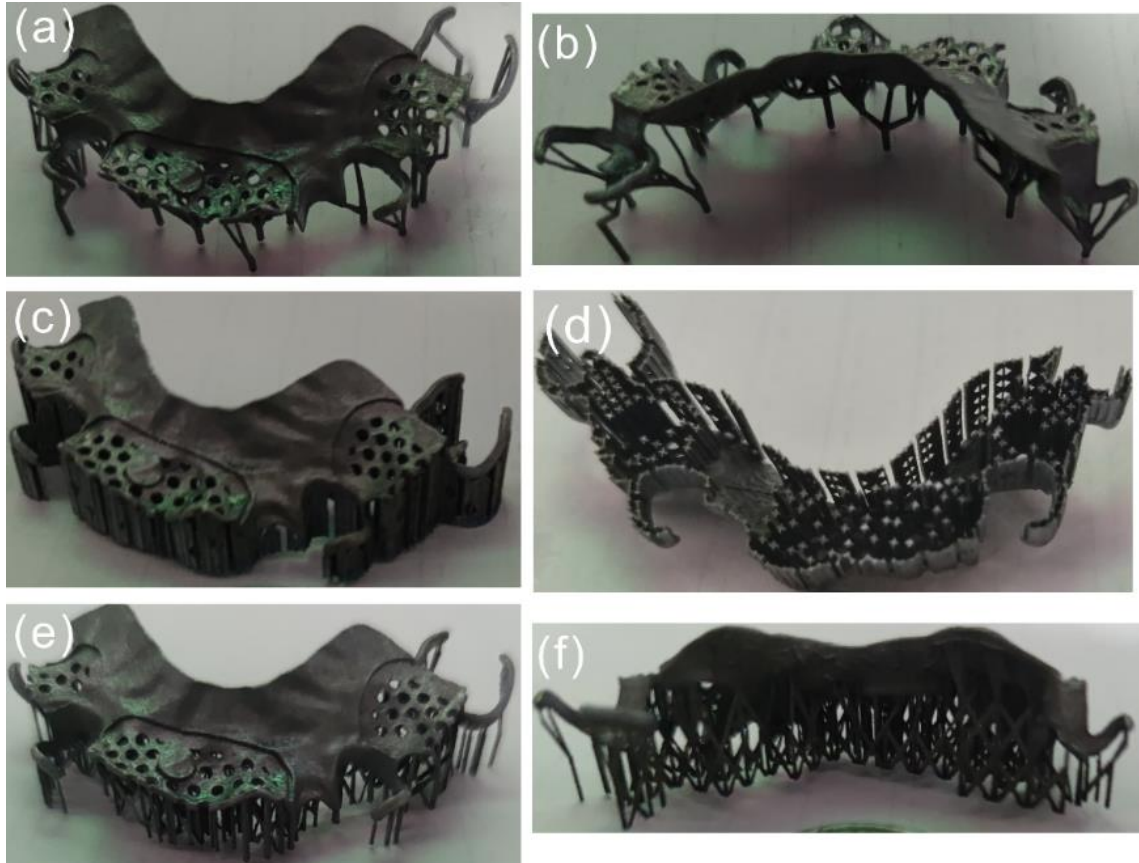
Figure 4.53. Comparison of printing results: (a, b). Solid tree-shaped support structures; (c, d). Profeta (cone & wall) support structures; (e, f). Profeta (lattice-liked) support structures.

4.3.3.3. Lattice configuration results

According to the lattice support structure methods above, two lattice support structures, TPMS-based and Voronoi-skin, are obtained. To ensure the manufacturability of the support structures, the size of the voxel used in TPMS-based method is set as 0.6 mm. Figure 4.54 shows the corresponding TPMS-based support solutions based on the Pareto front in Figure 4.52. With regards to the Voronoi-skin support structures, the density of points (ρ) on the skin surface is 4 pcs/mm^2. The trisection random points strategy is applied to ensure the skin structure is linked to the support points. The Pareto results are illustrated in Figure 4.55. To validate the proposed lattice support methods, four solutions in both Pareto fronts are selected for physical experiments. Figure 4.56 presents the printing results with two lattice support methods. As shown in Figure 4.56, the support structure of TPMS-1 fractured during post-processing. A possible reason is that the thickness or/and voxel size of the TPMS structure are too thin/small to withstand post-processing. Voronoi-skin support structures can ensure a good mechanical characteristic during the post-processing stage. In the next research step, the size of the voxel, the thickness of TPMS and the parameter settings for the Voronoi-skin support structure will be investigated.
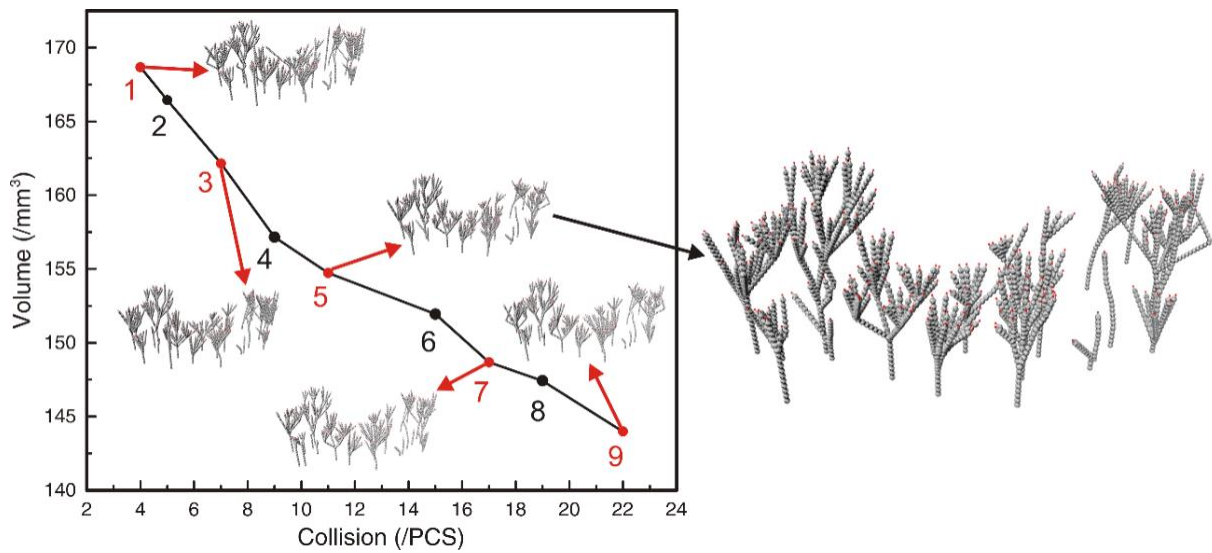
Figure 4.54. TPMS-based support structures on the Pareto front.
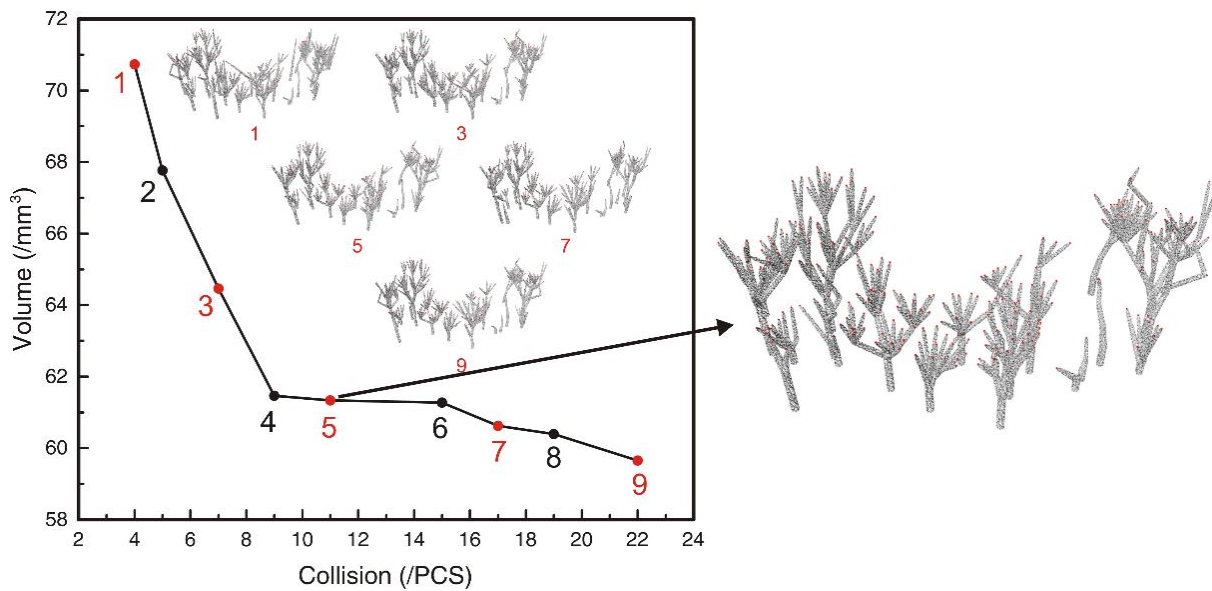
Figure 4.55. Voronoi-skin support structures on the Pareto front.
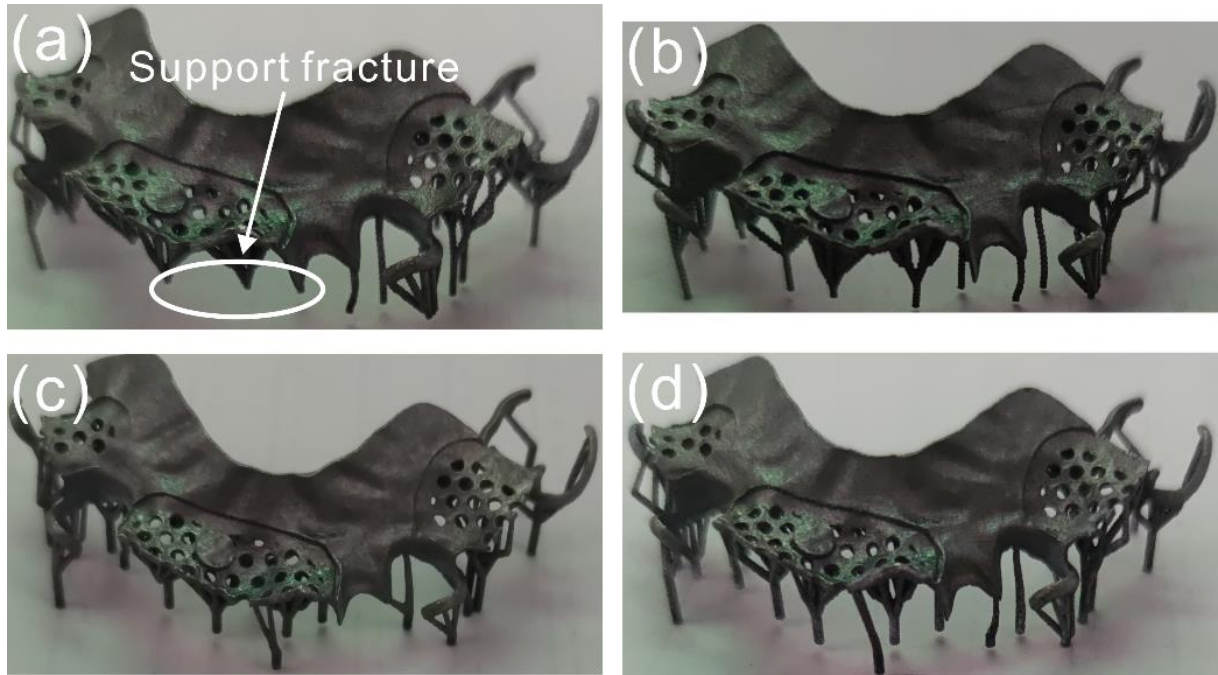
Figure 4.56. Printing results of the four lattice support structures: (a). #1. TPMS-based support structures (support fracture during part removal from the build base); (b). #2. TPMS-based support structure; (c). #3. Voronoi-skin support structure; (d). #4. Voronoi-skin support structure.

4.3.4. Comparison results

After the post-processing of the support structures, Table 4.3 shows the printing analysis results for five support generation methods: solid tree-shaped, TPMS-based, Voronoi-skin, Profeta-wall, and Profeta-lattice. In the comparison, TPMS-based lattice supports have the worst surface roughness. The surface accuracies of solid, Voronoi and Profeta are very good since the printed model can be directed into the assembly prototype model. Compared to Profeta tools, the proposed method can consume support material less. The average savings are 47.62% (ranging from 38.10% to 53.97%). The main confusion is that the volumes of lattice support structures are too far from the actual support models. The error may be caused in the tool-path generation and laser parameter setting. For example, the jump speed of the laser at different nodes can cause the heat accumulation on the tool-path. Hence, the lattice size is too small to be fabricated by using the conventional slicing method. The core work of the next step is to avoid the problem of the drastic increase in volume via the support structure defined by tool-path directly. Based on the printing results above, solid tree-shaped and Voronoi-skin approaches are further compared with other support automation generation tools in the next subsection.

Table 4.3. Printing result and comparison for five methods.

Solution	Solid	TPMS-1	TPMS-2	Voronoi-3	Voronoi-4	Profeta-wall	Profeta-lattice
V_s (g)	1.26	1.46	1.43	1.29	1.26	1.95	1.93
V_p (g)	3.24	3.26	3.34	3.25	3.30	3.26	3.24
R_a	Best	Worst	Worst	Good	Good	Better	Better

$\mathbf{V_s}$: support volume; $\mathbf{V_p}$: component volume; $\mathbf{R_a}$: surface roughness.

To further illustrate the comparison and the advantages of the proposed method, another case is employed to compare the proposed method with other widely-used support generation methods. In this case, the maximum overhang angle is defined at 60° for a better surface quality based on specific requirements for some customized patients. The maximum overhang distance is still set at 1 mm. A CoCrMo alloy is used to produce the component with the Profeta SLM medical fabrication machine. Figure 4.56 shows the printing results of six methods on the build base. Profeta-wall, E-stage, Meshmixer and a direct cone method are compared with solid tree-shaped and Voronoi-skin support. With regards to Meshmixer, its support structures cannot play a stable and qualified support during the printing. Figure 4.57(b) presents its unqualified support. The support material generated by other five methods can provide a valid support for the overhang areas. Table 4.4 summarizes statistics for all models showing support weight, model weight and surface roughness. The results show that the methods proposed can achieve significant material saving with a good surface roughness. As to the solid tree-shaped support, the average support savings are 59.92% (ranging from 36.80% to 71.04%). The average savings for the Voronoi-skin method are 61.17% (ranging from 46.75% to 75.60%). The amounts of support material saved for each method are presented in Figure 4.58. Compared to Meshmixer, the savings were 29.25% and 40.38% for solid and Voronoi supports, respectively. In addition, the Meshmixer result cannot be assembled due to extensive deformation. Compared to the E-stage method, our methods (solid and Voronoi-skin) can save more than 36.8%. The main reason may be that support points are significantly reduced before support generation. By using the optimized support points, the direct cone method can achieve a stable support. Less support material also means faster support removal and a cleaner surface.
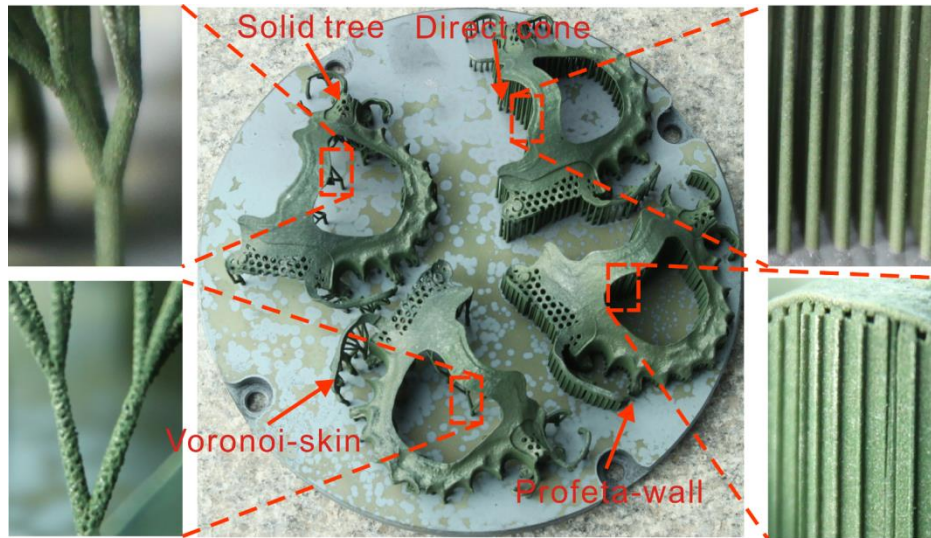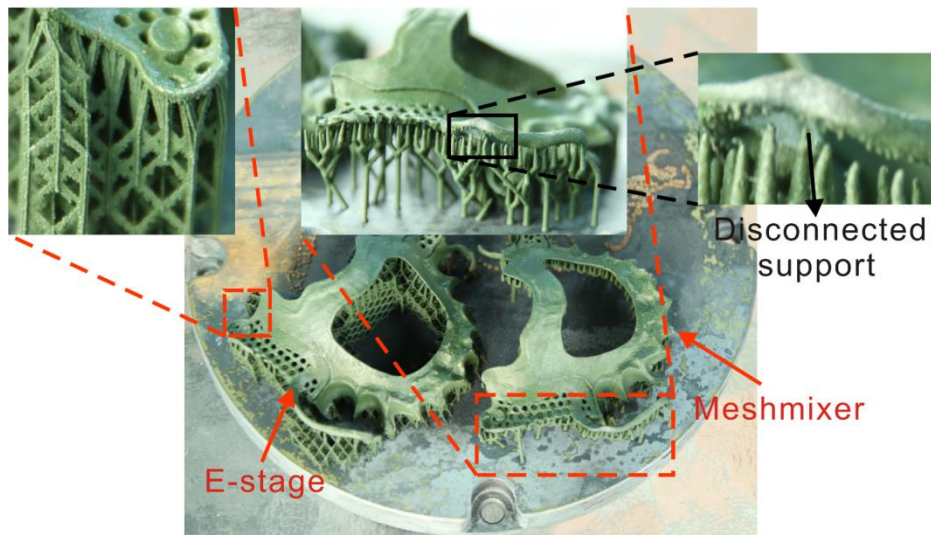
Figure 4.57. SLM Printing results of the six methods.

Table 4.4. Printing results and comparison for the six sup ort methods.

Solution	Solid	Voronoi-skin	Profeta-wall	E-stage	Meshmixer	Cone
V_s (g)	6.99	5.89	24.14	11.06	9.88	15.17
V_p (g)	18.49	18.77	18.38	18.33	17.35	18.13
R_a	Best	Good	Better	Good	Worst	Good

V_s: support volume; V_p: component volume; R_a: surface roughness.
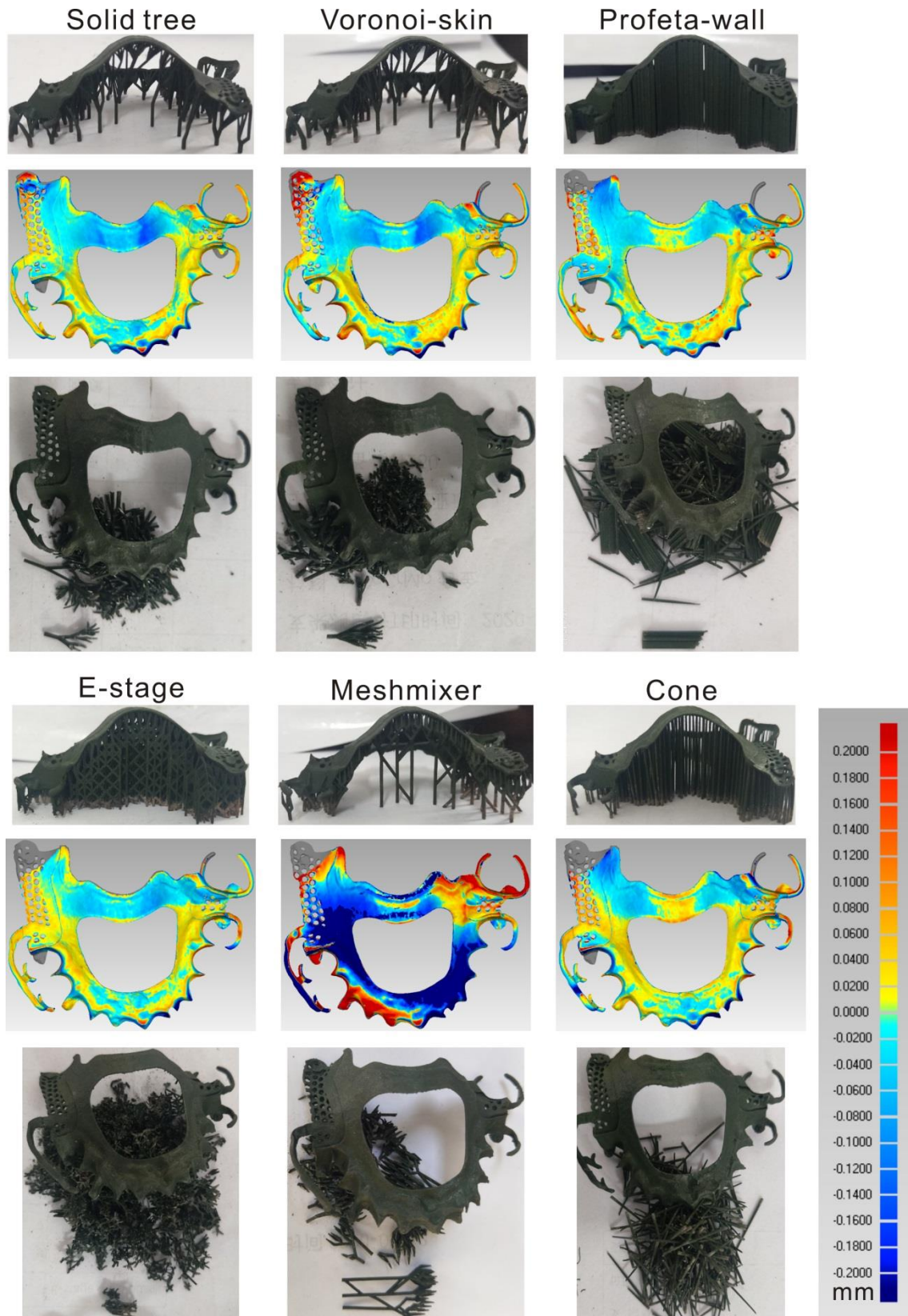
Figure 4.58. Support structure generated by the six methods.

4.4. Summary

This chapter proposes a new support point optimization method to detect support relevant overhang areas and generate optimal support points on the overhang areas of complex components in AM. Point, edge and face overhangs are discussed, respectively, to determine the sequence of generating support points. A new equilateral-triangle periodic support point pattern is proposed to optimize the support point distribution on the support relevant overhang areas. The proposed method has potential to be applied to more types of support structure generation, especially those from complex and porous components.

This chapter also presents a novel porous support structure design and optimization method which contains a set of sub-optimization methods. Bio-inspired tree structures are obtained by using a knowledge and generative method to meet the application requirements: to be lightweight, self-supporting and easy-to-remove. To enhance the heat-diffusion property, two lattice configuration methods are applied to the previously generated solid tree structures. The experimental results and comparison study show that the proposed method exhibits the state-of-the-art performance since it can greatly reduce the amount raw materials needed for the support structure and ensure a better printing quality.

Chapter 5. Toolpath-based constructive design methods for lattice structures configuration

In this chapter, a toolpath configuration method using the island strategy is proposed to populate toolpath scanning for TO results to generate multi-topology Voronoi-based lattice structures. The proposed method has three main steps. The first step is the generation of modified Voronoi cells derived from TO results, the second is to generate qualified lattice structures via multiple toolpath scanning strategies, and the last is to conduct optimization to obtain multi-topology lattice structures via multi-objective evolutionary algorithm. A novel knowledge-based toolpath constructive design method is also proposed to generate high-precision graded lattice unit cells with manufacturability. It integrates implicit modeling, variable distance field, direct slicing and fine toolpath configuration to construct qualified toolpaths without any intermediate steps. To save computation time in part-scale lattice design, predefined different types or sizes of graded lattice unit cells are populated and assembled into a given design space directly.

5.1. A toolpath-based constructive generative design for thickness-varying Voronoi lattice structures

In this section, a toolpath-based constructive generative design method is proposed to generate thickness-varying Voronoi lattice structures in 2D. Figure 5.1 shows the workflow. At first, a multi-objective TO method is used to select an approximate TO result, which removes excess material according to design requirement. Based on the selected TO result, the Voronoi algorithm is carried out to generate modified Voronoi cells. Then, a toolpath constructive method is developed to construct thickness-varying Voronoi cells. By using a multi-objective evolutionary algorithm, an optimized Pareto front is obtained for further decision-making. The detail about the proposed workflow will be discussed in the remaining section.
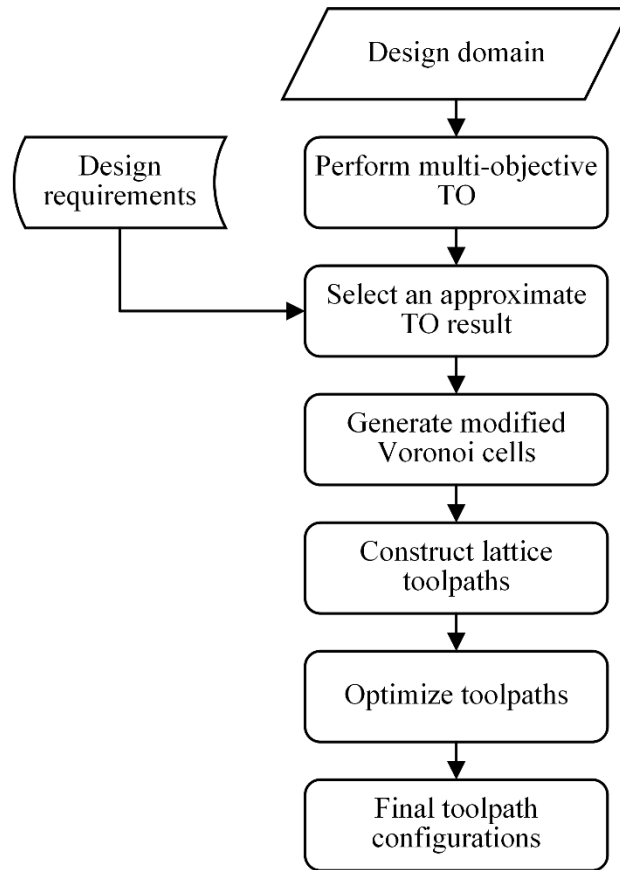
Figure 5.1. A workflow of the proposed toolpath constructive design method based on a TO result.

5.1.1. Selection of an approximate TO result

Currently, lattice structures are usually used to directly infill the design domain. Compared with the traditional direct lattice filling method using simple lattice patterns, such as polygonal unit cells, PSL-driven lattice infill can provide a more stable mechanical performance, which were demonstrated in [154, 169]. Figure 5.2 gives two PSL-based lattice infills. Although the PSL method enable to obtain an optimal material distribution, the areas with sparse material distribution as shown in Figure 5.2 is hardly stressed. Hence, PSL with optimized TO was proposed to remove these areas with less stress in [117] (as illustrated in Figure 2.20 and Figure 2.21).
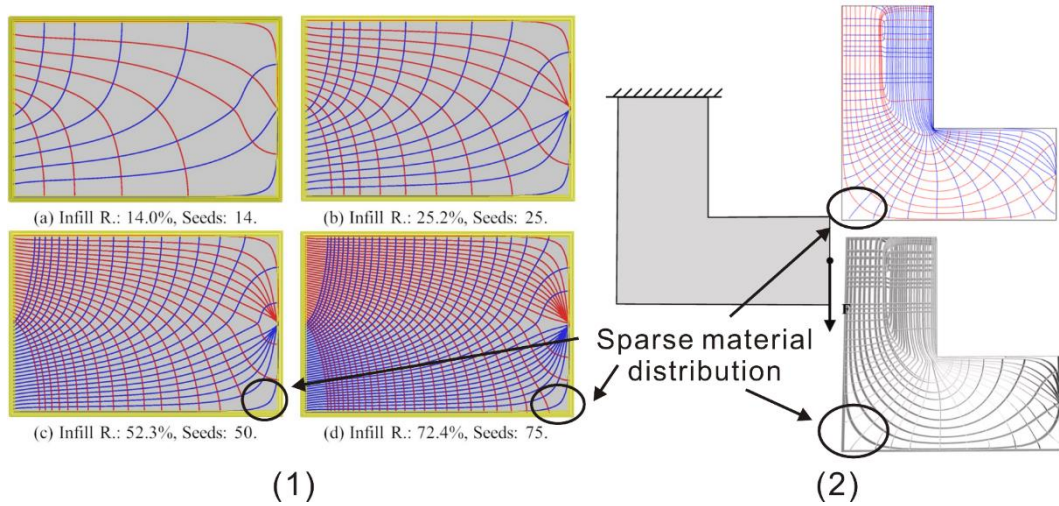
Figure 5.2. Lattice filling based on Principal Stress Lines (PSL): (a). Function-aware toolpath infill [154]; (b). Lattice infill based on force-flow [169].

In order to remove the areas with spare material distribution, a multi-objective TO method is used to obtain an approximate Pareto front, as illustrated in Figure 5.3. To select a TO result as a temple for lattice generation, an approximate candidate area in gray is ensured with reference to design require-ment in green. The size of the candidate area can be adaptively selected according to the specific num-ber of TO results on the Pareto front. Almost all TO candidates in the candidate area can be selected as a TO result served for lattice generation in the next stage. Here, a TO result is selected and shown in the right of the Figure 5.3.
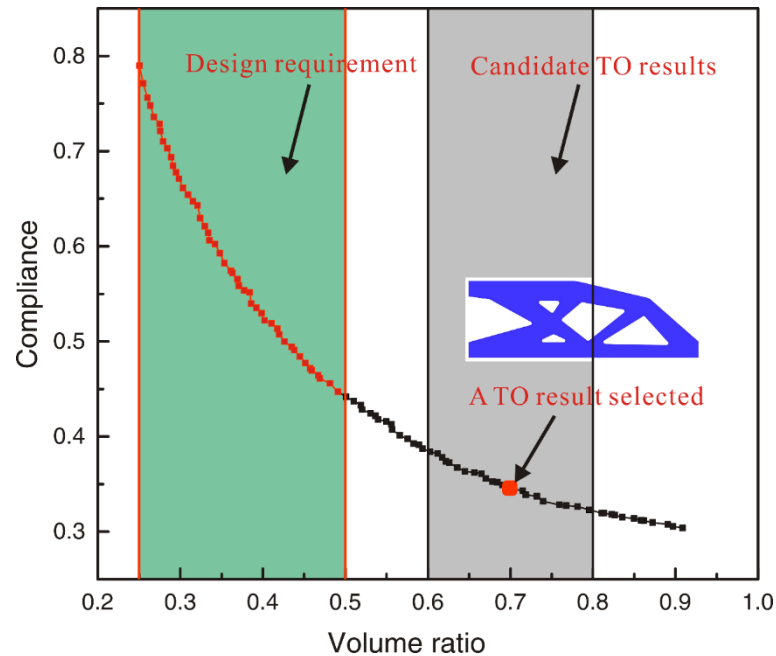
Figure 5.3. Selection of a TO result for lattice toolpaths' generation.

5.1.2. Generation of modified Voronoi cells

The proposed method uses the Voronoi tessellation algorithm to generate closed cells in the optimized TO result. Toolpath is then directly populated within the closed Voronoi cells. The toolpath generation of Voronoi cells in 2D is presented in Figure 5.4.
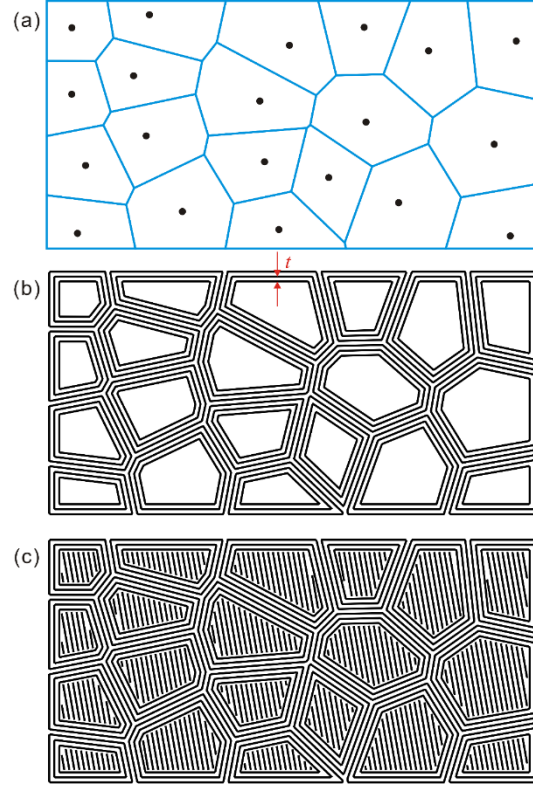
Figure 5.4. (a). Voronoi cells with random point distribution; (b). Partially infill using contour; (c). Fully infill using contour and zigzag.

For a given design domain, seed points are generated in the space randomly. Then, the Voronoi tessellation algorithm is applied to generate Voronoi cells. In order to ensure the connectivity among the Voronoi cells, two kinds of scans, contour and zigzag, are applied. The contour scanning is responsible for keeping the shape of the Voronoi cells and zigzag scanning is used to infill within the inner areas. Figure 5.4(b) shows the contour scanning of the Voronoi cells. To ensure a robust mechanical property of AM parts, hatch spacing should ensure a sufficient degree of melt pool overlap between adjacent toolpaths. Hence, the distance between two consecutive contours should respect hatch spacing (t) of AM machine. Figure 5.4(c) presents the two types of scans for the cells. TO methods can obtain an optimal material distribution for a given design problem. The material distribution can match the distribution of stress magnitude and direction by removing excess material. To generate functional Voronoi cells in the optimized TO results, Figure 5.5 gives the workflow of modified Voronoi cells' generation.

```
┌─────────────────────────────┐
│          TO result          │
└─────────────────────────────┘
              │
              ▼
┌─────────────────────────────┐
│   Decompose the TO result   │
│   into curve boundaries B₁  │
└─────────────────────────────┘
              │
              ▼
┌─────────────────────────────┐
│     Make contour operation  │
│   for the boundaries and    │
│         set as B₂           │
└─────────────────────────────┘
              │
              ▼
┌─────────────────────────────┐
│  Generate seed points in    │
│         the B₂              │
└─────────────────────────────┘
              │
              ▼
┌─────────────────────────────┐
│  Create original Voronoi    │
│           cells             │
└─────────────────────────────┘
              │
              ▼
┌─────────────────────────────┐
│  Perform Boolean            │
│  intersection between       │
│  Voronoi cells and B₂       │
└─────────────────────────────┘
              │
              ▼
┌─────────────────────────────┐
│  Obtain modified Voronoi    │
│          cells              │
└─────────────────────────────┘
              │
              ▼
┌─────────────────────────────┐
│    Toolpath configuration   │
└─────────────────────────────┘
```
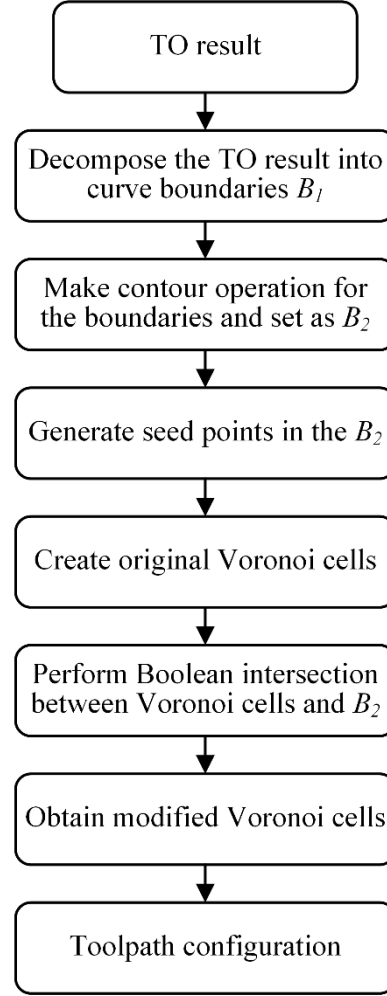
Figure 5.5. Workflow of modified Voronoi cells' generation for TO results.

The TO result can be obtained from any TO methods. Firstly, the TO shape (S) is decomposed into curve boundaries, call outer boundary B_1 and inner boundaries B_2, as shown in Figure 5.6(a). Based on the AM machine specifications, contour scanning is performed to keep the shape of the TO result. A half-hatch-spacing contour scan is used to obtain contour boundary C_1, C_2 shown in Figure 5.6(b). An enlarged picture is presented in Figure 5.7(c).

$$S = \Omega_{B_1} - \Omega_{B_2}$$
(5-

Seed points p_i ($i = 1, 2, ..., n$) with random distribution are arranged within the B_2. According to the seed points' distribution, original Voronoi cells V_{ci} are generated as illustrated in Figure 5.6(c). Next, a Boolean intersection between the original Voronoi cells and contour boundaries B_2 is performed to obtain modified Voronoi cells S_V, which will be used to do the toolpath configuration. Figure 5.6(e) presents the modified Voronoi cells derived by the TO result.

141

$$S_V = \sum_{i=1}^{n}(V_{ci} \cap S) \qquad (5\text{-}2)$$

(a)

(b)

(c)

(d)

(e)
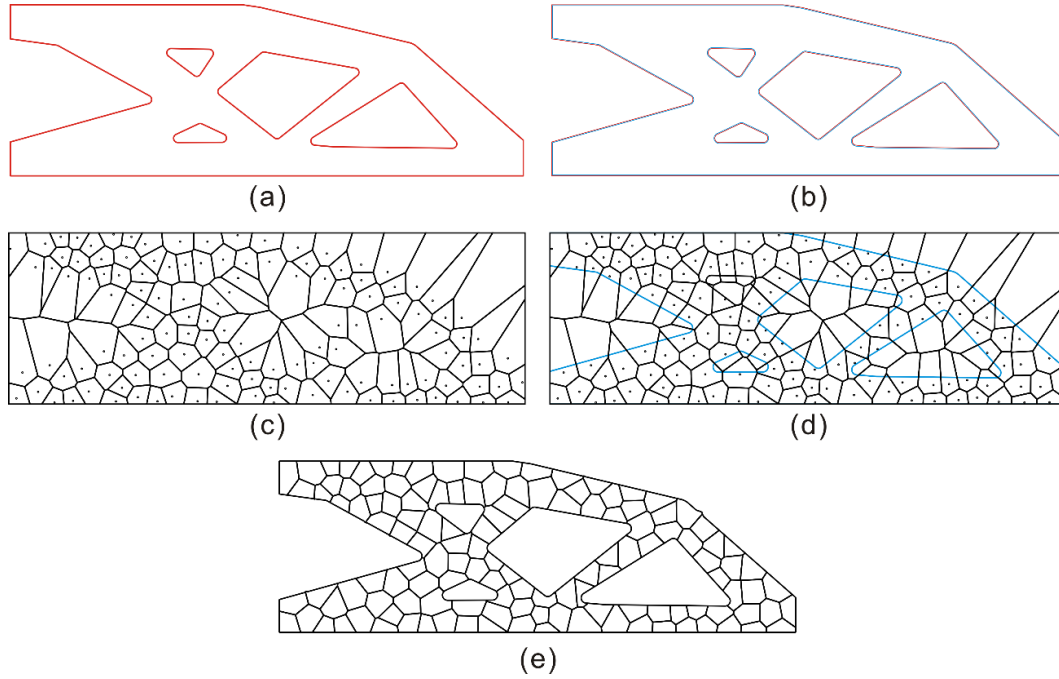
Figure 5.6. Overview of modified Voronoi cells' generation for a TO result (S): (a). A topology shape (S); (b). The topology shape (B_1, B_2) and corresponding contours (C_1, C_2); (c). Original Voronoi cells (V_{ci}); (d). Boolean intersection between contours and Voronoi cells; (e). Final modified Voronoi cells (S_V).

Here, the number of contour operation for the boundaries of the TO result is set as 1. It means the distance between the boundary and the corresponding contour is half of hatch spacing ($t/2$). The hatch spacing is the distance between two adjacent toolpath track. Figure 5.7 shows the definition of hatch spacing.
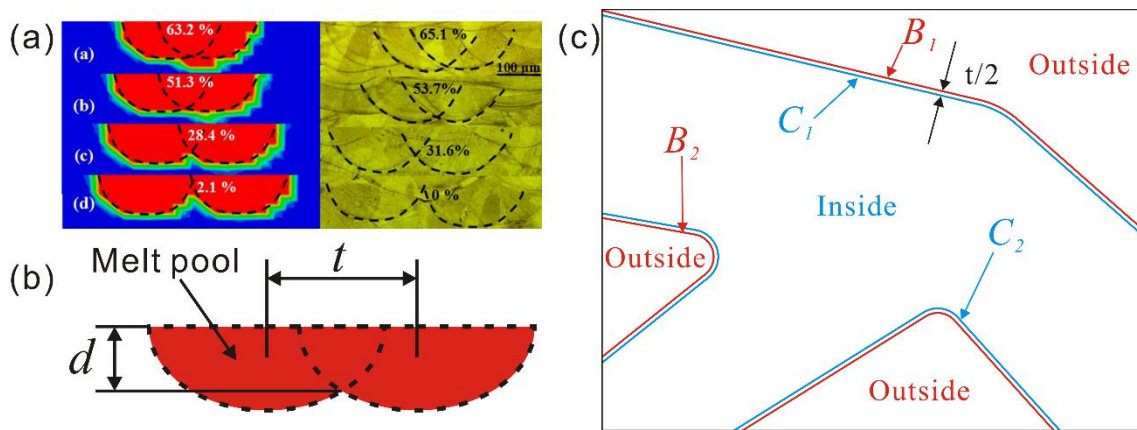
Figure 5.7. (a, b). A SLM melt pool [139]; (c). A partial enlarged picture of Figure 5.6(b).

142

5.1.3. Multiple scanning strategies for the modified Voronoi cells

A toolpath-based topology generation method is proposed in this subsection. The proposed method uses multi-layer contour scans to control the thickness of Voronoi cells and zigzag scan to ensure whether to infill the Voronoi cells inside. Figure 5.8 shows a multi-contour scanning strategy. For a given Voronoi cell (the red polyline), the first contour should keep the shape of the Voronoi cell. Hence, the distance between outside boundary of the Voronoi cell and the $1st$ contour is half of hatch spacing ($t/2$) for the specific AM process. Likewise, the distance between the last contour and inside boundary is also $t/2$. There are n-layer contour in Figure 5.8(a), hence, the distance between inside and outside boundary is nt. The area between the two boundaries is called the topology shape. The corresponding toolpaths of the topology shape are all n contours. In addition, to infill the whole Voronoi cell, the zigzag scanning strategy can be used to fill within the inside boundary as shown in Figure 5.8(b).
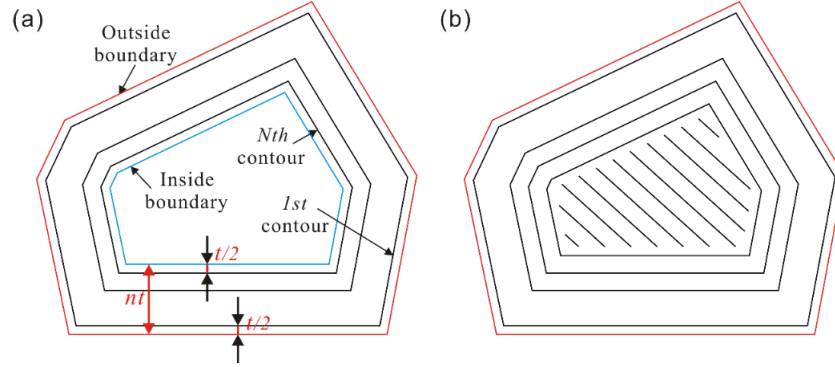
Figure 5.8. Multi-layer contour strategy of a Voronoi cell: (a). Multi-layer contour scanning; (b). Combined scanning with contour and zigzag.

The proposed toolpath-based topology generation method is applied to create a porous structure. Figure 5.9 shows different Voronoi cells based on multi-layer contours and zigzag scanning strategies. For a given Voronoi cell (a red polyline) in Figure 5.9(a-1), different multi-layer contour scanning strategies are used to generate different thicknesses of topology shapes. Figure 5.9(a-c) show three kinds of contour scanning and the corresponding topology shapes, respectively. In Figure 5.9(d), the zigzag scan is responsible for the infill of inside boundary of the Voronoi cell.
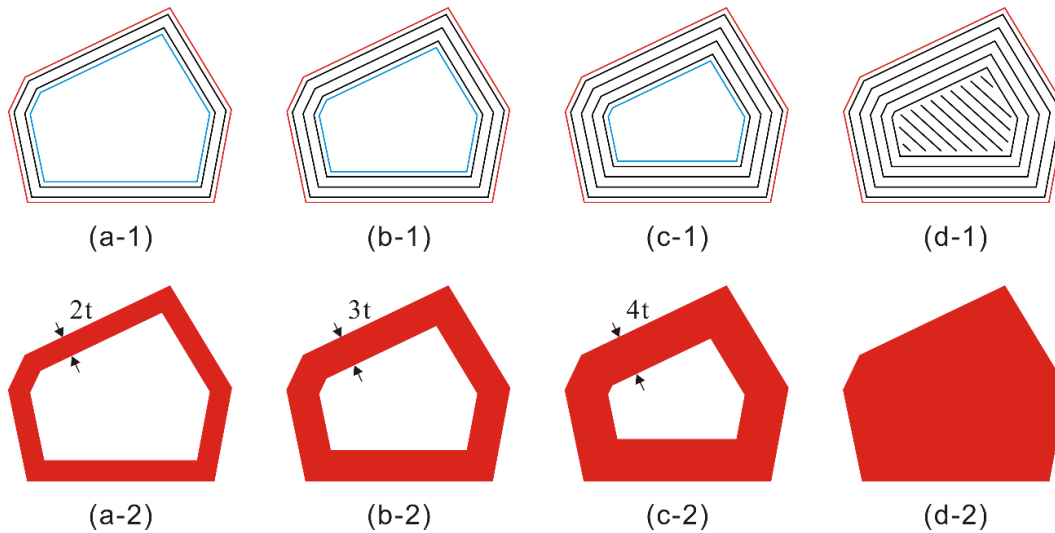
Figure 5.9. Toolpaths and the corresponding topology shapes via multiple scanning strategies for a Voronoi cell.

The multi-layer contour scanning strategy with random zigzag is applied to generate a porous structure for a rectangle design domain. Figure 5.10 shows the result. First, uniform seed points with random distribution are generated in the design domain. Voronoi tessellation algorithm is run to obtain Voronoi cells. Then, by multi-layer contour strategy and random zigzag infill, toolpath is populated into the Voronoi cells. For zigzag infill, there is no inside boundary. The inside boundaries of contour infill are obtained as space area. The final topology shape defined by toolpath is shown in Figure 5.10(d).
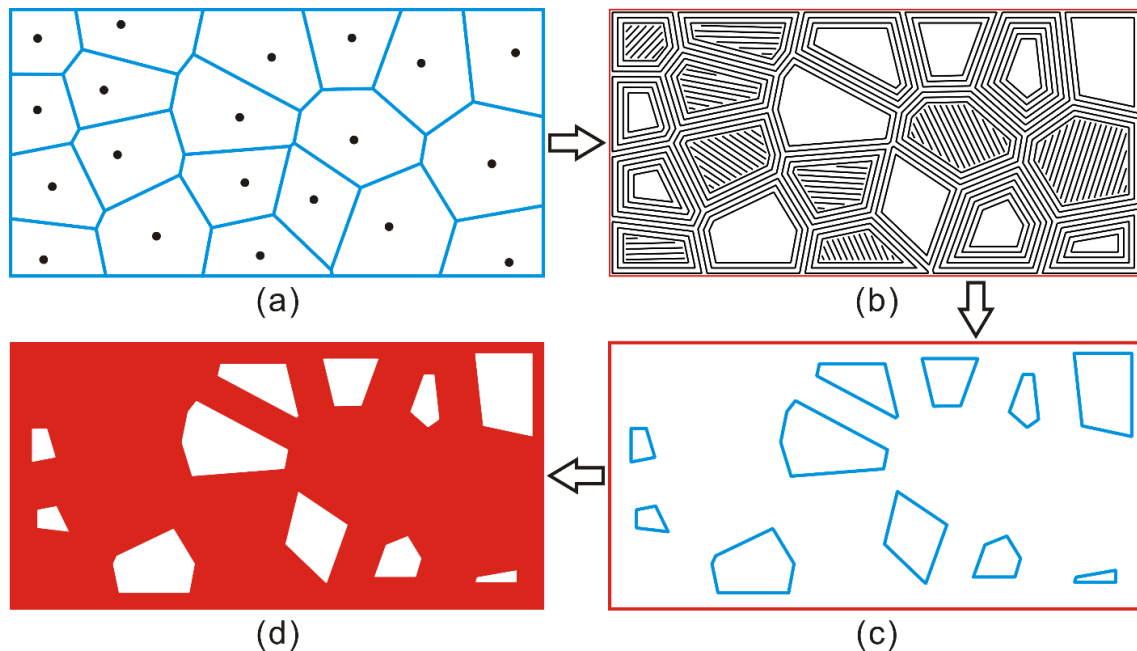
Figure 5.10. Multiple scanning strategies for Voronoi cells in a rectangle: (a). Voronoi cells; (b). Different types of scanning strategies in the Voronoi cells; (c). Inside and outside boundaries; (d). Topology shape.

144

5.1.4. Toolpath scanning optimization via MOEA

In order to conduct multi-objective optimization and generate a large number of alternative scanning strategies, the NSGA-II [162], is adopted to obtain a set of Pareto-optimal solutions. The algorithm flowchart is presented in Figure 5.11 below.
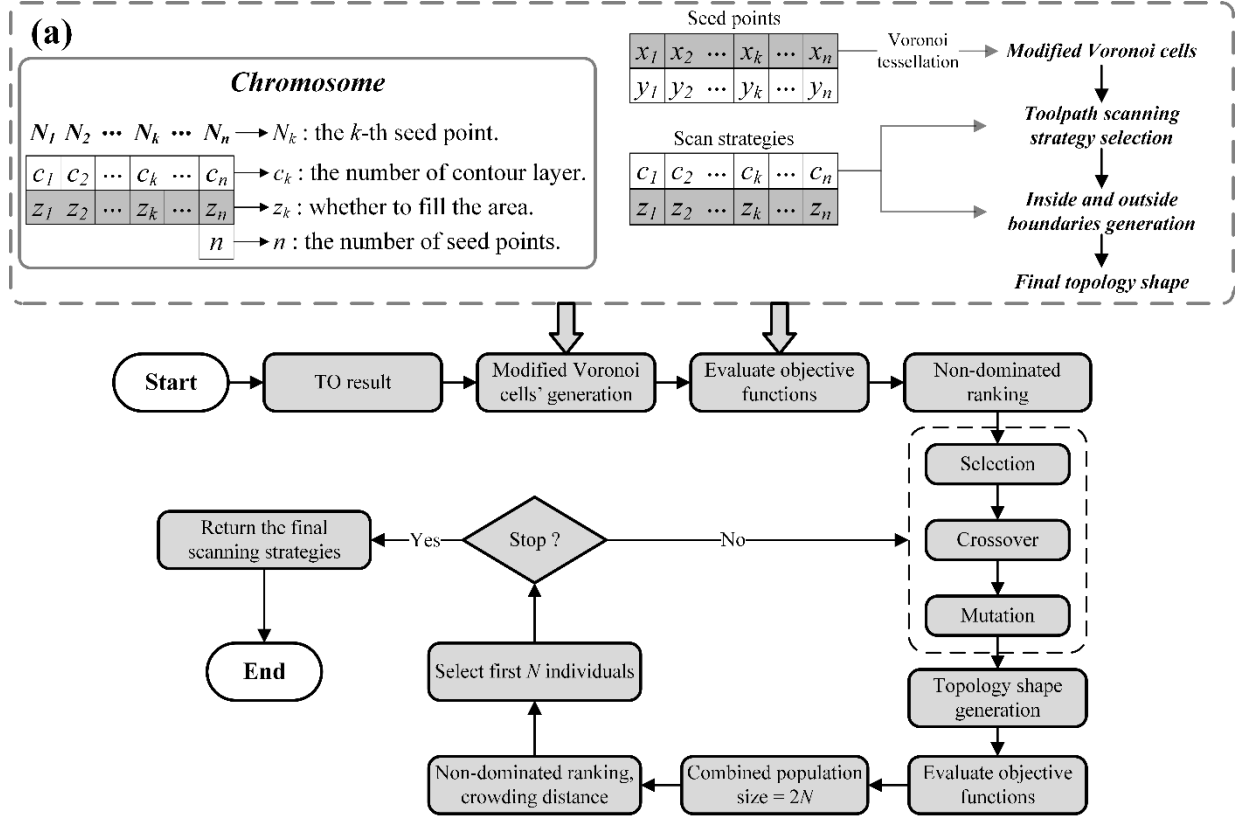
Figure 5.11. Workflow of toolpath-based optimization method based on an optimized mesoscale TO result.

In Figure 5.11(a), the relationship between chromosome and topology shape is set out to explain the geometry generation. The TO result can be derived from any 2D TO method. The modified Voronoi cells are defined by the number (n) and position (x_i, y_i) of seed nodes using the Voronoi tessellation algorithm. From the perspective of part scale as well as considering a great number of seed points are generated based on a uniform strategy, the coordinate change of the same number of seed points between different groups has little effect on the distribution of Voronoi cells. Hence, only the number of seed points are considered design variables for the proposed method.

To achieve different thicknesses for different Voronoi cells, multi-layer contour scan strategies (c_i) are used to generate inside boundaries. However, for certain Voronoi cells, fully infill may have a better mechanical performance. Hence, the zigzag scan strategy is used to infill the whole Voronoi cell. z_i

represents whether it needs to be infilled for seed point p_i. Three types of variables (c_i, z_i, and n) are set for constructing a porous topology geometry. Two objective functions are defined to minimize the volume and compliance. The GA parameters and its coding are also shown in Figure 5.11(a).

To explain the generation of lattice toolpaths using different kinds of scanning strategies, a GA example is shown in Figure 5.12. The chromosomes of two parents are illustrated in the top of the figure. c_i ($i = 1, 2, ..., 10$) means the number of contour operation for *ith* modified Voronoi cell V_{mi}. z_i represents whether the modified Voronoi cell V_{mi} needs to be filled, where 0 means filled and 1 means unfilled. The corresponding toolpath configurations are shown in Figure 5.13(b) and (c), respectively. By using a crossover operation, two offspring are obtained. The chromosomes are shown in the bottom of Figure 5.12. The corresponding toolpath configurations are exhibited in 5.13(d) and (e), respectively. In this example, two-layer contour operation is applied to generate outer contours. Voronoi cells are shown in Figure 5.13(a).
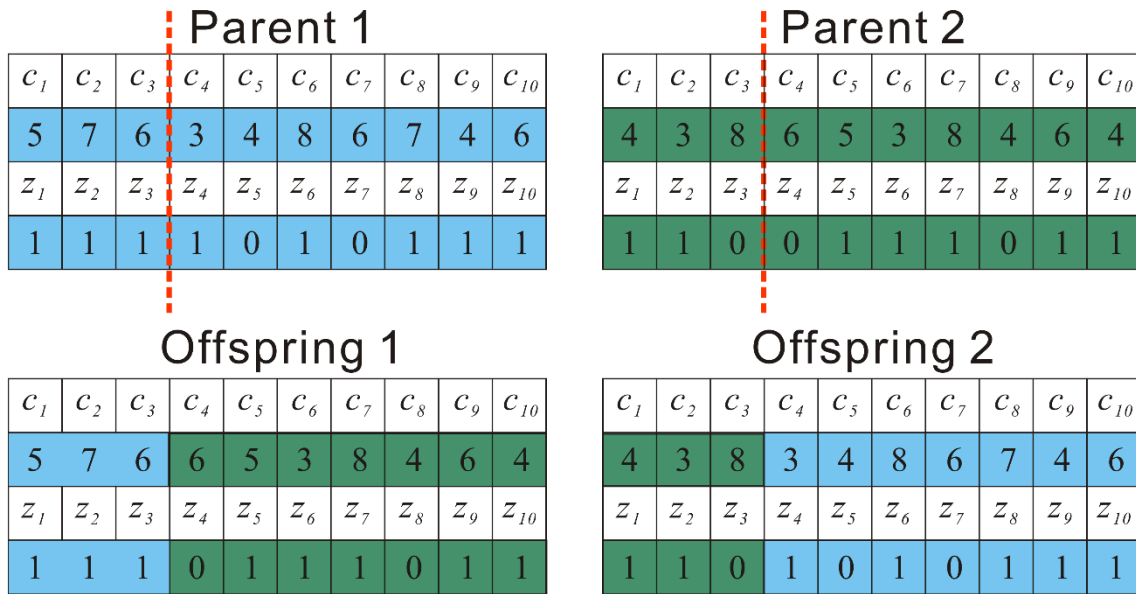
Figure 5.12. The chromosome representations of the two parents and offspring.
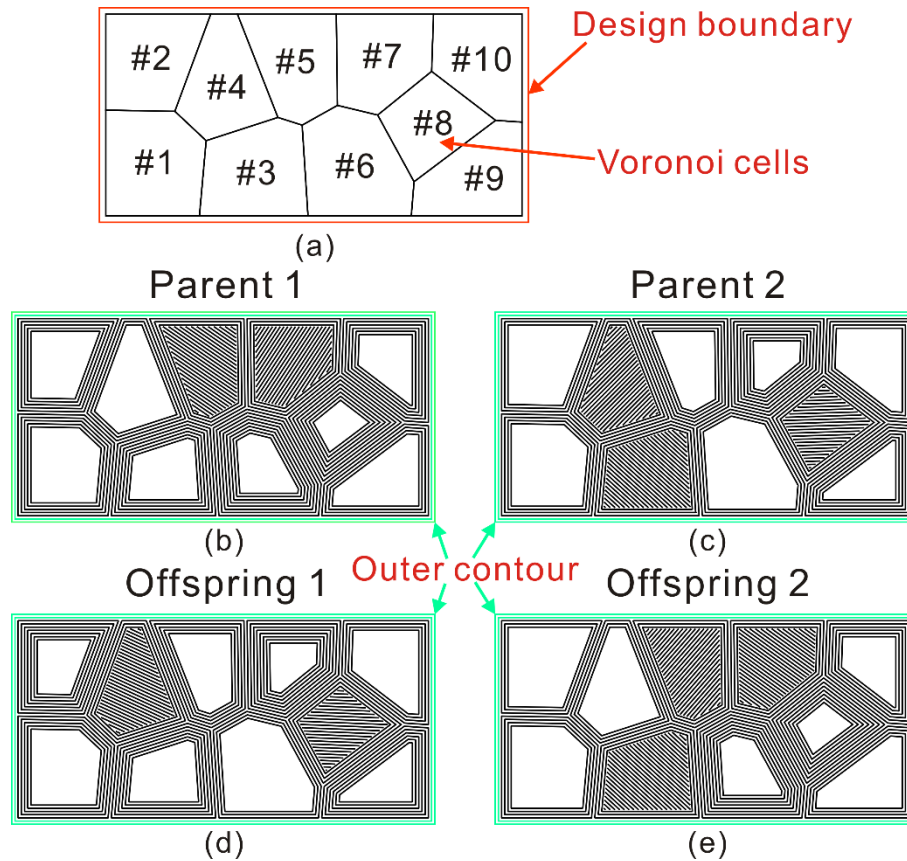
Figure 5.13. Toolpath configuration representation for the two parents and offspring.

Figure 5.14 shows the influence of the number of seed nodes for toolpath configuration in Voronoi-based lattice structures. A two-layer contour scanning strategy is carried out to generate toolpath configuration for Voronoi cells.
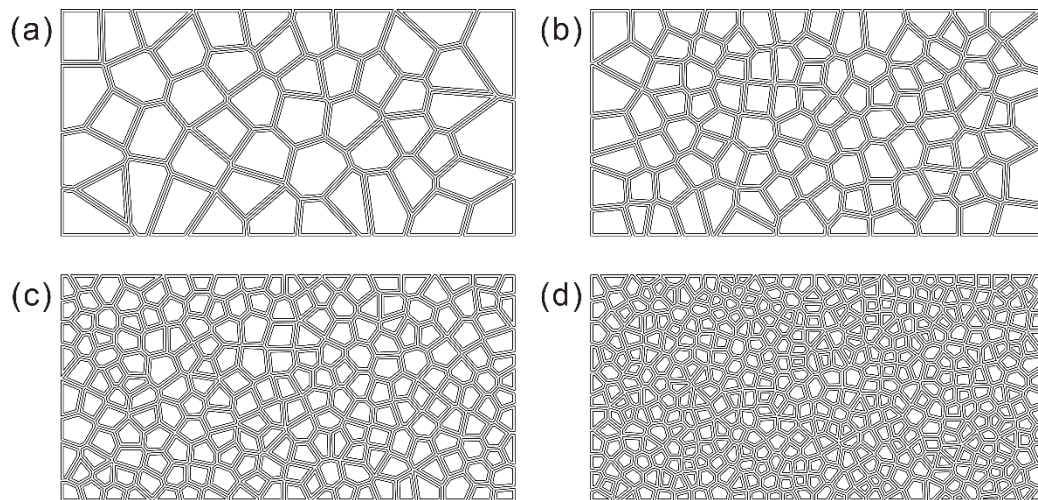
Figure 5.14. The influence of the number of seed points on the toolpath configuration using the same scanning strategy: (a). $n = 50$; (b). $n = 100$; (c). $n = 200$; (d). $n = 400$.

To achieve a uniform random points distribution, Lloyds Voronoi algorithm can be used to optimize the points' position. After the Lloyds Voronoi optimization, new random points will be very near the centroids of the Voronoi cells. Hence, the shape and size will be more uniform. Figure 5.15 shows the two Voronoi cells (V_i^T, V_i^L) using the tradition Voronoi algorithm and the Lloyds Voronoi algorithm, respectively. There are 100 random points in the design domain (40×20 *mm*). The area of each Voronoi cell can be called S_i^T, S_i^L. The mean area (μ) and variance (*Var*) of the Voronoi cells for the two algorithm are calculated based on the following equations:

$$\mu = \frac{1}{n}\sum_{i=1}^{n} S_i \tag{5-3}$$

$$Var = E\left[(S_i - \mu)^2\right] = \frac{1}{n}(S_i - \mu)^2 \tag{5-4}$$

The mean area and variable for the traditional Voronoi algorithm are $\mu^T = 8$, $Var^T = 2.5566$, respectively. For the Lloyds Voronoi algorithm with 50 iterations, the value of variable is $Var^L = 0.2533$. Obviously, the optimized random points distribution has a more uniform Voronoi cells' distribution than that of the original algorithm. By using the optimized points, well-shaped convex Voronoi cells can be obtained, which will be easier for contour or zigzag scanning strategies.
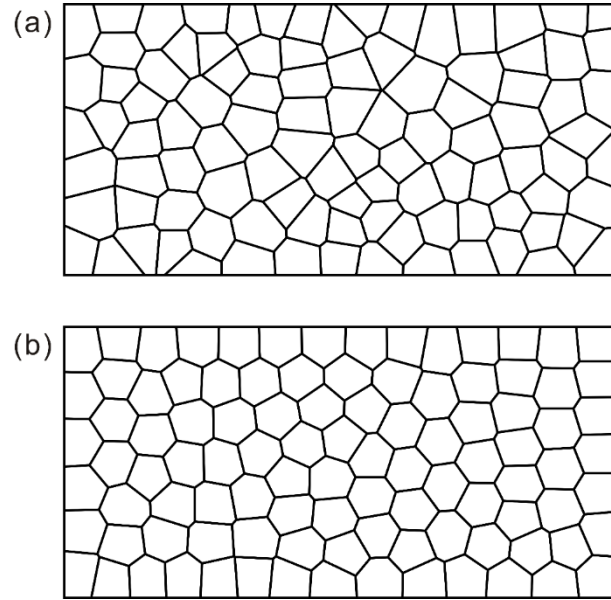
Figure 5.15. Generation strategies of seed points: (a). the random generation; (b). the Lloyds algorithm.

5.1.5. Case study

In this subsection, a TO result, as shown in Figure 5.16, is used to validate the proposed toolpath con-figuration method. Parameters in the standard NSGA-II algorithm are defined in Table 5.1. For the toolpath configuration optimization problem, the values of the crossover probability of 0.9 and the crossover distribution index are set to 20, and a mutation probability of 0.3 and a mutation distribution index of 20 are adopted. In order to solve the compliance minimization problem volume V and compli-ance C are minimized simultaneously. The optimization problem is formulated as:

$$Min : \begin{cases} f_1 = V/V_{max} \\ f_2 = u^T K u \end{cases}$$

(5-

Where V is the volume of the final geometry, V_{max} is the volume of the design domain, u is the dis-placement vector, K is the global stiffness matrix. 2D triangular meshing technique is applied to mesh the geometry and calculate the compliance.
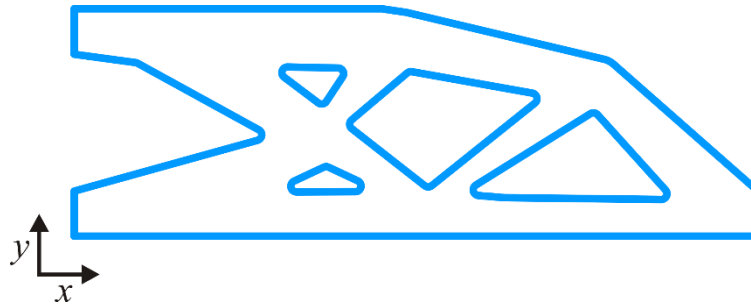
Figure 5.16. The TO result.

Table 5.1. Parameters definition of NSGA-II algorithm.

Option	Description
Crossover probability	0.9
Crossover distribution index	20
Mutation probability	0.3
Mutation distribution index	20

The design domain and boundaries for the cantilever beam problem is defined by using a previous build orientation method in Figure 5.17. The design domain is $3L \times L$ and a point force $F = 100N$ is applied to the boundary. The initial parameter of the optimization problem is set as: population size, 20; stop criterion, 100 generations. Table 5.2 lists a series of parameters used in the problem.
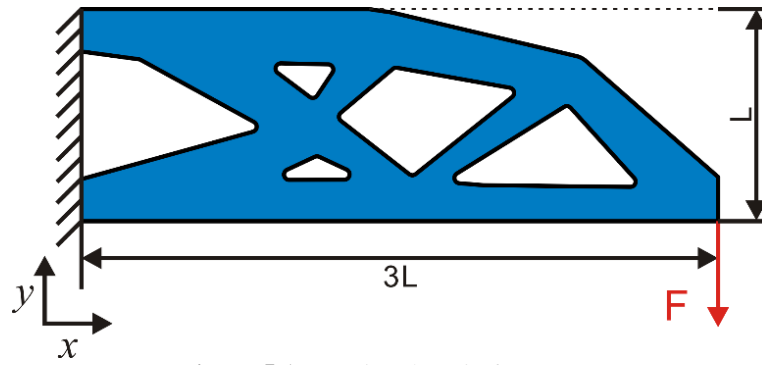
Figure 5.17. Design domain for case 1.

Table 5.2. Parameters used in the cantilever beam problem.

Option	Description
Population size	20
Generations	100
Force (F)	100 N

According to the proposed toolpath configuration method, random seed nodes are uniformly generated in the TO result. Subsequently, Voronoi cells are determined based on the distribution of seed nodes via the Voronoi tessellation algorithm. Then, different scanning strategies, c_i and z_i, are arranged to infill within the Voronoi cells. The initial parameter of the proposed method is set as: population size, 20; stop criterion of the optimization, 100 generations. The Pareto-optimal solutions obtained for the optimization problem are indicated in Figure 5.18. Each point on the Pareto front represents a design shape for the corresponding volume ratio.
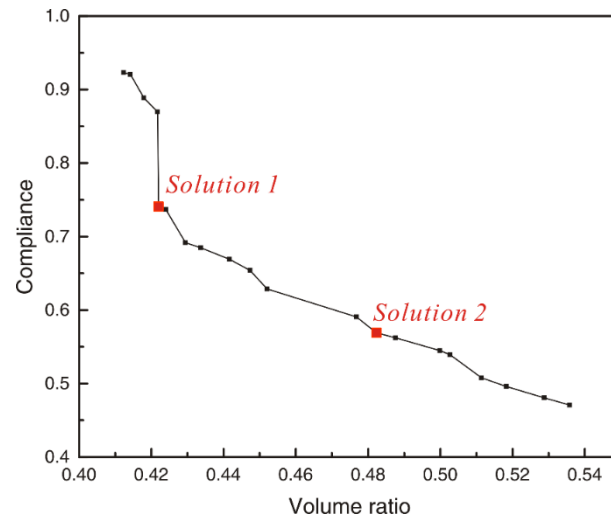
Figure 5.18. Pareto-optimal solutions for the toolpath configuration design method.

Figure 5.19 shows two solutions in the Pareto front. Figure 5.19(a) and (c) present the two topology shapes, the corresponding toolpath configurations are recorded in Figure 5.19(b) and (d), respectively.
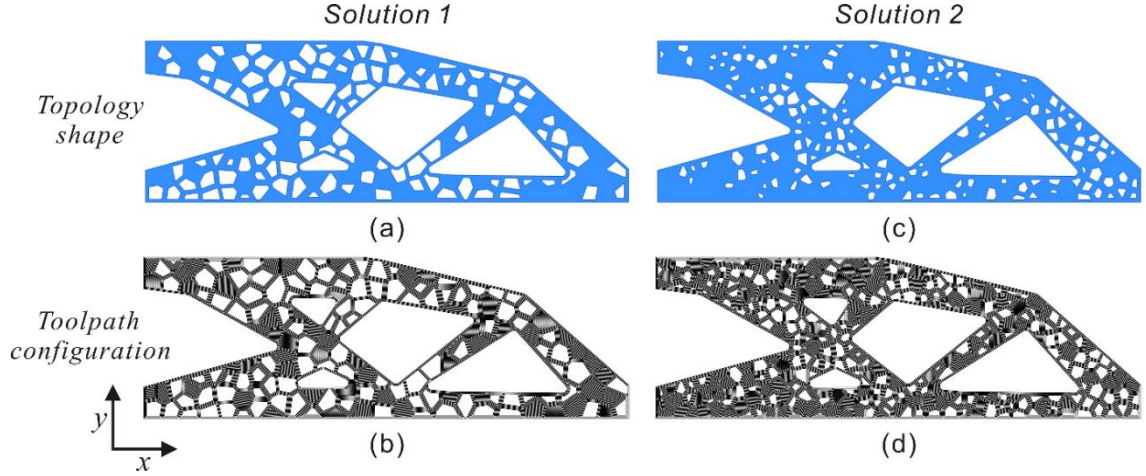
Figure 5.19. Two solutions in the Pareto front: (a). Topology shape of solution 1; (b). Toolpath configuration of solution 1; (c). Topology shape of solution 2; (d). Toolpath configuration of solution 2.

5.2. A knowledge-based toolpath constructive design method for high-precision graded TPMS structures

5.2.1. Method overview

Current part-scale lattice design methods cause accuracy loss and manufacturability uncertainty in AM preparation stages. STL model conversion and slicing can lead to loss of shape accuracy and sur-face quality, while unqualified toolpaths may cause printing failures, e.g. pores or re-melting in powder-bed fusion process. Moreover, all these steps are time-consuming due to large size of model file. Different from the traditional CAD-STL-Slice-Toolpath modeling, the proposed method uses solid-free modeling method to generate toolpath configuration directly. Figure 5.20 shows the proposed knowledge-based toolpath configuration method for designing graded TPMS-based porous structures.
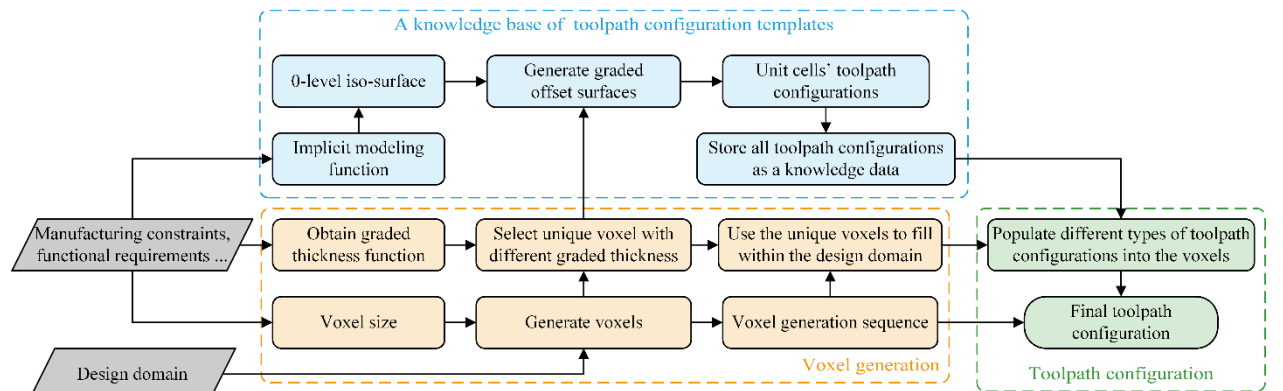
Figure 5.20. Flowchart of the proposed knowledge-based toolpath constructive method for designing graded TPMS-based porous structures.

The proposed method has three modules to manage the toolpath configuration. First, a given design domain is decomposed into voxels based on certain requirements, e.g. manufacturing constraints or functional requirements, as shown in Figure 5.21. Here, we suppose that all voxels have the same size and are filled with the same type of lattice unit cell. In this process, the fabrication sequence can be also defined to facilitate the toolpath configuration for voxels in different positions. Then, according to the graded thickness, unique voxels with different graded thickness information are selected to serve for graded offset surfaces generation.
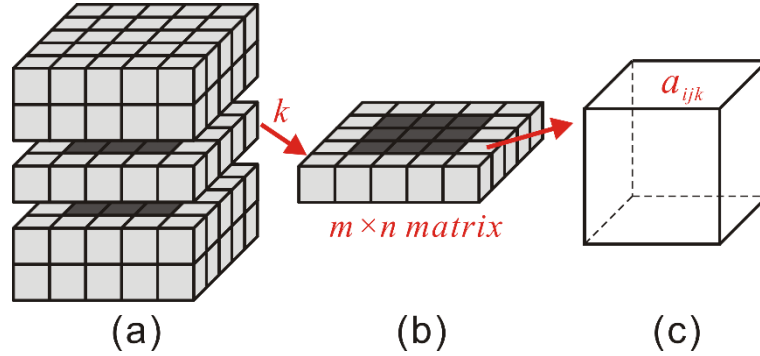
Figure 5.21. Voxel decomposition process: (a). Voxel representation in three-dimensional matrix; (b). A two-dimensional matrix; (c). A voxel a_{ijk} .

In the module of the knowledge data for unit cells' toolpath configuration, an implicit function is used to create 0-level iso-surface via the Marching Cubes (MC) algorithm [170]. According to thickness information of different voxels, offset surfaces are built by using different distance field functions. Then, toolpaths are populated into the area between two offset surfaces directly. Moreover, different types of toolpath patterns are utilized to infill the slice contours. At the same time, jump path can be also defined in the toolpath configuration. Finally, these toolpath configuration units are as infilling templates, filling knowledge units, which can be selected to infill the voxels.

In the third module, the toolpath information stored in the templates is selected to populate for repro-duction into the voxels (a_{ijk}) of different positions. In addition, the scanning sequence and path of mul-tiple lasers can also be assembled into the output file of final toolpath configuration. By using the pro-posed knowledge-based toolpath configuration method, computational time and memory can be saved significantly.

5.2.2. TPMS structure generation

As a type of implicit surface, TPMS structures have a precise parametric form, known as the Enneper-Weierstrass formula [143, 171]. The coordinates of the surfaces can be described as:

$$\begin{cases} x = \mathrm{Re}\left(e^{i\theta}\int_{\varpi_0}^{\varpi}\left(1-\tau^2\right)R(\tau)d\tau\right) \\ y = \mathrm{Re}\left(e^{i\theta}\int_{\varpi_0}^{\varpi}i\left(1+\tau^2\right)R(\tau)d\tau\right) \\ z = \mathrm{Re}\left(e^{i\theta}\int_{\varpi_0}^{\varpi}2\tau R(\tau)d\tau\right) \end{cases}$$

(5-

Where $i^2 = -1$, $\tau = \tau_a + i\tau_b$, θ is the Bonnet angle and $\mathrm{Re}(x)$ returns the real part of function x [171]. For three common surfaces, Schwarz Primitive, Diamond and Schoen Gyroid, the Bonnet angle are $90°$, $0°$ and $38.0147°$, respectively. The relation associates the Weierstrass function $R(\tau)$ with a unique surface $r(\tau_a, \tau_b)$ which is ensured to be minimal [171]. The Weierstrass function for the three common TPMS unit cells is expressed by:

$$R(\tau) = \frac{1}{\sqrt{\tau^8 - 14\tau^2 + 1}}$$

(5-

The implicit method uses a single-value function of three variables to describe approximated TPMS with periodic surfaces [171]. The most commonly TPMS structures, P, D, G, I-WP and F-RD surfaces, can be expressed by the following nodal equations:

$$\begin{aligned} \phi_P(x,y,z) &= \cos(\omega x) + \cos(\omega y) + \cos(\omega z) = C \\ \phi_D(x,y,z) &= \cos(\omega x - \omega y)\cos(\omega z) + \sin(\omega x - \omega y)\sin(\omega z) = C \\ \phi_G(x,y,z) &= \cos(\omega x)\sin(\omega y) + \cos(\omega y)\sin(\omega z) + \cos(\omega z)\sin(\omega x) = C \\ \phi_{I-WP}(x,y,z) &= 2\left[\cos(\omega x)\cos(\omega y) + \cos(\omega y)\cos(\omega z) + \cos(\omega z)\cos(\omega x)\right] \\ &\quad -\left[\cos(2\omega x) + \cos(2\omega y) + \cos(2\omega z)\right] = C \\ \phi_{F-RD}(x,y,z) &= 4\cos(\omega x)\cos(\omega y)\cos(\omega z) \\ &\quad -\left[\cos(2\omega x)\cos(2\omega y) + \cos(2\omega y)\cos(2\omega z) + \cos(2\omega z)\cos(2\omega x)\right] = C \end{aligned}$$

(5-

Where x, y, z are the spatial coordinates, $\omega = 2\pi/l$ and L is the size of the lattice unit cell, C can control the surface expansion. The surface Γ, a zero-level set of Φ, represents the interface regions which divide the unit cell into two distinct spaces. Figure 5.22 shows the three TPMS structures accomplished with the polygonization of Γ by using the MC algorithm.
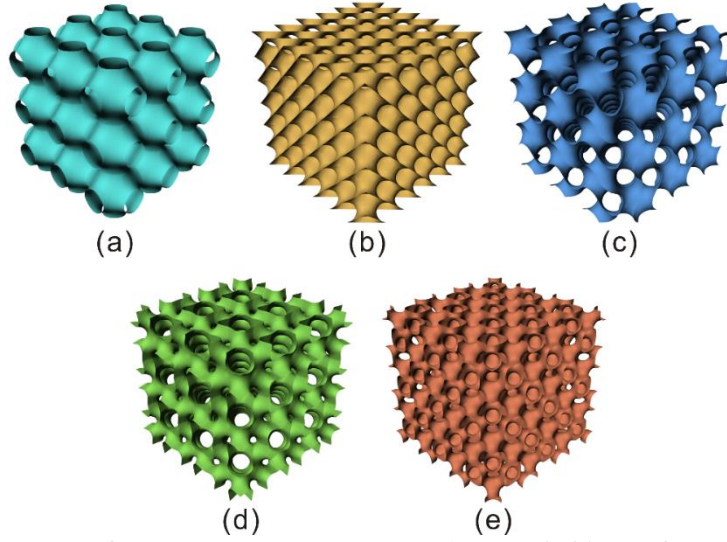
Figure 5.22. Different types of TPMS structures (3*3): (a). Schwarz Primitive surface; (b). Schwarz Diamond surface; (c). Schoen Gyroid surface; (d). I-WP surface; (e). F-RD surface.

In order to explain the 3D MC algorithm, the MS algorithm in 2D is illustrated in Figure 5.23. The MS algorithm is used to provide a piecewise-liner approximation to a 2D object [172]. To describe an implicit function, the design domain is divided into a 2D grid. Each nodes of the grid can be calculated by the implicit function. Figure 5.23(a) enumerates all 16 intersection situations, which show the representations of all lines in the 2D space. Hollow and solid points indicate the position of the grid nodes inside and outside of the 0-iso-line, respectively. The linear interpolation method is usually applied to draw the lines. Take the square in Figure 5.23(b) as an example, four nodes satisfy $f(p_1) < 0$, $f(p_2) > 0$, $f(p_3) < 0$, $f(p_4) < 0$ with $f(p)$ being the value of the implicit function on each node. To extract the line from the square, valid grid edges need to be detected. For a valid edge, the grid nodes p_i and p_{i+1} should satisfy the following:

$$f(p_i)f(p_{i+1}) < 0 \tag{5-9}$$

Hence, two valid edges in Figure 5.23(b) are $p_1 p_2$ and $p_2 p_3$. The intersection P can be calculated via the linear interpolation approach as:

$$f((1-\alpha)p_i + \alpha p_{i+1}) = 0 \tag{5-}$$

Based on the intersection situations of the MS algorithm, the connection of all intersection P can be determined to construct an approximate 0-iso-line. The resolution of the grid can be improved to obtain a high-precision 0-iso-line.
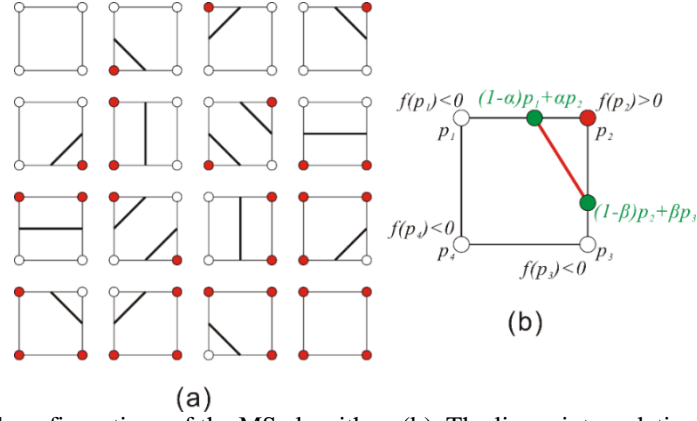
Figure 5.23. (a). All configurations of the MS algorithm; (b). The linear interpolation method for a square.

5.2.3. Graded offset surfaces generation for two types of TPMS unit cells

In this subsection, a MC-based distance field method is proposed to generate graded TPMS offset surfaces. First at all, an example implicit cylinder ($x^2 + y^2 - 9 = 0$) is generated via MC algorithm in Figure 5.24. For grid points with iso-surface values greater than zero, these points lie outside of the circle. All those with negative values lie inside of it. In order to generate an offset surface, a distance field is used to measure the distance between grid points and the mesh surface. The distance field can be described by the following equation [173]:

$$f(p) = dis(p, \partial H) - r$$

Where p are the grid points and H is the given cylinder generated by the MC algorithm. The distance field represents the minimum distance from these grids to the given model. For these points outside H, the function will return the distance with positive. The distance values are seen as negative for these points inside. Hence, the offset value r can be either negative or positive.
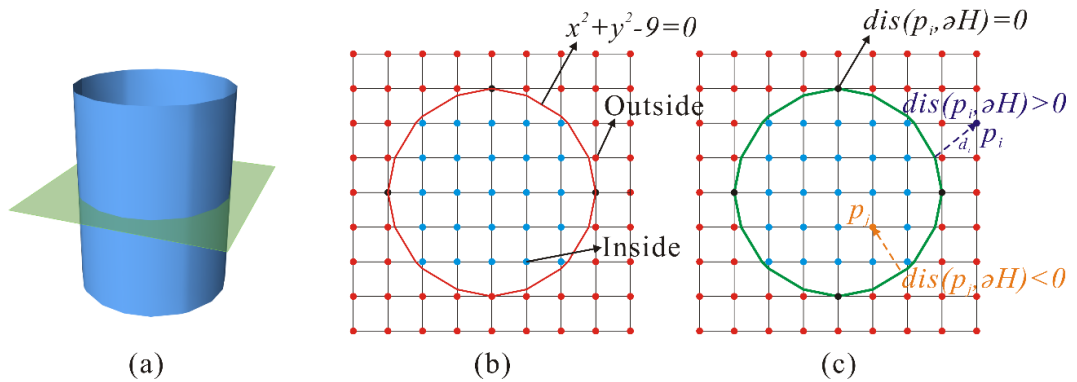
Figure 5.24. An implicit cylinder generation using the Marching Cubes algorithm in 2D.

155

To explain it easily, Figure 5.25 show the generation of the inside and outside offset cylinder in 2D. To generate an offset cycle, an offset value is needed to calculate the distance field. Here, the offset value is set as $r = \pm 1$. The distance field is computed to return the MC algorithm. Two offset circles in 2D are shown in Figure 5.25.
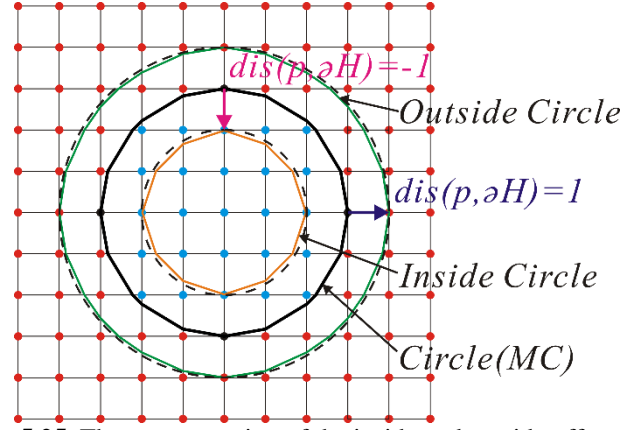
Figure 5.25. The representation of the inside and outside offset circles.

The distance filed function can also be used to generate a graded offset surface by describing a thickness field based on geometry information. For example, a distance field of deformed circles can be expressed as:

$$f(p) = dis(p_i, \partial H) \pm (\frac{p_i^x}{6} + 1)$$

(5-

Where p_i^x is the x-axis coordinate of point p_i. Figure 5.26 shows two graded offset circles via a graded thickness filed. Hence, the proposed method can be also applied to generate offset TPMS surfaces.
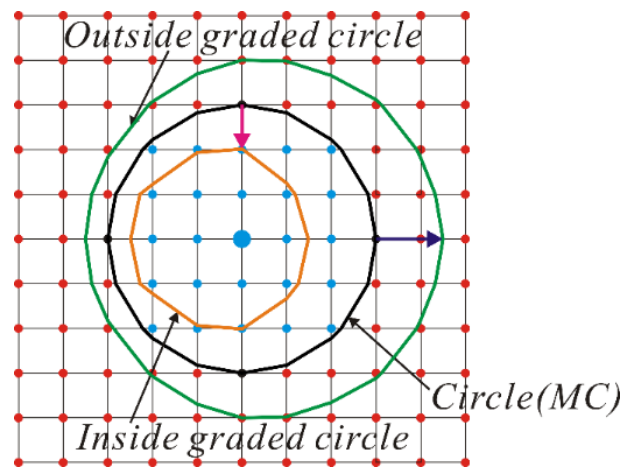
Figure 5.26. Graded offset circles generation.

By controlling the resolution of MC algorithm, the precision of graded offset surfaces can be improved. To describe the impact of resolution, a sphere is represented by the implicit expression. The mathematical expression can be defined by:

$$f(S) = \sqrt{x^2 + y^2 + z^2} - R$$

Where x, y, z are the spatial coordinates and R represents the radius of the sphere. Figure 5.27 shows different spheres with different resolutions. The radius is defined as 3 mm.
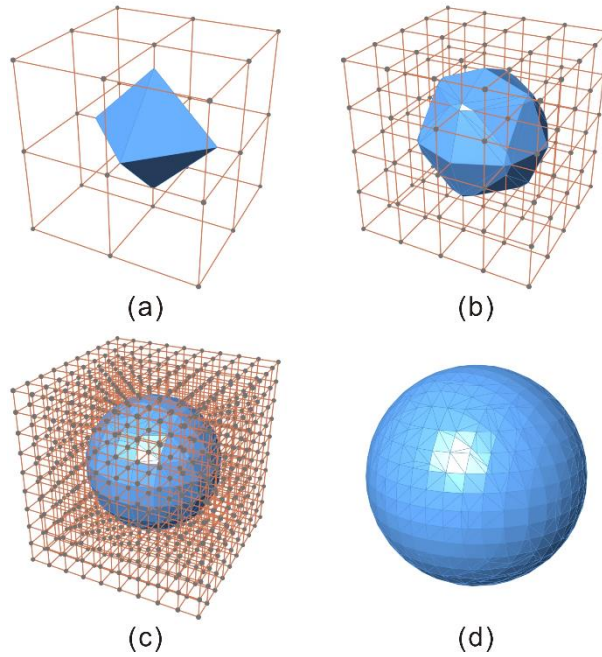
Figure 5.27. Different spheres with different resolution setting: (a). resolution = 3; (b): resolution = 5; (c). resolution = 10; (d). resolution = 20.

Two types of TPMS unit cells, Schwarz P and G surfaces are used to generate offset surfaces inside and outside for implicitly designing graded high-precision TPMS structures. The size of voxel bounding the TPMS unit cell is $2 \times 2 \times 2 \, mm$. To generate a graded P and G surfaces, two graded thickness function are given in the following:

$$t_z^P = \pm \frac{1}{10} \left(2\sin \frac{\pi(p_z + 1)}{4} + 1 \right), \ (-1 \le p_z < 1)$$

$$t_z^G = \pm \frac{1}{10} \left(\sin \left(\frac{\pi(p_z + 1)}{4} \right) + 1 \right), \ (-1 \le p_z < 1)$$

Where t_z^P, t_z^G is the offset distances for the standard P and G surfaces, respectively. p_z represents the coordinate value of points on the standard P and G surfaces. The MC algorithm is applied to generate

the standard P and G surfaces with the $60 \times 60 \times 60$ resolution. Figure 5.28 and Figure 5.29 show the three kinds of P and G surfaces and their combination, respectively.
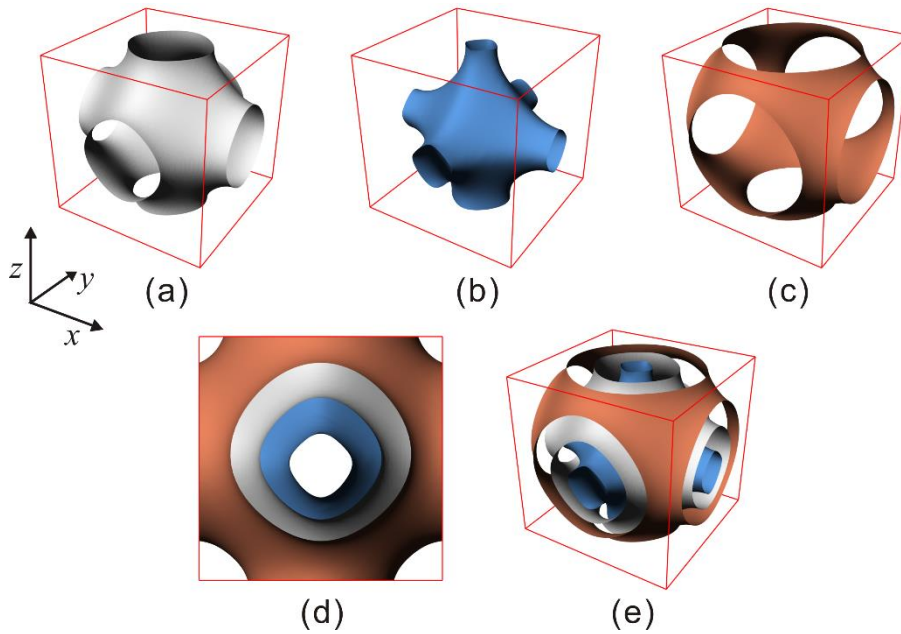
Figure 5.28. Graded offset P surface generation: (a). Standard P surface; (b). Inside offset surface; (c). Outside offset surface; (d). Front view of the three surfaces; (e). Perspective view.
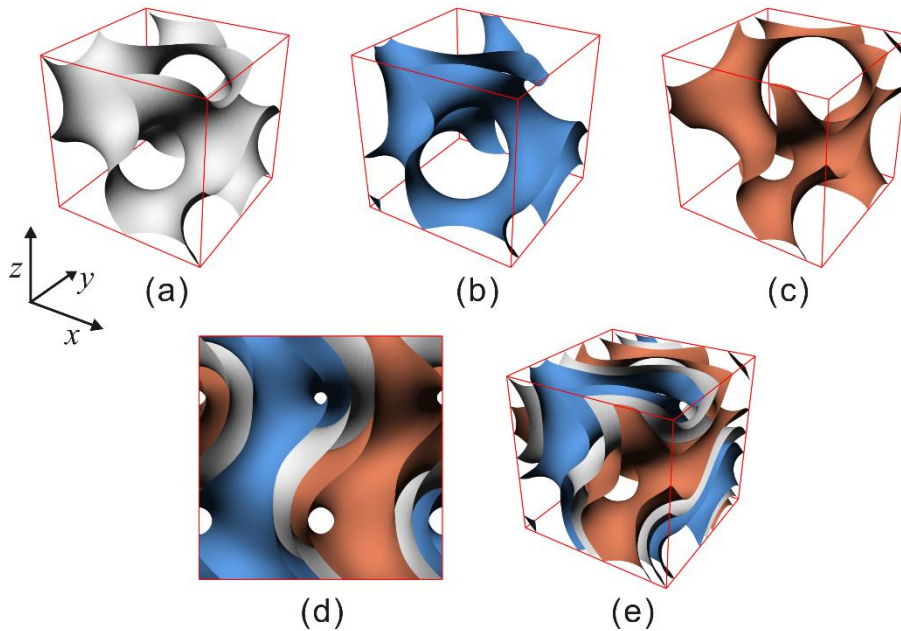
Figure 5.29. Graded offset G surface generation: (a). Standard G surface; (b). Inside offset surface; (c). Outside offset surface; (d). Front view of the three surfaces; (e). Perspective view.

5.2.4. Toolpath infill for graded offset surfaces

As mentioned above, the MC based distance field can construct offset surfaces with different gradients for a TPMS unit cell. To save computing time and memory, a toolpath configuration method is devel-

oped in this subsection. The proposed method allows us to slice offset surfaces directly. Different types of scanning strategies can be applied in the slices. In addition, unqualified slices are converted to be qualified by rotation and translation operations. Figure 5.30 give a workflow of the toolpath configuration generation method for a graded TPMS-based unit cell example.
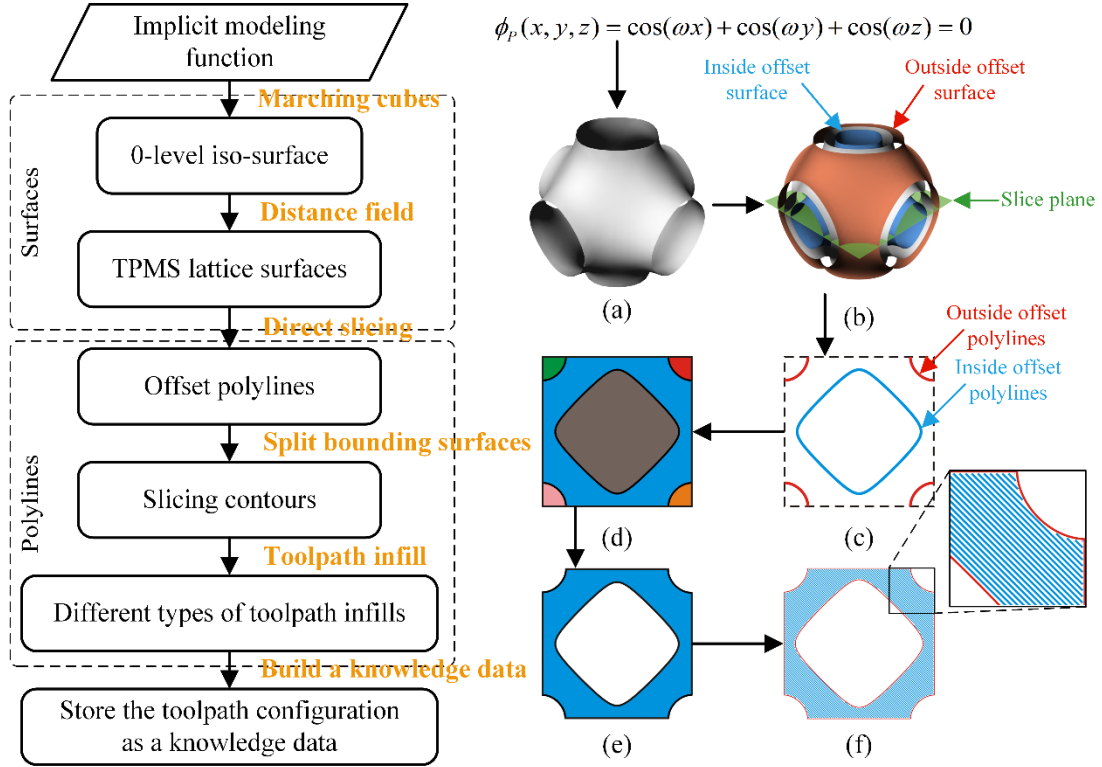
Figure 5.30. Workflow of toolpath configuration generation for a graded TPMS-based unit cell example.

By using the MC-based distance field, graded offset surfaces are obtained. The surface precision can be adjusted by changing the resolution of x, y, z in the voxel. Figure 5.30(b-f) show the main steps of the direct slicing method. A slice plane in Figure 5.30(b) is applied to slice the offset surfaces. The distance between two adjacent slice planes should respect the layer thickness. Two kinds of intersection polylines, called outside and inside offset polylines, are obtained to split the bounding surface in Figure 5.30(c, d). The surface enclosed by the two intersection polylines is the slicing contour. Different types of toolpaths can be used to populate within the slicing contour. To ensure the manufacturability of the contour toolpath, the MS algorithm is used to generate intersection-free contours [173]. The detailed method can be seen in Figure 5.25. Noticed that resolution should respect the following expression to ensure the qualified intersection-free contour generation in Figure 5.31.

$$L \leq n \frac{d}{2}$$

Where L is the size of the voxel, n represents the resolution of the MS algorithm, and d is the hatch spacing of an AM processing. In Figure 5.30(f), a contour pattern is used to scan the boundary of the slice contour and parallel-vector toolpath is filled within the contour pattern. This combined toolpath configuration is more suitable for the island scanning technique.
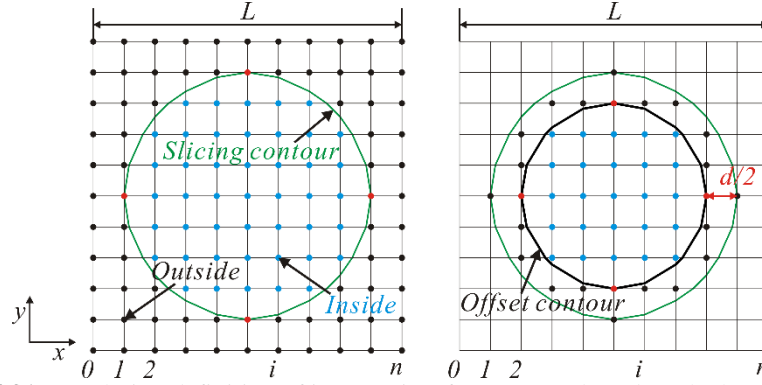
Figure 5.31. Resolution definition of intersection-free contour based on the hatch spacing.

5.2.4.1. Direct toolpath infill for offset surfaces

In this section, two types of TPMS unit cells, Schwarz P surface and OCTO surface are used to generate toolpath configurations directly for implicitly designing graded high-precision TPMS structures. Table 11 gives a process parameter definition.

Table 5.3. Process parameter definition.

Voxel size L (mm)	Layer thickness t (μm)	Hatch spacing d (μm)
2*2*2	20	30

Offset surfaces inside and outside are sliced directly based on the layer thickness. The slicing model of graded P structure is shown in Figure 5.32.
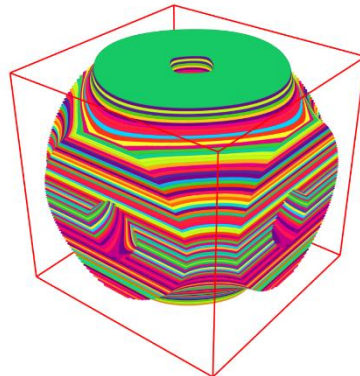
Figure 5.32. The slicing model of graded P structure.

Two parallel-vector scanning strategies, island and continuous strategies, are applied to construct tool-path configurations for the graded P structure. Figure 5.33 presents the two parallel-vector techniques with island and non-island scanning modes. A $90°$ rotation with x axis in scan orientation is performed after each layer. For the island scanning mode, unjoined toolpath configurations are filled within the voxel directly. For the parallel-vector technique, the toolpaths of mutual contact between two adjacent voxels are joined together, as shown in the right of Figure 5.33.
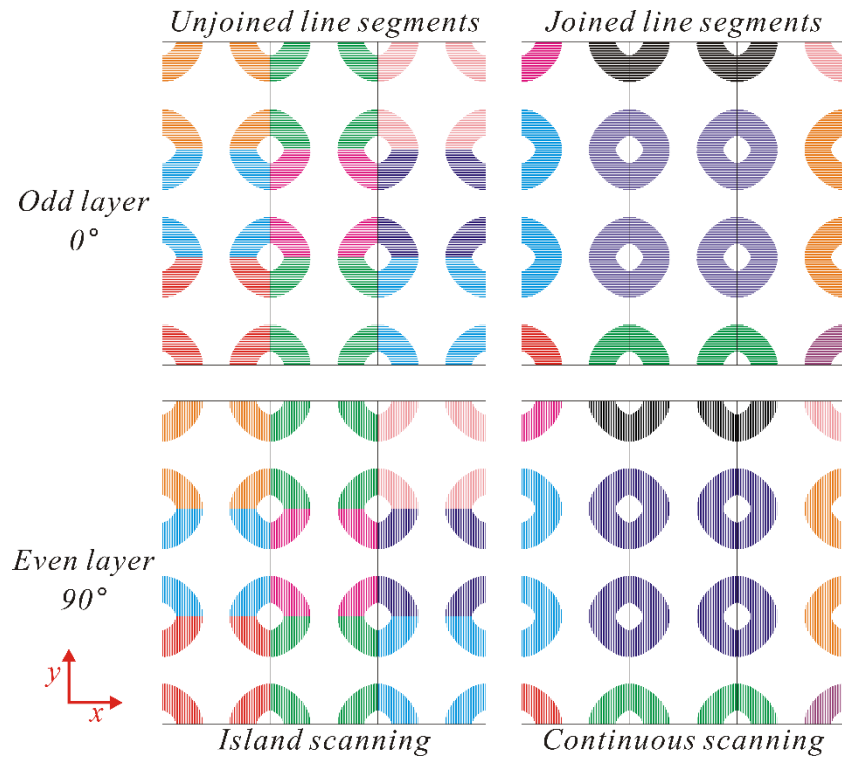
Figure 5.33. Two parallel-vector scan strategies of the alternative layers

In addition, the contour scan is also performed in the toolpath configuration. Figure 5.34 presents the toolpath in the layer 24 and 25. A $67°$ rotation with initial angle $45°$ is conducted in this scanning mode.

Layer 24   Layer 25
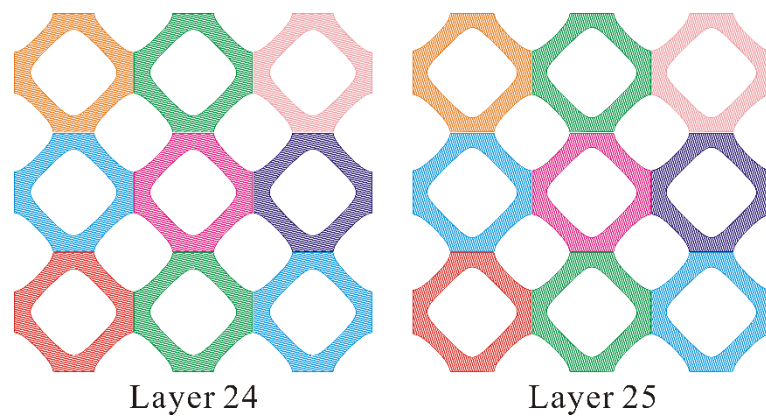
A more complex TPMS unit cell, Schoen OCTO surface, is applied to generate a graded TPMS structure. The mathematical function is described as:

$$\phi_{OCTO}(x, y, z) = 4 \times \big(\cos(\omega x)\cos(\omega y) + \cos(\omega y)\cos(\omega z) + \cos(\omega z)\cos(\omega x)\big)$$
$$-2.8 \times \cos(\omega x)\cos(\omega y)\cos(\omega z) + (\cos(\omega x) + \cos(\omega y) + \cos(\omega z)) + 1.5 = C$$

(5-17)

A graded thickness function is utilized in the OCTO surface as follows:

$$t_z^{OCTO} = \pm \frac{1}{20}\left(2\sin\frac{\pi(p_z + 1)}{4} + 1\right), \ (-1 \le p_z < 1)$$

(5-

Figure 5.35 shows the graded offset surfaces of standard OCTO surface and its slicing model. The resolution of the MC algorithm is defined to $100 \times 100 \times 100$. The voxel size is $2 \times 2 \times 2$ mm.

(a)   (b)
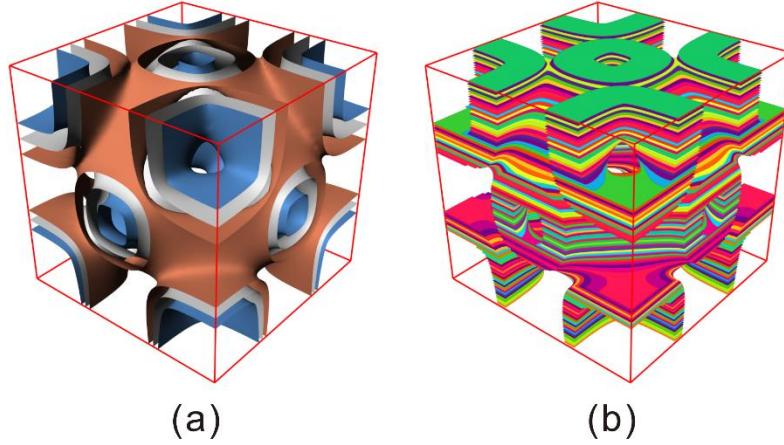
Figure 5.35. Graded offset surfaces and slicing model of OCTO surface.

Three scanning strategies, island with parallel-vector, parallel-vector and island with combined scans are used to generate toolpath configurations for the graded OCTO unit cell. The three strategies are presented in Figure 5.36.

Island scan model   Parallel-vector scan model   Island model with combined scans
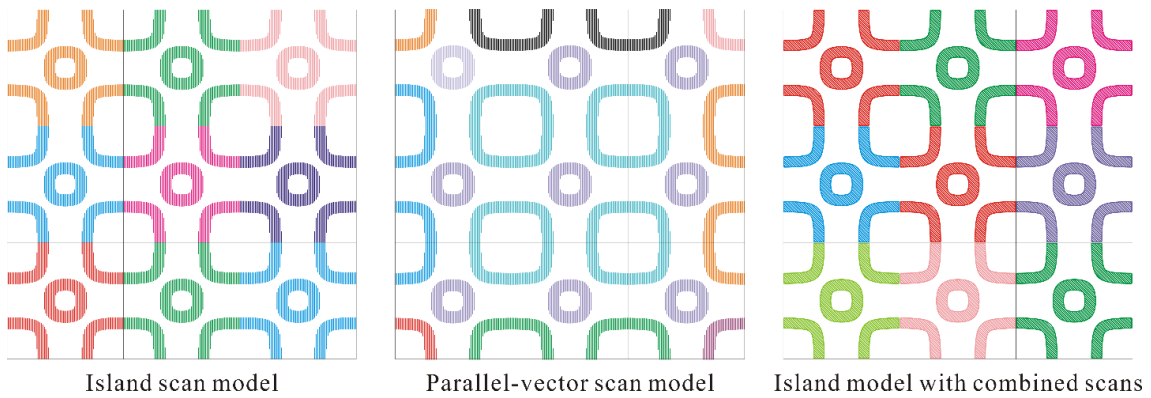
Figure 5.36. Three scanning strategies with $90°$ related to the x-axis.

The island scanning strategy with contour and parallel-vector modes to construct toolpath configurations for the two graded TPMS structures as shown in Figure 5.37. Toolpaths in different layers are also shown in the figure.
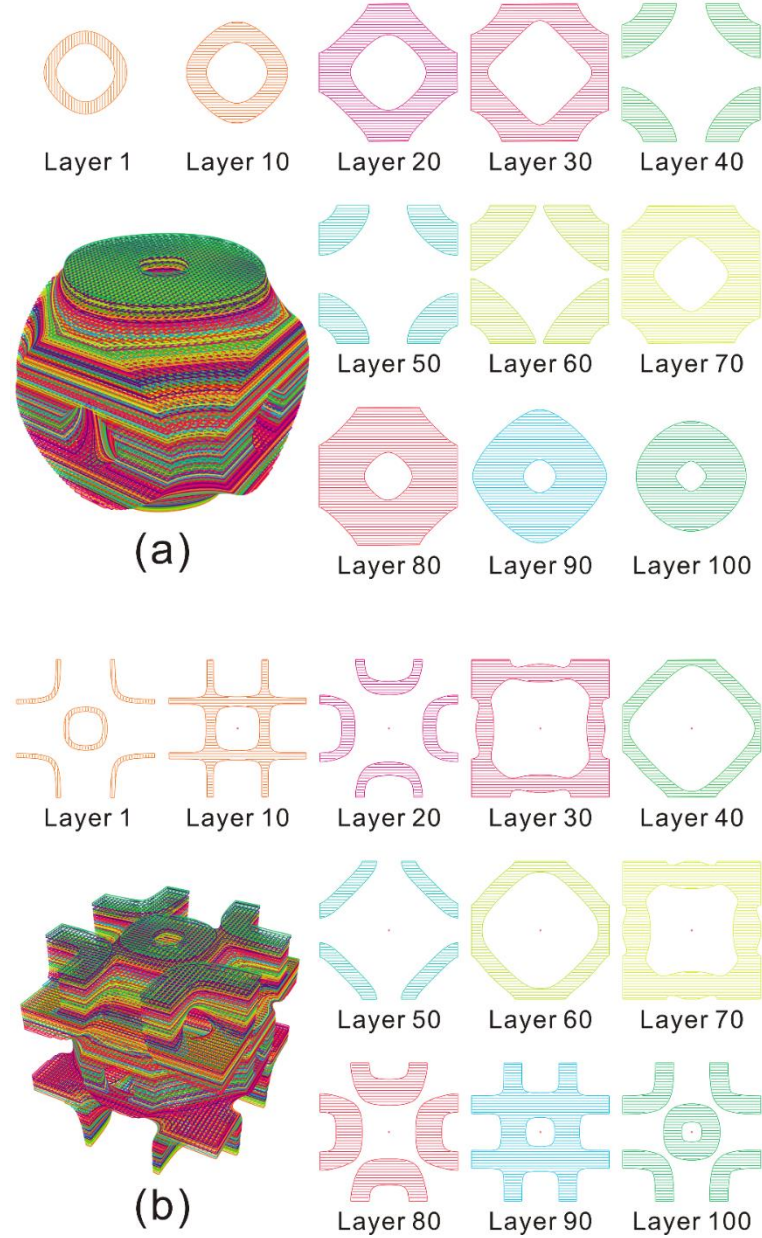
Figure 5.37. Two toolpath configurations for graded P and OCTO structure unit cells: (a). Toolpath configuration of the graded P structure; (b). Toolpath configuration of the graded OCTO structure.

To assemble a final toolpath configuration of a part-scale graded structure, Figure 5.38 shows a graded toolpath configuration assembly along z direction.

(a)   (b)   (c)   (d)
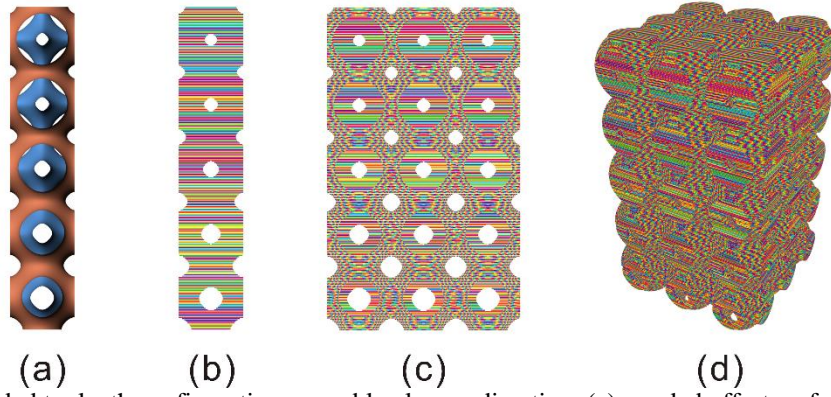
Figure 5.38. A graded toolpath configuration assembly along z direction: (a). graded offset surfaces; (b). graded toolpath configurations of unique voxels; (c). front view of the toolpath assembly; (d). perspective view of the assembly.

5.2.4.2. Indirect toolpath infill for offset surfaces

For certain offset surfaces, small slices will appear when generating slicing models. Figure 5.39 shows a toolpath configuration for a slice of G offset surfaces. In Figure 5.39(c), a small slice occurs in the slicing model. It is not easy to ensure a qualified toolpath for this kind of small slices. However, the small slice can be fused with adjacent slices. To make the small slice qualified, rotation operation is applied in Figure 5.40. First, the unqualified slice is recognized according to size constraint. The slice recognized is rotated around z_1 axis where it is located as shown in Figure 5.40(b). Then, the unqualified slice rotated is performed another rotation operation around the z direction of the voxel. Finally, the unqualified slice after rotation is merged with other slices at the same layer together, as shown in Figure 5.40(d).
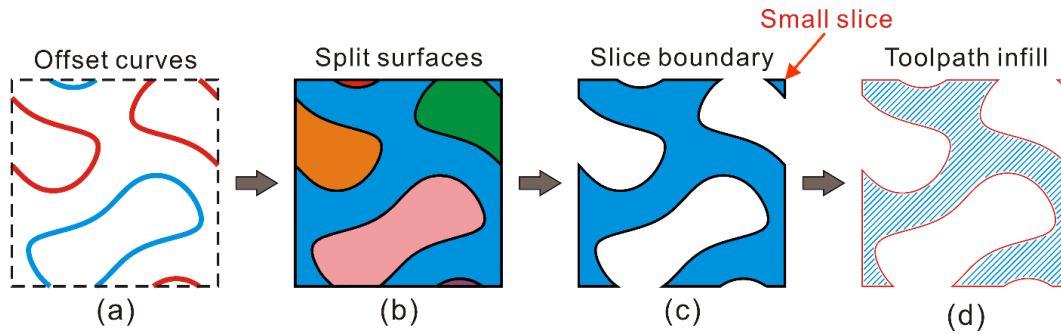
Figure 5.39. A toolpath configuration in a slice of a G offset structure: (a). Offset curves; (b). Split surfaces; (c). Slice boundary; (d). Toolpath infill.
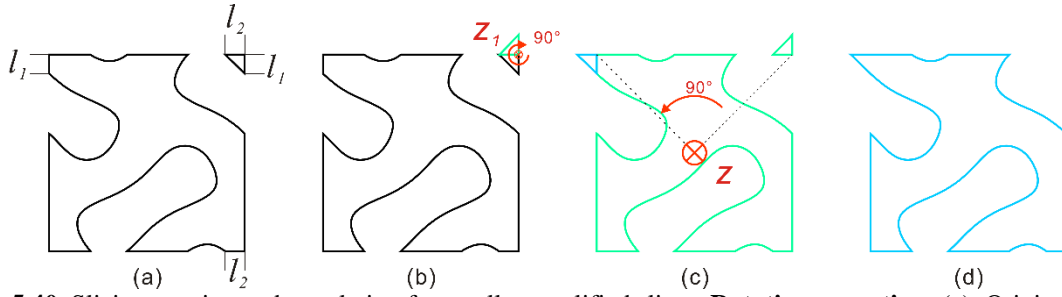
Figure 5.40. Slicing rotation and translation for small unqualified slices. **Rotation operation:** (a). Original slices; (b). The unqualified slice's rotation around z_1 direction; (c). Rotation around z direction; (d). Final qualified slice.

Figure 5.41(a) shows a 2×2 slice model used in Figure 5.40. Before merging, there are 8 slices in Figure 5.41(a). After fusing the small isolated slices with adjacent slices, four main slices left. Hence, small unqualified slices enable to be transformed by merging with connected qualified slices.
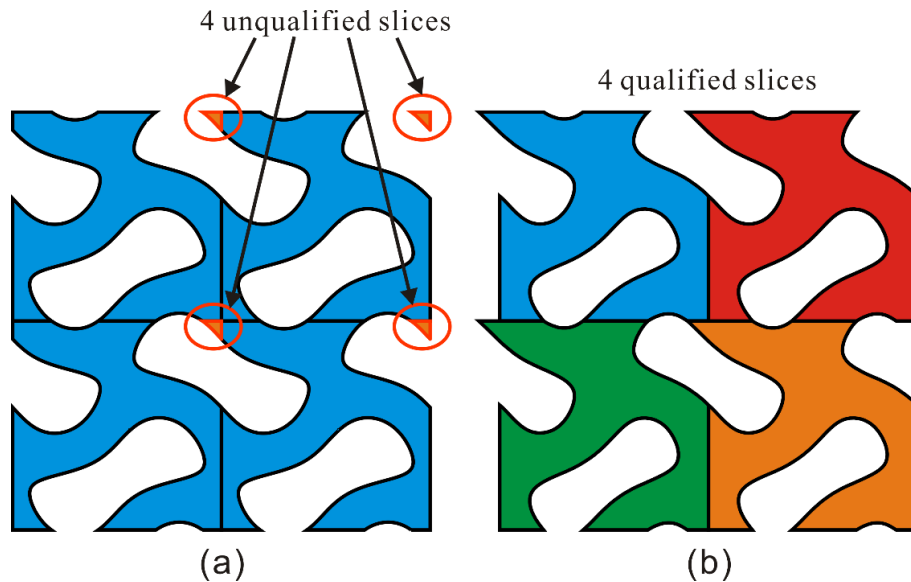
Figure 5.41. Slicing translation and rotation for a small unqualified slice: (a). 2×2 slicing configurations with 4 unqualified slices; (b). 2×2 transformed slicing configuration with qualified slices.

To make toolpath configuration of each voxel qualified, unqualified slices need to be transformed. Figure 5.42 shows a flowchart of qualified toolpath configuration for graded TPMS unit cells.
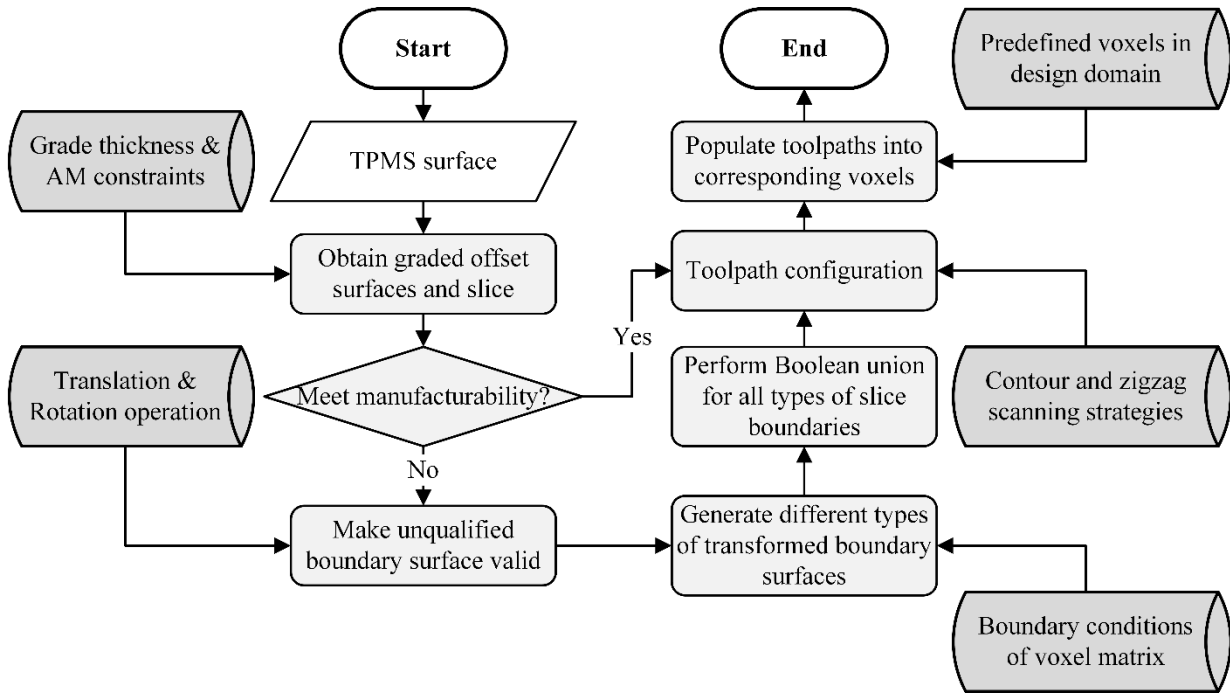
Figure 5.42. Flowchart of qualified toolpath configuration for graded TPMS unit cells.

The process starts with a standard TPMS unit cell. Offset surfaces inside and outside are obtained based on graded thickness information and AM constraints. Then, direct slicing is used to slice the offset surfaces inside and outside. Followed by Figure 5.42, the slicing model can be generated directly. Next, the manufacturability of the slicing model is analyzed based on AM constraints. Here, small slices are identified as shown in Figure 5.43.
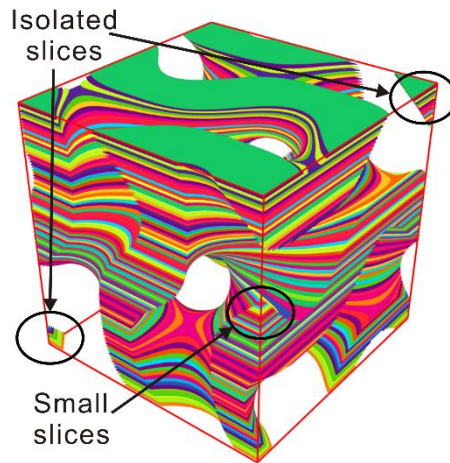
Figure 5.43. Small and isolated slices of the graded G unit cell.

By model rotation operation, the small and isolated slices unqualified are transformed to merge with the slices in the same layer. Figure 5.44 shows the transformation procedure of unqualified slicing model. First, slicing model is analyzed according to the AM constraints. Small and isolated slice sections are extracted as shown in Figure 5.44(a). The two kinds of slices are identified to unqualified slices. Figure

5.44(b) records these unqualified slices in two view. By model rotation operation in Figure 5.40, unqualified slices are transformed to fuse with slices in the same layer, as shown in Figure 5.44(c). Finally, a Boolean union operation is performed to combine unqualified slices with the adjacent qualified slices in the same layer. The final qualified slicing model is shown in Figure 5.44(d).
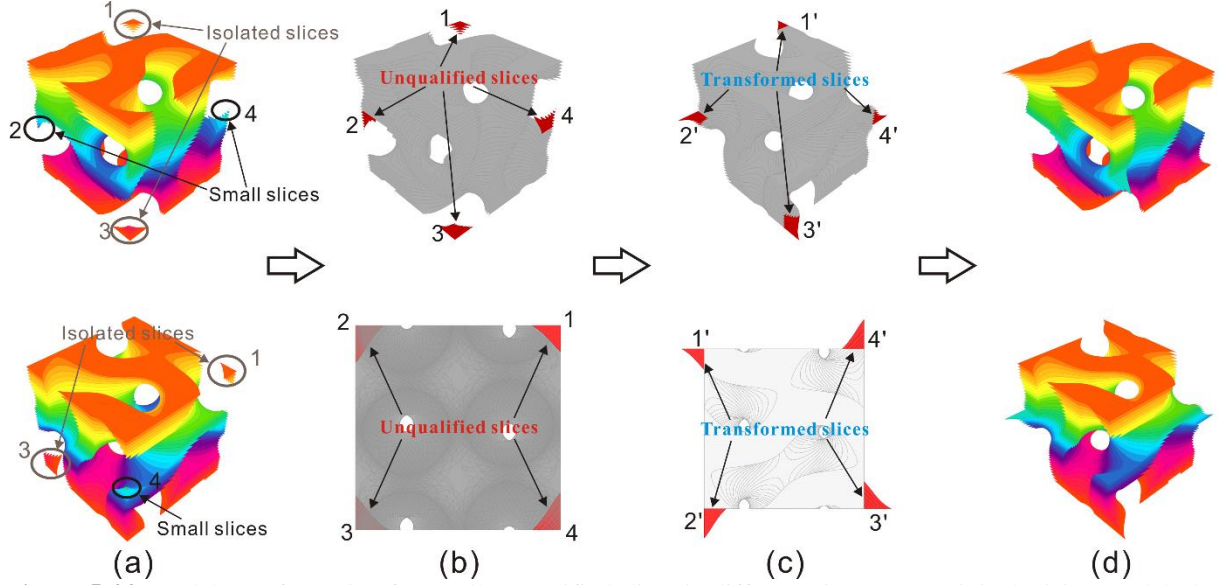
Figure 5.44. Model transformation for small unqualified slices in different views: (a). Original slicing model; (b). Identified unqualified slices; (c). Transformed slices; (d). The final qualified slice model.

In Figure 5.44(c), the transformed slices are arranged at the boundary of voxels. However, when the transformed slicing model is populated in the boundary of design domain, the transformed slices beyond the design domain need to be removed. A top view of boundary condition for a voxel is described in Figure 5.45.
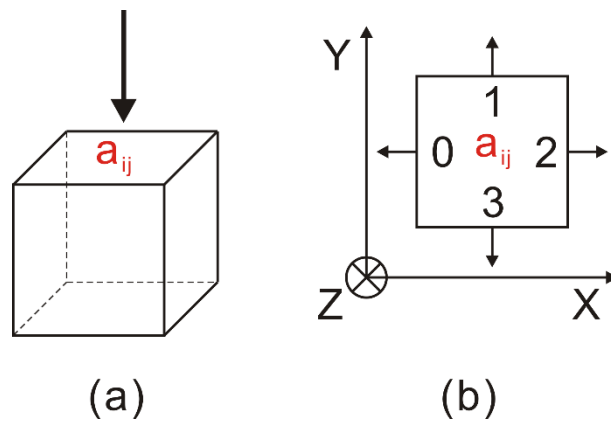
Figure 5.45. Boundary condition of a voxel from the top view.

According to the boundary condition of voxels in the design domain, the number of all types of transformed slicing models can be calculated as followed:

$$m = \sum_{i=0}^{4} C_4^i = C_4^0 + C_4^1 + C_4^2 + C_4^3 + C_4^4 = 1 + 4 + 6 + 4 + 1 = 16 \qquad (5\text{-}15)$$

Where m is the number of all transformation situation for unqualified slices. To describe all transformation situations of unqualified slices, four types of voxel matrix arrangements, $m \times n$, $m \times 1$, $1 \times n$ and 1×1, are summarized as followed. Figure 5.46 shows the $m \times n$ voxel matrix arrangement and different types of boundary condition representations.
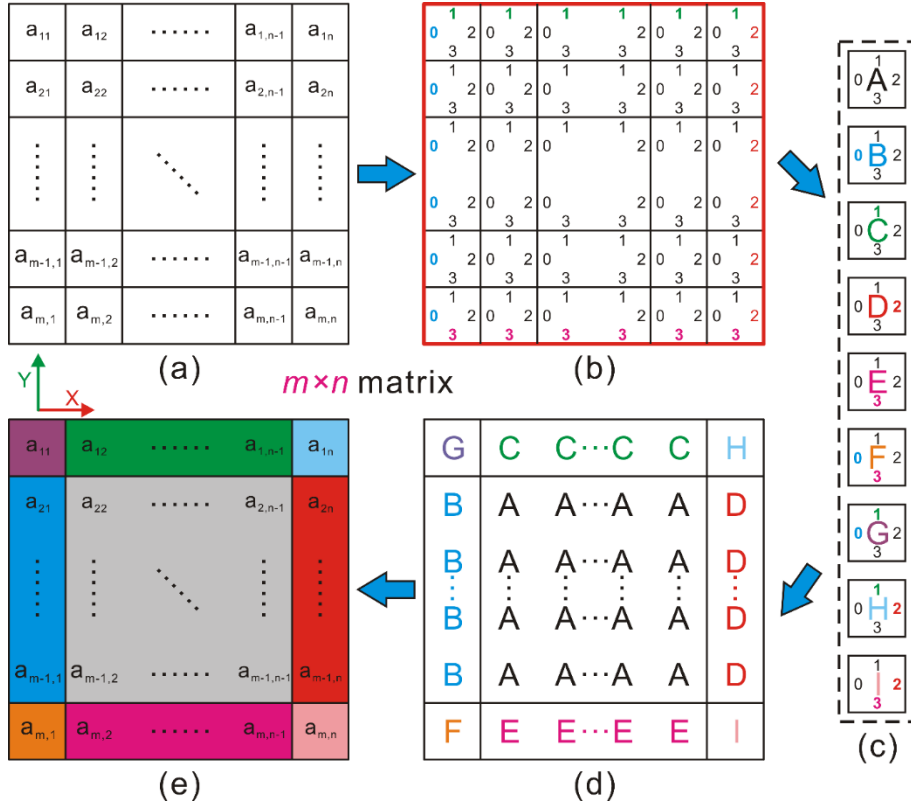
Figure 5.46. The $m \times n$ voxel matrix arrangement: (a). $m \times n$ voxel; (b). Boundary condition of the voxel matrix; (c). all types of boundary conditions A-I; (d). Project all types of boundary condition into voxel matrix; (e). Use different colors to present the voxel matrix.

In Figure 5.46(a), a $m \times n$ voxel matrix is presented. Based on the boundary representation in Figure 5.45, all voxels' boundaries at the boundary of design domain are presented in different colors as shown in Figure 5.46(b). All types of boundaries for all voxels are summarized in Figure 5.46(c). These unique boundary conditions with different colors are projected into voxel matrix as shown in Figure 5.46(d, e). By model translation and rotation operations, slice models and the corresponding toolpath configurations of the $m \times n$ voxel matrix are shown in Figure 5.47 and Figure 5.48. A one-layer contour scanning strategy with zigzag infill is applied to generate the toolpath configurations.
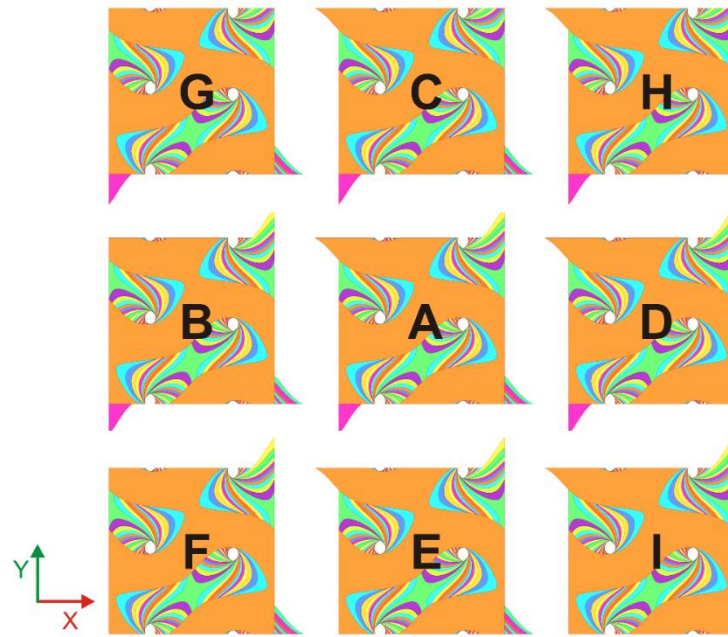
Figure 5.47. All slice models of the $m \times n$ voxel matrix.
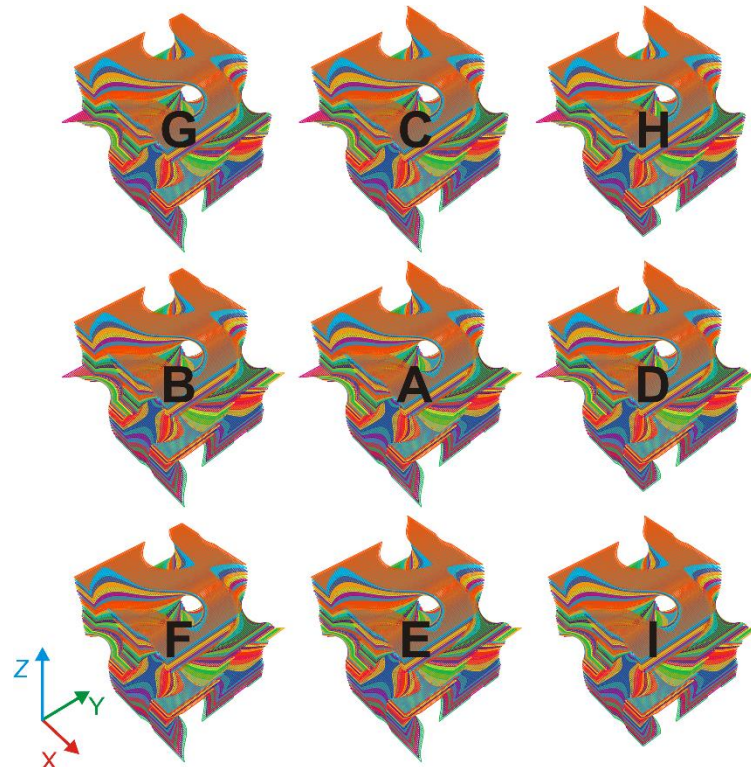
Figure 5.48. Toolpath configuration models of the $m \times n$ voxel matrix.

However, the $m \times n$ voxel matrix is not able to describe all voxels at the boundary of any design domain. Two other voxel matrix representations are shown in Figure 5.49. The corresponding boundary

169

condition of voxels are recorded in different colors. Figure 5.49(c) lists the recorded voxel representations.
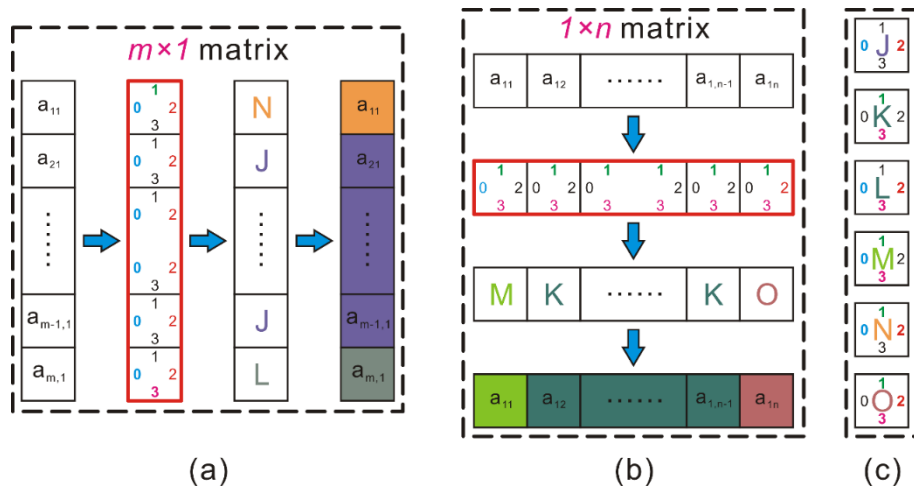
Figure 5.49. (a). The $m \times 1$ voxel matrix and different kinds of boundary condition representation; (b). The $1 \times n$ voxel matrix and different kinds of boundary condition representation; (c). All kinds of boundary conditions J-O.

Parallel scanning strategy with one-layer contour is also used to generate toolpath configurations for the recorded voxel representation in Figure 5.49(c). Figure 5.50 and Figure 5.51 show the corresponding toolpath configurations, respectively.
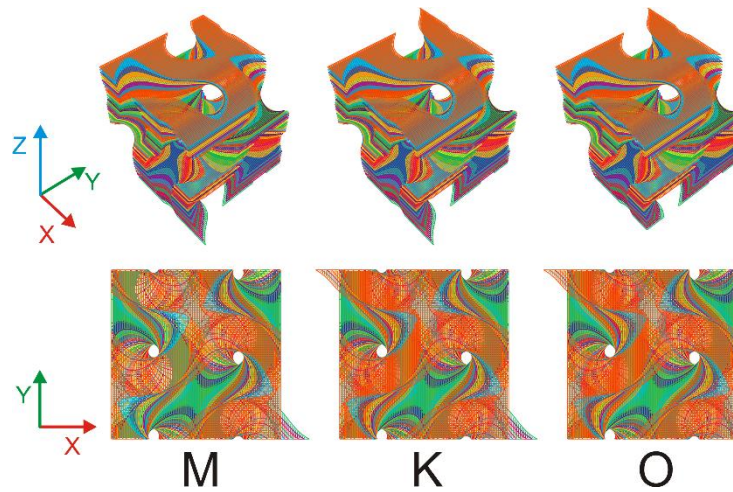
Figure 5.50. Toolpath configuration of the G unit cell in the $m \times 1$ voxel matrix.

170
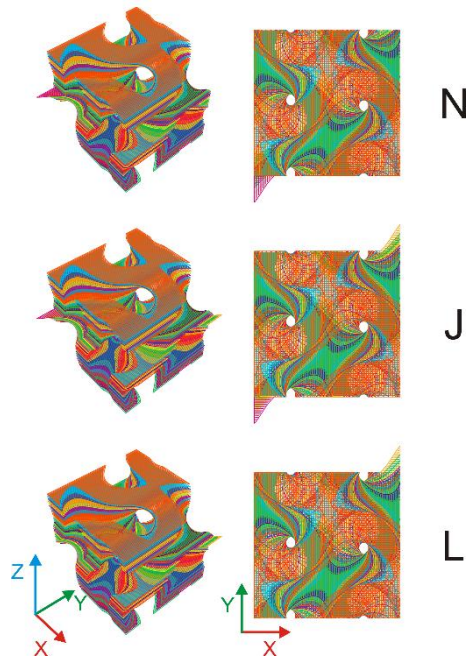
Figure 5.51. Toolpath configuration of the G unit cell in the $1 \times n$ voxel matrix.

To describe all voxel representations with different boundary condition, Figure 5.52 gives a voxel configuration. In the voxel configuration, all types of boundary conditions are summarized and all labels are marked at the voxels. All toolpath configurations are labeled using these symbols to achieve toolpath configuration automatically. A toolpath configuration in different layers for graded G structure is shown in Figure 5.53.
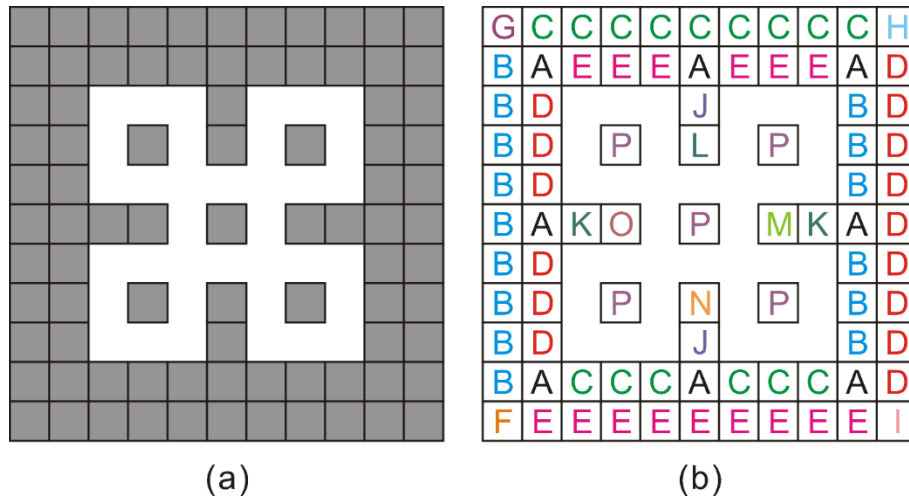
Figure 5.52. A voxel configuration with all types of boundary conditions: (a). Voxel matrix; (b). Voxel matric marked with different labels from A to P.
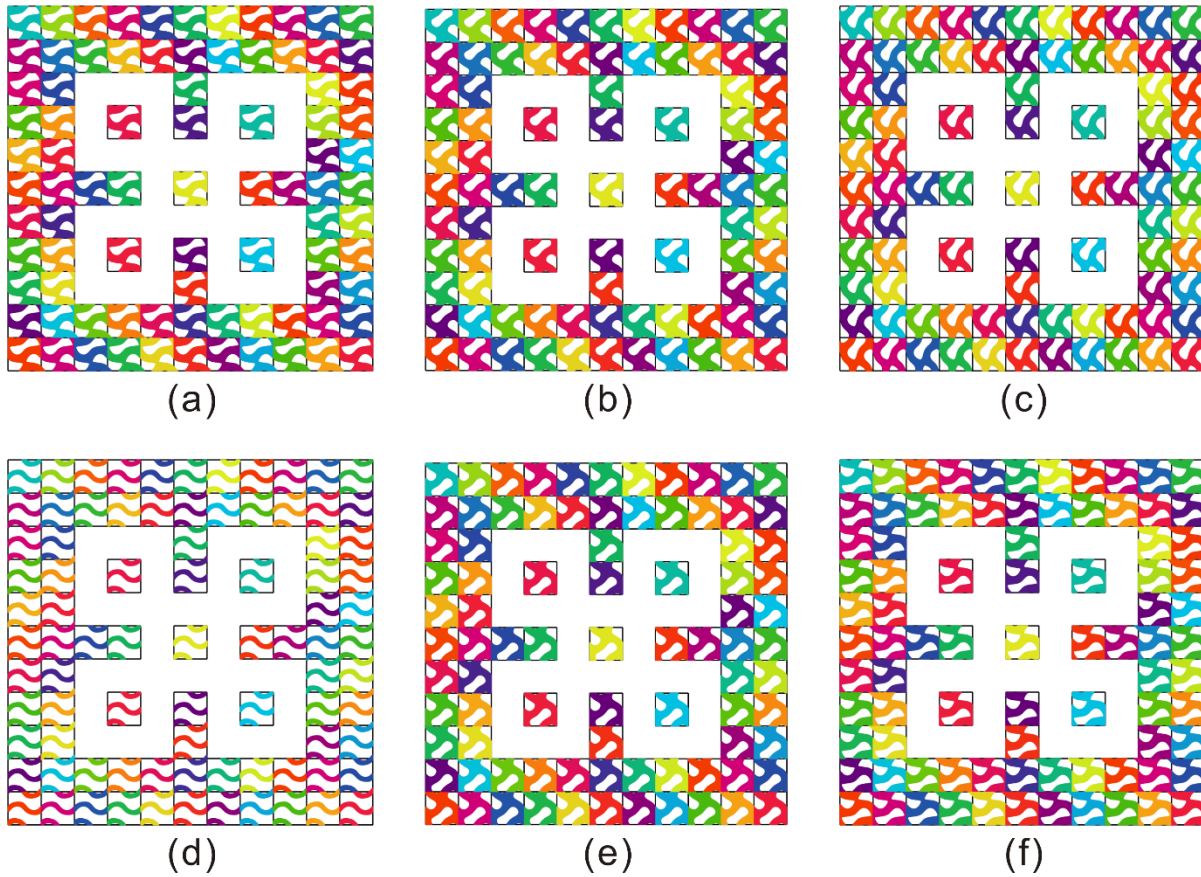
Figure 5.53. Toolpath configuration for different layers for the voxel configuration in Figure 5.46: (a). Layer 1; (b). Layer 5; (c). Layer 10; (d). Layer 20; (e). Layer 37; (f). Layer 40.

Taking into account that many part-scale lightweight structures with TPMS sheet usually use the same type and size lattice unit cell, the toolpath configuration for a single TPMS lattice unit cell can be seen as a knowledge data set, parametric template, stored in a knowledge-based system. Therefore, a set of toolpath configurations for graded TPMS unit cells can be predefined and stored in a knowledge base. It means that the proposed knowledge-based toolpath configuration method allows us to populate predefined toolpath configuration into voxels directly and generate 3D toolpath model to approaching the desired CAD model in an implicit way, which is similar to the proposed toolpath construction method in [146]. The objective of this kind of method is to build a processing model directly, toolpath model, to approach the explicit CAD model in an implicit way but with ensured manufacturability and save time and memory cost along the AM digital processing chain. To achieve different kinds of scanning strategies, the infilled toolpaths can be analyzed further with consideration of more AM constraints, e.g. heat diffusion and micro evolution of mechanical tomography and resulted properties. In current stage, due to limitation of accurate prediction models on thermal and properties, knowledge based method applies predefined toolpath pattern, as proposed in this research, can have positive meaning to ensure each voxel's volume building quality since all the predefined cellular scanning strategies and toolpaths can

be evaluated with experiments. However, there is still open question hard to answer. Cellular blocks may have accumulative effect/impact to the global part when designing big size components, especially for large metallic components printing. But for some other AM process that has not critical impact by the thermal effect, e.g. jetting process, the proposed method can result to much better printing qualities as compared to current AM design and preprocessing methods.

5.3. Summary

In this chapter, a toolpath configuration method is proposed to design Voronoi-based multi-topology lattice structures. The combination scanning strategy is developed to infill within modified Voronoi cells. For the combination strategy, multi-contour scanning is used to generate thickness-varying Voronoi lattice cells. Zigzag scanning is used to infill the Voronoi cells inside fully. The void density of lattice structures is able to adjust by controlling the number of seed nodes uniformly. The thickness of each Voronoi cells can be also governed by changing the number of multi-layer contour scanning. For Voronoi cells with high performance requirement, zigzag contour will be used to populate within the Voronoi cell. Hence, the proposed method can use toolpath to construct a topology shape without any model conversion. At the same time, the proposed method can be used to design graded channels by changing the number of contour in different layers. The proposed knowledge-based toolpath constructive method can design graded TPMS structures more efficiently with qualified toolpaths and robust manufacturability. It has more potential to become a new digital framework for design complex uniform or graded porous structures with greatly reduced geometric modeling time and printing preparation time and improve printing accuracy since there is no CAD modeling neither meshing where accuracy loss happens.

Chapter 6. Conclusion and perspectives

The research is devoted to the design methodology aspect of Additive Manufacturing, DfAM. The proposed methodologies are inspired by the unique capability of AM technologies, "adding material". It means the part is built from 0. The additive way in the thesis is also called "constructive". Given toolpath is the language of most AM machines, a toolpath constructive design framework for AM is proposed to populate toolpath from knowledge base directly for avoiding various pre-processing stages. Hence, the main contributions can be summarized into two keywords, qualified and constructive. "Qualified" is for ensuring manufacturability of AM and "Constructive" is for following the unique capability of AM to make design. All proposed methods focus on geometric modeling in AM stages and do not consider many post-processing and the full AM value chain. In this chapter, main contributions of the thesis are summarized and limitations of the proposed methods.

6.1. Main contributions of the research

6.1.1. Contributions in Macroscale of DfAM

Qualified CSG-based generative design for AM

A new CSG-based generative design method is proposed to generate and search for optimal qualified AM design solutions. General AM manufacturing constraints are analyzed and modelled to support practical DfAM needs. Different from the traditional TO method, it has the potential to deal with the self-supported problem through an explicit geometrical representation. The main contribution of this work is the introduction of a CSG geometry representation for self-supported topology optimization for AM and the realization of parametric control of explicit geometries with smooth boundaries. The application of geometric shape control points in the TO operation can greatly reduce the number of design variables and release the potential of evolutionary algorithm-based TO methods. Furthermore, a major advantage of the proposed method is to obtain strong convex Pareto sets, which are qualified design solutions for conflicting objective functions. Hence, a Pareto-optimal set can represent the trade-off for further decision making when compromise should be made with diverse preferences in specific applications.

Pattern-based constructive generative design for support structure in AM

A support point determination method is proposed to detect support relevant overhang areas and generate optimal support points on the overhang areas of complex components in AM. With a new support point pattern, the redundancy of current support point distribution is alleviated. Hence, the proposed method can help decrease the number of unnecessary support points on the overhang areas significantly, thereby reducing the support volume and the post-processing time while ensuring manufacturability. The method has also potential to be applied to more types of support structure generation, especially those from complex and porous components. It may be used with existing support structure design methods to further reduce the support volume, improve the surface quality and decrease the post-processing time. Hence, it can be developed as a key function for printing preparation software tools in industry.

A knowledge-based support structure design and optimization method is proposed which contains a set of sub-optimization methods. The bio-inspired tree structures can meet the application requirements: to be lightweight, self-supporting and easy-to-remove. By lattice configuration methods, the proposed method exhibits good performance since it can greatly reduce the amount raw materials needed for the support structure and ensure a better printing quality. If the post-processing time is taken into consideration, the method may show an additional advantage as compared with others due to the fact that it is easy-to-remove and fewer contact support points need repairing. Hence, it has great potential to be adopted for complex shapes and high-value components, e.g. aerospace and medical components, manufacturing in other AM processes where support structures are one of the main concerns.

6.1.2. Contributions in Mesoscale & Microscale of DfAM

Toolpath constructive design methods for lattice structures

A new toolpath constructive method is proposed to design thickness-varying Voronoi-based multi-topology lattice structures. Different kinds of scanning strategy are developed to infill within modified Voronoi cells. Multi-contour scanning is used to generate thickness-varying Voronoi lattice cells and zigzag scanning is used to infill the Voronoi cells inside fully. The main contribution is that the proposed method can use toolpath to construct a topology shape without any model conversion.

A novel knowledge-based toolpath constructive design method to generate high-precision graded lattice unit cells with manufacturability is proposed. It integrates implicit modeling, variable distance field, direct slicing and fine toolpath configuration to construct qualified toolpaths without any intermediate steps. It has potential to become a new digital framework for design complex uniform or graded porous

structures with greatly reduced geometric modeling time and printing preparation time and improve printing accuracy since there is no CAD modeling neither meshing where accuracy loss happens. Hence, it can be used to improve industrial application of part-scale porous structures with fine and gradient porous features.

6.2. Limitations of the research

6.2.1. Limitations and future plans in Macroscale of DfAM

Qualified CSG-based generative design for AM

Currently, the proposed CSG-GD method only adopts the Delaunay triangulation mesh to generate topology skeleton and defines quite simple primitive shapes. Therefore, to further improve this method, more skeleton generation methods should be investigated and the NURBS-based unit shape definition method could be explored, which may be helpful in embedding more complex AM manufacturing constraints. For some non-convex design domains with complex boundaries, the proposed method would possibly encounter some difficulty. To reduce the complexity, a set of geometric operations could be used to decompose the design domain into multiple simpler convex geometries. In the future work, complex design domains will be explored to extend the proposed method and isogeometric analysis (IGA) will be applied to the framework [174].

Pattern-based constructive generative design for support structure in AM

There is still space for improvement in the proposed support point determination method. Firstly, the heat diffusion and thermal stress deformation should be considered in the support point generation for large size metallic components. One solution is to conduct the thermal stress by predefined support points where the thermal stress is too large. Secondly, a part of the face overhang areas can be supported by the local non-supported areas, called self-support caused by the maximum printing bridge length. Hence, how to simplify the support relevant face overhang areas still plays a key role in the support point generation. In addition, the slicing method could provide a better solution for detecting the support relevant overhang areas. Support point distribution is one of the key factors that impact shape accuracy. To further demonstrate the support point optimization method, different types of support structures can be populated under support points with different positions. These are the necessary investigations for further research.

The proposed support structure generation method can still be improved and pose several critical challenges for future work:

(1). In this method, the build orientation of the components is predefined to be fixed. If the rotation of a CAD model is allowed, then the problem complexity and solution space would increase dramatically. It should be a challenge to solve the coupled problem, build orientation determination and support structure generation [51].

(2). All predefined tree-shaped structures are populated on the build plane, and there is no inter-link between the independent trees. Theoretically, we can add inter-brunches to different trees to enhance their self-support capability. In this way, more support volume may be reduced, but the computation and optimization may be more complicated.

(3). This work only presents relatively small-size dental components for a comparative study. When the components and their porous support structures are relatively large-scale, the computation cost will increase dramatically. To further benchmark this study, large-scale components from other application domains may be selected in the future.

6.2.2. Limitations and future plans in Mesoscale and Microscale of DfAM

Toolpath-based constructive generative design for thickness-varying Voronoi lattice structures

The proposed toolpath constructive generative design method for Voronoi lattice structures can achieve a direct toolpath construction without any model conversion, but we did not take toolpath airtime into account for extrusion-based AM processes [175]. For L-PBF process, laser travel route also needs to be considered [146]. In addition, other scanning strategies will be also studied in the future. Since toolpath is used to construct qualified design solutions directly, another interesting issue is how to embed process settings into toolpath for reducing thermal stress and deformations. Moreover, the proposed method may be used to design graded channels by changing the number of contour in different layers. It can be used to design heat sink and fluid channel in the future.

Knowledge-based toolpath constructive design for graded TPMS structures

The proposed knowledge-based toolpath constructive design method can only generate fine toolpaths along the Z direction for the indirect toolpath filling method, since unqualified slice pieces need to be transformed into qualified via model conversion to assemble with qualified pieces. To demonstrate the

proposed method, the L-PBF process will be used to fabricate fine porous gradient structures that are needed in diverse applications. In addition, more TPMS structures and toolpath patterns will be bench-marked in experiments to help construct qualified toolpath pattern knowledge base for configuration design.

6.3. Perspectives on DfAM

6.3.1. Perspectives of the CSG-GD method

A 3D GD method will be extended in the next stage. To avoid the emergence of closed internal holes in the L-PBF process, open lattice unit cells will be applied to fill into the 3D structure. Hybrid AM (HAM) comes out recently to combine both of the pros of AM and traditional processing techs, e.g. machining, to further improve the design freedom and design quality. Hybrid AM processes forms new manufacturing constraints to be considered for design. For the direct energy deposition process integrated with a CNC machine, self-support constraints will be ignored. In this process, decomposition methods usually need to be done for toolpath generation. Extracting medial-axis skeletons is one of decomposition methods that was used in wire-arc AM (WAAM) process [176]. Therefore, the proposed method may be easy to integrated with skeleton-based decomposition method to achieve a model partition. In addition, more manufacturing constraints of hybrid AM processes can be considered to support the design for hybrid AM process. For example, minimum and maximum size constraints can be achieved by controlling the radius of each node. In addition, we can add more control points to manipulate the shape of each skeleton so as to obtain complex NURBS-based skeletons, which can release more potential of the proposed CSG-GD method. Of course, this will cause more variables to increase the computing time and cost.
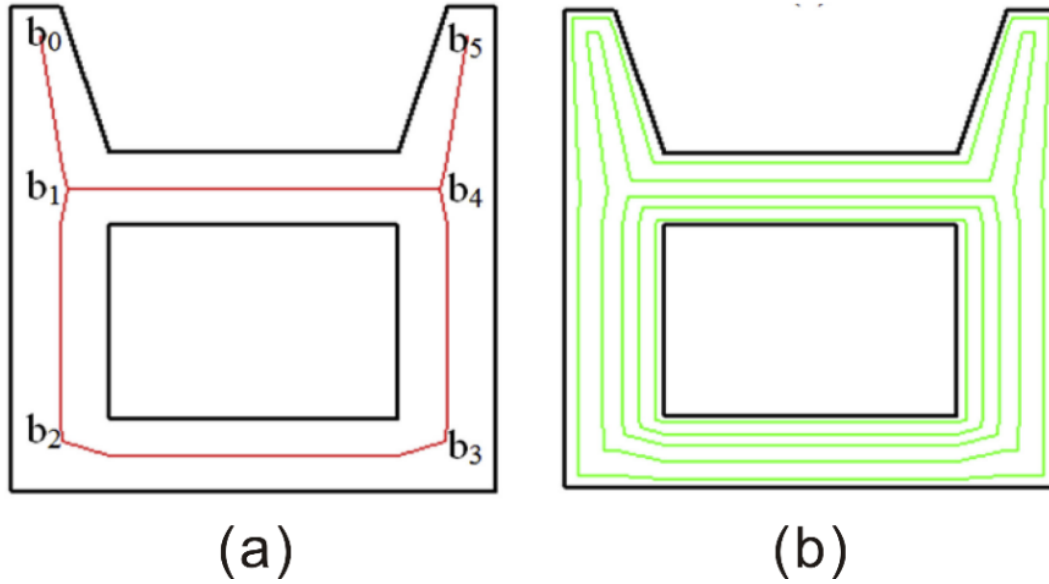
Figure 6.1. Illustration of an adaptive toolpath generation for a geometry: (a). A general skeleton and branch loop formation; (b). Final generated adaptive toolpaths. [176].

6.3.2. Perspectives of the pattern-based support structure generation method

Combined with the support point optimization method, the proposed support design method can reduce the support volume for qualified design solutions. However, current porous structures still have a problem of being time-consuming due to the large number of geometric entities and their related operations in slicing and toolpath generation. Toolpath may be used to construct support design directly based on the skeleton of support structures. For the solid support structure, the overhang angle and orientation of skeleton can influence the toolpath. For the TPMS-based support structure, the knowledge-based toolpath constructive method in Chapter 5.2 can be used to generate fine toolpath. The main issue is how to handle the toolpath generation in the intersection of skeletons. One possible solution is to perform Boolean operation using toolpath directly.

6.3.3. Perspectives of the toolpath constructive design method

The two toolpath-based constructive design methods construct processing models with qualified printing toolpaths directly. Therefore, the process parameters setting should respect properties of the powder material and types of AM machines. To make the use of the toolpath constructive methods, first, we need to understand the specific AM process and the required performance of AM parts to be printed for selecting suitable process settings.

To release more potential of the proposed knowledge-based TPMS design method in the L-PBF process, it is essential to build a knowledge dataset of toolpath configuration based on different materials and

AM machines. For different kinds of powder material and scanning strategies, the toolpath temples may be different, especially for island scanning strategy. Since physical experiments and process simulations are time-consuming and expensive, the surrogate model can be used to explore suitable processing settings for different types of scanning strategies. Moreover, the author would like to exploit more applications in multi-material and 4D printing designs [177], where direct writing techs, which is convenient for defining toolpath construction rules, are widely used.

6.3.4. Perspectives of a multi-field-driven toolpath-oriented DfAM framework

Toolpath-oriented: Integrating processing and manufacturing within design method becomes more important in full AM digital chain. All designs will finally be translated into a language that AM machine can recognize. Generally, AM processes are driven by G-code or toolpath. Therefore, the proposed toolpath-based constructive design method provides a new horizon for current DfAM framework. In traditional DfAM framework, a design needs to go through many processing stages, including CAD building, STL conversion, slicing, toolpath filling, et al. Toolpath-oriented design enables to simplify the complex pre-processing stages.

Performance-field: In order to distribute the material to be in harmony with stress magnitude and direction, force-flow design can be generated according to the FEA results [99]. The material can be distributed along the force-flow to control the material's anisotropy. Hence, force-flow-based toolpath can achieve the dual control of geometry and performance. More perspectives about DfAM framework of force-flow can be found in [99].

Material-field: In the proposed method, distance field is applied to construct graded-thickness TPMS toolpath temples. Other fields may be also developed into the method. For example, multiple powder feeders can be utilized to achieve a multi-material printing in multi-material directed energy deposition (DED) process. Material field may be integrated into the toolpath temples. By embedding the control of different powder feeders into specific toolpaths, multi-material components can be fabricated. Figure 6.2 shows a DED process with thermal monitoring [178] and a functional gradient design [179]. The multi-material toolpath definition can be also used in 4D printing.
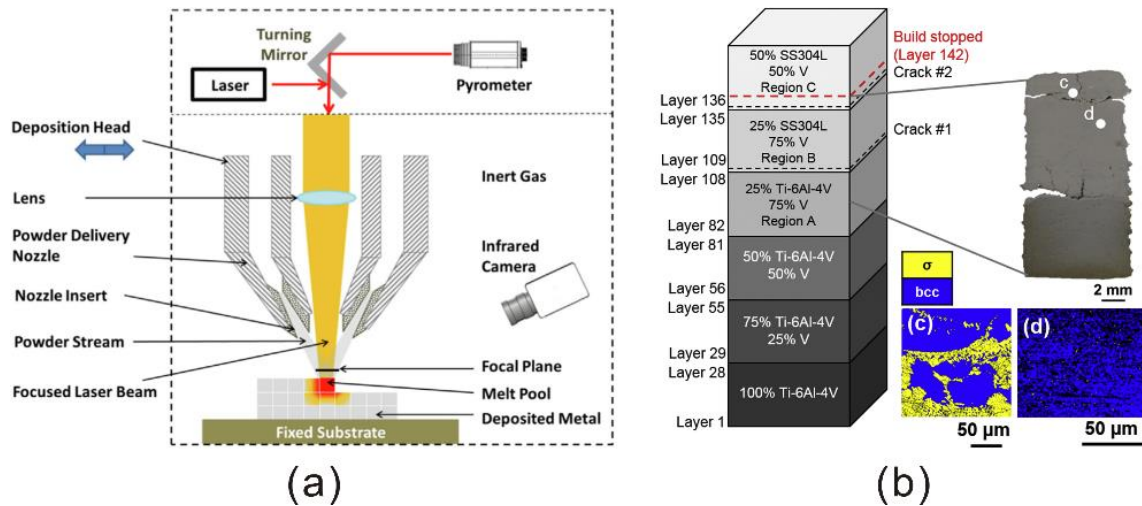
Figure 6.2. (a). Schematic of blown powder directed energy deposition process with thermal monitoring [178]; (b). Functional gradient design with an intermediate V section showing cracking at the dissimilar metal interfaces [179].

Function-field: Another advantage of the proposed toolpath-oriented DfAM framework is that toolpath can be manipulated directly to achieve specific functional properties. For example, functional surfaces can be obtained via a Boolean operation between AM toolpath and functional surfaces. It can be used to embed sensors or other monitors into AM parts. By performing Boolean operation, the method can be also applied to reduce part count for part consolidation.

Machine-field: Toolpath is not only the language of AM machine, but also for subtractive manufacturing. The constructed AM toolpath may be used as an assist path for post processing or hybrid AM process. For example, many AM parts usually needs post processing for surface roughness or tolerance requirement. The AM toolpaths has potential to provide an assist for better post processing and functional requirement. Many researchers are paying more attention on multi-laser AM machines. Toolpath model partition will be also much easier to assign multi-laser collaboration tasks while toolpath configuration.

A DfAM framework was proposed to map the important relationships among design attributes in [10, 180]. The DfAM problem formulation should take product, material and manufacturing designs into consideration simultaneously for qualified design solutions. Hence, process, structure, property and behavior were integrated within the DfAM framework to seek design solutions that are more suitable for AM process. The proposed toolpath-oriented constructive design method has possible potential to couple with more DfAM process. The main reason is that toolpath can embed more parameters in the AM digital chain into design so as to reflect the complex coupling relationships in DfAM framework better. Given that toolpath can integrate effects of many fields into final design solutions, Figure 6.4

shows a possible multi-filed-driven toolpath-oriented DfAM framework. The mechanism of the framework can also be extended to other physical fields, such as temperature-field in printing. Based on the temperature field in printing, how to adjust the toolpath configuration to achieve a closed loop control in AM process is also an open issue. Manufacturability problem is also a big issue for DfAM. The combination of knowledge-based toolpath temples and computational methods would provide a solution for the DfAM framework to achieve qualified AM design solutions [14]. More potential about the field-driven toolpath-oriented DfAM framework will be explored further in the future.
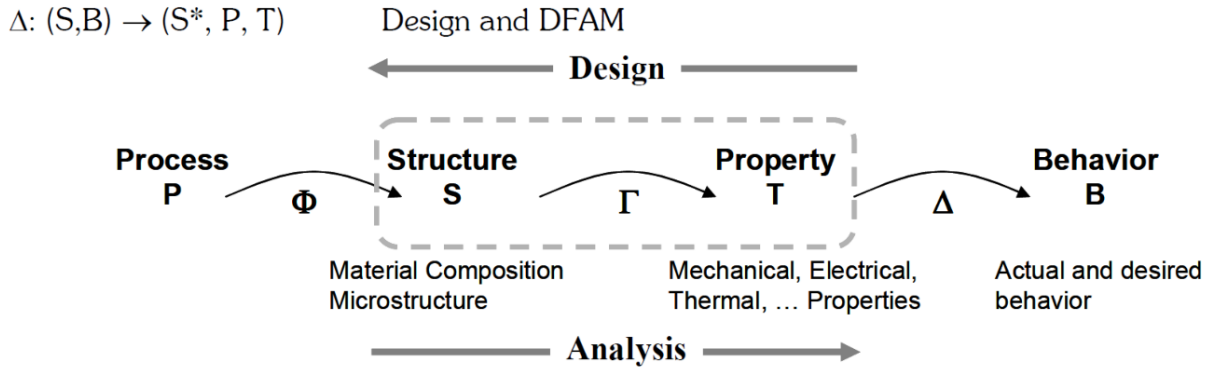
Figure 6.3. Process-Structure-Property-Behavior Mapping for DfAM. [180].
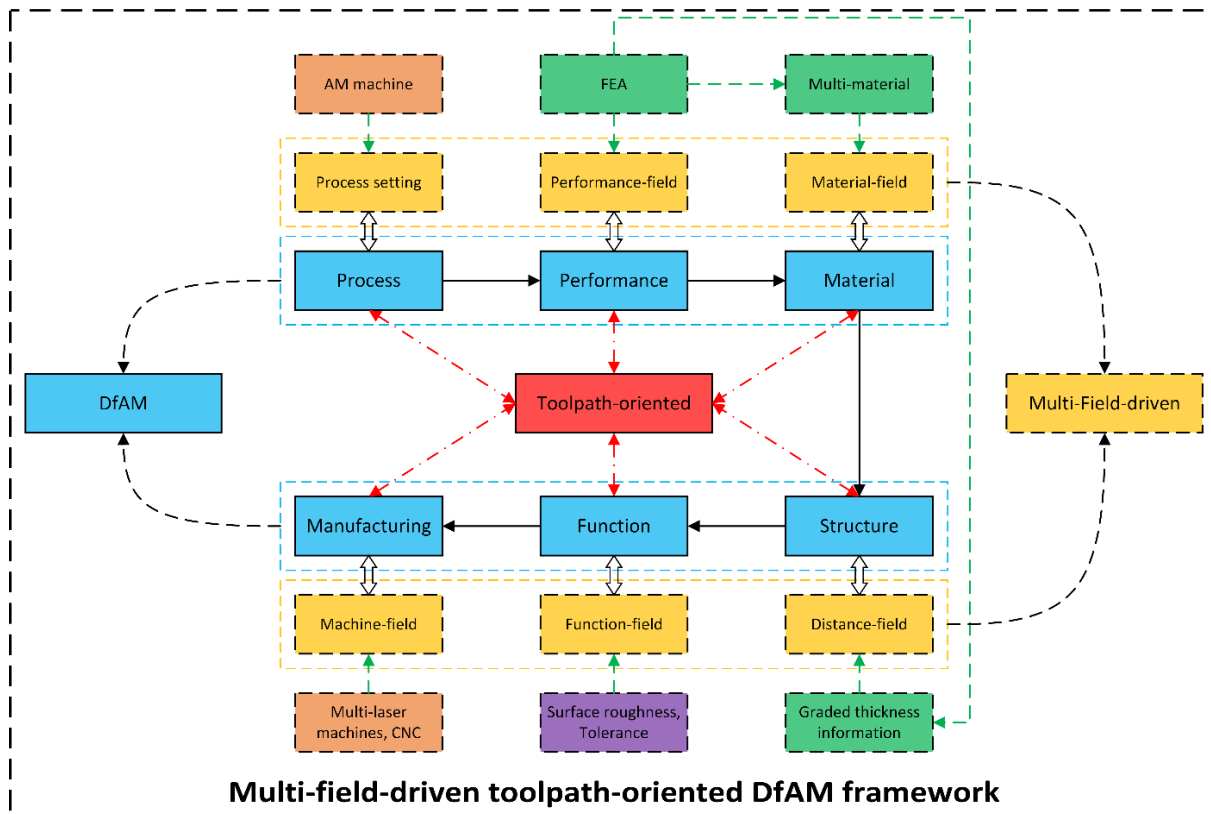
Figure 6.4. The proposed multi-field-driven toolpath-oriented DfAM framework.

Appendix

The main algorithms proposed are given in the appendix, including the CSG-based generative deign for qualified AM, pattern-based constructive generative design for support structure, and toolpath-based constructive design methods for lattice structure configuration.

A.1. CSG-based generative design for qualified AM

Two main algorithms are given below. Algorithm 1 shows the generation of adaptive Delaunay triangulation skeleton. Algorithm 2 gives the topological geometry construction of qualified CSG-based components.

Algorithm 1: Generate adaptive Delaunay triangulation skeleton

Input: Moveing nodes $\boldsymbol{N_m}$, Fixed nodes $\boldsymbol{N_f}$, Threshold value $\boldsymbol{t_v}$.
Output: Delaunay triangulation skeleton $\boldsymbol{S_D}$.

1 **forall** *Nodes N_{mi}: $(x_i, y_i) \leftarrow N_m$* **do**
2     $i \leftarrow 0$;
3   **while** $N_m \neq \emptyset$ **do**
4   Pick nodes N_{mi} from N_m to N_{Ci};
5        $N_m \leftarrow N_m - N_{mi}$;
6   **forall** N_{mj} *of* N_m **do**
7   **if** *minimal distance(N_{mj}, N_C)* $\leq t_v$ **then**
8              $N_C \leftarrow N_{mj} + N_C$;
9   **else**
10   Keep N_{mj} in N_m;
11   **end**
12   **end**
13       $N_m \leftarrow N_m - N_C$;
14       $i \leftarrow i + 1$;
15   **end**
16 **end**
17 Generate new adaptive moving nodes N_G;
18 $N \leftarrow N_G + N_f$;
19 $S_D \leftarrow \text{Delaunay}(N)$;

Algorithm 2: Generate qualified CSG-based topogical geometry

Input: Delaynay skeletons S_D, Node weight W, Maximum overhang angle θ_{max},
Maximum overhang distance D_{max}, Design domain G_D.

Output: Topological geometry G.

1   $R \leftarrow W$;
2   $G_P \leftarrow \emptyset$;
3   **for** $k \leftarrow 0$ to $n-1$ **do**
4   Generate Circle C_{Nk1}, C_{Nk2};
5   Build tangent lines T_{k1}, T_{k2};
6   Generate P_k;
7   **if** $S_{T_{k1}} \leq \theta_{max}$ **then**
8   Keep P_k;
9   **else**
10   **if** $L_{proj,k} \leq D_{max}$ **then**
11   Keep P_k;
12   **end**
13   **end**
14     $\Omega_{G_P} \leftarrow \Omega_{G_P} \cup \Omega_{P_k}$;
15     $k \leftarrow k + 1$;
16 **end**
17 $\Omega_G \leftarrow \Omega_{G_P} \cap \Omega_{G_D}$;

A.2. Pattern-based constructive generative design for support structure in AM

Four main algorithms about parametric support structure generation are presented here. Support points obtained from the support determination method are grouped and clustered based on the distance between these points in Algorithm 3 and 4, as shown in Figure 4.33.

Algorithm 3: Group support points

Input: Support point set S_p, Calibrated coordinate value $z_0, ..., z_m$.

Output: Point group $G_1, ..., G_m$.

1   **forall** *Point p_i: $(x_i, y_i, z_i) \leftarrow p_i$* **do**
2   **if** z_i in (z_j, z_{j+1}) **then**
3       $G_j \leftarrow p_i$;
4   **end**
5     $i \leftarrow i + 1$;
6 **end**

Algorithm 4: Cluster support point groups

Input: Group G, Threshold t.
Output: Point cluster $C_1, ..., C_n$.

1 **foreach** *Group G_i in G* **do**
2 | Pick point P_{ik} from G_i to C_{il};
3 | **while** $G_i \neq \emptyset$ **do**
4 | | **for** $p_{ij} \in P_{iC}$ **do**
5 | | | **if** *minimal distance$(p_{ij}, C_{il}) \leq t$* **then**
6 | | | | $C_{il} \leftarrow p_{ij}$;
7 | | | **else**
8 | | | | Keep p_{ij} in P_{iC};
9 | | | **end**
10 | | **end**
11 | | Update $G_i \leftarrow G_i - P_{iC}$;
12 | **end**
13 **end**

For each cluster, a parametric square is populated under points in the cluster. Parametric L-system trees are rooted into the squares to generate qualified support skeletons. Then, a MOEA algorithm is applied to generate alternative design solutions. Algorithm 6 gives main details about alternative support design solutions generation.

Algorithm 5: Generate square patterns

Input: Cluster C, Angle α.
Output: Square S_{ij}.

1 **foreach** *Cluster C_i in C* **do**
2 | $C_i \leftarrow l_i + \alpha_i$;
3 | Caluclate N_i;
4 **end**
5 Reture the best solution $\sum_{i=1}^{n} S_{i,best}$ with $N_{i,best}$;

Algorithm 6: Generate alternative tree-shaped support structures

Input: Support point set S_p, Square $S_k(k = 1, ..., n)$, Predefined parameterized trees s_k, Step length h_i, Step scale a_k, Initial position p_k, Initial orientation α_k, Base thickness t_b, Minimal thickness t_{min}, Maximum length L_{max}, Minimum length L_{min}, Maximum overhang angle θ_{max}.
Output: Tree-shaped support structures V_{Ap}.

1 **forall** *Square S_i in S* **do**
2 | Original tree skeleton $T_i \leftarrow s_i, h_i, a_i, p_i, \alpha_i$;
3 | Select qualified shortest connections T_{Qj} of $S_{Qp} \leftarrow L_{max}, L_{min}, \theta_{max}$;
4 | $S_{Up} \leftarrow S_p - S_{Qp}$;
5 | **forall** *S_{Upk} of S_{Up}* **do**
6 | | Draw vertical lines V_{Upk};
7 | **end**
8 | All pruned tree skeletons $T_{Ap} \leftarrow T_{Qj} + V_{Up}$;
9 | $V_{Ap} \leftarrow T_{Ap} + t_b + t_{min}$;
10 **end**

A.3. Toolpath-based constructive design methods for lattice structure configuration

Main key algorithms for toolpath-based constructive design methods are given below.

A.3.1. A toolpath-based constructive generative design for thickness-varying Voronoi lattice structures

Two types of toolpaths based on the Marching square algorithm are introduced to obtain intersection-free toolpaths. The two kinds of toolpaths (Algorithm 7 and 8) are used to construct Voronoi lattice cells (Algorithm 9) according to AM parameters.

Algorithm 7: Contour toolpath configuration via Marching Square algorithm

Input: Surface boundary S_b, Hatch spacing S_H, Resolution t_{re}.
Output: N-layer contour toolpath T_c.

1 $B_{bb} \leftarrow Boundingbox(S_b)$;
2 Calculate infill point density $D_p \leftarrow f(B_{bb}, t_{re})$;
3 Generate P_{MS}, L_{MS};
4 **if** P_{MS_i} *in* S_b **then**
5 | Add P_{MS_i} to P_{In};
6 **else**
7 | Add P_{MS_i} to P_{Out};
8 **end**
9 **foreach** P_{In_i} *in* P_{In} **do**
10 | $D_{In_i} \leftarrow -distance(P_{In_i}, S_b)$;
11 **end**
12 **foreach** P_{Out_j} *in* P_{Out} **do**
13 | $D_{Out_j} \leftarrow distance(P_{Out_j}, S_b)$;
14 **end**
15 **foreach** $k \leftarrow 1$ *to* n **do**
16 | $V_{n_k} \leftarrow D_k - \frac{(2n-1) \times S_H}{2}$;
17 | Contour $T_{c_n} \leftarrow MarchingSquare(P_{MS}, V_{n_k})$;
18 **end**
19 Contour $T_c \leftarrow \sum_{i=1}^{n}$ Contour T_{c_i};

Algorithm 8: Zigzag toolpath configuration via Marching Square algorithm

---

Input: Surface boundary S_b, Hatch spacing S_H, Resolution t_{re}, Rotation angle β.

Output: Zigzag toolpath T_z.

1   Infill area $S_z \leftarrow$ Funtion(Contour T_{c1});
2   $S_{bb} \leftarrow$ Boundingbox(S_b);
3   $T_{Ori_z} \leftarrow$ Zigzag(S_{bb}, S_H, β);
4   Ziazag $T_z \leftarrow T_{Ori_z}$ in S_b;

Algorithm 9: Toolpath constructive design for thickness-varying Voronoi lattice structures

---

Input: The number of random points n, Hatch spacing S_H, Resolution t_{re}, Rotation angle β, Contour infill $\sum_{i=1}^{n} c_i$, Zigzag infill $\sum_{j=1}^{n} z_j$, Topological geometry G.

Output: Toolpath configuration T_c, T_z.

1   Generate n random points P in Ω_G;
2   Voronoicells $V_c \leftarrow$ Voronoi(P, Ω_G);
3   **for** $i \leftarrow 1$ **to** n **do**
4   **if** $c_i > 0$ **then**
5       $T_{cc_i} \leftarrow \sum_{j=1}^{c_i}$ Contour $T_c(V_{c_i}, \frac{(2j-1) \times S_H}{2})$;
6       $S_{z_i} \leftarrow$ Contour $T_c(V_{c_i}, c_i \times S_H)$;
7   **else**
8       $S_{z_i} \leftarrow$ Contour $T_c(V_{c_i}, \frac{S_H}{2})$;
9   **end**
10   **end**
11   **for** $i \leftarrow 1$ **to** n **do**
12   **if** $z_i > 0$ **then**
13       $T_{zz_i} \leftarrow$ Zigzag $T_z(S_{z_i}, S_H, \beta)$;
14   **end**
15   **end**

A.3.2. A knowledge-based toolpath constructive design method for high-precision graded TPMS structures

The proposed algorithms used in Chapter 5.1 are applied to construct graded TPMS lattice unit cell. The main algorithm is shown to present the construction of knowledge-based lattice toolpaths.

Algorithm 10: Knowledge-based toolpath configuration for high-precision graded TPMS lattice structures

---

Input: TPMS function F_T, Size of uinit cell S, Resolution of MC algorithm t_{MC}, Graded thickness t_G, Layer thickness t_L, Hatch spacing S_H, Resolution of MS algorithm t_{MS}, Rotation angle β, Contour infill c.

Output: Toolpath configuration T.

1   0-iso-surface $T_0 \leftarrow$ MarchingCubes(F_T, S, t_{MC});

2   Uniform points $p_{MC}(t_{MC})$;

3   $D_{p_{MC}} \leftarrow$ distance (p_u, T_0);

4   Graded surface values $V_{MC} \leftarrow D_{p_{MC}} - t_G$;

5   Graded TPMS $S_G \leftarrow$ MarchingCubes(V_{MC}, p_{MC}) ;

6   $N_L \leftarrow S \div t_L$;

7   **for** $i \leftarrow$ *1* **to** n **do**

8      $P_i \leftarrow$ PlaneXY(0,0,(i-1)$\times t_L$);

9   Polylines $C_{P_i} \leftarrow$ BooleanIntersection(S_G, P_i);

10   BoundingSurface $S_{b_i} \leftarrow$ BooleanIntersection(Cell, P_i);

11   SplitAreas $A_{S_i} \leftarrow$ BooleanSplit(S_{b_i}, P_i);

12   Contour $T_{c_i} \leftarrow \sum_{j=1}^{c_i}$ Contour $T_c(A_{S_i}, \frac{(2c_i-1)\times S_H}{2})$;

13   ZigzagAreas $S_{z_i} \leftarrow$ Contour $T_c(A_{S_i}, c_i \times S_H)$;

14   RotationAngle $\beta z_i \leftarrow i \times \beta$;

15   Zigzag $T_{z_i} \leftarrow$ Zigzag $T_z(S_{z_i}, S_H, \beta_{z_i})$;

16     $T_i \leftarrow T_{c_i} + T_{z_i}$;

17   **end**

18   $T \leftarrow \sum_{k=1}^{N_L} T_k$;

List of Publications

- **Journal Articles:**

[1] Yicha ZHANG, **Zhiping WANG**, Alain BERNARD, et al. Bio-inspired generative design for support structure generation and optimization in Additive Manufacturing (AM). ***CIRP Annals***, 2020, 69(1): 117-120.

[2] **Zhiping WANG**, Yicha ZHANG, Alain BERNARD. A constructive solid geometry-based generative design method for additive manufacturing. ***Additive Manufacturing***, 2021, 41: 101952.

[3] **Zhiping WANG**, Yicha ZHANG, Alain BERNARD, et al. Support point determination for support structure design in additive manufacturing. ***Additive Manufacturing***, 2021, 47: 102341.

[4] **Zhiping WANG**, Yicha ZHANG, Alain BERNARD. Lightweight porous support structure design for additive manufacturing via knowledge-based bio-inspired volume generation and lattice configuration. ***Computer-Aided Design***, 2021. (Under review)

[5] **Zhiping WANG**, Yicha ZHANG, Alain BERNARD. A toolpath-based constructive generative design method for thickness-varying Voronoi lattice structures. ***Rapid Prototyping Journal***. (To be submitted)

- **International Conference Papers:**

[6] **Zhiping WANG**, Yicha ZHANG, Alain BERNARD, et al. Stiffness modulation for soft robot joint via lattice structure configuration design, ***CIRP Design Conference***, *Procedia CIRP*, 2021, 100: 732-737.

[7] **Zhiping WANG**, Yicha ZHANG, Alain BERNARD. A novel knowledge-based toolpath constructive approach for designing high-precision graded TPMS lattice structure. ***Solid Freeform Fabrication SYMPOSIUM 2021***, 2021, 1185-1201.

[8] Zhen HONG, **Zhiping WANG**, Sihao DENG, Yicha ZHANG, Alain BERNARD, Tool Path Generation and Optimization for Hybrid Additive Manufacturing. ***Solid Freeform Fabrication SYMPOSIUM 2021***, 2021, 1167-1184.

References

[1] A. Standard, "Standard terminology for additive manufacturing technologies," *ASTM International F2792-12a,* 2012.

[2] D. T. Pham and R. S. Gault, "A comparison of rapid prototyping technologies," *International Journal of machine tools and manufacture,* vol. 38, no. 10-11, pp. 1257-1287, 1998.

[3] J.-P. Kruth, "Material incress manufacturing by rapid prototyping techniques," *CIRP annals,* vol. 40, no. 2, pp. 603-614, 1991.

[4] J.-P. Kruth, M.-C. Leu, and T. Nakagawa, "Progress in additive manufacturing and rapid prototyping," *Cirp Annals,* vol. 47, no. 2, pp. 525-540, 1998.

[5] M. K. Thompson *et al.*, "Design for Additive Manufacturing: Trends, opportunities, considerations, and constraints," *CIRP Annals,* vol. 65, no. 2, pp. 737-760, 2016, doi: 10.1016/j.cirp.2016.05.004.

[6] V. K. Champagne, *The cold spray materials deposition process*. Elsevier, 2007.

[7] I. Gibson, D. Rosen, B. Stucker, and M. Khorasani, "Introduction and basic principles," in *Additive manufacturing technologies*: Springer, 2021, pp. 1-21.

[8] T. DebRoy *et al.*, "Additive manufacturing of metallic components – Process, structure and properties," *Progress in Materials Science,* vol. 92, pp. 112-224, 2018, doi: 10.1016/j.pmatsci.2017.10.001.

[9] M. Schmidt *et al.*, "Laser based additive manufacturing in industry and academia," *CIRP Annals,* vol. 66, no. 2, pp. 561-583, 2017, doi: 10.1016/j.cirp.2017.05.011.

[10] D. W. Rosen, "Research supporting principles for design for additive manufacturing," *Virtual and Physical Prototyping,* vol. 9, no. 4, pp. 225-232, 2014, doi: 10.1080/17452759.2014.951530.

[11] N. Lebaal, Y. Zhang, F. Demoly, S. Roth, S. Gomes, and A. Bernard, "Optimised lattice structure configuration for additive manufacturing," *CIRP Annals,* vol. 69, no. 1, pp. 117-120, 2019, doi: 10.1016/j.cirp.2019.04.054.

[12] Y. Xiong *et al.*, "Data-Driven Design Space Exploration and Exploitation for Design for Additive Manufacturing," *Journal of Mechanical Design,* vol. 141, no. 10, 2019, doi: 10.1115/1.4043587.

[13] D. W. Rosen, "A review of synthesis methods for additive manufacturing," *Virtual and Physical Prototyping,* vol. 11, no. 4, pp. 305-317, 2016, doi: 10.1080/17452759.2016.1240208.

[14] T. Vaneker, A. Bernard, G. Moroni, I. Gibson, and Y. Zhang, "Design for additive manufacturing: Framework and methodology," *CIRP Annals,* vol. 69, no. 2, pp. 578-599, 2020, doi: 10.1016/j.cirp.2020.05.006.

[15] I. Gibson, D. Rosen, B. Stucker, and M. Khorasani, "Design for additive manufacturing," in *Additive manufacturing technologies*: Springer, 2021, pp. 555-607.

References

[16]   D. Gu, X. Shi, R. Poprawe, D. L. Bourell, R. Setchi, and J. Zhu, "Material-structure-performance integrated laser-metal additive manufacturing," *Science,* vol. 372, no. 6545, May 28 2021, doi: 10.1126/science.abg1487.

[17]   E. Tempelman, "Lightweight materials, lightweight design?," in *Materials experience*: Elsevier, 2014, pp. 247-258.

[18]   K. Zeng, D. Pal, C. Teng, and B. E. Stucker, "Evaluations of effective thermal conductivity of support structures in selective laser melting," *Additive Manufacturing,* vol. 6, pp. 67-73, 2015, doi: 10.1016/j.addma.2015.03.004.

[19]   M. Cloots, A. Spierings, and K. Wegener, "Assessing new support minimizing strategies for the additive manufacturing technology SLM," in *24th International SFF Symposium-An Additive Manufacturing Conference, Austin, USA, University of Texas at Austin*, 2013, pp. 631-643.

[20]   Y. Tang and Y. F. Zhao, "A survey of the design methods for additive manufacturing to improve functional performance," *Rapid Prototyping Journal,* vol. 22, no. 3, pp. 569-590, 2016, doi: 10.1108/rpj-01-2015-0011.

[21]   P. W. Mani Mahesh, and Haeseong Jee, "Design rules for additive manufacturing: a catrgorization," *ASME 2017 International Design Engineering Technical Conference and Computers and Information in Engineering Conference,* 2017.

[22]   Y. Zhang, A. Bernard, R. K. Gupta, and R. Harik, "Evaluating the Design for Additive Manufacturing: A Process Planning Perspective," *Procedia CIRP,* vol. 21, pp. 144-150, 2014, doi: 10.1016/j.procir.2014.03.179.

[23]   J. Kranz, D. Herzog, and C. Emmelmann, "Design guidelines for laser additive manufacturing of lightweight structures in TiAl6V4," *Journal of Laser Applications,* vol. 27, no. S1, 2015, doi: 10.2351/1.4885235.

[24]   O. Diegel, A. Nordin, and D. Motte, *A Practical Guide to Design for Additive Manufacturing.* Springer, 2019.

[25]   G. A. O. Adam and D. Zimmer, "Design for Additive Manufacturing—Element transitions and aggregated structures," *CIRP Journal of Manufacturing Science and Technology,* vol. 7, no. 1, pp. 20-28, 2014, doi: 10.1016/j.cirpj.2013.10.001.

[26]   Y. Shi, Y. Zhang, S. Baek, W. De Backer, and R. Harik, "Manufacturability analysis for additive manufacturing using a novel feature recognition technique," *Computer-Aided Design and Applications,* vol. 15, no. 6, pp. 941-952, 2018, doi: 10.1080/16864360.2018.1462574.

[27]   Y. Zhang, Z. Wang, Y. Zhang, S. Gomes, and A. Bernard, "Bio-inspired generative design for support structure generation and optimization in Additive Manufacturing (AM)," *CIRP Annals,* vol. 69, no. 1, pp. 117-120, 2020, doi: 10.1016/j.cirp.2020.04.091.

[28]   M. P. Bendsoe and O. Sigmund, *Topology optimization: theory, methods, and applications.* Springer Science & Business Media, 2013.

[29]   O. Sigmund and K. Maute, "Topology optimization approaches," *Structural and Multidisciplinary Optimization,* vol. 48, no. 6, pp. 1031-1055, 2013, doi: 10.1007/s00158-013-0978-6.

[30] M. Leary, L. Merli, F. Torti, M. Mazur, and M. Brandt, "Optimal topology for additive manufacture: A method for enabling additive manufacture of support-free optimal structures," *Materials & Design,* vol. 63, pp. 678-690, 2014, doi: 10.1016/j.matdes.2014.06.015.

[31] A. T. Gaynor, N. A. Meisel, C. B. Williams, and J. K. Guest, "Topology Optimization for Additive Manufacturing: Considering Maximum Overhang Constraint," presented at the 15th AIAA/ISSMO Multidisciplinary Analysis and Optimization Conference, 2014.

[32] A. T. Gaynor and J. K. Guest, "Topology optimization considering overhang constraints: Eliminating sacrificial support material in additive manufacturing through design," *Structural and Multidisciplinary Optimization,* vol. 54, no. 5, pp. 1157-1172, 2016, doi: 10.1007/s00158-016-1551-x.

[33] M. Langelaar, "An additive manufacturing filter for topology optimization of print-ready designs," *Structural and Multidisciplinary Optimization,* vol. 55, no. 3, pp. 871-883, 2016, doi: 10.1007/s00158-016-1522-2.

[34] M. Langelaar, "Topology optimization of 3D self-supporting structures for additive manufacturing," *Additive Manufacturing,* vol. 12, pp. 60-70, 2016, doi: 10.1016/j.addma.2016.06.010.

[35] C. Wang, X. Qian, W. D. Gerstler, and J. Shubrooks, "Boundary Slope Control in Topology Optimization for Additive Manufacturing: For Self-Support and Surface Roughness," *Journal of Manufacturing Science and Engineering,* vol. 141, no. 9, 2019, doi: 10.1115/1.4043978.

[36] B. Barroqueiro, A. Andrade-Campos, and R. A. F. Valente, "Designing Self Supported SLM Structures via Topology Optimization," *Journal of Manufacturing and Materials Processing,* vol. 3, no. 3, 2019, doi: 10.3390/jmmp3030068.

[37] Y.-F. Fu, B. Rolfe, L. N. S. Chiu, Y. Wang, X. Huang, and K. Ghabraie, "Design and experimental validation of self-supporting topologies for additive manufacturing," *Virtual and Physical Prototyping,* vol. 14, no. 4, pp. 382-394, 2019, doi: 10.1080/17452759.2019.1637023.

[38] Y.-F. Fu, B. Rolfe, L. N. S. Chiu, Y. Wang, X. Huang, and K. Ghabraie, "Parametric studies and manufacturability experiments on smooth self-supporting topologies," *Virtual and Physical Prototyping,* vol. 15, no. 1, pp. 22-34, 2019, doi: 10.1080/17452759.2019.1644185.

[39] C. J. Thore, H. A. Grundström, B. Torstenfelt, and A. Klarbring, "Penalty regulation of overhang in topology optimization for additive manufacturing," *Structural and Multidisciplinary Optimization,* 2019, doi: 10.1007/s00158-019-02194-x.

[40] M. L. Zhao Dengyang, and Yusheng Liu, "Self-supporting topology optimization for additive manufacturing," *arXiv,* vol. 1708.07364, 2017.

[41] G. Allaire, F. Jouve, and A.-M. Toader, "Structural optimization using sensitivity analysis and a level-set method," *Journal of Computational Physics,* vol. 194, no. 1, pp. 363-393, 2004, doi: 10.1016/j.jcp.2003.09.032.

[42] N. P. van Dijk, K. Maute, M. Langelaar, and F. van Keulen, "Level-set methods for structural topology optimization: a review," *Structural and Multidisciplinary Optimization,* vol. 48, no. 3, pp. 437-472, 2013, doi: 10.1007/s00158-013-0912-y.

[43] X. Guo, W. Zhang, and W. Zhong, "Doing Topology Optimization Explicitly and Geometrically—A New Moving Morphable Components Based Framework," *Journal of Applied Mechanics,* vol. 81, no. 8, 2014, doi: 10.1115/1.4027609.

197

References

[44] W. Zhang, J. Yuan, J. Zhang, and X. Guo, "A new topology optimization approach based on Moving Morphable Components (MMC) and the ersatz material model," *Structural and Multidisciplinary Optimization,* vol. 53, no. 6, pp. 1243-1260, 2015, doi: 10.1007/s00158-015-1372-3.

[45] W. Zhang *et al.*, "Explicit three dimensional topology optimization via Moving Morphable Void (MMV) approach," *Computer Methods in Applied Mechanics and Engineering,* vol. 322, pp. 590-614, 2017, doi: 10.1016/j.cma.2017.05.002.

[46] G. Allaire, C. Dapogny, R. Estevez, A. Faure, and G. Michailidis, "Structural optimization under overhang constraints imposed by additive manufacturing technologies," *Journal of Computational Physics,* vol. 351, pp. 295-328, 2017, doi: 10.1016/j.jcp.2017.09.041.

[47] Y. Wang, J. Gao, and Z. Kang, "Level set-based topology optimization with overhang constraint: Towards support-free additive manufacturing," *Computer Methods in Applied Mechanics and Engineering,* vol. 339, pp. 591-614, 2018, doi: 10.1016/j.cma.2018.04.040.

[48] X. Guo, J. Zhou, W. Zhang, Z. Du, C. Liu, and Y. Liu, "Self-supporting structure design in additive manufacturing through explicit topology optimization," *Computer Methods in Applied Mechanics and Engineering,* vol. 323, pp. 27-63, 2017, doi: 10.1016/j.cma.2017.05.003.

[49] A. M. Mirzendehdel and K. Suresh, "Support structure constrained topology optimization for additive manufacturing," *Computer-Aided Design,* vol. 81, pp. 1-13, 2016, doi: 10.1016/j.cad.2016.08.006.

[50] M. Langelaar, "Integrated component-support topology optimization for additive manufacturing with post-machining," *Rapid Prototyping Journal,* vol. 25, no. 2, pp. 255-265, 2019, doi: 10.1108/rpj-12-2017-0246.

[51] Y. Zhang, A. Bernard, R. Harik, and K. P. Karunakaran, "Build orientation optimization for multi-part production in additive manufacturing," *Journal of Intelligent Manufacturing,* vol. 28, no. 6, pp. 1393-1407, 2015, doi: 10.1007/s10845-015-1057-1.

[52] Y. Zhang and A. Bernard, "A KBE CAPP framework for qualified additive manufacturing," *CIRP Annals,* vol. 67, no. 1, pp. 467-470, 2018, doi: 10.1016/j.cirp.2018.04.045.

[53] M. Langelaar, "Combined optimization of part topology, support structure layout and build orientation for additive manufacturing," *Structural and Multidisciplinary Optimization,* vol. 57, no. 5, pp. 1985-2004, 2018, doi: 10.1007/s00158-017-1877-z.

[54] O. Sigmund, "On the usefulness of non-gradient approaches in topology optimization," *Structural and Multidisciplinary Optimization,* vol. 43, no. 5, pp. 589-596, 2011, doi: 10.1007/s00158-011-0638-7.

[55] N. Aulig and M. Olhofer, "Evolutionary computation for topology optimization of mechanical structures: An overview of representations," in *2016 IEEE Congress on Evolutionary Computation (CEC)*, 2016: IEEE, pp. 1948-1955.

[56] D. Guirguis *et al.*, "Evolutionary Black-box Topology Optimization: Challenges and Promises," *IEEE Transactions on Evolutionary Computation,* pp. 1-1, 2019, doi: 10.1109/tevc.2019.2954411.

[57] G. R. Zavala, A. J. Nebro, F. Luna, and C. A. Coello Coello, "A survey of multi-objective metaheuristics applied to structural optimization," *Structural and Multidisciplinary Optimization,* vol. 49, no. 4, pp. 537-558, 2013, doi: 10.1007/s00158-013-0996-4.

[58]   A. E. Eiben and J. E. Smith, *Introduction to evolutionary computing*. Springer, 2003.

[59]   B. R. Bielefeldt, E. Akleman, G. W. Reich, P. S. Beran, and D. J. Hartl, "L-System-Generated Mechanism Topology Optimization Using Graph-Based Interpretation," *Journal of Mechanisms and Robotics,* vol. 11, no. 2, 2019, doi: 10.1115/1.4042512.

[60]   B. R. Bielefeldt, G. W. Reich, P. S. Beran, and D. J. Hartl, "Development and validation of a genetic L-System programming framework for topology optimization of multifunctional structures," *Computers & Structures,* vol. 218, pp. 152-169, 2019, doi: 10.1016/j.compstruc.2019.02.005.

[61]   N. Aulig and M. Olhofer, "Neuro-evolutionary topology optimization of structures by utilizing local state features," presented at the Proceedings of the 2014 conference on Genetic and evolutionary computation - GECCO '14, 2014.

[62]   K. O. Stanley, "Compositional pattern producing networks: A novel abstraction of development," *Genetic Programming and Evolvable Machines,* vol. 8, no. 2, pp. 131-162, 2007, doi: 10.1007/s10710-007-9028-8.

[63]   H. Hamda and M. Schoenauer, "Topological optimum design with evolutionary algorithms," *Journal of convex analysis,* vol. 9, no. 2, pp. 503-518, 2002.

[64]   F. Ahmed, K. Deb, and B. Bhattacharya, "Structural topology optimization using multi-objective genetic algorithm with constructive solid geometry representation," *Applied Soft Computing,* vol. 39, pp. 240-250, 2016, doi: 10.1016/j.asoc.2015.10.063.

[65]   A. Pandey, R. Datta, and B. Bhattacharya, "Topology optimization of compliant structures and mechanisms using constructive solid geometry for 2-d and 3-d applications," *Soft Computing,* vol. 21, no. 5, pp. 1157-1179, 2015, doi: 10.1007/s00500-015-1845-8.

[66]   J. A. Madeira, H. C. Rodrigues, and H. Pina, "Multiobjective topology optimization of structures using genetic algorithms with chromosome repairing," *Structural and Multidisciplinary Optimization,* vol. 32, no. 1, pp. 31-39, 2006, doi: 10.1007/s00158-006-0007-0.

[67]   Y. Sato, K. Izui, T. Yamada, and S. Nishiwaki, "Pareto frontier exploration in multiobjective topology optimization using adaptive weighting and point selection schemes," *Structural and Multidisciplinary Optimization,* vol. 55, no. 2, pp. 409-422, 2016, doi: 10.1007/s00158-016-1499-x.

[68]   A. Cardillo, G. Cascini, F. S. Frillici, and F. Rotini, "Multi-objective topology optimization through GA-based hybridization of partial solutions," *Engineering with Computers,* vol. 29, no. 3, pp. 287-306, 2012, doi: 10.1007/s00366-012-0272-z.

[69]   V. Singh and N. Gu, "Towards an integrated generative design framework," *Design Studies,* vol. 33, no. 2, pp. 185-207, 2012, doi: 10.1016/j.destud.2011.06.001.

[70]   I. Jowers, C. Earl, and G. Stiny, "Shapes, structures and shape grammar implementation," *Computer-Aided Design,* vol. 111, pp. 80-92, 2019, doi: 10.1016/j.cad.2019.02.001.

[71]   B. Bochenek and K. Tajs-Zielińska, "Novel local rules of cellular automata applied to topology and size optimization," *Engineering Optimization,* vol. 44, no. 1, pp. 23-35, 2012, doi: 10.1080/0305215x.2011.561843.

References

[72]   S. Krish, "A practical generative design method," *Computer-Aided Design,* vol. 43, no. 1, pp. 88-100, 2011, doi: 10.1016/j.cad.2010.09.009.

[73]   S. Goguelin, J. M. Flynn, W. P. Essink, and V. Dhokia, "A Data Visualization Dashboard for Exploring the Additive Manufacturing Solution Space," *Procedia CIRP,* vol. 60, pp. 193-198, 2017, doi: 10.1016/j.procir.2017.01.016.

[74]   V. Dhokia, W. P. Essink, and J. M. Flynn, "A generative multi-agent design methodology for additively manufactured parts inspired by termite nest building," *CIRP Annals,* vol. 66, no. 1, pp. 153-156, 2017, doi: 10.1016/j.cirp.2017.04.039.

[75]   W. P. Essink, J. M. Flynn, S. Goguelin, and V. Dhokia, "Hybrid Ants: A New Approach for Geometry Creation for Additive and Hybrid Manufacturing," *Procedia CIRP,* vol. 60, pp. 199-204, 2017, doi: 10.1016/j.procir.2017.01.022.

[76]   S. Oh, Y. Jung, S. Kim, I. Lee, and N. Kang, "Deep Generative Design: Integration of Topology Optimization and Generative Models," *Journal of Mechanical Design,* vol. 141, no. 11, 2019, doi: 10.1115/1.4044229.

[77]   H. Sun and L. Ma, "Generative Design by Using Exploration Approaches of Reinforcement Learning in Density-Based Structural Topology Optimization," *Designs,* vol. 4, no. 2, 2020, doi: 10.3390/designs4020010.

[78]   A. Hussein, L. Hao, C. Yan, R. Everson, and P. Young, "Advanced lattice support structures for metal additive manufacturing," *Journal of Materials Processing Technology,* vol. 213, no. 7, pp. 1019-1026, 2013, doi: 10.1016/j.jmatprotec.2013.01.020.

[79]   S. Kapil *et al.*, "Optimal space filling for additive manufacturing," *Rapid Prototyping Journal,* vol. 22, no. 4, pp. 660-675, 2016, doi: 10.1108/rpj-03-2015-0034.

[80]   L. Cheng and A. To, "Part-scale build orientation optimization for minimizing residual stress and support volume for metal additive manufacturing: Theory and experimental validation," *Computer-Aided Design,* vol. 113, pp. 1-23, 2019, doi: 10.1016/j.cad.2019.03.004.

[81]   J. L. Bartlett and X. Li, "An overview of residual stresses in metal powder bed fusion," *Additive Manufacturing,* vol. 27, pp. 131-149, 2019, doi: 10.1016/j.addma.2019.02.020.

[82]   G. Strano, L. Hao, R. M. Everson, and K. E. Evans, "A new approach to the design and optimisation of support structures in additive manufacturing," *The International Journal of Advanced Manufacturing Technology,* vol. 66, no. 9-12, pp. 1247-1254, 2012, doi: 10.1007/s00170-012-4403-x.

[83]   F. Calignano, "Design optimization of supports for overhanging structures in aluminum and titanium alloys by selective laser melting," *Materials & Design,* vol. 64, pp. 203-213, 2014.

[84]   J. Dumas, J. Hergel, and S. Lefebvre, "Bridging the gap: Automated steady scaffoldings for 3d printing," *ACM Transactions on Graphics (TOG),* vol. 33, no. 4, pp. 1-10, 2014.

[85]   J. Jiang, X. Xu, and J. Stringer, "Support Structures for Additive Manufacturing: A Review," *Journal of Manufacturing and Materials Processing,* vol. 2, no. 4, 2018, doi: 10.3390/jmmp2040064.

[86]   R. Schmidt and N. Umetani, "Branching support structures for 3D printing," in *ACM SIGGRAPH 2014 Studio*, 2014, pp. 1-1.

[87]   J. Vanek, J. A. G. Galicia, and B. Benes, "Clever Support: Efficient Support Structure Generation for Digital Fabrication," *Computer Graphics Forum,* vol. 33, no. 5, pp. 117-125, 2014, doi: 10.1111/cgf.12437.

[88]   L. Zhu, R. Feng, X. Li, J. Xi, and X. Wei, "A Tree-Shaped Support Structure for Additive Manufacturing Generated by Using a Hybrid of Particle Swarm Optimization and Greedy Algorithm," *Journal of Computing and Information Science in Engineering,* vol. 19, no. 4, 2019, doi: 10.1115/1.4043530.

[89]   L. Zhu, R. Feng, X. Li, J. Xi, and X. Wei, "Design of lightweight tree-shaped internal support structures for 3D printed shell models," *Rapid Prototyping Journal,* vol. 25, no. 9, pp. 1552-1564, 2019, doi: 10.1108/rpj-04-2019-0108.

[90]   N. Zhang, L.-C. Zhang, Y. Chen, and Y.-S. Shi, "Local Barycenter Based Efficient Tree-Support Generation for 3D Printing," *Computer-Aided Design,* vol. 115, pp. 277-292, 2019, doi: 10.1016/j.cad.2019.06.004.

[91]   B. Vaissier, J.-P. Pernot, L. Chougrani, and P. Véron, "Genetic-algorithm based framework for lattice support structure optimization in additive manufacturing," *Computer-Aided Design,* vol. 110, pp. 11-23, 2019, doi: 10.1016/j.cad.2018.12.007.

[92]   M. X. Gan and C. H. Wong, "Practical support structures for selective laser melting," *Journal of Materials Processing Technology,* vol. 238, pp. 474-484, 2016, doi: 10.1016/j.jmatprotec.2016.08.006.

[93]   A. B. S. M. Cloots, K. Wegener, "Assessing new support minimizing strategies for the additive manufacturing technology SLM," presented at the Solid freeform fabrication symposium, 2013.

[94]   R. Vaidya and S. Anand, "Optimum Support Structure Generation for Additive Manufacturing Using Unit Cell Structures and Support Removal Constraint," *Procedia Manufacturing,* vol. 5, pp. 1043-1059, 2016, doi: 10.1016/j.promfg.2016.08.072.

[95]   N. U. Schmidt Ryan, "Branching Support Structures for 3D Printing," presented at the ACM SIGGRAPH 2014 Studio, 2014.

[96]   J. Dumas, J. Hergel, and S. Lefebvre, "Bridging the gap: automated steady scaffoldings for 3D printing," *ACM Transactions on Graphics,* vol. 33, no. 4, pp. 1-10, 2014, doi: 10.1145/2601097.2601153.

[97]   T. A. Schaedler and W. B. Carter, "Architected Cellular Materials," *Annual Review of Materials Research,* vol. 46, no. 1, pp. 187-210, 2016, doi: 10.1146/annurev-matsci-070115-031624.

[98]   M. Helou and S. Kara, "Design, analysis and manufacturing of lattice structures: an overview," *International Journal of Computer Integrated Manufacturing,* vol. 31, no. 3, pp. 243-261, 2017, doi: 10.1080/0951192x.2017.1407456.

[99]   S. Li, Y. Xin, Y. Yu, and Y. Wang, "Design for additive manufacturing from a force-flow perspective," *Materials & Design,* vol. 204, 2021, doi: 10.1016/j.matdes.2021.109664.

[100]   C. H. P. Nguyen and Y. Choi, "Concurrent density distribution and build orientation optimization of additively manufactured functionally graded lattice structures," *Computer-Aided Design,* vol. 127, 2020, doi: 10.1016/j.cad.2020.102884.

References

[101] D. Li, W. Liao, N. Dai, G. Dong, Y. Tang, and Y. M. Xie, "Optimal design and modeling of gyroid-based functionally graded cellular structures for additive manufacturing," *Computer-Aided Design,* vol. 104, pp. 87-99, 2018, doi: 10.1016/j.cad.2018.06.003.

[102] L. Chougrani, J.-P. Pernot, P. Véron, and S. Abed, "Lattice structure lightweight triangulation for additive manufacturing," *Computer-Aided Design,* vol. 90, pp. 95-104, 2017, doi: 10.1016/j.cad.2017.05.016.

[103] T. Maconachie *et al.*, "SLM lattice structures: Properties, performance, applications and challenges," *Materials & Design,* vol. 183, 2019, doi: 10.1016/j.matdes.2019.108137.

[104] N. A. F. V.S. Deshpande, M.F. Ashby, "Effective properties of the octet-truss lattice material," *Journal of the Mechanics and Physics of Solids,* vol. 49, no. 8, pp. 1747-1769, 2001.

[105] M. Leary *et al.*, "Inconel 625 lattice structures manufactured by selective laser melting (SLM): Mechanical properties, deformation and failure modes," *Materials & Design,* vol. 157, pp. 179-199, 2018, doi: 10.1016/j.matdes.2018.06.010.

[106] M. F. Ashby, "The properties of foams and lattices," *Philosophical Transactions of the Royal Society A: Mathematical, Physical and Engineering Sciences,* vol. 364, no. 1838, pp. 15-30, 2005, doi: 10.1098/rsta.2005.1678.

[107] S. Catchpole-Smith, R. R. J. Sélo, A. W. Davis, I. A. Ashcroft, C. J. Tuck, and A. Clare, "Thermal conductivity of TPMS lattice structures manufactured via laser powder bed fusion," *Additive Manufacturing,* vol. 30, 2019, doi: 10.1016/j.addma.2019.100846.

[108] M. Fantini, M. Curto, and F. De Crescenzio, "A method to design biomimetic scaffolds for bone tissue engineering based on Voronoi lattices," *Virtual and Physical Prototyping,* vol. 11, no. 2, pp. 77-90, 2016, doi: 10.1080/17452759.2016.1172301.

[109] Y. Tang, G. Dong, and Y. F. Zhao, "A hybrid geometric modeling method for lattice structures fabricated by additive manufacturing," *The International Journal of Advanced Manufacturing Technology,* vol. 102, no. 9-12, pp. 4011-4030, 2019, doi: 10.1007/s00170-019-03308-x.

[110] J. Nguyen, S.-i. Park, and D. Rosen, "Heuristic optimization method for cellular structure design of light weight components," *International Journal of Precision Engineering and Manufacturing,* vol. 14, no. 6, pp. 1071-1078, 2013, doi: 10.1007/s12541-013-0144-5.

[111] X. Huang and Y. M. Xie, "Convergent and mesh-independent solutions for the bi-directional evolutionary structural optimization method," *Finite Elements in Analysis and Design,* vol. 43, no. 14, pp. 1039-1049, 2007, doi: 10.1016/j.finel.2007.06.006.

[112] Y. Tang, A. Kurtz, and Y. F. Zhao, "Bidirectional Evolutionary Structural Optimization (BESO) based design method for lattice structure to be fabricated by additive manufacturing," *Computer-Aided Design,* vol. 69, pp. 91-101, 2015, doi: 10.1016/j.cad.2015.06.001.

[113] Y. Wang, L. Zhang, S. Daynes, H. Zhang, S. Feih, and M. Y. Wang, "Design of graded lattice structure with optimized mesostructures for additive manufacturing," *Materials & Design,* vol. 142, pp. 114-123, 2018, doi: 10.1016/j.matdes.2018.01.011.

[114] T. Wu and S. Li, "An efficient multiscale optimization method for conformal lattice materials," *Structural and Multidisciplinary Optimization,* 2020, doi: 10.1007/s00158-020-02739-5.

[115] Y. Liu, S. Zhuo, Y. Xiao, G. Zheng, G. Dong, and Y. F. Zhao, "Rapid Modeling and Design Optimization of Multi-Topology Lattice Structure Based on Unit-Cell Library," *Journal of Mechanical Design,* vol. 142, no. 9, 2020, doi: 10.1115/1.4046812.

[116] G. Dong, Y. Tang, D. Li, and Y. F. Zhao, "Design and optimization of solid lattice hybrid structures fabricated by additive manufacturing," *Additive Manufacturing,* vol. 33, 2020, doi: 10.1016/j.addma.2020.101116.

[117] J. Lee, C. Kwon, J. Yoo, S. Min, T. Nomura, and E. M. Dede, "Design of spatially-varying orthotropic infill structures using multiscale topology optimization and explicit de-homogenization," *Additive Manufacturing,* vol. 40, 2021, doi: 10.1016/j.addma.2021.101920.

[118] Q. T. Do, C. H. P. Nguyen, and Y. Choi, "Homogenization-based optimum design of additively manufactured Voronoi cellular structures," *Additive Manufacturing,* vol. 45, 2021, doi: 10.1016/j.addma.2021.102057.

[119] H.-Y. Lei, J.-R. Li, Z.-J. Xu, and Q.-H. Wang, "Parametric design of Voronoi-based lattice porous structures," *Materials & Design,* vol. 191, 2020, doi: 10.1016/j.matdes.2020.108607.

[120] W. Wang, C. Zheng, F. Tang, and Y. Zhang, "A practical redesign method for functional additive manufacturing," *Procedia CIRP,* vol. 100, pp. 566-570, 2021.

[121] Y. Wang, K.-M. Yu, C. C. L. Wang, and Y. Zhang, "Automatic design of conformal cooling circuits for rapid tooling," *Computer-Aided Design,* vol. 43, no. 8, pp. 1001-1010, 2011, doi: 10.1016/j.cad.2011.04.011.

[122] Y. Wang, K.-M. Yu, and C. C. L. Wang, "Spiral and conformal cooling in plastic injection molding," *Computer-Aided Design,* vol. 63, pp. 1-11, 2015, doi: 10.1016/j.cad.2014.11.012.

[123] Y. Tang, Z. Gao, and Y. F. Zhao, "Design of Conformal Porous Structures for the Cooling System of an Injection Mold Fabricated by Additive Manufacturing Process," *Journal of Mechanical Design,* vol. 141, no. 10, 2019, doi: 10.1115/1.4043680.

[124] B. Vaissier, J.-P. Pernot, L. Chougrani, and P. Véron, "Parametric design of graded truss lattice structures for enhanced thermal dissipation," *Computer-Aided Design,* vol. 115, pp. 1-12, 2019, doi: 10.1016/j.cad.2019.05.022.

[125] S. Yun, D. Lee, D. S. Jang, M. Lee, and Y. Kim, "Numerical analysis on thermo-fluid–structural performance of graded lattice channels produced by metal additive manufacturing," *Applied Thermal Engineering,* vol. 193, 2021, doi: 10.1016/j.applthermaleng.2021.117024.

[126] D.-J. Yoo, "Computer-aided porous scaffold design for tissue engineering using triply periodic minimal surfaces," *International Journal of Precision Engineering and Manufacturing,* vol. 12, no. 1, pp. 61-71, 2011, doi: 10.1007/s12541-011-0008-9.

[127] X. Shi *et al.*, "Design optimization of multimorphology surface-based lattice structures with density gradients," *The International Journal of Advanced Manufacturing Technology,* 2021, doi: 10.1007/s00170-021-07175-3.

[128] D. Li, N. Dai, Y. Tang, G. Dong, and Y. F. Zhao, "Design and Optimization of Graded Cellular Structures With Triply Periodic Level Surface-Based Topological Shapes," *Journal of Mechanical Design,* vol. 141, no. 7, 2019, doi: 10.1115/1.4042617.

References

[129]   D. Wu and C. Huang, "Thermal conductivity model of open-cell foam suitable for wide span of porosities," *International Journal of Heat and Mass Transfer,* vol. 130, pp. 1075-1086, 2019, doi: 10.1016/j.ijheatmasstransfer.2018.11.016.

[130]   L. Yang, C. Yan, C. Han, P. Chen, S. Yang, and Y. Shi, "Mechanical response of a triply periodic minimal surface cellular structures manufactured by selective laser melting," *International Journal of Mechanical Sciences,* vol. 148, pp. 149-157, 2018, doi: 10.1016/j.ijmecsci.2018.08.039.

[131]   Z. Cai, Z. Liu, X. Hu, H. Kuang, and J. Zhai, "The effect of porosity on the mechanical properties of 3D-printed triply periodic minimal surface (TPMS) bioscaffold," *Bio-Design and Manufacturing,* vol. 2, no. 4, pp. 242-255, 2019, doi: 10.1007/s42242-019-00054-7.

[132]   F. Caiazzo, V. Alfieri, and B. D. Bujazha, "Additive manufacturing of biomorphic scaffolds for bone tissue engineering," *The International Journal of Advanced Manufacturing Technology,* vol. 113, no. 9-10, pp. 2909-2923, 2021, doi: 10.1007/s00170-021-06773-5.

[133]   R. Guerreiro, T. Pires, J. M. Guedes, P. R. Fernandes, and A. P. G. Castro, "On the Tortuosity of TPMS Scaffolds for Tissue Engineering," *Symmetry,* vol. 12, no. 4, 2020, doi: 10.3390/sym12040596.

[134]   D. J. Yoo, "Porous scaffold design using the distance field and triply periodic minimal surface models," *Biomaterials,* vol. 32, no. 31, pp. 7741-54, Nov 2011, doi: 10.1016/j.biomaterials.2011.07.019.

[135]   S. Hashmi, *Comprehensive materials processing*. Newnes, 2014.

[136]   H. Jia, H. Sun, H. Wang, Y. Wu, and H. Wang, "Scanning strategy in selective laser melting (SLM): a review," *The International Journal of Advanced Manufacturing Technology,* vol. 113, no. 9-10, pp. 2413-2435, 2021, doi: 10.1007/s00170-021-06810-3.

[137]   X. Liu, "Four alternative patterns of the Hilbert curve," *Applied Mathematics and Computation,* vol. 147, no. 3, pp. 741-752, 2004, doi: 10.1016/s0096-3003(02)00808-1.

[138]   S. Shaikh, N. Kumar, P. K. Jain, and P. Tandon, "Hilbert Curve Based Toolpath for FDM Process," in *CAD/CAM, Robotics and Factories of the Future*, (Lecture Notes in Mechanical Engineering, 2016, ch. Chapter 72, pp. 751-759.

[139]   Z. Dong, Y. Liu, W. Wen, J. Ge, and J. Liang, "Effect of Hatch Spacing on Melt Pool and As-built Quality During Selective Laser Melting of Stainless Steel: Modeling and Experimental Approaches," *Materials (Basel),* vol. 12, no. 1, Dec 24 2018, doi: 10.3390/ma12010050.

[140]   N. T. Aboulkhair, N. M. Everitt, I. Ashcroft, and C. Tuck, "Reducing porosity in AlSi10Mg parts processed by selective laser melting," *Additive Manufacturing,* vol. 1-4, pp. 77-86, 2014, doi: 10.1016/j.addma.2014.08.001.

[141]   I. Gibson, D. Rosen, B. Stucker, and M. Khorasani, "Powder Bed Fusion," in *Additive Manufacturing Technologies*: Springer, 2021, pp. 125-170.

[142]   J. C. Steuben, A. P. Iliopoulos, and J. G. Michopoulos, "Implicit slicing for functionally tailored additive manufacturing," *Computer-Aided Design,* vol. 77, pp. 107-119, 2016, doi: 10.1016/j.cad.2016.04.003.

[143] J. Feng, J. Fu, Z. Lin, C. Shang, and X. Niu, "Layered infill area generation from triply periodic minimal surfaces for additive manufacturing," *Computer-Aided Design,* vol. 107, pp. 50-63, 2019, doi: 10.1016/j.cad.2018.09.005.

[144] J. Ding, Q. Zou, S. Qu, P. Bartolo, X. Song, and C. C. L. Wang, "STL-free design and manufacturing paradigm for high-precision powder bed fusion," *CIRP Annals,* 2021, doi: 10.1016/j.cirp.2021.03.012.

[145] R. Ponche, O. Kerbrat, P. Mognol, and J.-Y. Hascoet, "A novel methodology of design for Additive Manufacturing applied to Additive Laser Manufacturing process," *Robotics and Computer-Integrated Manufacturing,* vol. 30, no. 4, pp. 389-398, 2014, doi: 10.1016/j.rcim.2013.12.001.

[146] Y. Zhang, S. Tan, L. Ding, and A. Bernard, "A toolpath-based layer construction method for designing & printing porous structure," *CIRP Annals,* 2021, doi: 10.1016/j.cirp.2021.04.020.

[147] H. Yu, H. Hong, S. Cao, and R. Ahmad, "Topology Optimization for Multipatch Fused Deposition Modeling 3D Printing," *Applied Sciences,* vol. 10, no. 3, 2020, doi: 10.3390/app10030943.

[148] E. Fernández, C. Ayas, M. Langelaar, and P. Duysinx, "Topology optimisation for large-scale additive manufacturing: generating designs tailored to the deposition nozzle size," *Virtual and Physical Prototyping,* vol. 16, no. 2, pp. 196-220, 2021, doi: 10.1080/17452759.2021.1914893.

[149] V. Mishra, C. Ayas, M. Langelaar, and F. van Keulen, "Simultaneous topology and deposition direction optimization for Wire and Arc Additive Manufacturing," *Manufacturing Letters,* 2021, doi: 10.1016/j.mfglet.2021.05.011.

[150] G. Vantyghem, W. De Corte, E. Shakour, and O. Amir, "3D printing of a post-tensioned concrete girder designed by topology optimization," *Automation in Construction,* vol. 112, 2020, doi: 10.1016/j.autcon.2020.103084.

[151] J. Liu and H. Yu, "Concurrent deposition path planning and structural topology optimization for additive manufacturing," *Rapid Prototyping Journal,* vol. 23, no. 5, pp. 930-942, 2017, doi: 10.1108/rpj-05-2016-0087.

[152] C. Dapogny, R. Estevez, A. Faure, and G. Michailidis, "Shape and topology optimization considering anisotropic features induced by additive manufacturing processes," *Computer Methods in Applied Mechanics and Engineering,* vol. 344, pp. 626-665, 2019, doi: 10.1016/j.cma.2018.09.036.

[153] J. Liu and A. C. To, "Deposition path planning-integrated structural topology optimization for 3D additive manufacturing subject to self-support constraint," *Computer-Aided Design,* vol. 91, pp. 27-45, 2017, doi: 10.1016/j.cad.2017.05.003.

[154] E. Sales, T.-H. Kwok, and Y. Chen, "Function-aware slicing using principal stress line for toolpath planning in additive manufacturing," *Journal of Manufacturing Processes,* vol. 64, pp. 1420-1433, 2021, doi: 10.1016/j.jmapro.2021.02.050.

[155] Y. Li, K. Xu, X. Liu, M. Yang, J. Gao, and P. Maropoulos, "Stress-oriented 3D printing path optimization based on image processing algorithms for reinforced load-bearing parts," *CIRP Annals,* 2021, doi: 10.1016/j.cirp.2021.04.037.

References

[156] Y. Zhang, R. Harik, G. Fadel, and A. Bernard, "A statistical method for build orientation determination in additive manufacturing," *Rapid Prototyping Journal,* 2018, doi: 10.1108/rpj-04-2018-0102.

[157] Y. Zhang, W. De Backer, R. Harik, and A. Bernard, "Build Orientation Determination for Multi-material Deposition Additive Manufacturing with Continuous Fibers," *Procedia CIRP,* vol. 50, pp. 414-419, 2016, doi: 10.1016/j.procir.2016.04.119.

[158] J. Olsen and I. Y. Kim, "Design for additive manufacturing: 3D simultaneous topology and build orientation optimization," *Structural and Multidisciplinary Optimization,* 2020, doi: 10.1007/s00158-020-02590-8.

[159] D. Thomas, "A deep dive into metal 3D printing," presented at the Laser 3D Manufacturing VI, 2019.

[160] H. Yu and J. Liu, "Self-Support Topology Optimization With Horizontal Overhangs for Additive Manufacturing," *Journal of Manufacturing Science and Engineering,* vol. 142, no. 9, 2020, doi: 10.1115/1.4047352.

[161] S. Bureerat and K. Sriworamas, "Simultaneous topology and sizing optimization of a water distribution network using a hybrid multiobjective evolutionary algorithm," *Applied Soft Computing,* vol. 13, no. 8, pp. 3693-3702, 2013, doi: 10.1016/j.asoc.2013.04.005.

[162] A. P. Kalyanmoy Deb, Sameer Agarwal, and T. Meyarivan, "A fast and elitist multiobjective genetic algorithm: NSGA-II," *IEEE Transactions on Evolutionary Computation,* vol. Vol. 6, No. 2, 2002.

[163] K. Suresh, "A 199-line Matlab code for Pareto-optimal tracing in topology optimization," *Structural and Multidisciplinary Optimization,* vol. 42, no. 5, pp. 665-679, 2010, doi: 10.1007/s00158-010-0534-6.

[164] P. Wei, Z. Li, X. Li, and M. Y. Wang, "An 88-line MATLAB code for the parameterized level set method based topology optimization using radial basis functions," *Structural and Multidisciplinary Optimization,* vol. 58, no. 2, pp. 831-849, 2018, doi: 10.1007/s00158-018-1904-8.

[165] "Profeta." http://www.profeta.cn/ (accessed.

[166] G. Rozenberg and A. Salomaa, *The mathematical theory of L systems*. Academic press, 1980.

[167] K. Deb, A. Pratap, S. Agarwal, and T. Meyarivan, "A fast and elitist multiobjective genetic algorithm: NSGA-II," *IEEE transactions on evolutionary computation,* vol. 6, no. 2, pp. 182-197, 2002.

[168] Y. Wang, "Periodic surface modeling for computer aided nano design," *Computer-Aided Design,* vol. 39, no. 3, pp. 179-189, 2007, doi: 10.1016/j.cad.2006.09.005.

[169] S. Li, S. Wang, Y. Yu, X. Zhang, and Y. Wang, "Design of heterogeneous mesoscale structure for high mechanical properties based on force-flow: 2D geometries," *Additive Manufacturing,* vol. 46, 2021, doi: 10.1016/j.addma.2021.102063.

[170] W. E. Lorensen and H. E. Cline, "Marching cubes: A high resolution 3D surface construction algorithm," presented at the Proceedings of the 14th annual conference on Computer graphics and interactive techniques - SIGGRAPH '87, 1987.

[171] S. Rajagopalan and R. A. Robb, "Schwarz meets Schwann: design and fabrication of biomorphic and durataxic tissue engineering scaffolds," *Med Image Anal,* vol. 10, no. 5, pp. 693-712, Oct 2006, doi: 10.1016/j.media.2006.06.001.

[172] C. Maple, "Geometric design and space planning using the marching squares and marching cube algorithms," in *2003 international conference on geometric modeling and graphics, 2003. Proceedings*, 2003: IEEE, pp. 90-95.

[173] S. Liu and C. C. Wang, "Fast intersection-free offset surface generation from freeform models with triangular meshes," *IEEE Transactions on Automation Science and Engineering,* vol. 8, no. 2, pp. 347-360, 2010.

[174] Y. Bazilevs *et al.*, "Isogeometric analysis using T-splines," *Computer Methods in Applied Mechanics and Engineering,* vol. 199, no. 5-8, pp. 229-263, 2010, doi: 10.1016/j.cma.2009.02.036.

[175] T. R. Weller, D. R. Weller, L. C. d. A. Rodrigues, and N. Volpato, "A framework for tool-path airtime optimization in material extrusion additive manufacturing," *Robotics and Computer-Integrated Manufacturing,* vol. 67, 2021, doi: 10.1016/j.rcim.2020.101999.

[176] D. Ding, Z. Pan, D. Cuiuri, H. Li, and N. Larkin, "Adaptive path planning for wire-feed additive manufacturing using medial axis transformation," *Journal of Cleaner Production,* vol. 133, pp. 942-952, 2016, doi: 10.1016/j.jclepro.2016.06.036.

[177] Z. Zhang and S. Joshi, "Slice data representation and format for multi-material objects for additive manufacturing processes," *Rapid Prototyping Journal,* vol. 23, no. 1, pp. 149-161, 2017, doi: 10.1108/rpj-04-2014-0047.

[178] S. M. Thompson, L. Bian, N. Shamsaei, and A. Yadollahi, "An overview of Direct Laser Deposition for additive manufacturing; Part I: Transport phenomena, modeling and diagnostics," *Additive Manufacturing,* vol. 8, pp. 36-62, 2015, doi: 10.1016/j.addma.2015.07.001.

[179] L. D. Bobbio *et al.*, "Characterization of a functionally graded material of Ti-6Al-4V to 304L stainless steel with an intermediate V section," *Journal of Alloys and Compounds,* vol. 742, pp. 1031-1036, 2018, doi: 10.1016/j.jallcom.2018.01.156.

[180] D. W. Rosen, "Computer-Aided Design for Additive Manufacturing of Cellular Structures," *Computer-Aided Design & Applications,* vol. 4, no. 5, pp. 585-594, 2007, doi: 10.1080/16864360.2007.10738493.

Titre : **Méthodes de conception générative constructive pour la fabrication additive qualifiée**

Mots clés : Conception pour la FA, manufacturabilité, conception générative, conception constructive, système basé sur la connaissance

Résumé : Les technologies de fabrication additive (FA) donnent de plus en plus de liberté de conception aux concepteurs et aux ingénieurs pour concevoir et définir des géométries et des compositions de matériaux très complexes. En raison d'un traitement couche par couche, les contraintes, méthodes, outils et processus de conception en FA sont différents de ceux des processus de fabrication traditionnels. Les méthodes et outils de conception traditionnels ne peuvent pas répondre aux besoins de la conception en FA. Par conséquent, un nouveau domaine de recherche, la conception pour la FA (Design for AM - DfAM), a émergé pour répondre à ce besoin. Cependant, les méthodes de DfAM existantes sont soit des lignes directrices, soit des outils de calculs, qui ont une prise en compte limitée des contraintes couplées le long de la chaîne de traitement numérique de la FA et peinent à garantir la fabricabilité de la conception en FA. Pour contribuer à l'obtention d'une conception qualifiée en FA, ce travail de thèse se concentre sur trois problèmes existants typiques dans le domaine du DfAM : premièrement, comment assurer la fabricabilité dans le processus d'optimisation topologique ? Deuxièmement, comment concevoir des structures de supports allégées, faciles à retirer pour le post-traitement et de diffusion de chaleur conviviales pour assurer la précision de la forme et améliorer la rugosité de surface des pièces imprimées ? Enfin, comment éviter les pertes de précision lors de la préparation de l'impression de structures en treillis

complexes et assurer leur fabricabilité lors de la conception ?

Pour résoudre les trois problèmes identifiés, ce travail de thèse propose un ensemble de nouvelles méthodes de conception générative constructive : 1. Méthode de conception générative basée sur un modèle CSG pour assurer la fabricabilité dans l'optimisation de la topologie de la structure allégée ; 2. Méthode de conception générative constructive basée sur des modèles pour optimiser la conception de la structure de supports et 3. Conception constructive inversée basée sur les « parcours d'outils » pour obtenir directement des modèles de traitement de structures poreuses ou de réseaux complexes correspondants avec des « parcours d'outils » d'impression qualifiés. Les trois méthodes proposées intègrent les contraintes de processus de FA, réalisent un contrôle paramétrique et économisent des coûts de calcul dans le processus de conception pour obtenir un ensemble de solutions de conception candidates avec une fabrication garantie. Un ensemble d'études comparatives avec les méthodes DfAM existantes et quelques études de cas expérimentaux dans des applications médicales ont démontré les avantages des méthodes proposées. Ces méthodes constructives peuvent avoir un grand potentiel d'application pour être adoptées comme outils de conception et de prise de décision pour d'autres applications industrielles lorsqu'un DfAM qualifié est requis.

Title: **Constructive generative design methods for qualified additive manufacturing**

Keywords: Design for AM, manufacturability, generative design, constructive design, knowledge-based system

Abstract: Additive manufacturing (AM) technologies give more and more design freedom to designers and engineers to design and define highly complex geometries and material compositions. Due to a layer-by-layer processing, the constraints, methods, tools and processes of design in AM are different from that in traditional manufacturing processes. Traditional design methods and tools cannot meet the needs of design in AM. Therefore, a new research field, design for AM (DfAM), has emerged to serve this need. However, existing DfAM methods are either guidelines or pure computation-based, which have limited consideration of coupled constraints along the AM digital processing chain and are difficult to ensure manufacturability of design in AM. To obtain qualified design in AM, this research focuses on three typical existing problems in DfAM domain: Firstly, how to ensure manufacturability in (topology optimization) TO process? Secondly, how to design support structures with lightweight, easy-to-remove for post-processing and friendly heat-diffusion properties to ensure shape accuracy and improve surface roughness of printed parts? Finally, how to avoid accuracy loss in printing preparation of complex lattice structures and ensure their manufacturability in design?

To solve the three identified problems, this research developed a set of new constructive genera-tive design methods: 1. CSG-based generative design method to ensure manufacturability in light-weight topology optimization; 2. Pattern-based constructive generative design method to optimize support structure design and 3. Toolpath-based inversed constructive design to directly ob-tain processing models of corresponding complex lattice or porous structures with qualified print-ing toolpaths. The three proposed methods can well embed AM process constraints, realize para-metric control and save computation cost in design process to obtain a set of candidate design solutions with ensured manufacturability. A set of comparison studies with existing DfAM meth-ods and a couple of experiment case studies in medical applications demonstrated the methods' advantages. These constructive methods may have large application potential to be adopted as design and decision making tools for other industrial applications when qualified DfAM is required.